2019

Seeding hydrogen propellant in nuclear thermal propulsion engines

Dennis Nikitaev

SEEDING HYDROGEN PROPELLANT IN NUCLEAR THERMAL PROPULSION ENGINES

by

DENNIS NIKITAEV

A THESIS

Submitted in partial fulfillment of the requirements
for the degree of Master of Science in Engineering in
The Department of Mechanical and Aerospace Engineering
of
The School of Graduate Studies
of
The University of Alabama in Huntsville

HUNTSVILLE, ALABAMA

2019

In presenting this thesis in partial fulfillment of the requirements for a master's degree from The University of Alabama in Huntsville, I agree that the Library of this University shall make it freely available for inspection. I further agree that permission for extensive copying for scholarly purposes may be granted by my advisor or, in his/her absence, by the Chair of the Department or the Dean of the School of Graduate Studies. It is also understood that due recognition shall be given to me and to The University of Alabama in Huntsville in any scholarly use which may be made of any material in this thesis.

9/30/19

Dennis Dmitriyevich Nikitaev (Date)

THESIS APPROVAL FORM

Submitted by Dennis Dmitriyevich Nikitaev in partial fulfillment of the requirements for the degree of Master of Science in Engineering in Aerospace Systems Engineering and accepted on behalf of the Faculty of the School of Graduate Studies by the thesis committee.

We, the undersigned members of the Graduate Faculty of The University of Alabama in Huntsville, certify that we have advised and/or supervised the candidate of the work described in this thesis. We further certify that we have reviewed the thesis manuscript and approve it in partial fulfillment of the requirements for the degree of Master of Science in Engineering in Aerospace Systems Engineering.

Robert A Frederick Jr
Dr. Robert Frederick (Date) Committee Chair

Dale Thomas Oct '19
Dr. L. Dale Thomas (Date) Advisor

Jason T Cassibry 10/28/19
Dr. Jason Cassibry (Date) Committee Member

10/29/19
Dr. Keith Hollingsworth (Date) Department Chair

Shankar Mahalingam 10/30/19
Dr. Shankar Mahalingam (Date) College Dean

11/1/19
Dr. David Berkowitz (Date) Graduate Dean

ABSTRACT

School of Graduate Studies

The University of Alabama in Huntsville

Using the NASA Design Reference Architecture, Nuclear Thermal Propulsion engine and Mars transfer vehicle models were developed to numerically examine the effects of adding heavy noble gases into the hydrogen propellant stream (seeding) on round trip transit times (baseline of 357 days). Seeded hydrogen, up to maximum seed mass concentration (MSMC) 55.85%, increased engine and vehicle performance by reducing pressure losses, decreasing reactor power, and increasing the overall change in velocity while assuming constant vehicle volume and dry mass. The tradeoff was lowered specific impulse and increased net propellant mass, resulting in increased vehicle wetted mass. Vehicle performance increased at MSMC and provided a best case 32-day reduction in transit time vs. pure hydrogen. Vehicle performance was comparable to densified pure hydrogen at 30% seed mass concentration. When taken in combination with densified hydrogen, vehicle performance increased further by providing a 41-day reduction in transit time at MSMC.

Abstract Approval: Committee Chair

Dr. Robert Frederick

Department Chair

Dr. Keith Hollingsworth

Graduate Dean

Dr. David Berkowitz

ACKNOWLEDGEMENTS

The research described in this thesis would not be possible without the assistance, mentoring, and support of several people that deserve to be mentioned. First, I would like to thank Dr. Dale Thomas for providing me the opportunity to work on this research at the University of Alabama in Huntsville as well as for his guidance, mentoring, and conveying his wisdom. Second, William Knuth for his input on the turbomachinery aspects. Third, the thesis committee members, Dr. Robert Frederick and Dr. Jason Cassibry, for taking their time to review and commenting on this work. Fourth, NASA NTP Program Office for sponsoring this research. And fifth, Dr. Alexander Barzilov and Dr. William Culbreth of the University of Nevada in Las Vegas for their advising on the undergraduate portion of this research.

Lastly, I would like to thank my wife, family, and friends both in Huntsville, AL and Las Vegas, NV for supporting me through this journey and listening for countless hours as I bounced ideas back and forth with them. In particular, I would like to thank my friend and previous coworker, David Guzman, for providing the push I needed to go back to school for engineering, without you, this would not have been possible!

TABLE OF CONTENTS

Page

LIST OF FIGURES

LIST OF TABLES

LIST OF SYMBOLS

Symbol	Definition
A_e	Nozzle exit cross sectional area.
A_s	Surface area.
c	Speed of sound.
c_p	Specific heat capacity at constant pressure.
c_v	Specific heat capacity at constant pressure.
D, d	Diameter.
f	Friction factor.
f, XX%-mo	Molar fraction.
f_m, XX%-ma	Mass Fraction.
f_X	X fraction.
F	Thrust.
g	Earth's gravity constant at sea level.
H	Pressure head.
h	Enthalpy.
$\hbar$	Convective heat transfer coefficient.
K	Thermal conductivity.
I_{sp}	Specific impulse.
M	Mach number.
m	Mass.
$\dot{m}$	Mass flow rate.
mw	Molecular weight.
n	Number of moles.
P_X	Pressure of or at X.

PR	Pressure ratio.
Pr	Prandtl's number.
$\dot{Q}$	Heat transfer rate.
$\dot{W}$	Power or work rate.
r	Radius.
$\Re$	Ideal gas constant.
Re	Reynolds' number.
T_X	Temperature of or at X.
t	Thickness.
$\forall$	Volume.
v	Specific volume.
V	Velocity.
v_e	Velocity of the exhaust plume with respect to the vehicle.
X_s	Any symbol with the s subscript refers to the X property of the seed species.
X_H	Any symbol with the H subscript refers to the X property of the main lattice species, usually hydrogen.
X_{X_n}	Any symbol with the X_n subscript refers to the X property of the n species.
y	Height.
z	Axial position.
α	Reactor core buckling.
γ	Ratio of specific heats.
η	Efficiency.
μ	Viscosity.
ρ	Density.
ω	Rotational velocity.

CHAPTER 1

INTRODUCTION

1.1 Background and Challenges

Nuclear Thermal Propulsion (NTP) is a concept that dates back to the late 1950's when the government commissioned Project Rover to develop nuclear thermal propulsion engines for ballistic missiles. After the space race started, this project went under the umbrella of the Nuclear Engine for Rocket Vehicle Application (NERVA) program. This program was tasked to develop an efficient engine for allowing humans to travel to Mars. It developed an engine that had twice the efficiency of chemical rocket engines but still provided comparable thrust required for deep space transport of sizeable payloads including humans and the associated life support systems. This program set the baseline for nuclear propulsion and provided experimental data which is still relevant today. Unfortunately, the program was cancelled in 1973 in the favor of the development of a reusable launch vehicle now known as the Space Shuttle [1]. A mission to Mars seemed to always be the goal just beyond the horizon of our current technologies and ion engines were the propulsion system of choice for a long time until they proved to lack the required thrust even though their efficiency was unmatched. It was in 2017 that NASA decided to consider NTP again due to its relatively high thrust and high specific impulse (Isp) [2].

Aerojet Rocketdyne (AR) has recently developed a power balance model of an NTP engine as well as a vehicle architecture for a Mars Transfer Vehicle (MTV). This vehicle will be assembled in a highly elliptical orbit around Earth extending from Low Earth Orbit (LEO) to cislunar space in order to take advantage of smaller required changes in velocity to escape Earth's sphere of influence. Due to regulations and public safety, the NTP engine is developed as a deep space propulsion system for large payloads including crewed missions. This thesis will focus primarily on AR's engine model, their vehicle architecture, and their proposed mission to Mars as a reference for analyzing the effects of alternative propellants, primarily seeded hydrogen. [3] [4]

It is important to distinguish the terms "fuel" and "propellant" when referencing NTP systems. Unlike chemical propulsion where the fuel and propellant are one and the same, the fuel in NTP systems refers only to the substances providing the thermal energy. These substances are usually compounds with uranium such as uranium nitride, uranium carbide, and uranium dioxide. The propellant in NTP systems is the fluid that flows through the engine and absorbs the heat generated by the fuel to create thrust. NTP systems typically use hydrogen as the sole propellant due to its low molecular weight which yields high Isp. However, hydrogen also has a high specific heat capacity resulting in excellent energy absorption properties which demand high power requirements on the reactor. Hydrogen must also be stored at 20 K which may require very efficient cryocoolers depending on tank structure and duration of storage. Due to its low density, hydrogen requires extremely large tanks which result in mass increase and often must be kept in shape by pressure stabilization. However, pressure stabilized tanks tend to be extremely thin and prone to

micrometeorite damage [5]. Furthermore, the large tank volume often yields a large surface area onto which space radiation is deposited.

Alternative propellants to hydrogen have been considered and examined in the past with methane and ammonia among the most common. Both of these species are known to dissociate at the high temperatures found in an NTP system yielding a high molar fraction of hydrogen, however, the energy required to dissociate their bonds was found to far exceed the energy required to heat pure hydrogen. Moreover, the resulting dissociated mixture contains heavier species such as carbon, nitrogen, and trace combinations of them with hydrogen; this results in lower specific impulse comparable to that of highly efficient chemical engines.

A study done in the early 1970's by NASA on the nuclear gas core reactor examined the heat transfer between fissioning uranium hexafluoride plasma and hydrogen gas. It was found that at the considered temperatures for the fuel and propellant of 55,000 K [6] and 15,000 K respectively, hydrogen was optically thin to the incident radiation which was supposed to heat it. The solution was to introduce a seed which would absorb the radiative heat coming in from the plasma and then convectively transfer it to hydrogen. Essentially, seeding hydrogen in the gas core reactor made radiative heat transfer more effective [7].

By examining schematics and models of past and current NTP systems, this study found that due to hydrogen's excellent energy absorptive properties, the nuclear thermal reactor (NTR) is required to deliver over 3 to 4 times the power of commercial power water reactors per kilogram of fluid flow in order to provide the same temperature rise. Moreover, hydrogen's low density results in a high volumetric flow rate which introduces large

pressure drops within the engine ducts resulting in larger diameter ducts and an overall heavier engine structure to contain the pressures.

1.2 Proposed Solution to Challenges

The overarching goal of NTP is to provide better efficiency with comparable thrust of chemical engines. Current designs achieve this by setting chamber conditions directly upstream of the nozzle by providing high enough temperature and pressure required to yield high specific impulse but still within the operating range of current materials. However, there are three primary areas upstream of the chamber which can be improved. These areas are propellant storage density, energy storage (heat capacity), and duct pressure loss. Higher propellant storage density allows more propellant mass to be stored within the same volume., lower energy storage or heat capacity lowers the required wattage of the reactor, and lower duct pressure loss allows the NTP system to deliver higher thrust.

In this study, a similar approach to NASA's gas core reactor was taken in modifying hydrogen's unfavorable properties by introducing an impurity or seed. The requirements of this seed are to be chemically neutral, readily miscible, be in a supercritical state throughout the conditions found inside the reactor, and have more favorable properties than hydrogen. These favorable properties include lower specific heat capacity, higher boiling point, higher density, and comparable price and availability. The elements that will fit the physically preferred properties are the heavier noble gases: argon, krypton, and xenon, of which the most economical is argon. This study will examine all three of these noble gases but focus in detail on argon for engine and vehicle performance.

CHAPTER 2

LITERATURE REVIEW

2.1 Background

Nuclear Thermal Propulsion (NTP) is a concept which dates back to the late 1950's through the early 1970's originally undertaken by the Nuclear Engine for Rocket Vehicle Application (NERVA) project with a goal of creating a propulsion system capable of transporting humans to Mars. Unlike chemical propulsion, NTP does not depend on combustion of an oxidizer and fuel to produce thrust; instead, a propellant is pumped into a nuclear reactor and heated to high temperatures before being expelled through the nozzle. Essentially, the NTP based engine is a monopropellant system. [1]

The propellant of choice in NTP systems is hydrogen due to its low molecular weight which yields a high specific impulse (Isp) according to equation 2.1a. The Isp ultimately affects the vehicle mass with higher Isp values yielding lower vehicle mass for the same change in velocity. Equation 2.1b could be used to calculate the normalized Isp of a propellant component. That is, the mass flow rate of a component of interest is put in

as the mass flow rate instead of the total mass flow rate of the propellant while keeping the thrust the same.

$$I_{sp} = \frac{1}{g}\sqrt{\frac{2\gamma}{\gamma - 1}\frac{\Re}{mw}T_o\left(1 - \frac{T_e}{T_o}\right)} \tag{2.1a}$$

$$I_{sp} = \frac{F}{\dot{m}g} \tag{2.1b}$$

According to compressible flow theory, lower molecular weight yields higher speed of sound and thus higher exit velocity for a given nozzle design. The speed of sound for an ideal gas and the thrust for a rocket engine in a vacuum are given by equations 2.2 and 2.3 respectively.

$$c_e = \sqrt{\gamma\frac{\Re}{mw}T_e} \tag{2.2}$$

$$F = \dot{m}V_e = \rho_e A_e V_e^2 = \rho_e A_e (cM_e)^2 = \rho_e A_e\left(\sqrt{\gamma\frac{\Re}{mw}T_e}M_e\right)^2 = \frac{\rho_e A_e \gamma \Re T_e M_e^2}{mw} \tag{2.3}$$

Specific impulse plays an important part in determining the efficiency of a rocket engine and the molecular weight of the gas being expelled from the nozzle is a key parameter which determines it. Hydrogen gas is the lightest of all molecules, however it is not easy to work with this substance in a system context. Hydrogen's boiling point at standard atmospheric pressure is around 20 K and can be extended slightly above 30 K at

relatively high pressures [8]. Both of these temperatures are extremely low and require specially coated tanks to maintain hydrogen in a liquid state and potentially requires high efficiency cryocoolers for long term storage. This thermal management is a difficult challenge since hydrogen's density is low and requires high volume tanks yielding high surface area which allows incident radiation to deposit heat and is further compounded by the length of a round trip to Mars – approximately 3 years. This extra surface area, however, can also provide some aid in rejecting this incident heat back out to space.

Moving hydrogen from the tanks to the engines provides another challenge of pressure loss within the propellant ducts as liquid hydrogen has low density which yields high volumetric flow rate. If this pressure loss allows the pressure inside the ducts to go below the vapor pressure, hydrogen will boil and will not be pressurized by the turbopumps rendering the engine non-operational. Due to hydrogen's high Isp, an NTP engine must have a sufficiently powerful reactor to provide sufficiently high chamber temperature to realize hydrogen's high specific impulse. The relationship between the chamber temperature T_o and Isp is seen in equation 2.1.

Due to these challenges, alternative propellants have been proposed with the most common being methane (CH_4), ammonia (NH_3), water (H_2O), and carbon dioxide (CO_2). The Mars Transfer Vehicle (MTV) propellant and payload mass optimization was performed which focused on replacing liquid hydrogen with methane, carbon dioxide, and water in order to lessen some of the storage challenges associated with pure liquid hydrogen. The aggregation of the analyzed vehicle was allowed to have four SLS launches

(3 launches for propellant and engines and 1 launch for crewed payload) and four distinct orbital maneuvers (Trans Mars Injection, Mars Orbit Insertion, Trans Earth Injection, and Earth Orbit Insertion). This yielded propellant tanks that were too massive to launch into the aggregation orbit and did not satisfy the Space Launch System (SLS) payload capacity. However, if the propellant tanks were allowed to be smaller with more SLS launches and the vehicle was allowed to perform only three orbital maneuvers (cancelling the Earth Orbit Insertion maneuver and leaving the returning vehicle in a heliocentric disposal orbit), the MTV could have been theoretically constructed. The conclusion was that an MTV with pure hydrogen will be beneficial at high aggregation orbits and that pure hydrogen tank volume was a limiting factor for the SLS when launching into lower aggregation orbits. Further, the cryogenic challenges for hydrogen storage were found to be similar to those of methane. [9]

Ammonia was also researched as a potential propellant along with an ammonia-alcohol mixture by the Soviet Union for a nuclear rocket engine (ЯРД). Liquid hydrogen as well as hydrogen mixed with a small amount of methane was also proposed, but technology for testing it in ЯРД was not yet matured at the time. Originally, this engine was to be used on a ballistic missile ЯХР-2, but was later proposed to be put on the second stage of the soviet moon rocket N-1. Due to time constraints during the space race, research on ЯРД was dismissed and the N-1's propulsion systems were made to be chemical on all stages using RP-1 (kerosene) as the fuel and LOX as the oxidizer. The Soviet Union proposed methane as an additional impurity to hydrogen, however, the response of ЯРД was not examined. This work and those mentioned previously show that alternative

propellants to hydrogen and impurities added to hydrogen have been considered by both the Soviet Union and the United States during the Space Race. However, this work does not explore the details for the reasons behind considering methane as an additive. Instead, it mentions that the ammonia-alcohol mixture was considered because the Soviet space program did not have the capabilities for liquid hydrogen storage at the time. [10]

A study on an NTP based Mars ascent vehicle considered using Martian indigenous resources. This vehicle was referred to as the nuclear rocket using Indigenous Martian Fuel (NIMF). These resources included methane, carbon dioxide, water, nitrogen, and pure argon. Thermal dissociation was not incorporated, but instead, coking was mentioned as a potential concern for methane hinting that thermal dissociation was expected. Table 2.1 summarizes these results on the Isp for selected alternative propellants for an NTP system which resulted in generally lower values than for hydrogen of ~900 s at 2700 K. The majority of the work on NIMF focused on the fact that using indigenous resources would yield a much lighter vehicle and might even allow for a transfer and ascent vehicle to be one and the same. It further provided some Mars mission examples as well as a manned Titan hopper. It should be noted that this study neither considered reactor power nor the turbomachinery performance for each of these propellants. [11]

Table 2.1: Isp of Selected Indigenous Martian Propellants in Seconds [11]

Temperature (K)	CO_2	Water H_2O	Methane CH_4	CO or O_2	Argon Ar
1400	162	222	460	162	110
2800	283	370	606	253	165
3000	310	393	625	264	172
3200	337	418	644	274	178
3500	381	458	671	289	187

Among the common alternatives, methane and ammonia have the highest hydrogen content, relatively high density, and higher boiling points when compared to pure hydrogen. However, it is expected that upon entering the reactor, thermal dissociation will break apart the molecular bonds. For a given nozzle throat diameter and chamber temperature, due to the energy required to break these bonds apart, the reactor power required will be higher than that for pure hydrogen. This is due to the fact that the dissociation reactions of methane and ammonia are endothermic – the molecules absorb heat as they split [12] [13] [14]. The Isp of these dissociated heavier molecules will also be lower requiring a higher mass flow rate through the reactor to achieve this thrust level. This is because the mass content of carbon in methane and nitrogen in ammonia are around 75% and 86% respectively.

During the same time that the project NERVA was active, NASA and the United Aircraft Internal Research Program were investigating the nuclear lightbulb. This engine involved fissioning uranium hexafluoride plasma at 55,000 K [6] contained by fused silica depositing heat by radiation into hydrogen propellant which would reach temperatures in

excess of 15,000 K and provide extremely high Isp of around 2000 to 3000 seconds. The majority of the heat was given off as ultraviolet radiation to which fused silica is optically thin. However, hydrogen is also optically thin to this wavelength at these temperatures. In order to increase the effectiveness of radiation heat transfer, tungsten particles are used to seed the hydrogen. Titanium vapor may also be adequate [7]. These particles would absorb the ultraviolet radiation and then convectively transfer this heat to hydrogen. This work has shown that additives to hydrogen for the purpose of enhanced heat transfer have been considered and researched before. Furthermore, tungsten particles have relatively high molecular weight which reduces the specific impulse while increasing the radiative heat transfer from the reactor. [15]

2.2 Proposed Solution and Seeded Propellant

In the favor of keeping the total reactor power the same as it has been calculated for pure hydrogen by numerous studies [1] [3] [16] [17] [18], or perhaps even lessen it, hydrogen should not be bonded with its impurity upon entering the reactor in order to avoid spending energy on dissociating the bonds. In order to ensure that no unwanted chemical reactions occur and the propellant channels do not experience coking or other congestions under the extreme conditions found in the reactor, noble gases will be analyzed as the added impurities or “seeds” instead. The general idea behind seeded propellant is to densify the propellant, increase the effectiveness of convective heat transfer, and reduce internal pressure losses. Hydrogen and argon have been examined before and have been found to not form stable chemical compounds at low temperatures nor form any compounds at high temperatures [19]. Furthermore, krypton only forms compounds with fluorine between 77

K and 90 K [20]; and xenon bonds with hydrogen at pressures only above 50,000 atm [21] where the maximum expected pressure of an NTP system is below 200 atm [3]. Argon and other heavy noble gases by themselves are primarily used for ion propulsion which ionizes gases and magnetically accelerates their atoms to high velocities thus producing thrust. These gases are also used in reaction control system (RCS) thrusters as cold propellants [22]. Therefore, this seed has the option of increasing engine performance and, at the same time, being the propellant for RCS.

A study was done which analytically explored the injection of an inert gas into a chemical rocket combustion chamber for a Mars ascent vehicle using Martian indigenous resources as a continuation of the same effort from the NIMF. The result was that the Isp decreased for the engine in general when an inert gas was added into the oxygen and hydrogen mixture as shown in Figure 2.1.

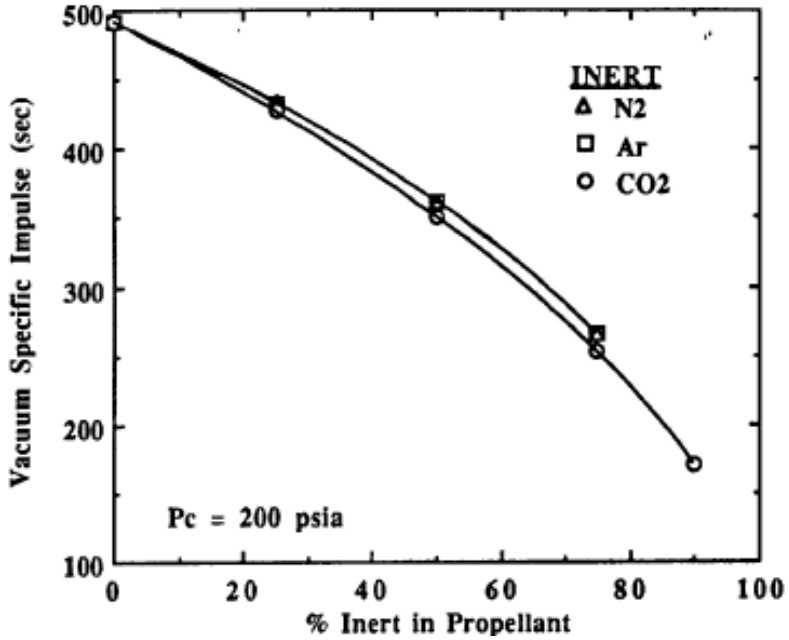

Figure 2.1: Effect on propellant specific impulse of addition of inert reaction mass to H2-O2 fueled engine [23]

However, if only hydrogen and oxygen were analyzed, their normalized Isp increased as shown in Figure 2.2 via equation 2.1b. The definition of normalized Isp has been presented earlier in this chapter. Therefore, the normalized Isp for the resources brought from Earth increased as a result of adding indigenous inert gases. It was concluded that the injection of an inert gas into a rocket combustion chamber decreased overall propellant mass that was to be brought from Earth by 10% to 13.5% with the most savings being between 60% and 80% inert mass fraction [23]. This is significant because analyses were completed on the performance of a rocket engine which used a mixture of traditional propellant with inert gases without finding any fundamental drawbacks.

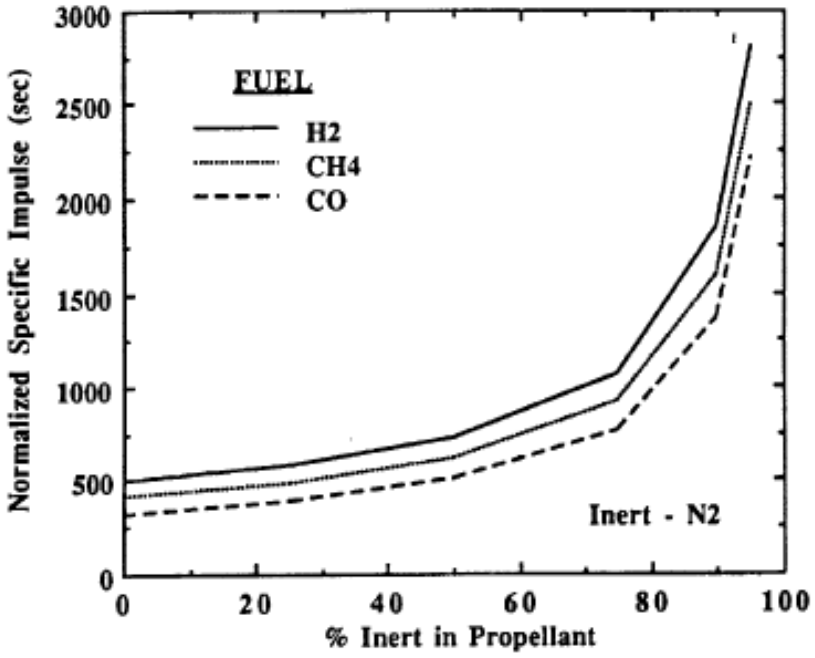

Figure 2.2: Isp (F+O) [Specific impulse normalized to fuel and oxidizer flow], showing effect of addition of inert reaction mass to hydrogen, methane, and carbon monoxide fueled engines [23]

To date, no research has been conducted to analyze seeding hydrogen with noble gases to run through an NTP based system. Further, the studies that have been conducted on alternative propellants in rocket engines did not have high fidelity simulation models and were only able to provide engine performance parameters rather than an in-depth view of engine performance complete with the additional load on the turbomachinery. The main overarching question of this thesis then becomes: *how does adding a noble gas impurity to pure hydrogen affect engine and vehicle performance?* In order to answer this question and find out what further questions to ask, further review of studies that involve the addition of noble gases into hydrogen and rocket engines must be conducted.

Noble gases are non-reactive, have low specific heat capacities, have high densities – especially in the liquid state, and most can be stored at temperatures achievable by a single stage cryocooler [24]. Due to the later, helium and neon have been disqualified as candidates and the focus will be on argon, krypton, and xenon. These seeds will not run through the main turbomachinery or cooling channels, but will instead be mixed into hydrogen directly before it is injected into the reactor. There are multiple reasons for this:

1. Supercritical hydrogen exits the pumps at very low temperatures (~50 K). Introducing a seed such as argon or heavier can cause the seed to form solid particles within the duct and damage it. This is due to the freezing point being very close (within 20 K) to the boiling point on average of any considered seed.
2. Due to hydrogen's excellent energy storage properties, it is preferable for it alone to run through the turbines in favor of reducing the temperature drops.

Dedicated seed turbomachinery will be used to pressurize the seed for this investigation. Hydrogen will flow through the seed turbine and the main turbines simultaneously. A quantitative analysis of the flow through the turbomachinery is provided in Appendix B.

3. After hydrogen exits the turbomachinery, it has already exhausted almost half of the pressure to which it was initially pressurized, a seed only needs to be pressurized to that pressure thus alleviating some of the work that hydrogen has to do inside the seed turbine. Further, the pressure to which the seed will be pressurized will be above its critical pressure. After the seed has been pressurized, it will run through ducts on the outside of the reactor to be heated above it's critical temperature. Since these two species will be mixed when they are both in their supercritical phase, they will be completely miscible with each other due to supercritical fluid properties [25]. The rate of diffusion, however, varies and a study on supercritical diffusion of argon into supercritical hydrogen has not yet been done. For this investigation, it is assumed that the rate of diffusion will be instantaneous due to turbulent flow. It should be noted that Dr. Martin Poliakoff, a leading expert in supercritical fluids, confirmed the reasonableness of this assumption (refer to Appendix C for the correspondence) [26]. Supercritical argon, krypton, and xenon diffusion into supercritical hydrogen is outside the scope of this study and is left for future research.

It is expected that the increased overall density will increase the net pressure coming out of the turbomachinery, the decreased overall heat capacity will decrease the required reactor power given constant propellant temperature coming out of the reactor, and the pressure loss through the hydrogen ducts will be less since less hydrogen will be flowing through ducts of the same length and diameter. All of this will contribute to less strain on the turbomachinery and reactor which can also result in an engine with a slightly lower mass and/or longer life if vehicle reusability is considered. In summary, the seed inside hydrogen is expected to densify the propellant, improve convective heat transfer, and reduce pressure drops through the turbomachinery. Each of these improvements will now be reviewed and compared with previous research.

2.2.1 Densifying the Propellant

There have been many studies conducted for propellant densification in an attempt to primarily limit the size of propellant tanks to save vehicle mass. The most commonly referenced of these studies include physical testing conducted by NASA Lewis Research Center [27], historical review of densification tests over the past 50 years up until the publication year 2000 conducted by NASA Glenn Research Center [28], and R&D processes for increasing density of cryogenic propellants conducted by the University of Central Florida [29]. The traditional approach was to decrease propellant temperature for densification and decrease propellant pressure to allow for thinner walled vessels resulting in decreased vehicle dry mass. However, the majority of these studies focused on launch vehicles, primarily the X-33 single stage to orbit (SSTO) vehicle, which would use all of the densified propellant within minutes. The reduced tank pressure would not affect engine

performance since gravity and acceleration during launch will provide the minimum required inlet pressure for the turbomachinery. These studies neither examined the capability for introducing more propellant within the same volume, nor did they examine propellant densification via additives.

Long-term in-space densified liquid hydrogen storage was examined by the United Launch Alliance (ULA) complete with thermodynamic modelling and experimentation with the primary focus on the Thermodynamic Cryogen Subcooler (TCS) and its upgraded components due to recent technological updates. These upgraded components coupled with experimental testing showed the capability for providing densified liquid hydrogen for launch vehicles as well as the plausibility of long-term in-space densified hydrogen storage [30]. Analytical modeling and simulation were performed in two studies resulting in the conclusion that densified propellant with zero boil off will decrease vehicle mass [31] [32]. These studies examined only the storage of densified liquid hydrogen for in-orbit refueling depots with a tank pressure of 0.133 atmospheres which is less than the current NASA DRA 5 tank pressure of 2 atmospheres [16]. The consequences of this are that the turbomachinery of the engine would not function properly with the lack of tank pressure during in-space burn events rendering this approach to densifying hydrogen propellant as impractical for usage on a vehicle, although well suited for the in-orbit refueling depot that the study considered.

A more recent study focused on propellant tanks that would store liquid hydrogen at atmospheric pressure and at temperatures between 14 K and 20 K – just above

hydrogen's freezing point. It was found that densifying hydrogen at these conditions resulted in some flexibility considering the propellant tank sizes and liquid hydrogen mass with the potential of increasing the total change in velocity by increasing propellant mass by up to 8.16% given the same volume. The exact value of total change in velocity depends on the inert payload and initial propellant masses. Smaller propellant tanks tend to absorb less space radiation and do not attenuate the radiation coming from the engine as effectively, thus resulting in an overall decrease in the heat that must be removed by the cryocoolers. [33] Given all of this, the first question that will help answer the overarching question of this thesis is: *can the propellant mass increase further than 8.16% given the same volume and provide a larger change in velocity than densified hydrogen?*

2.2.2 Increasing the Effectiveness of Convective Heat Transfer

Convective heat transfer is the mode of transferring heat between fluids and solids. This mode of heat transfer is highly dependent upon the properties of the working fluid, especially the specific heat capacity, viscosity, and thermal conductivity [34]. Some fluids, such as oil, water, and ethylene glycol are poor heat transfer fluids, but their use is still preferred due to their accessibility. In order to increase their heat transfer, solid nanoparticles have been injected turning these once conventional fluids into nanofluids. A nanofluid's properties can be tuned according to the size of the nanoparticles, their material, and their concentration (usually 1%-5% volume). These small concentrations can increase the thermal conductivity by 20% to 60%. [35] A future study may examine seeding hydrogen with solid nanoparticles instead of noble gases. Foreseeable challenges would be

the techniques used to inject and mix nanoparticles into hydrogen as well as the possibility of fuel element channel congestion similar to that of coking from methane.

When seeding the heavier noble gases into the hydrogen stream, a similar effect to injecting nanoparticles is expected to occur. However, instead of tuning the viscosity and thermal conductivity, the specific heat capacity and density of the fluid are tuned instead. The viscosity and thermal conductivity will be calculated by using the partial sums method [36] [37]. The specific heat capacity will be calculated by using the equation of state [38]. Both of these mechanisms will be explained in Chapter 4.

Since the seeded propellant is a mixture, the critical point will be affected by the addition of the seed. There have been several very complex analytical and numerical formulations for finding critical points of a fluid mixture usually derived from the equation of state. Although these formulations can provide a general idea of the trend that the true critical temperatures and pressures follow, the numerical values may have up to a 10% to 30% percent error depending on the mixture components. Therefore, the only way to reliably determine the critical point of a mixture is to run experiments and tabulate the results. [39] [40] Unfortunately, no study was conducted on the critical point of hydrogen mixed with any noble gas except helium. However, a simple approximation can provide an idea of the critical point of seeded hydrogen by invoking the use of the lever rule based on the molar fraction of the seed resulting in the calculation of the pseudocritical point. Further, since this mixture contains diatomic and monoatomic substances, the pseudocritical point should be within about 5% of the true critical point. [41]

The second question that will help answer the overarching question of this thesis then becomes: *how much does the noble gas seed increase the overall convective heat transfer of pure hydrogen?* This question needs to be answered in terms of multiple parameters such as the Reynolds number, Prandtl number, heat transfer coefficient, etc. The critical points of seeded hydrogen will also need to be located as a function of percent seed in order to determine the phase of the fluid.

2.2.3 Reducing Internal Pressure Losses

Duct pressure losses are affected by duct diameter, duct length, fluid density, mass flow rate, and fluid viscosity. The magnitude of the effect that the viscosity has on pressure loss can be negligible or substantial depending on the fluid. The duct diameter, fluid density, and mass flow rate contribute to the fluid velocity which is the primary factor affecting the pressure loss followed by the duct length. In the NTP engine utilizing seeded propellant, the hydrogen and seed flows will be separate from each other until mixing together before entering the reactor core. The reasons for this have been explained previously in the beginning of section 2.2 with quantitative details available in Appendix B. The consequences of this are reduced duct pressure loss in the turbomachinery lines due to lower hydrogen mass flow rate. The mathematical relations for duct pressure loss and the relations among the parameters introduced in this subsection are described in detail in Chapter 4. Therefore, the third and final question that will help answer the overarching question of this thesis is: *how much pressure loss can be avoided when using seeded hydrogen as the propellant as opposed to pure hydrogen?*

2.3 Summary

Previous research has shown that even though hydrogen provides the best engine performance, it does not necessarily provide the best overall vehicle architecture and feasibility given its challenges of low density, low boiling point, and high specific heat capacity. Many alternative propellants for NTP derived engines were proposed and analyzed at high levels but none of these studies went into the intricacies such as different reactor power levels and the effects on the engine turbomachinery that come with varying the propellant. Further, these studies only focused on replacing the hydrogen propellant inside the NTP system completely with the alternative rather than adding varying amounts of this alternative into hydrogen. The addition of inert gases into a chemical rocket engine in varying amounts was analyzed for Martian ascent vehicles only and not the transfer vehicles. Densified hydrogen was analyzed primarily for launch vehicles and very few studies analyzed it for an MTV.

This literature review results in the following research question with three follow up questions:

Research Question:

How does the addition of an inert noble gas, a seed, into the hydrogen propellant affect the engine performance as well as the overall vehicle performance and architecture and whether this will be better than simply densifying pure hydrogen propellant?

To answer this, three follow up questions must be answered first:

1st Follow Up Research Question:

Can seeding hydrogen provide a higher density increase percentage and also yield better overall change in velocity than densified hydrogen?

2nd Follow Up Research Question:

How is convective heat transfer affected by the addition of the seed?

3rd Follow Up Research Question:

How does adding a seed affect the internal engine pressure losses?

As discussed, densified hydrogen yields a propellant mass increase of 8.16% given the same volume. The 1st follow up question addresses this, but to answer this question, the effect that the seed has on engine performance has to be examined which is addressed by

the 2nd and 3rd follow up questions. The answer to these two remaining follow up questions depends on a multitude of various interrelated parameters of which two are the most important: the specific heat capacity and the density. Lower specific heat capacity will yield lower reactor power levels while high density will yield lower fluid velocity which in turn reduces internal pressure losses. Once the answers to the questions regarding density, convective heat transfer, and internal pressure losses have been answered, it will become apparent how adding a noble gas impurity to pure hydrogen affects engine and vehicle performance – the overarching question.

CHAPTER 3

METHODOLOGY

There is one overarching question that this thesis will attempt to answer: How does seeded hydrogen affect engine performance? In order to answer this, the following three questions must be first addressed:

1. Can seeded hydrogen increase overall propellant density higher than 8.16% as seen with densified pure hydrogen and also provide higher change in velocity with the same vehicle volume?
2. How does the addition of a seed affect the convective heat transfer between the propellant and the reactor?
3. How does the addition of a seed affect internal pressure losses?

This chapter will explain the methodology that will be used to answer these questions.

3.1 Density (1st Follow Up Question)

In seeded hydrogen, the seed, a noble gas, is kept in a separate tank than hydrogen since these substances' freezing and boiling points differ greatly. Furthermore, the ability to adjust the amount of seed in the hydrogen propellant can be beneficial by adding another degree of freedom in the engine operation. On the bulk density level, the combined density of these fluids will need to be treated as the density of a mixture. Unfortunately, the standard formulas used to calculate the density of a mixture depend on knowing the volume that each substance occupies as well as their respective masses. Due to the fact that the amount of seed can be described by either the molar fraction of the seed or the mass fraction of the seed, the volume that the seed and hydrogen occupy is not explicitly known. Moreover, it is desired to prove that the method used to calculate the density of this pseudo mixture is correct.

Therefore, two analytical formulations of the density based on the molar fraction of the seed will be independently developed. The first formulation will use the thermodynamic property of specific volume for each substance. The second formulation will use the definition of density: mass over volume. If these two formulations provide the same analytical formula in terms of the molar fraction of the seed, then the approach for calculating the density of this pseudo mixture will be validated. Using this result, the mass of the vehicle will be calculated given the bulk propellant tank volume and the molar fraction of the seed. This will then yield the answer to the first part of question 1 which asks if seeded hydrogen can provide a density increase of over 8.16% as seen in densified

hydrogen. The second part of this question which asks the seeded propellant to provide more change in velocity than densified hydrogen, is related to the engine performance which will become evident after answering the next two questions.

3.2 Convective Heat Transfer (2nd Follow Up Question)

The process for providing the answer to question 2 will be much more complicated than that for the first part of question 1 as it involves analyzing particular fluid states inside the engine as the propellant flows through it. To accomplish this, a model of the fluid flow through the engine must be constructed and this model must be based on a validated and functioning engine model. Although NERVA had very detailed documentation on their engines, they did not necessarily have an in-depth view of the fluid states at key points along the fluid flow path. Furthermore, the current NASA DRA 5 calls for a slightly different design than that of NERVA and NASA has tasked Aerojet Rocketdyne (AR) to develop it. Their model provides the in-depth view of the state that pure hydrogen is in along its flow path and can be used as a valid source to both model and compare.

All of this leads to the first task in attempting to answer question 2: build an accurate model of the AR engine which can then be modified to accommodate the additional turbomachinery and ducting for the seed. Although a single MATLAB code can be used to model this engine, using Simulink will be better as it will provide a visualization of the engine flow schematic as well as the ability to separate each engine component by blocks allowing a much easier and more robust work flow and solution to unknown variables. The engine components that will be modeled are the pumps, turbines, reactor, nozzle, and ducts.

Since only very basic parameters for each component are known, the fluid states before and after each component will be used to solve for the rest of the parameters which will be highly important in analyzing the flow profile as it varies while adding the seed.

Once the engine model is built, it will provide fluid flow parameters which will then be tuned to match those of the AR model [42]. Once tuned, this model will be modified to accommodate for the geometry and several parameters of a NERVA engine for further validation. If this model passes and matches the performance parameters of both the AR model and NERVA, then it will be concluded that the results given by this model are accurate and that the Simulink model has been validated. Then this model will be modified to accommodate for the turbomachinery and ducting required for introducing the seed into the hydrogen flow just before it enters the reactor. By setting the amount of seed to be zero, the model will then be validated again to ensure that the addition of these components did not invalidate it and that it still gives the same values as it did in the non-modified case.

The equations used to calculate the convective heat transfer and those parameters that affect it are presented in Chapter 4. These equations are valid for mixtures as stated by their sources and should provide reliable values concerning the convective heat transfer of the mixture inside the reactor. Further validations of the assumptions used such as “the mixture will remain supercritical as it flows through the reactor” will be analyzed separately from the model using the flow conditions and the lever rule for calculating the pseudocritical points. At this stage, the model should provide insight on the required reactor

power level given the amount of seed introduced into the propellant along with other performance parameters which will be able to answer question 2.

3.3 Pressure Losses (3rd Follow Up Question)

Question 3 asks how much pressure loss will be inside the engine due to the addition of the seed. The model developed for answering question 2 will be employed to provide the answer to this question. Pressure is lost inside this engine by two means: turbines to produce work and pressure loss from flow inside ducts. The percentage by which the propellant is densified and the mass flow rate through the nozzle throat both depend on the molar fraction of the seed and are the keys in determining how much pressure loss will be experienced by the propellant. The maximum mass flow rate through the throat depends on the pressure and temperature of the propellant exiting the reactor, the overall molar mass of the mixture, ratio of specific heats, and the nozzle throat area. The nozzle throat area and temperature of the propellant exiting the reactor will remain constant since the fuel is designed to operate at a specific temperature and the nozzle cannot be physically changed during engine operation.

The overall molar mass of the mixture will be fixed based on the molar fraction of the seed. This leaves the pressure of the propellant coming out of the reactor and the ratio of specific heats to be the variables that would need to be solved by an iterative method as they depend upon a myriad of other parameters that are affected by the temperature and pressure at every point in the flow throughout the engine. The Simulink model will be able to provide these values and show a point of convergence where the changes in the pressure

loss through the ducts equalize with the changes in the mass flow rate through the nozzle throat. As the mass flow rate through the throat changes for a given molar fraction of the seed, so do the pressure losses. The turbines have a set pressure ratio, therefore, the pressure losses before the turbines affect the pressure coming out of the turbines. Consequently, if it is found that the pressure losses are lower before the turbines, the pressure coming out of the turbines will be higher. After leaving the turbines, the hydrogen flow will be mixed with the seed and enter the reactor. The mass flow rate through the throat of the nozzle and the pressure coming from the reactor will dictate the performance of the engine through parameters such as thrust and Isp. Once the converged parameters from the model have been extracted at various molar fractions of the seed, question 3 can be answered.

The answers to questions 2 and 3 alone are not enough to answer the second part of question 1 which asks if seeded propellant will provide a larger change in velocity than densified hydrogen. This will involve using Tsiolkovsky's ideal rocket equation (shown in Chapter 4) and inputting the parameters of the vehicle utilizing pure hydrogen [43], densified hydrogen [33], and seeded hydrogen. The seeded hydrogen parameters will be taken from the Simulink model. The analysis of densified seeded hydrogen through the engine is left for future research due to the fact that the volumetric flow rate of densified hydrogen differs from that of pure hydrogen resulting in the need for differently designed pumps. However, a basic vehicle analysis could still be made with the assumption that engine performance with densified hydrogen will be the same given that the appropriate changes to the turbomachinery have been made. The ideal rocket equation will provide

comparison curves for the change in velocity as a function of the molar amount of seed which will answer the second part of question 1.

The results will be comprised of best and worst case scenarios to provide the range of expected vehicle performance. The criteria of determining the best and worst case is the propellant mass allocated to the reaction control and orbital maneuvering systems. The best case scenario keeps these masses the same while the worst case scenario allows these masses to grow, and therefore, infringe upon the remaining propellant volume used for the main thrust events. Upon answering all three questions, their answers will provide insight into how seeded propellant affects engine and vehicle performance, thus answering the overarching research question.

The remaining structure of this thesis is laid out as such: Analytical formulations of relevant theories and mathematical expressions will be explored in Chapter 4. Chapter 5 will include the steps taken to create an NTP engine model as well as its validation process. Chapter 6 will focus on adding various amounts of the seed to the hydrogen and examining engine performance via the engine model. Finally, Chapter 7 will examine the overall vehicle performance given a specific seed and the seed amount using patched conics orbital mechanics. Additional information as well as 3D fluid parameter plots as functions of temperatures and pressure are provided in the appendices.

CHAPTER 4

ANALYTICAL FORMULATIONS

4.1 Review of Compressible Flow Equations

Compressible flow equations are derived from isentropic relations. This assumption is acceptable as nozzle efficiencies are usually between 95% to 99% [44]. The isentropic relations from thermodynamics are shown in equation 4.1. For a de Laval Nozzle, these isentropic relations are expressed as equations 4.2 through 4.4 where the x subscript represents that value at the x length along the nozzle. The Mach number can be determined through the use of the transcendental area ratio equation 4.5. The maximum mass flow rate through the de Laval Nozzle, shown in equation 4.6, occurs when the flow is choked which happens at the throat denoted by the "*" superscript. The Isp and thrust equations were introduced in section 2 as equations 2.1a, 2.1b, and 2.3 respectively.

$$\frac{P_2}{P_1} = \left(\frac{T_2}{T_1}\right)^{\frac{\gamma}{\gamma-1}} = \left(\frac{\rho_2}{\rho_1}\right)^{\gamma} \tag{4.1}$$

$$\frac{T_0}{T_x} = 1 + \frac{\gamma - 1}{2} M_x^2 \tag{4.2}$$

$$\frac{P_0}{P_x} = \left(1 + \frac{\gamma - 1}{2} M_x^2\right)^{\frac{\gamma}{\gamma - 1}} \tag{4.3}$$

$$\frac{\rho_0}{\rho_x} = \left(1 + \frac{\gamma - 1}{2} M_x^2\right)^{\frac{1}{\gamma - 1}} \tag{4.4}$$

$$\frac{A^*}{A_x} = M_x \left[\frac{\frac{\gamma + 1}{2}}{1 + \frac{\gamma - 1}{2} M_x^2}\right]^{\frac{\gamma + 1}{2(\gamma - 1)}} \tag{4.5}$$

$$\dot{m}_{max} = P_0 A^* \sqrt{\frac{\gamma}{RT_0}} \cdot \left(\frac{2}{\gamma + 1}\right)^{\frac{\gamma + 1}{2(\gamma - 1)}} \tag{4.6}$$

4.2 Density

4.2.1 Specific Volume Approach

From thermodynamics, when two species are mixed, their intensive properties can be found on a mole or mass fraction basis, based on whether the property of interest is in terms of units per mole or units per unit mass. Since density is usually given in terms of volume per unit mass and specific volume is the reciprocal of density, the mass fraction basis will be used. Furthermore, the seed amount will be in terms of molar fraction due to the fact that gas mixture composition is usually given in terms of mole fractions. The density derivation will assume liquid states for both the main lattice and seed species, and thus incompressibility. The relationship between specific volume and density of a mixture is shown as equation 4.7. The derivation using this method may be found in Appendix H.1 and the final result is seen in equation 4.8 where subscripts *H* and *s* refer to hydrogen and the seed respectively.

$$v = \sum_{i=1}^{n} f_{m_i} v_i \Rightarrow \rho = \left[\sum_{i=1}^{n} f_{m_i} v_i\right]^{-1} \tag{4.7}$$

$$\rho = \frac{\rho_H \rho_s [(1 - f_s) m w_H + f_s m w_s]}{(1 - f_s) m w_H \rho_s + f_s m w_s \rho_H} \tag{4.8}$$

4.2.2 Mass Over Volume Approach

The overall propellant density was rederived by using the definition of density shown in equation 4.9. The derivation using this method may be found in Appendix H.2 and the final result is seen in equation 4.10.

$$\forall = \frac{m}{\rho} \tag{4.9}$$

$$\rho = \frac{\rho_H \rho_s [(1 - f_s) m w_H + f_s m w_s]}{(1 - f_s) m w_H \rho_s + f_s m w_s \rho_H} \tag{4.10}$$

4.3 Heat Transfer

Convective heat transfer is the mode of transferring heat between fluids and solids. The information in this section was taken from Mill's Heat Transfer textbook [34]. Newton's law of cooling is the most common equation used to express convective heat transfer and is shown in equation 4.11. In this equation, $\dot{Q}$ is the rate of heat transfer, A_s is the surface area, T_s is the temperature of the surface, and T_∞ is the environmental temperature or the temperature of the fluid.

$$\dot{Q} = \hbar A_s (T_s - T_\infty) \tag{4.11}$$

The convective heat transfer coefficient $\hbar$ was historically set as some value by Isaac Newton as he could not find a correlation for it during his time. Since then, this coefficient has had many interpretations and formulations ranging from expressions for laminar flow of inviscid fluids in smooth ducts to turbulent flow of viscous fluids in rough ducts. Since in rocket engine ducts the fluid flow is turbulent, the ducts are not ideally smooth and have bends, and the fluids involved are very much viscous, the Gnielinski correlation for the convective heat transfer coefficient will be used and is displayed as equation 4.12a. Due to duct roughness and the desire for a closed form solution, Wood's empirical correlation for the friction factor f will be used and is seen in equation 4.12b. For reference, the Reynolds number and the Prandtl number are shown in equations 4.12c and 4.12d respectively.

$$\hbar = \frac{K}{D_{hyd}} \frac{\frac{f}{8} Pr(Re - 1000)}{1 + 12.7\left(\frac{f}{8}\right)^{1/2} (Pr^{2/3} - 1)} \tag{4.12a}$$

$$f = 0.094\left(\frac{\varepsilon}{D_{hyd}}\right)^{0.225} + 0.53\frac{\varepsilon}{D_{hyd}} + \frac{88\left(\frac{\varepsilon}{D_{hyd}}\right)^{0.44}}{Re^{1.62\left(\frac{\varepsilon}{D_{hyd}}\right)^{0.134}}} \tag{4.12b}$$

$$Re = \frac{\text{inertial forces}}{\text{viscous forces}} = \frac{VD_{hyd}}{\nu} = \frac{\rho V D_{hyd}}{\mu} = \frac{4\dot{m}}{\pi \mu D_{hyd}} \tag{4.12c}$$

$$Pr = \frac{\text{viscous diffusion rate}}{\text{thermal diffusion rate}} = \frac{\nu}{\frac{\rho K}{c_p}} = \frac{\mu c_p}{K} \tag{4.12d}$$

When analyzing the change in temperature of a fluid flowing through a duct heated by internal forced convection, a secondary set of equations are required which have been taken from Cengel's Heat Transfer textbook [45]. The heat transfer rate for fluid flow through a duct is shown in equation 4.13 where ΔT_{ln} is the logarithmic mean temperature difference. Here, T_i is the fluid inlet temperature and T_e is the fluid exit temperature. The logarithmic mean temperature difference term comes from the fact that the fluid temperature varies logarithmically along the length of a duct rather than linearly as it would have been described in equation 4.11 if $T_s - T_\infty$ were to be replaced by $T_i - T_e$ of the fluid. However, the classic heat capacity formula is still valid and is shown in equation 4.14. By setting equations 4.13 and 4.14 equal to each other, an expression for the fluid temperature at the duct exit is formulated and shown in equation 4.15.

$$\dot{Q} = \hbar A_s \Delta T_{ln} = \hbar A_s \frac{T_i - T_e}{\ln\left(\frac{T_s - T_e}{T_s - T_i}\right)} \tag{4.13}$$

$$\dot{Q} = \dot{m} c_p (T_e - T_i) = \dot{m}(h_e - h_i) \tag{4.14}$$

$$T_e = T_s - (T_s - T_i)\exp\left(-\frac{\hbar A_s}{\dot{m} c_p}\right) \tag{4.15}$$

By expanding equation 4.15 to capture all of the terms mentioned in equations 4.12a-4.12d, equation 4.16 shows that the exit temperature of the fluid is highly dependent on the thermophysical properties of that fluid. These properties are specific to each fluid and can be tuned to desirable values by introducing mixtures.

$$T_e = T_s - (T_s - T_i)\exp\left(-\frac{A_s}{\dot{m}D_{hyd}}\frac{\frac{f}{8}\left(\rho V D_{hyd} - 1000\mu\right)}{1 + 12.7\left(\frac{f}{8}\right)^{1/2}\left[\left(\frac{\mu c_p}{K}\right)^{2/3} - 1\right]}\right) \tag{4.16}$$

Based on equation 4.16, the primary fluid thermophysical properties of interest are the specific heat capacity, viscosity, and thermal conductivity. Based on the Beattie-Bridgeman equation of state for gas mixtures [38], the approximate equations for the specific heat capacities of gas mixtures are given by equations 4.17a and 4.17b. In these equations, A_0 and c are parameter constants occurring in the equation of state as described by Beattie and calculated by a thermophysical property library called CoolProp [46] in this study.

$$c_p = \sum_{i=1}^{n} f_{m_i} c_{p_i} + P\left[\frac{2\left(\sum_{i=1}^{n} f_{m_i} A_{0i}^{1/2}\right)^2}{RT^2} + \frac{12\sum_{i=1}^{n} f_{m_i} c_i}{T^4}\right] \tag{4.17a}$$

$$c_v = \sum_{i=1}^{n} f_{m_i} c_{v_i} + P\frac{6\sum_{i=1}^{n} f_{m_i} c_i}{T^4} \tag{4.17b}$$

There is no well-defined simple viscosity formula for mixtures containing very high hydrogen concentrations [36]. Furthermore, the CoolProp library [46] has viscosity and thermal conductivity mixture models for the hydrogen/argon and hydrogen/helium mixtures but lacks them for the hydrogen/krypton and hydrogen/xenon mixtures. In order to find the correct formula to use for determining the viscosity of heavy noble gas mixtures with high hydrogen content, the hydrogen/argon and hydrogen/helium mixtures were used as the validation since models for them are available. The Gambill equation 4.18a was used

as the fundamental equation for the viscosity of a binary mixture with its exponents modified until the curve fitted the model. This equation will then be applied to a hydrogen/helium mixture for secondary validation. After doing this, equation 4.18b for a high hydrogen content mixture with noble gases was found and Figure 4.1 shows the close fit of this equation with the hydrogen/argon and hydrogen/helium models as well as the divergence of the Gambill equation.

$$\mu_{mix} = \left(f_H \mu_H^{1/3} + f_s \mu_s^{1/3}\right)^3 \tag{4.18a}$$

$$\mu_{mix} = \left(f_H \mu_H^{1/200} + f_s \mu_s^{1/200}\right)^{200} \tag{4.18b}$$

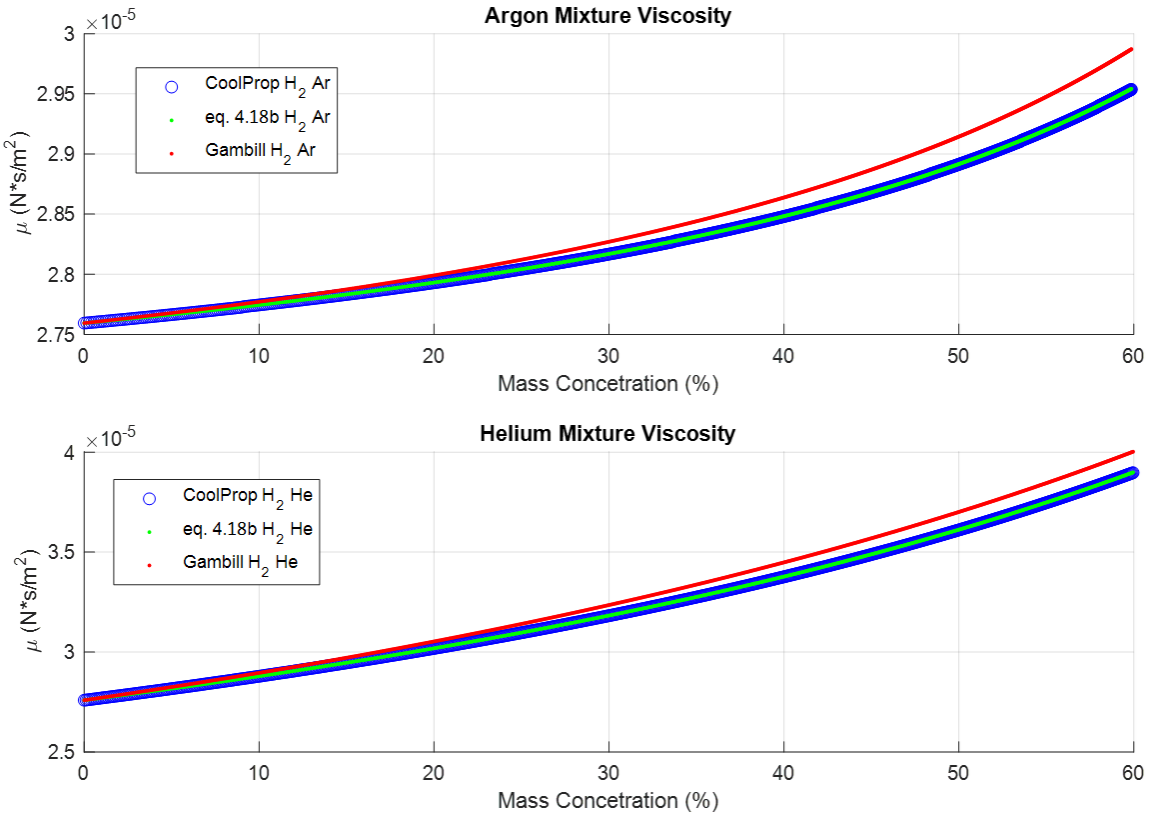

Figure 4.1: Viscosity Equation Validation

The thermal conductivity for binary mixtures is shown as equation 4.19 [37] and a similar validation against the CoolProp library [46] was performed to validate that this equation is correct for hydrogen/krypton and hydrogen/xenon mixtures. This validation is shown in Figure 4.2.

$$K_{mix} = f_H K_H + f_s K_s \tag{4.19}$$

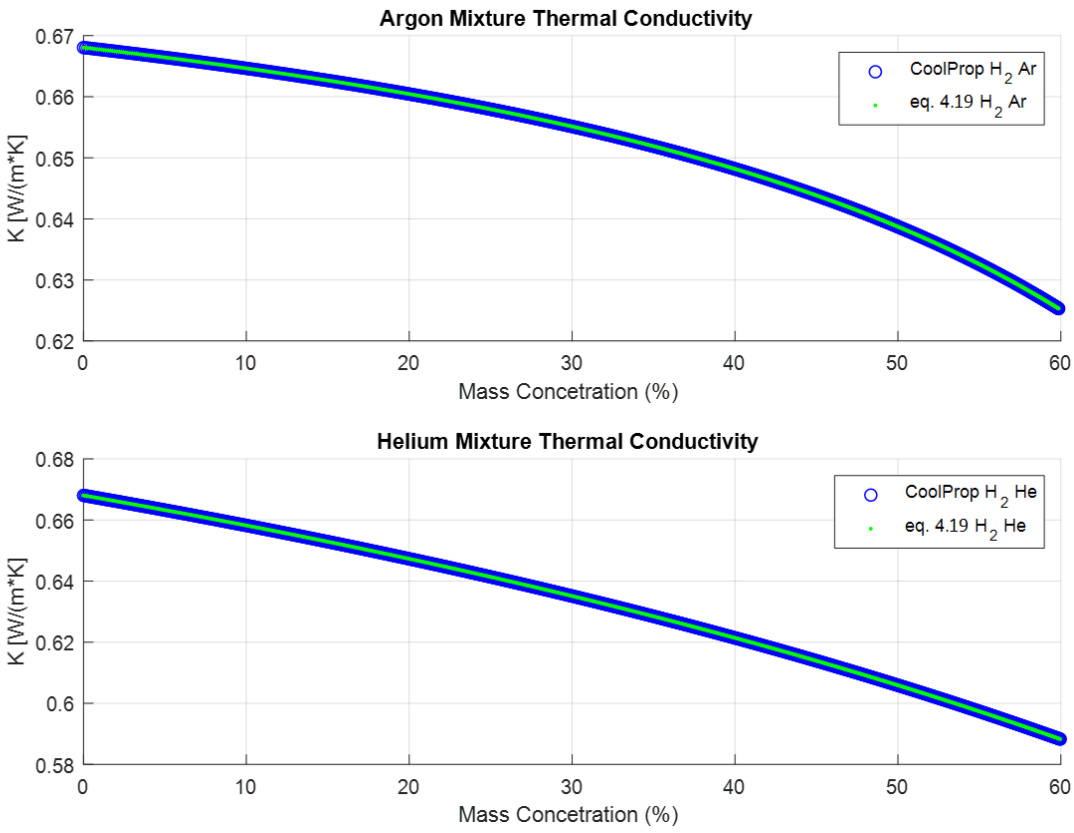

Figure 4.2: Thermal Conductivity Equation Validation

The reactor thermal distribution will be calculated using bulk assumptions (no thermal variation in radial directions). Future research will incorporate radial thermal distribution using a Bessel function based solution method. The limitations of the bulk

analysis are primarily involved with losing all fidelity in the radial direction. However, the general results and the fidelity that are required for the analysis in this thesis are adequate. The surface temperature of the fuel element channels is listed as equation 4.20a [17]. In this equation, L is the fuel element channel length, α is the reactor buckling, $\forall_f$ is the volume of the fuel. Since the fuel elements are hexagon shaped, the individual channels will have fuel in a hexagonal shape around them. Therefore inner radius r_i and outer radius r_o in equation 4.20a come from transforming this channel with hexagonal fuel around it into a tube.

The propellant temperature will become a function of the surface temperature as seen in equation 4.20b. It should be noted that equations 4.20a and 4.20b are interdependent upon one another and require to be solved simultaneously. The temperature of the propellant also depends upon its previous temperature as well as the state of the fluid. By utilizing a step method with a relatively small step size compared to the total length of the channel, the thermal distribution may be obtained with confidence. Furthermore, the maximum temperature of the fuel defined by equation 4.20d [47] is dependent upon the surface temperature of the channel from equation 4.20a, the heat absorbed by the propellant during the step from equation 4.20c, and the thermal conductivity of the fuel. The latter is a function of the material and will be discussed in Chapter 5.

$$T_s(z) = T_p(z) + \frac{\alpha \dot{Q} L (r_o^2 - r_i^2) \cos\left[\alpha\left(\frac{L}{2} - z\right)\right]}{4\hbar(z) r_i \forall_f \sin\left(\frac{\alpha L}{2}\right)} \tag{4.20a}$$

$$T_p(z) = T_s(z) - \left(T_s(Z) - T_p(z-1)\right)\exp\left(-\frac{A_s}{\dot{m}D_{hyd}}\frac{\frac{f(z)}{8}\left(\rho(z)V(z)D_{hyd} - 1000\mu\right)}{1 + 12.7\left(\frac{f(z)}{8}\right)^{1/2}\left[\left(\frac{\mu(z)c_p(z)}{K(z)}\right)^{2/3} - 1\right]}\right) \quad (4.20b)$$

$$\dot{q}(z) = \dot{m}\left(h(z) - h(z-1)\right) \quad (4.20c)$$

$$T_{f_{max}}(z) = T_s(z) + \frac{\dot{q}(z)\ln\left(\frac{r_o}{r_i}\right)}{2\pi K_f(z)L} \quad (4.20d)$$

4.4 Pressure Loss

Pressure losses occur in two main structures in any liquid rocket engine which are the turbines of the turbopumps and the ducts connecting various components of the engine. The turbines usually have a set operating pressure ratio while the pressure loss inside the ducts depends on duct diameter, duct length, mass flow rate, internal roughness, duct bends, and fluid viscosity. The pressure loss in a cylindrical duct is described by the Darcy-Weisbach equation 4.21a. The friction factor that is used is the same as in equation 4.12b. The friction factor is a function of the Reynold's number as well as the duct roughness or $f = f(\mathrm{Re}, \varepsilon)$. Since most rocket engines deal with a mass flow rate rather than fluid velocity, the Darcy-Weisbach equation as well as the Reynold's number is written in terms of mass flow rate to be more readily applicable as seen in equation 4.12c. The velocity V is also written in terms of mass flow rate $V = \frac{4\dot{m}}{\rho\pi D^2}$. Therefore, 4.21a can be expanded and is shown as equation 4.21b where the hydraulic diameter D_{hyd} has been replaced by the cylindrical duct diameter, D.

$$\Delta P = f\frac{\rho L V^2}{2D} \tag{4.21a}$$

$$\Delta P = \frac{1}{\pi^2}\left[0.752\left(\frac{\varepsilon}{D}\right)^{0.225} + 4.24\frac{\varepsilon}{D} + 704\left(\frac{\varepsilon}{D}\right)^{0.44}\left(\frac{\pi\mu D}{4\dot{m}}\right)^{1.62\left(\frac{\varepsilon}{D}\right)^{0.134}}\right]\frac{L\dot{m}^2}{\rho D^5} \tag{4.21b}$$

Equation 4.21b shows that the duct pressure loss is highly dependent on the mass flow rate and, even more so, on the inverse of the duct diameter followed by the inverse of density. The effect of fluid viscosity on duct pressure loss primarily depends on the ratio between the duct roughness to duct diameter and on the inverse of the mass flow rate. Therefore, if the duct diameter is fixed and the mass flow rate has a minimum value, the next logical parameter to alter would be the flow density. By adding an impurity like a heavy noble gas to hydrogen, the flow density increases as a function of molar fraction of the impurity according to equation 4.10. The pressure loss within a cylindrical duct is an inverse function of density, therefore, with an addition of this heavier impurity, the pressure loss will decrease.

4.5 Tsiolkovksy's Rocket Equation and Initial Seeded Propellant Volume

Tsiolkovsky's ideal rocket equation explains the relationship between the amount of propellant onboard a rocket, the exit velocity of the propellant, and the change in velocity that the rocket will experience if it used all of its propellant. This equation uses the ideal rocket model which assumes that the sum of all external forces is equal to zero. In other words, the effects of gravity and air resistance are neglected. Since the considered MTV is aggregated in orbit, the effects of drag and other external forces other than gravity are

negligible. Therefore, the use of this equation for this study is justified. The derivation of this equation is shown in Appendix H.3 with the final result shown in equation 4.22.

$$\Delta V = V_e \ln\left(\frac{m_i}{m_f}\right) \tag{4.22}$$

From Tsiolkovsky's equation, it is possible to derive the amount of propellant volume required to achieve a predetermined change in velocity given the propellant seed amount. The derivation of the initial seeded propellant volume is shown in Appendix H.4 with the final result shown in equation 4.23.

$$\forall_i = \frac{m_{dry}}{\frac{\rho_H \rho_S[(1-f_S)mw_H + f_S mw_S]}{(1-f_S)mw_H \rho_S + f_S mw_S \rho_H}} \frac{\left[\exp\left(\frac{\Delta V}{M_e\sqrt{\frac{2\bar{\gamma}\Re T_0}{[2+(\bar{\gamma}-1)M_e^2][(1-f_S)mw_H + f_S mw_S]}}}\right) - 1\right]}{\left[1 - f_\forall \exp\left(\frac{\Delta V}{M_e\sqrt{\frac{2\bar{\gamma}\Re T_0}{[2+(\bar{\gamma}-1)M_e^2][(1-f_S)mw_H + f_S mw_S]}}}\right)\right]} \tag{4.23}$$

If it is desired to minimize the vehicle propellant tank volume, a derivative must be taken with respect to the seed molar fraction, f_s, which will result in an expression extending through multiple pages. Minimization of initial volume will be much more effective if the minimum point of equation 4.23 is found numerically. Figure 4.3 shows the comparison among argon, krypton, and xenon for the percent of initial volume decrease for a specified ΔV with vehicle specifications taken from reference [4] using equation 4.23. The red 'x's show the maximum volume decrease before seed addition becomes unfavorable. Table 4.1 shows the details for these maximum values. It should be noted that only the growth of the propellant mass was accounted in this analysis without considering

the growth of other parameters such as the propellant mass reserved for the reactive control system or the orbital maneuvering system. This analysis only shows the relationship that seeded propellant has with initial vehicle volume given a change in velocity.

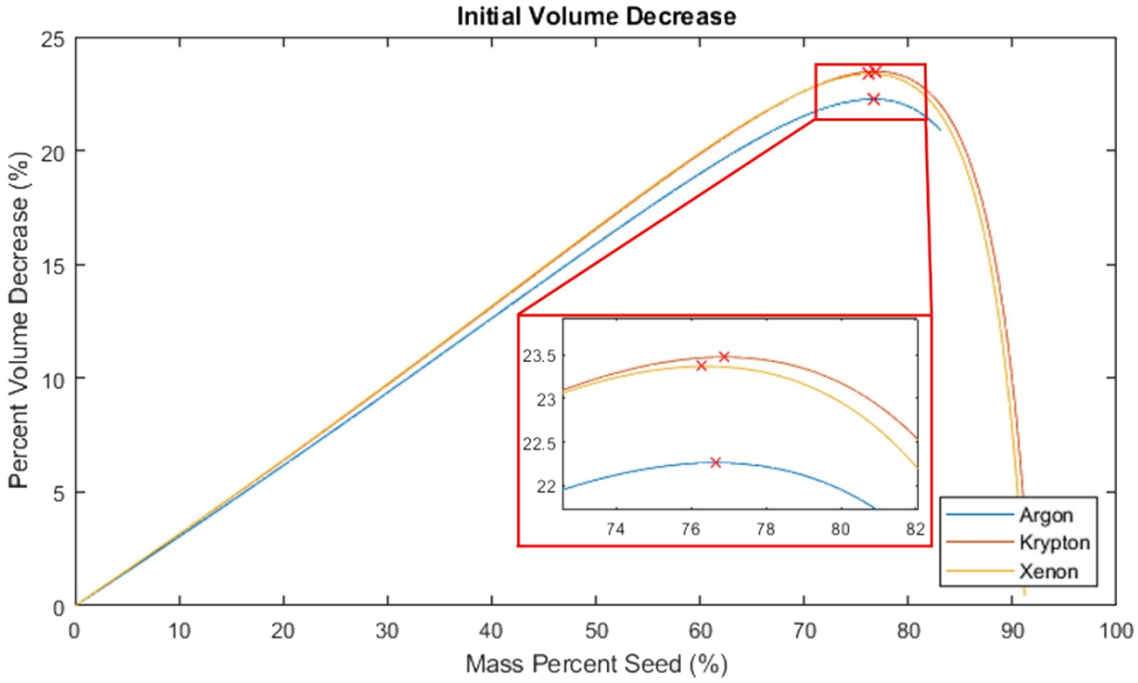

Figure 4.3: Initial Vehicle Volume as a Function of Molar Percent Seed

Table 4.1: Maximum Percent Volume Decrease

Seed	**Molar Percent Seed (%)**	**Mass Percent Seed (%)**	**Maximum Percent Volume Decrease (%)**
Argon	14.2	76.6338	22.2603
Krypton	7.4	76.8622	23.4775
Xenon	4.7	76.2586	23.3708

CHAPTER 5

NTP MODEL DEVELOPMENT

5.1 Aerojet Rocketdyne Engine Model

Before research on alternative propellants was started, a reliable NTP engine model had to be created. This model was based and tuned to Aerojet Rocketdyne's (AR) April 2019 engine model iteration with its flow diagram shown in Figure 5.1. In this schematic, the numbers are associated with key fluid states. The state legend is shown in Table 5.1, the fluid states are shown in Table 5.2 and a summary of the engine parameters are shown in Table 5.3. [42]

The flow starts out by exiting the propellant tank and flowing through the duct connecting the tank to the boost pump. State 1 describes the propellant's state just before entering the boost pump. This component is necessary to prevent cavitation at the inlet to the main pumps at state 2. State 3 is the state of maximum pressure and the hydrogen propellant is now a supercritical fluid due to temperature rises from pump inefficiencies and residual heat absorption from the reactor. After state 3, the flow splits to go to the regenerative cooling lines (state 4) and the moderator cooling lines (state 7). At state 5, the propellant has cooled the nozzle material and enters the control drums to cool them as well and exits out at state 6. At state 8, the propellant has flown through the outside of the

moderator element and is turned around to flow through the inside of the moderator element thus exiting out at state 9 (this will be explored in detail in Section 5.1.7.3). The flows from states 6 and 9 come together and mix at state 10 and proceed to split again to power the boost turbine (state 11 to 12) and through the main turbine circuit. The main turbine circuit consists of the main turbines (state 13 to 14) as well as a turbine bypass valve (TBV) (state 15 to 16) to control the amount of flow through the turbines and thus the mechanical power provided to the main pumps. The boost turbine valve (BTV) functions somewhat differently as it not only affects the amount of flow through the boost turbine but also to the main turbine circuit. The outlet of the main turbines (state 14) and the TBV (state 16) are mixed together at state 17. The boost turbine outlet flow (state 12) is mixed with that of state 17 and results in the pre-reactor state 18. After flowing through the reactor, the propellant enters the chamber at state 19 where it then proceeds to expand through the nozzle and generates thrust.

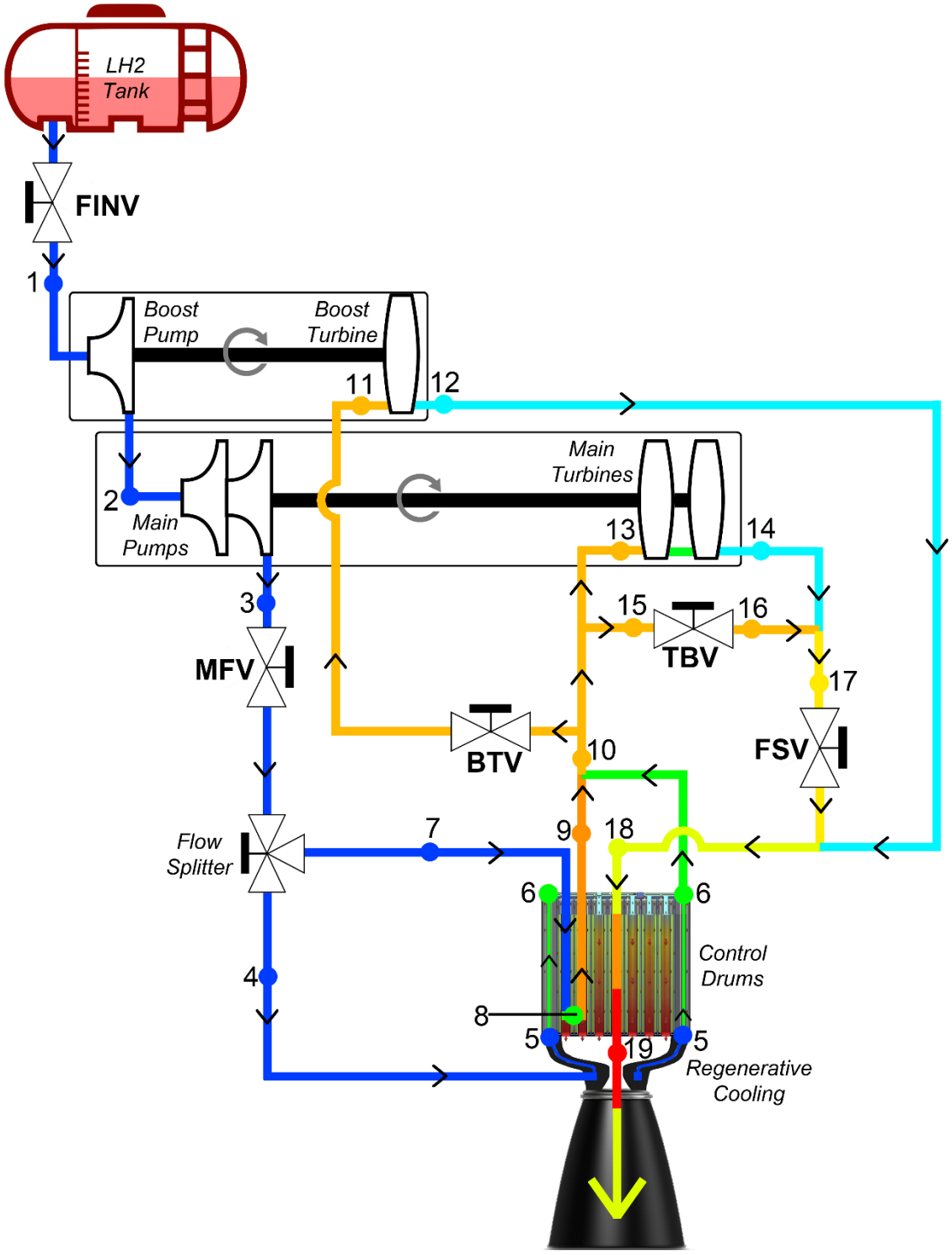

Figure 5.1: Engine Flow Diagram (Adapted from AR PBM 3.0 [3])

Table 5.1: State Legend

1	Pre-Boost Pump	**11**	Pre-Boost Turbine
2	Pre-Main Pumps	**12**	Post-Boost-Turbine
3	Maximum Pressure (Propellant is Supercritical)	**13**	Pre-Main Turbines
4	Pre-Regenerative Cooling	**14**	Post-Main Turbines
5	Post-Regenerative Cooling	**15**	Pre-Turbine Bypass Valve
6	Post-Control Drum Cooling	**16**	Post-Turbine Bypass Valve
7	Pre-Moderator Element Cooling	**17**	Turbine and Bypass Valve Flows Mix
8	Bottom of Moderator Element	**18**	Pre-Reactor State
9	Post-Moderator Element Cooling	**19**	Chamber State
10	Mixture of Post-Cooling Lines		

Table 5.2: AR Fluid States [3] [42]

Fluid State	Pressure (atm)	Temperature (K)	Mass Flow Rate (kg/s)
1	1.293	20.556	[REDACTED]
2	[REDACTED]	[REDACTED]	[REDACTED]
3	[REDACTED]	[REDACTED]	[REDACTED]
4	[REDACTED]	[REDACTED]	[REDACTED]
5	[REDACTED]	[REDACTED]	[REDACTED]
6	[REDACTED]	[REDACTED]	[REDACTED]
7	[REDACTED]	[REDACTED]	[REDACTED]
8	[REDACTED]	[REDACTED]	[REDACTED]
9	[REDACTED]	[REDACTED]	[REDACTED]
10	[REDACTED]	[REDACTED]	[REDACTED]
11	[REDACTED]	[REDACTED]	[REDACTED]
12	--	--	--
13	[REDACTED]	[REDACTED]	[REDACTED]
14	[REDACTED]	[REDACTED]	[REDACTED]
15	[REDACTED]	[REDACTED]	[REDACTED]
16	[REDACTED]	[REDACTED]	[REDACTED]
17	[REDACTED]	[REDACTED]	[REDACTED]
18	89.072	277.222	[REDACTED]
19	68.046	2650.000	[REDACTED]

Table 5.3: AR Engine Parameters [3] [42]

Reactor Power	[REDACTED] MW
Boost Turbopump RPM	[REDACTED]
Main Turbopump RPM	[REDACTED]
Nozzle Area Ratio	386:1
Nozzle Exit Diameter	2.1336 m
Vacuum Thrust	[REDACTED] kN
Vacuum Isp	[REDACTED] s

This engine model was reconstructed in Simulink with each component described by a MATLAB code. The flow states specified by AR were primarily stagnation values where the values before and after the pumps were assumed to be flow values. This was done because the use of stagnation values at states 1, 2, and 3 would set the flow values to below vapor pressure or require unrealistic duct diameters. The flow parameters through the ducts and tubes inside the reactor were reevaluated each millimeter through the flow thus enabling the observation of nuances, especially in regions of extreme temperature and/or pressure changes. At the beginning and ends of each duct, the flow values were reevaluated as stagnation values by using equations 5.1 and 5.2 for stagnation pressure and temperature respectively. The diameter and length of all of the ducts and lines had to be assumed as data for these components was not available. The assumed values yield the same flow property values within 1% of the AR values as will be shown later in this chapter. Temperature changes throughout the ducts and lines were assumed to be negligible and remained the same from inlet to outlet.

$$P_0 = P_{flow} + \frac{1}{2}\rho V^2 \tag{5.1}$$

$$T_0 = T_{flow} + \frac{V^2}{2c_p} \tag{5.2}$$

5.1.1 Propellant Tank

The propellant tank storage temperature and pressure were set to be 20.5556 K and 2.0414 atm respectively according to the vehicle architecture [4]. The propellant line leading from the tank to the boost pump inlet was set to have an arbitrary length of 4 meters and a diameter of 7.9 centimeters which yielded the flow values of state 1.

5.1.2 Boost Pump

The boost pump had a steady state rotational velocity of [REDACTED] RPM ([REDACTED] rad/s) [42] with which it produced a liquid hydrogen pressure head shown in equation 5.3.

$$H = \frac{P_{exit} - P_{available}}{g_0 \rho} \tag{5.3}$$

Referring to Figure 5.1 and Table 5.2, by taking liquid hydrogen at state 1, the boost pump pressurized it yielding state 2. Using these values, the pump efficiency (shown in equation 5.4), available and required net-positive suction head parameters (calculated by equations 5.5a and 5.5b respectively), specific speed (shown in equation 5.6), suction specific speed (shown in equation 5.7), Thoma cavitation parameter σ, and specific diameter were calculated.

$$\eta_{pump} = \frac{W_{pump}}{W_{shaft\ in}} = \frac{h_{out,isentropic} - h_{in}}{h_{out,actual} - h_{in}} \tag{5.4}$$

$$NPSH_a = \frac{P_{available} - P_{vapor}}{g\rho} \tag{5.5a}$$

$$NPSH_r = \frac{P_{required} - P_{vapor}}{g\rho} \tag{5.5b}$$

$$n_s = \frac{\omega\sqrt{Q}}{(g_0 H)^{3/4}} = \frac{\omega\sqrt{\frac{\dot{m}}{\rho}}}{\left(\frac{P_{exit} - P_{available}}{\rho}\right)^{3/4}} = \frac{\omega\rho^{1/4}\sqrt{\dot{m}}}{(P_{exit} - P_{available})^{3/4}} \tag{5.6}$$

$$s_s = \frac{\omega\sqrt{Q}}{(g_0 NPSH_a)^{3/4}} = \frac{\omega\sqrt{\frac{\dot{m}}{\rho}}}{\left(\frac{P_{available} - P_{vapor}}{\rho}\right)^{3/4}} = \frac{\omega\rho^{1/4}\sqrt{\dot{m}}}{\left(P_{available} - P_{vapor}\right)^{3/4}} \tag{5.7}$$

Both the Thoma cavitation parameter and specific diameter were doubly interpolated from a table using the suction specific speed, specific speed, and efficiency [17] with the MATLAB functions in Appendix D. Using the Thoma cavitation parameter, the minimum required pressure fed to the pump was calculated using equation 5.8.

$$\sigma = \frac{NPSH_r}{H} = \frac{P_{required} - P_{vapor}}{P_{exit} - P_{available}} \rightarrow P_{required} = \sigma(P_{exit} - P_{available}) + P_{vapor} \tag{5.8}$$

The hydrogen vapor pressure plot according to temperature [48] was included in Appendix A under Figure A.1.1 among other parameters. The work done and required by the boost pump was calculated by equations 5.9a and 5.9b respectively. Table 5.4 summarizes the boost pump's parameters by providing the given/calculated data and the

tuned parameters which yielded the fluid values specified by AR. It should be noted that the required net-pressure suction head was higher than the available net-pressure suction head by 0.7339 meters. Although this does produce cavitation, a 10% cavitation allowance is acceptable [49]. The incoming heat from the environment (radiation from the reactor and conduction from various components) was calculated using the first law of thermodynamics for an open system shown in equation 5.9c.

$$W_{pump} = \rho g Q H = \frac{\dot{m}(P_{exit} - P_{available})}{\rho} = \dot{m}(h_{out} - h_{in}) \tag{5.9a}$$

$$W_{shaft\ in} = \frac{W_{pump}}{\eta_{pump}} = \dot{m}\frac{(P_{exit} - P_{available})}{\rho\eta_{pump}} = \frac{\dot{m}(h_{out} - h_{in})}{\eta_{pump}} \tag{5.9b}$$

$$\frac{dE}{dt} = \dot{Q}_{in} - \dot{W}_{pump} + \sum_{i=1}^{n} \dot{m}_i \left[h_i + \frac{V_i^2}{2} + g y_i\right] - \sum_{e=1}^{n} \dot{m}_e \left[h_e + \frac{V_e^2}{2} + g y_e\right] \tag{5.9c}$$

The kinetic and potential energy terms were considered as negligible since the propellant flowed in and out of the pumps at almost identical velocities and the effects of gravity are ignored in space. The system was analyzed at steady state, therefore, the change in energy with respect to time $\frac{dE}{dt}$ was set to zero. Transient operation of the pump was calculated using the specific diameter formula (equation 5.10) since the pump diameter and pump head were known.

$$d_s = \frac{D(g_0 H)^{1/4}}{\sqrt{Q}} = \frac{D\left(\frac{P_{exit} - P_{available}}{\rho}\right)^{1/4}}{\sqrt{\frac{\dot{m}}{\rho}}} = \frac{D[\rho(P_{exit} - P_{available})]^{1/4}}{\sqrt{\dot{m}}} \tag{5.10}$$

Figure 5.2 shows the pump transient behavior. It is important to note that the head, specific speed, and suction specific speed were kept constant when calculating these transients. The peak efficiency for the boost pump is at a flow rate of around 6 kg/s and the efficiency is greater than at the maximum operational point over a wide range of flow rates. From analyzing different efficiency curves, the selected curve was the only one that allowed for reasonable performance (non-zero efficiency). This is due to the fact that during reactor shut down, the hydrogen propellant will still be flowing through the reactor to cool it down at lower flow rates. At this state, even though the turbines are required to produce less power, the flow rate through them is less, therefore, the pump efficiency should either increase or remain the same to provide an operational system. Furthermore, if this engine is throttled down, then the pumps should still function with the lower flow rates.

Table 5.4: Boost Pump Parameters *(Given values from* [42] *have been redacted)*

Parameter	**Given/Calculated**	
ω	[REDACTED]	RPM
H	[REDACTED]	m
$NPSH_a$	30.776	m
$NPSH_r$	30.603	m
η_{pump}	[REDACTED]	--
σ	0.122	--
n_s	1.956	--
s_s	9.652	--
d_s	3.348	--
W_{pump}	[REDACTED]	kW
$W_{in,required}$	[REDACTED]	kW
$Q_{in,external}$	133.360	kW
Diameter	0.083	m

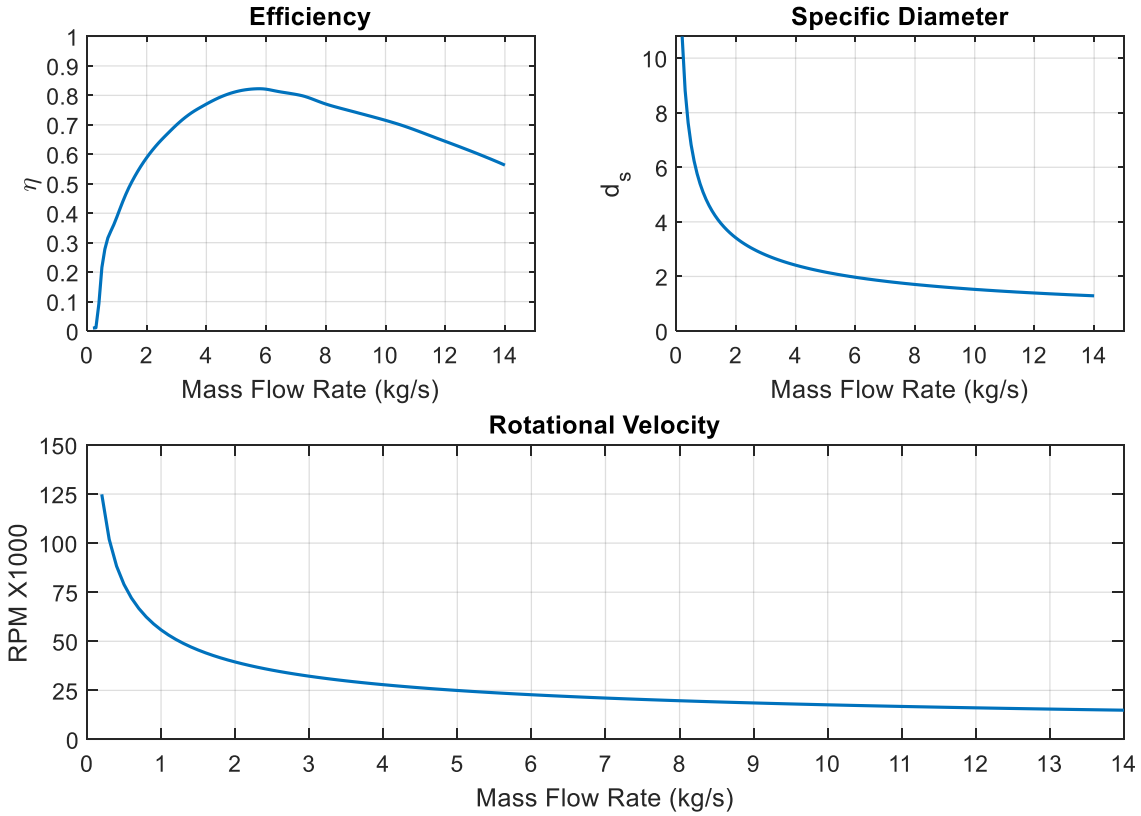

Figure 5.2: Boost Pump Transient Performance (Specific Speed, Suction Specific Speed, and Head were kept Constant)

5.1.3 Main Pumps

The main pumps have a design steady state rotational velocity of [REDACTED] RPM ([REDACTED] rad/s) [42] and are responsible for pressurizing the liquid hydrogen to the pressure in state 3 found in Table 5.2. There are two main pumps connected to a single shaft and are assumed to provide the same head each [3] [42] [49]. By using equation 5.11, the pressure outlet of main pump 1 was found. This fluid then goes through a duct to main pump 2 where it will experience a negligible pressure loss resulting in the available pressure for main pump 2 to be the same as the exit pressure of main pump 1. The process

for determining the parameters of the main pumps, which are shown in Table 5.5, was the same as it was for the boost pump. The transient operation, which is the same for both pumps, is shown in Figure 5.3.

$$P_{exit,1} = \frac{P_{exit,2} - P_{in,1}}{2} + P_{in,1} \approx P_{in,2} \tag{5.11}$$

Table 5.5: Main Pumps Parameters *(Given values from* [42] *have been redacted)*

	Main Pump 1		**Main Pump 2**	
Parameter	**Given/Calculated**		**Given/Calculated**	
ω	[REDACTED]	RPM	[REDACTED]	RPM
H	[REDACTED]	m	[REDACTED]	m
$NPSH_a$	216.234	m	12307	m
$NPSH_r$	222.028	m	12499	m
η_{pump}	[REDACTED]	--	[REDACTED]	--
σ	0.016	--	0.890	--
n_s	0.352	--	0.351	--
s_s	7.883	--	0.378	--
d_s	6.647	--	6.680	--
$\dot{W}_{pump}$	[REDACTED]	MW	[REDACTED]	MW
$\dot{W}_{in,required}$	[REDACTED]	MW	[REDACTED]	MW
$\dot{Q}_{in,external}$	836.740	kW	838.240	kW
Diameter	0.150	m	0.150	m

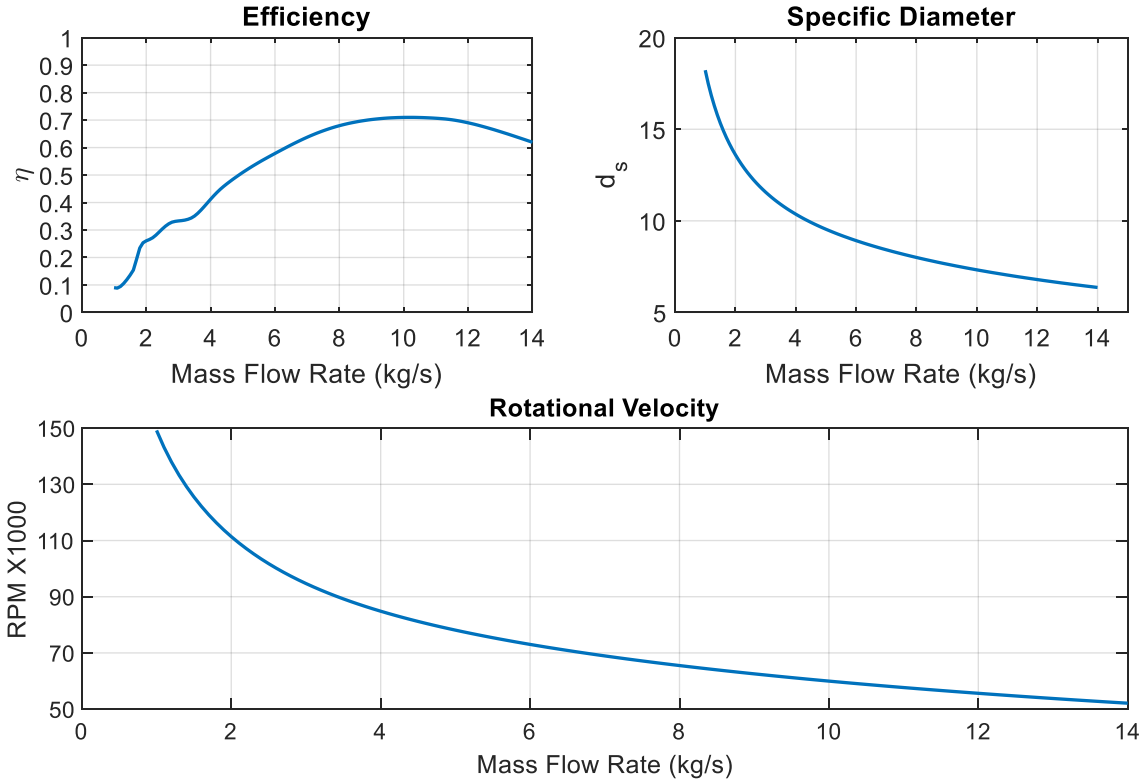

Figure 5.3: Main Pumps Transient Performance (Specific Speed, Suction Specific Speed, and Head were kept Constant)

5.1.4 Regenerative Cooling

Regenerative cooling is used to cool the throat of the nozzle as well as the converging and diverging sections of the nozzle which experience the highest temperatures. In turn, the propellant that flows through the regenerative cooling channels absorbs this heat and is often used in tandem with a pre-burner (in chemical engines) to drive the turbines of the turbopumps [50]. To calculate the amount of heat that the propellant inside the coolant channels absorbs from the propellant flowing inside the nozzle (the plume), the convective heat transfer coefficients of both flows was found. Furthermore, the heat transfer due to the temperature gradient through the nozzle material

with thermal conductivity K was also found. The only parameters available from the nozzle were the exit and throat diameters. The unknown parameters were: thermal conductivity, thickness of the nozzle between the coolant channels and main flow area, channel friction, and the total cross sectional area of the coolant channels. Since these parameters are directly responsible for the amount of heat transferred into the propellant flowing through the coolant channels, they were adjusted and tuned according to the required values provided in the AR model [3] [42].

The pressure loss due to friction and flow losses formula has been presented in Chapter 4 as equation 4.21b. For the pressure loss inside the coolant channels, the diameter D was replaced by the hydraulic diameter D_{hyd} and the resulting formula is shown as equation 5.12. The geometry of the coolant channels was mathematically assumed to be two concentric circular pipes with the propellant flowing in between them. This is acceptable because the nozzle length for each calculation is 1 mm. Therefore, mathematically, this nozzle is a series of concentric pipes with a thickness of 1 mm and stacked on top of each other to form the shape of a rocket nozzle. The equation for the hydraulic diameter for this geometry is shown in 5.13. The nozzle geometry was determined by examining a CAD model of the NTP engine designed by AR by the use of proportions of length to pixels in the image and the nozzle radius was fit to a parabolic curve as a function of length from the throat [3]. It was determined that the nozzle length from throat to exit was 4.606 m and the coolant channels run 1.038 m below and 0.448 m above the throat. Later in this section, Table 5.10 will show the nozzle parameters. Figure 5.4 shows the CAD drawing of the engine.

Figure 5.4: Aerojet Rocketdyne NTP CAD Drawing [43]

ΔP – Pressure loss

ε – Channel roughness

μ – Propellant viscosity

ρ – Propellant density

$$\Delta P = \frac{1}{\pi^2}\left[0.752\left(\frac{\varepsilon}{D_{hyd}}\right)^{0.225} + 4.24\frac{\varepsilon}{D_{hyd}} + 704\left(\frac{\varepsilon}{D_{hyd}}\right)^{0.44}\left(\frac{\pi\mu D_{hyd}}{4\dot{m}}\right)^{1.62\left(\frac{\varepsilon}{D_{hyd}}\right)^{0.134}}\right]\frac{L\dot{m}^2}{\rho D_{hyd}^5} \quad (5.12)$$

$$D_{hyd} = \sqrt{\frac{4A_c}{\pi}} \quad (5.13)$$

Using this geometry, inlet conditions (pressure, temperature T_{in}, and mass flow rate), and compressible flow relations (equations 4.2 through 4.6), the convective heat transfer coefficient was calculated using equations 4.12a through 4.12d for both the propellant inside the coolant channels $\hbar_c$ and the plume $\hbar_p$. For each millimeter of the propellant flow through the coolant channels, the inside T_i and outside T_o temperatures of the nozzle material were calculated as well as the temperature T_e and pressure drop (eq. 5.10) of the propellant leaving that 1 mm section.

The pressures and temperatures used for the calculation of the intermediate states at every millimeter were flow pressures and temperatures with the stagnation pressures and temperatures reported at the inlet and outlet only. The nozzle material selected was GRCop-84 for its thermophysical properties and test data which proved to be better for nozzle applications than the commonly used NARloy-Z [51] [52]. This nozzle material was selected in order for the values at state 5 to match AR's values. Furthermore, this nozzle material has been used in the RL-10 engine on which AR has based this NTP engine [3].

In order to find the coolant channel and inside nozzle material temperatures as well as the temperature of the propellant leaving the 1 mm section, a set of 3 equations (5.14a through 5.14c) were solved simultaneously. The derivation for these equations is provided

in Appendix E. In order to match the output coolant propellant temperature, the plume temperatures incident on the inner nozzle wall were assumed to be 67% of the calculated temperature by isentropic equations. Furthermore, the velocity incident on the inner nozzle wall had to be decreased by 50%. These assumptions are reasonable because any flow will have a boundary layer that transitions into the main flow conditions. Future research will examine the boundary layer on the inside wall of the nozzle and determine the flow conditions more rigorously.

Using these assumptions, the temperature distribution of the cooling propellant, coolant channels, nozzle inside, and plume have been graphed in Figure 5.5 and the output fluid state matches that of the AR model. In Figure 5.5, it can be observed that the pressure of the fluid drops faster around the throat. Furthermore, the temperature of the nozzle material is also the hottest around the throat. This is to be expected as the coolant fluid flows faster resulting in higher pressure drops; it also flows over a smaller area resulting in lower heat transfer and higher temperatures.

$$T_o = \frac{T_e \exp\left[\hbar_p A_{s_i}\left(T_p - T_i\right) + \hbar_c A_{s_o}(T_e - T_{in})\right] - T_{in}}{\exp\left[\hbar_p A_{s_i}\left(T_p - T_i\right) + \hbar_c A_{s_o}(T_e - T_{in})\right] - 1} \tag{5.14a}$$

$$T_i = \frac{2\pi KLT_o + T_p \hbar_p A_{s_i}\, ln\left(\frac{d + 2t_n}{d}\right)}{2\pi KL + \hbar_p A_{s_i}\, ln\left(\frac{d + 2t_n}{d}\right)} \tag{5.14b}$$

$$T_e = T_o - (T_o - T_{in})\exp\left(-\frac{\hbar_c A_{s_o}}{\dot{m} c_p}\right) \tag{5.14c}$$

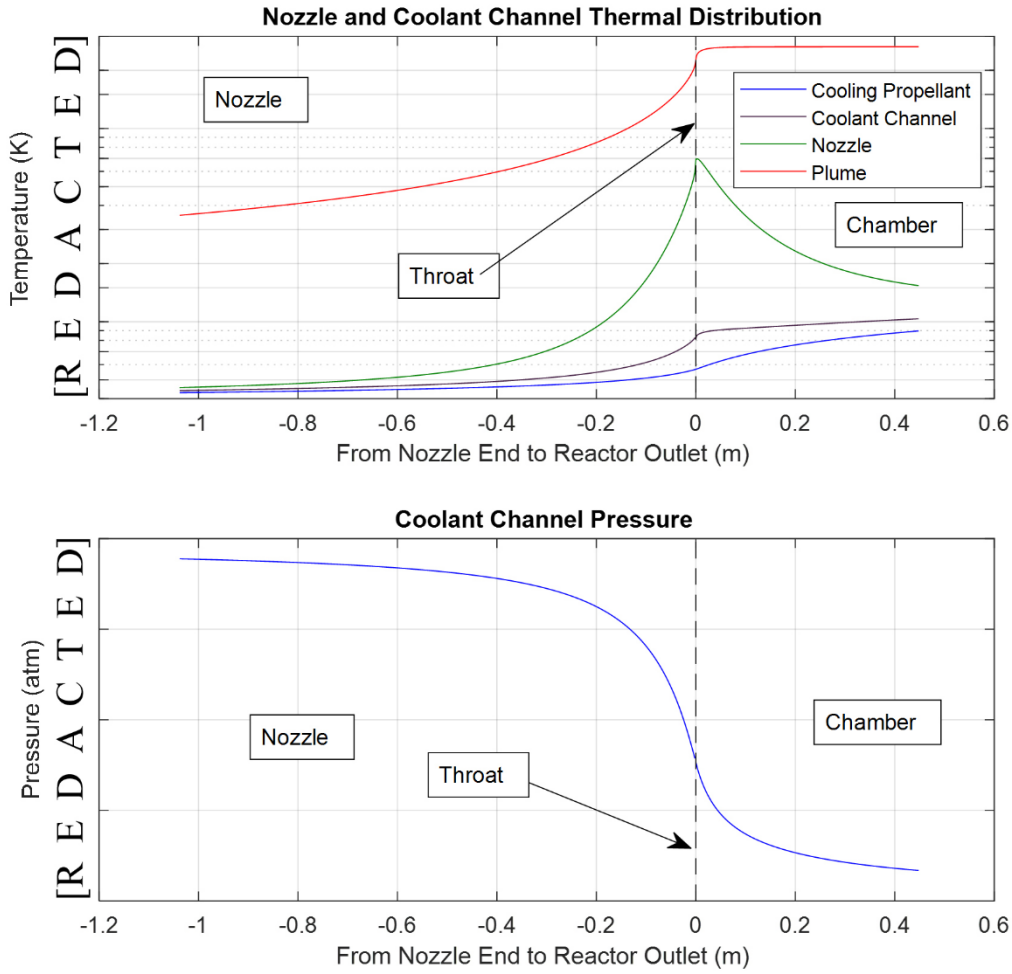

Figure 5.5: Nozzle and Coolant Channel Thermal Distribution and Pressure (Flow Conditions Only)

5.1.5 Main Turbines

The main turbines are tasked with providing the work that the main pumps require via shaft $\dot{W}_{turb} = \dot{W}_{pump}$. The information given by AR provided a net turbine stagnation pressure ratio PR_0 of [REDACTED] and an efficiency η_{turb} of [REDACTED]. This efficiency was assumed to be the maximum efficiency of each turbine during steady state operation at the stagnation conditions specified by AR. The stagnation pressure ratio of

each turbine and the diameter of the ducts connecting them were determined so that the efficiency of each turbine and the final turbine output stagnation conditions match that of AR values. Although the state of hydrogen is supercritical, it is further assumed that compressible flow and gas turbine equations are still applicable inside the turbines. Equations 5.1 and 5.2 will still be used for switching between stagnation and flow conditions inside the ducts. Since no further information was given about the turbines such as the rotor diameter, blade angle, efficiency curve, pressure ratio curve, or work generated as a function of flow rate, it will not be possible to incorporate the turbine rotational velocity. [53] [54]

Equation 5.15a was used as the general equation for determining the performance of each turbine. This equation was rearranged in equation 5.15b to solve for the turbine efficiency and was used for tuning the pressure ratio and duct diameters to match the stagnation conditions provided by AR. It was noticed that equation 5.15b can be written in terms of specific work (work done per kilogram of the flow) as seen in equation 5.15c.

$$\dot{W}_{turb} = \dot{m} c_p\left(T_{0_{in}}, P_{0_{in}}\right) T_{0_{in}} \eta_t \left[1 - \left(\frac{1}{PR_0}\right)^{(\gamma-1)/\gamma}\right] \tag{5.15a}$$

$$\eta_t = \frac{\dot{W}_{turb}}{\dot{m} c_p\left(T_{0_{in}}, P_{0_{in}}\right) T_{0_{in}} \left[1 - \left(\frac{1}{PR_0}\right)^{(\gamma-1)/\gamma}\right]} \tag{5.15b}$$

$$\eta_t = \frac{\dot{w}_{turb}}{c_p\left(T_{0_{in}}, P_{0_{in}}\right) T_{0_{in}} \left[1 - \left(\frac{1}{PR_0}\right)^{(\gamma-1)/\gamma}\right]} \tag{5.15c}$$

This was the criteria for evaluating the efficiency of the turbine if stagnation conditions change with a requirement that the turbine efficiency never goes above [REDACTED]; if it does, then the pressure ratio or duct diameters were modified. The fluid velocity inside the ducts was calculated using the mass flow through a pipe equation 5.16a. This equation was solved for the velocity of a fluid flowing through a circular duct shown in equation 5.16b.

$$\dot{m} = \rho A_c V \tag{5.16a}$$

$$V = \frac{4\dot{m}}{\rho \pi d^2} \tag{5.16b}$$

By using compressible flow relations shown in equations 4.2 and 4.3 and the speed of sound shown in equation 5.17, the stagnation conditions at the inlet and outlet of the turbine were found.

$$c = \sqrt{\gamma RT} \tag{5.17}$$

The temperature and ratio of specific heats used in determining the speed of sound was that of the flow conditions and not stagnation conditions. The stagnation fluid state at the outlet was evaluated by using the first law of thermodynamics modified for this case as seen in equation 5.18 and the determined pressure ratio of the respective turbine. Adjusting the pressure ratio of each turbine and the duct diameter at each inlet and outlet to match the efficiency of the turbines yielded the parameters of the turbines and ducts in Table 5.6. [53] [54]

$$0 = \dot{Q}_{in,external} - \dot{W}_{turb} + \dot{m}\left(h_{0_i} - h_{0_e}\right) \tag{5.18}$$

Table 5.6: Main Turbines Parameters *(Given values from* [42] *have been redacted)*

	Main Turbine 1	**Main Turbine 2**
Parameter	**Given/Calculated**	**Given/Calculated**
ω	[REDACTED] rad/s	[REDACTED] rad/s
PR_0	[REDACTED] --	[REDACTED] --
η_{turb}	[REDACTED] --	[REDACTED] --
T_{in}	[REDACTED] K	[REDACTED] K
P_{in}	[REDACTED] atm	[REDACTED] atm
T_{out}	[REDACTED] K	[REDACTED] K
P_{out}	[REDACTED] atm	[REDACTED] atm
$\dot{W}_{turb}$	[REDACTED] kW	[REDACTED] kW
$\dot{Q}_{in,external}$	122.08 kW	122.08 kW
d_{in}	0.0408 m	0.0564 m
d_{out}	0.044 m	0.063 m

5.1.6 Boost Turbine

The boost turbine is responsible for providing power to the boost pump. Since AR did not provide any information about the exit conditions of the boost turbine, assumptions were made and the exit conditions were calculated based on the inlet conditions of the boost turbine (Figure 5.1, state 11) and the conditions of the flow from the main turbines found before mixing (Figure 5.1, state 17) and after mixing (Figure 5.1, state 18). The work that this turbine produces is equal to the work required by the boost pump $\dot{W}_{turb} = \dot{W}_{pump}$. AR stated that the stagnation pressure ratio of this turbine is [REDACTED] which opens a variety of possibilities for the duct inlet and outlet diameters. Later designs (after the April 2019 iteration) routed the outlet of the boost turbine to the inlet of the FSV [43] which also

would have changed this pressure ratio. However, more detailed information on the later designs is unavailable at this time and future research will incorporate more up to date information.

To remedy all of this, the flow pressures of the exhaust of the FSV (main flow) and the boost turbine were used as the mixing pressures. The duct diameters were set so that the boost turbine flow pressure was slightly higher than that of the main flow while the stagnation conditions at the boost turbine inlet and outlet still provided the required [REDACTED] stagnation pressure ratio. This was accomplished by setting the duct diameter for the exhaust of the boost turbine to 2 cm ([REDACTED] kg/s flow rate) and the duct diameter of the main flow to 5.85 cm ([REDACTED] kg/s flow rate). The result was that the main flow was much faster (but still subsonic) than the boost turbine flow and therefore, had lower flow pressure according to equation 5.1 than the boost turbine flow thus discouraging any back flow.

AR has stated that the efficiency of this turbine is [REDACTED] [42] which allowed the use of the same method of calculating the inlet and outlet duct diameters as was used in the previous section on the main turbines. Since no assumption was made about the outlet temperature, it was assumed that the heat addition to this flow is negligible in order for the model state values to match that of the AR values. This assumption is valid because the flow rate through the turbine is very low which translates to a smaller turbine with less surface area onto which the radiative heat from the reactor may be deposited. Because the efficiency of this turbine is very low and the pressure drop is relatively high,

the turbine outlet temperature will be slightly lower than that of the inlet temperature since this component's functionality closely resembles a valve. Table 5.7 summarizes the boost turbine's parameters.

Table 5.7: Boost Turbine Parameters *(Given values from* [42] *have been redacted)*

Parameter	**Given/Calculated**	
ω	[REDACTED]	RPM
PR_0	[REDACTED]	--
η_{turb}	[REDACTED]	--
T_{in}	[REDACTED]	K
P_{in}	[REDACTED]	atm
T_{out}	297.002	K
P_{out}	86.79	atm
$\dot{W}_{turb}$	[REDACTED]	kW
$\dot{Q}_{in,external}$	0	kW
d_{in}	0.01	m
d_{out}	0.0175 to 0.02	m

5.1.7 Reactor

The information provided for the reactor included the fuel element geometry and reactor power [55]. A one-dimensional bulk analysis on the reactor thermal distribution was conducted with assumed constant radial thermal distribution. Although the bulk results should be sufficient in obtaining the conditions at state 19, they limit the fidelity that could be otherwise obtained in the radial direction and some of the nuances are lost. However, the bulk analysis is still acceptable since the goal of this analysis was to match the input and outlet reactor flow states to the AR model while capturing some of the axial nuances. Future research will take into account the radial thermal distribution as well as the neutron

flux. The reactor has three different flow paths running through it: (1) main reactor flow, (2) control drum cooling, and (3) moderator flow. Each flow path is unique and will be discussed separately in this section.

5.1.7.1 Main Reactor Flow

The propellant gains most of its thermal energy within the main reactor flow section. It is this section of the reactor that dictates the overall power distribution from which the rest of the components mentioned previously obtain their external source heat. There are a total [REDACTED] fuel elements with [REDACTED] channels per fuel element and a diameter of 0.00282 m per channel [42] [55]. A cross-sectional area of the fuel element is shown in Figure 5.6 where the yellow are the hydrogen propellant channels and the purple is the fuel. The reactor internal and external diameters are 0.682 m and 0.932 m respectively [55]. The area between the internal and external diameters houses the control drums which function as neutron reflectors or absorbers depending on the current and desired reactor power levels. When comparing states 18 and 19, there is considerable pressure drop which cannot be attributed to a direct flow through the reactor. No information was given on the details of this main flow through the reactor, therefore, the stagnation pressure drop was adjusted by adjusting the roughness of the channels while assuming a direct flow through the reactor until this calculated stagnation pressure drop matched the 21 atm stagnation pressure drop of the AR model [3]. The absolute roughness of the channel surface that provided this pressure drop was 470 μm. According to the standard table of material roughness [56], 470 μm corresponds to cast iron and concrete

which would be unreasonable for tungsten coating. However, a study that examined improving reactor fuel element heat transfer by modifying surface roughness explored absolute roughness values between 184 μm and 931 μm [57]. Thus, a channel roughness of 470 μm is a viable assumption for the use in a reactor fuel element.

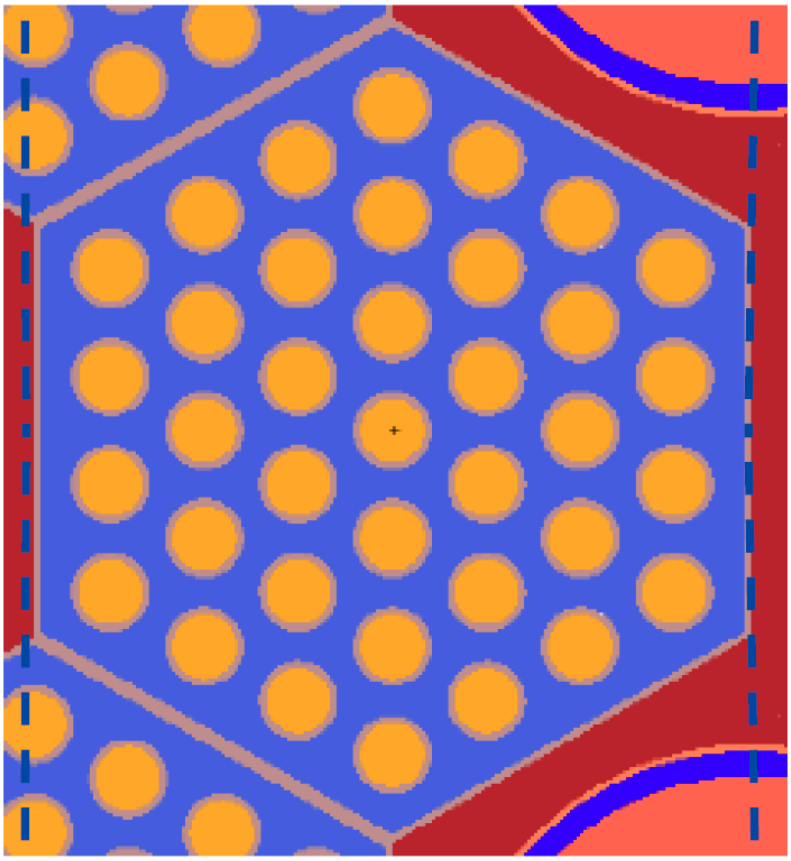

Figure 5.6: Cross-sectional Area of Fuel Element

The propellant temperature and channel wall temperature were calculated using equations 4.20a and 4.20b. The pressure loss was calculated by equation 4.20b. An iterative method was used to determine the required reactor power by setting the final reference temperature to be that of state 19, taking an assumed initial reactor power and adjusting

that reactor power until the output temperature converged with the reference temperature within a set range of ± 2 K. This range was chosen for accuracy and also a reasonable amount of iterations (under 20).

The calculated power did not incorporate into it the heating provided by neutron and gamma ray attenuation. Since hydrogen functions as both the propellant and the reactor moderator, the heat that it absorbed from this attenuation was significant. A study on the power absorbed by hydrogen from this attenuation was conducted by the National Institute of Standards and Technology (NIST) which calculated this attenuation to be anywhere between 14.29% to 22.49% [58]. Comparing the calculated reactor power to the power set forth by AR, the amount of heat provided by this neutron and gamma ray attenuation accounted for 12.13% of the total heat absorbed by the hydrogen propellant/moderator. This value is less than the lower bound from the NIST study because: (1) the bottom of the reactor does not provide any significant neutron reflection and (2) the hydrogen flow through the moderator elements and control drums absorb more of this neutron and gamma ray attenuation heat which will be explored in the later sections. Given this information, the reactor power required to heat the main hydrogen reactor flow was adjusted accordingly. Figure 5.7 shows the hydrogen propellant temperature, the channel surface temperature (eq. 4.42a), the maximum fuel temperature (eq. 4.42d), and the pressure (eq. 4.43b) as it flows through the reactor with the horizontal axis being the axial length of the reactor.

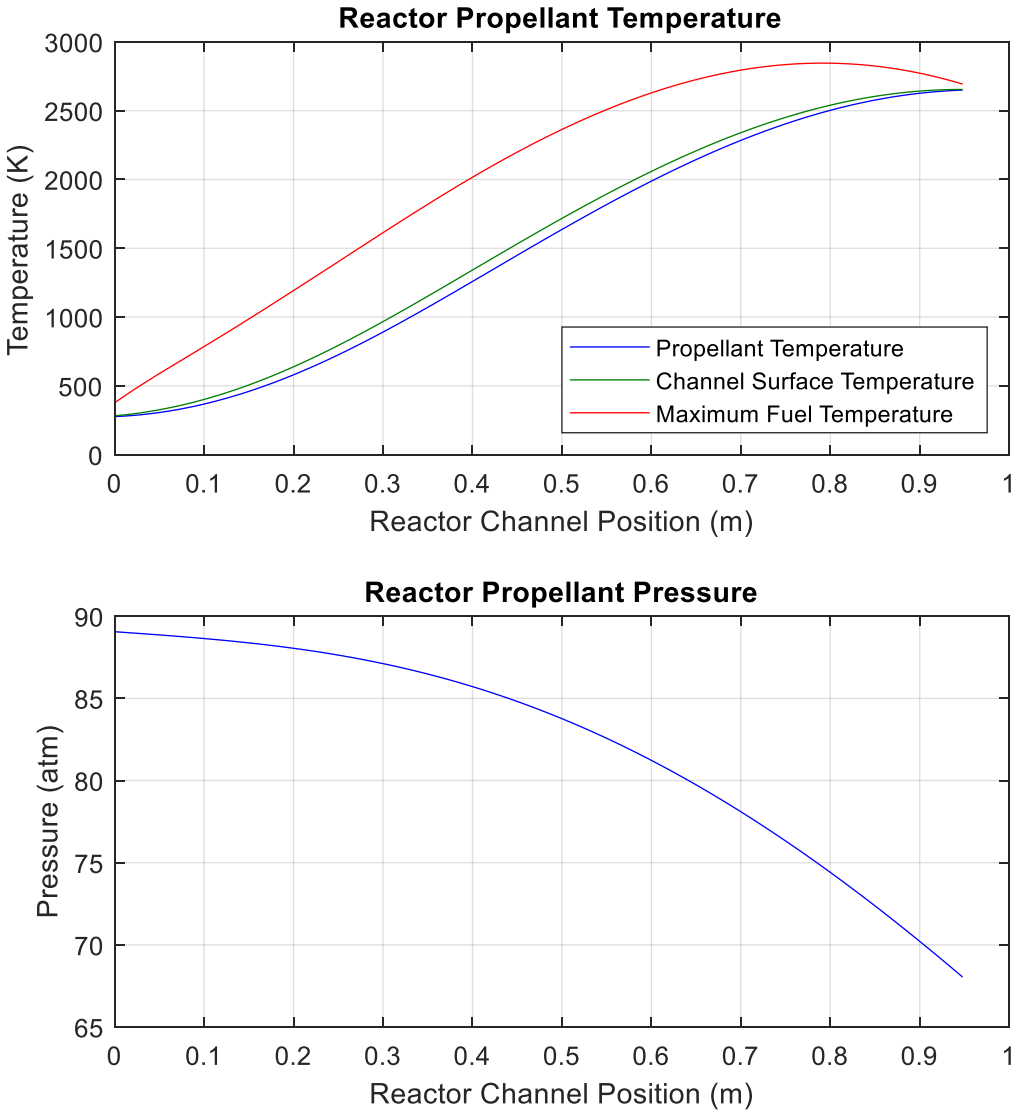

Figure 5.7: Reactor Temperature and Pressure

In Chapter 4, it was mentioned that the thermal conductivity of the fuel is a material property. The information received from AR included that the fuel material is uranium nitride (UN) with yttrium nitride (YN) mixture (UN, YN) with a tungsten (W) coating on the channel surface. The thermal conductivity of this material was neither given, nor could it be found in literature. Therefore, thermal conductivity was assumed to be that of uranium

nitride for which a correlation with temperature between 10 K and 1923 K is given in equation 5.19a [59]. The stated maximum fuel temperature by AR is much higher (2847 K) than the valid range of this equation. Furthermore, when this range was ignored, the thermal conductivity increased too much and provided a fuel temperature lower than stated by AR for the converged chamber stagnation temperature within ± 2 K of the AR values as discussed previously. Therefore, the coefficient and the power values were modified to agree with the AR data and shown in equation 5.19b.

Although this may not the true thermal conductivity of the fuel, it provides acceptable results. Figure 5.8 shows how the pure uranium nitride thermal conductivity differs from the adjusted thermal conductivity which incorporates yttrium nitride and the tungsten coating. It makes sense that the bulk thermal conductivity of the fuel element would be slightly better than the pure uranium nitride fuel due to advances in material processing. Once the true conductivity of the uranium nitride and yttrium nitride alloy is known for the operating temperature range, this assumption will be replaced. The reactor parameters are summarized in Table 5.8.

$$K(T) = 1.43T^{0.39} \tag{5.19a}$$

$$K(T) = 1.37T^{0.41} \tag{5.19b}$$

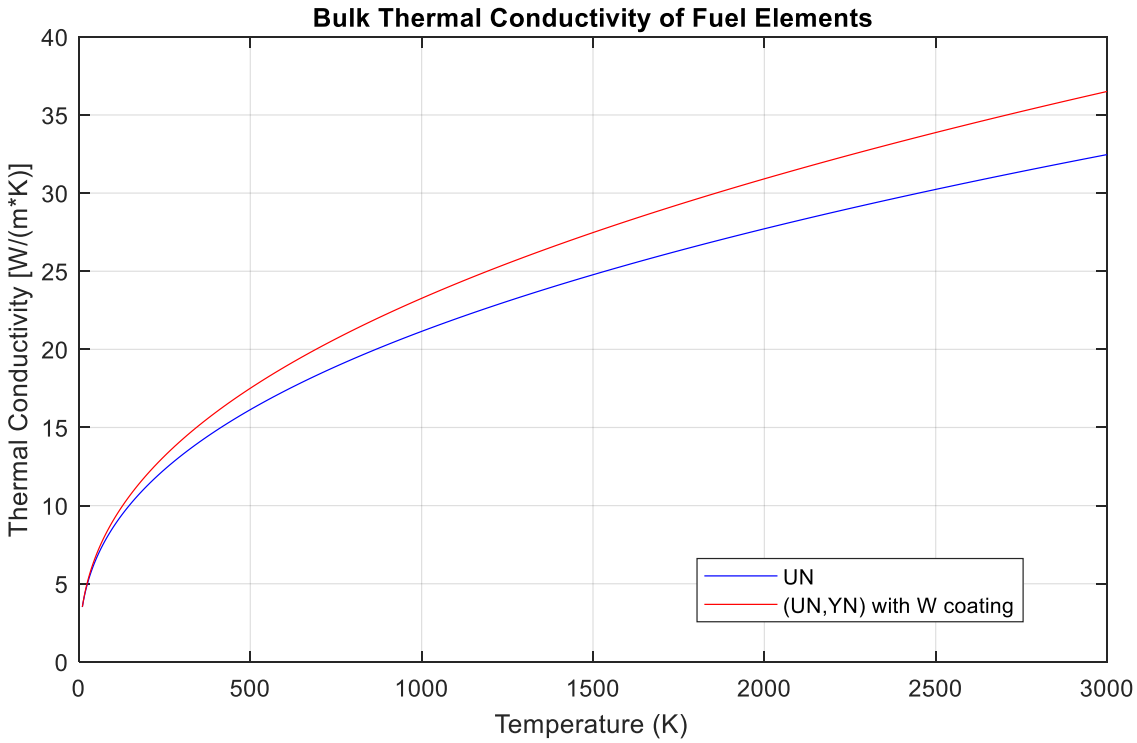

Figure 5.8: Comparison of thermal conductivity of UN and (UN, YN) with Tungsten Coating

Table 5.8: Reactor Parameters [42] [55]

Parameter	**Given/Calculated**
Length	0.950 m
Outer (Housing) Diameter	0.932 m
Inner Diameter	0.682 m
Number of Fuel Elements	[REDACTED] --
Number of Channels per Fuel Element	[REDACTED] --
Channel Roughness *(Assumed)*	470 μm
Total Reactor Power	[REDACTED] MW
Power Delivered to Main Flow	[REDACTED] MW
Power to Control Drums	[REDACTED] MW
Power to Moderator Elements	[REDACTED] MW
% Neutron and y-Ray Heating	12.13 %

5.1.7.2 Control Drum Cooling

The flow that enters the control drums is the flow that exits out of the regenerative nozzle coolant channels (state 5) from section 5.1.4. Due to lack of information, an assumption was formed that the control drums follow the same temperature curve as the fuel element channel surface temperature calculated by equation 4.20b. Further, the diameter, number of channels through which the propellant flows, and channel roughness had to also be assumed. By adjusting these assumed values, the appropriate values for the fluid exit state were reached. The assumed parameters of the control drum channels are listed in Table 5.9. The temperatures of the control drum surface and propellant along with the channel pressure are graphed in Figure 5.9. Here, the fluid temperature rises from the heat transfer occurring from the surface which is at a higher temperature. The pressure also decreases as the fluid flows through the control drum channels. Therefore, the model is behaving intuitively. The calculated heat deposited into the hydrogen flow was [REDACTED] MW. When comparing this value to the heat of [REDACTED] MW provided by AR, the difference is 0.1106% which is considered to be a rounding error.

Table 5.9: Control Drum Channel Parameters [55]

Parameter	**Given/Assumed**	
Number of Channels	16	--
Length	0.95	m
Diameter	0.0085	m
Roughness *(Assumed)*	3.7X10^-6	m
Neutron and Gamma Ray Attenuation	0	%

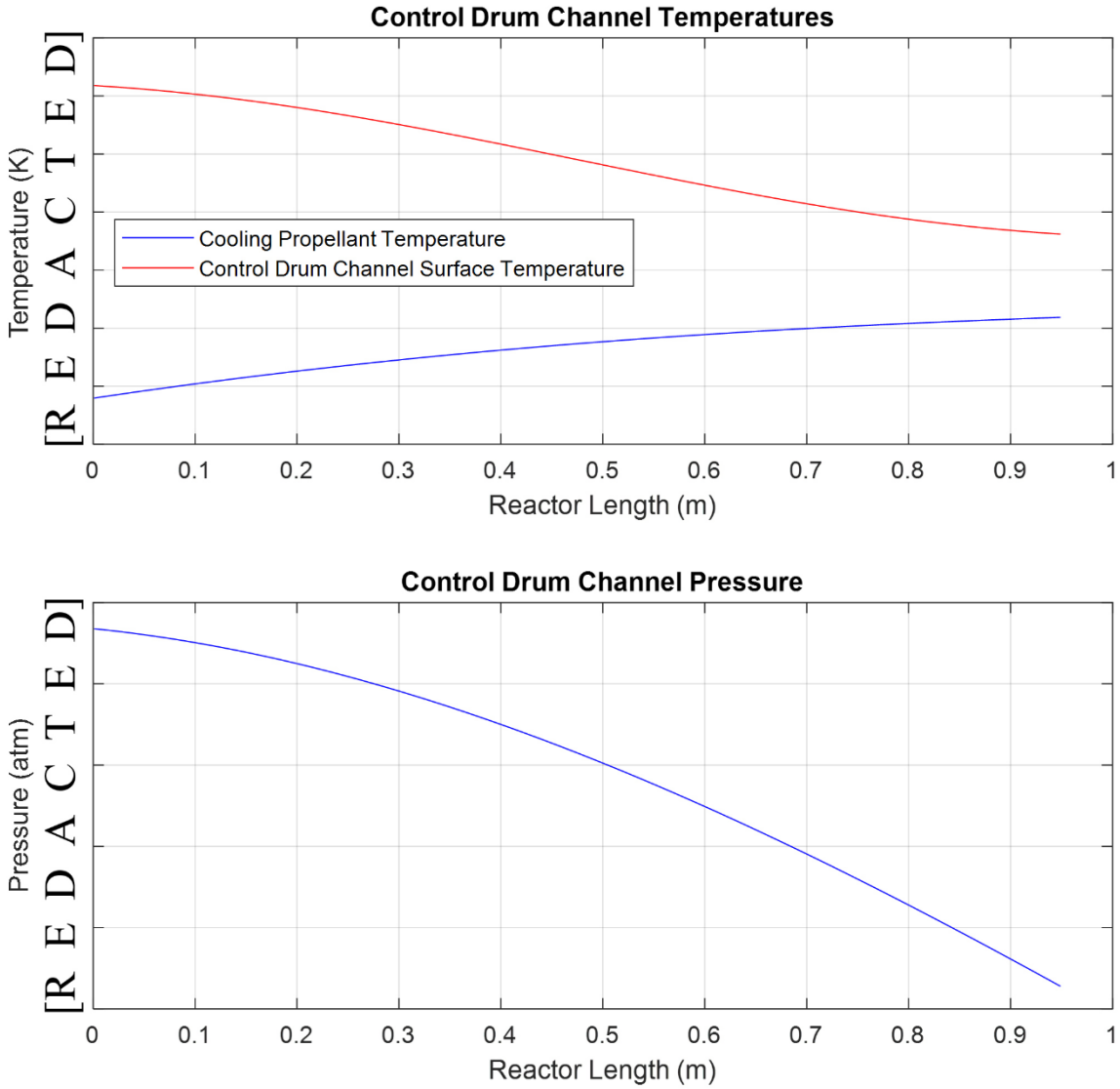

Figure 5.9: Control Drum Temperatures and Pressure

5.1.7.3 Moderator Flow

Hydrogen functions as both the propellant and moderator. There are [REDACTED] additional solid moderator elements that require cooling during reactor operation [42]. The hydrogen flow supply enters the surrounding cavity labelled A in Figure 5.9, changes direction at the bottom of the reactor while exhibiting a significant pressure loss through a

180 degree turn [60], and returns back up to the top of the reactor through the inner cavity labelled B in Figure 5.10. [61] The heat deposited into the propellant was calculated to be 45.6 MW. This value exactly matches that of AR.

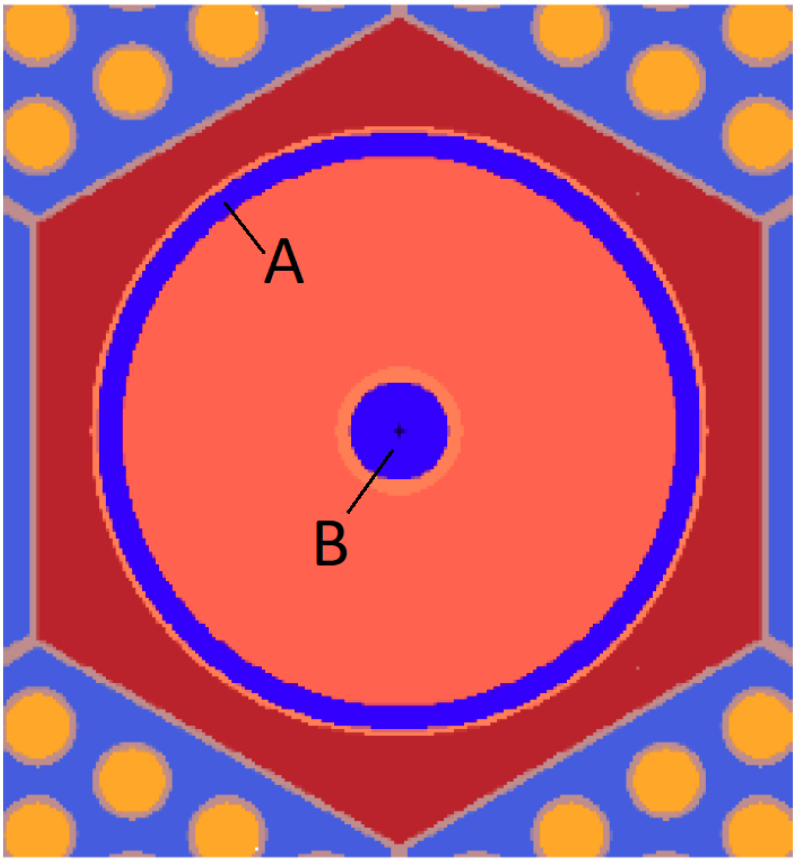

Figure 5.10: Cross-sectional Area of Moderator Element [55]

The parameters of the moderator channels are shown in Table 5.10 and the thermal distribution of the hydrogen propellant and moderator surface as well as the channel pressure are shown in Figure 5.11. The large difference in roughness between the supply and return flows was chosen to match the stagnation output state values in AR's engine model. These values may not reflect the true roughness values of the material and a 1 mm

roughness is slightly outside the range considered for reactor applications [56]. AR has also stated that they do not have an accurate model of the flow through the moderator elements (they have a "black box" for this component). However, they are confident that their model is still valid in determining the engine performance. [62]

Table 5.10: Moderator Element Parameters [42] [55]

Parameter	**Given/Assumed**	
Number of Moderator Elements	[REDACTED]	--
Length	0.95	m
Outer Diameter	0.0249	m
Inner Diameter	0.0225	m
Center Tube Diameter	0.0040	m
Supply Roughness *(Assumed)*	0.0010	m
Return Roughness *(Assumed)*	3.33X10^-10	m

The pressure loss when the flow switches from supply to return was calculated by using a pressure loss bend formula shown in equation 5.20 using flow pressure. The additional parameters were the radius of the bend R_{bend}, angle of the bend θ, and the bend coefficient κ_{bend} that was determined from a table. [60] Due to the use of the step method, small angles were used until their total summed to 180 degrees. This is shown in the pressure graph of Figure 5.11.

$$\Delta P = \frac{1}{2}\left(f\rho V^2 \frac{\pi R_{bend}}{D_{hyd}} \frac{\theta}{180} + \kappa_{bend}\rho V^2\right) \tag{5.20}$$

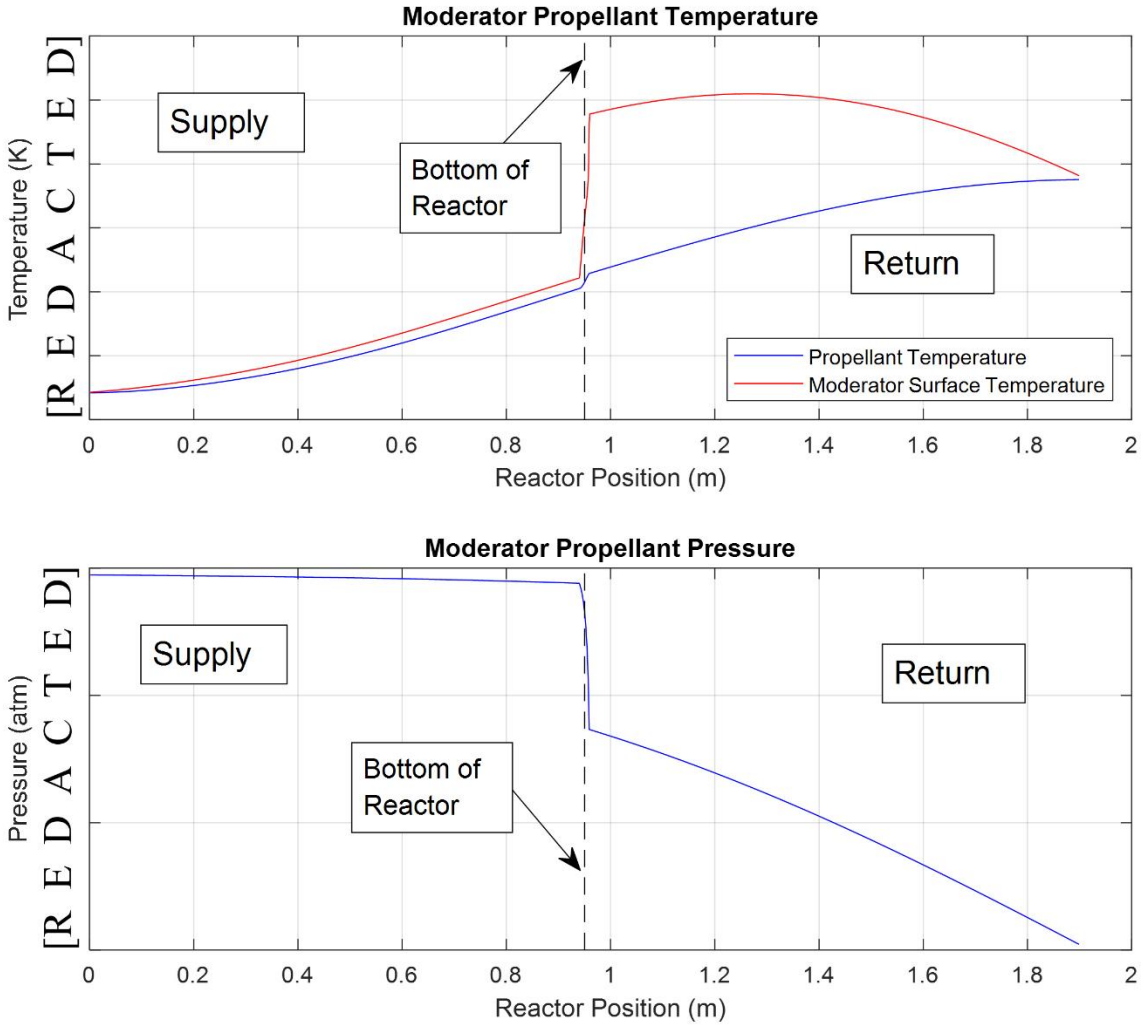

Figure 5.11: Moderator Propellant Flow Temperature and Flow Pressure

It should be noted that AR did not put the heat addition to the turbomachinery (12.57 MW) and regenerative cooling (2.7 MW) as part of the total reactor power. This could be that they were considering other external sources or simply the radiative heat from the reactor shell. Further, the sum of all the heat produced by neutron and gamma ray attenuation was summed to be 12.1311%, a lower value than the minimum experimentally determined by NIST. This discrepancy may be explained by the fact that the NIST reactor had reflector regions around the entire enclosure of the reactor while the NTP engine does

not have any barrier at the bottom of the reactor where the flow is pushed out through the nozzle. [58]

5.1.8 Nozzle

The nozzle is responsible for turning the thermal energy of the propellant into kinetic energy to produce thrust. The chamber conditions created at the reactor exit are a stagnation pressure of 68.046 atm and a stagnation temperature of 2650 K [3]. AR's nozzle design has a 386:1 area ratio [3] which translates into an exit Mach number of 7.485. During the first meter of expansion, some of the enthalpy of this flow is transferred into the coolant channel as discussed in section 5.1.4. After a total of 4.606 meters of axial expansion, the flow exits the nozzle at a pressure of 0.003471 atm and a temperature of 210 K [43]. The nozzle efficiency set forth by AR is [REDACTED] [42]. The produced thrust is [REDACTED] kN with an Isp of [REDACTED] seconds. The parameters of this nozzle are shown in Table 5.11.

Table 5.11: Nozzle Parameters [3] [42] [43]

Parameter	**Given/Assumed**	
Area Ratio	386:1	--
Throat Diameter	0.1087	m
Exit Diameter	2.1336	m
Length	4.6060	m
Distance of Regen Cooling from Throat	1.0386	m
Distance from Throat to Reactor	0.4480	m
Efficiency	[REDACTED]	%
Thrust	[REDACTED]	kN
Specific Impulse	[REDACTED]	s
Exit Temperature	210.7	K
Exit Pressure	0.003476	atm

5.2 Simulink Model and Validation

From the details of the components examined in section 5.1, a Simulink model was constructed with each component having its own block. This model and code are too large and extensive to include in this thesis (over 300 pages long), therefore, a Simulink model report is available upon request. This model runs in different conditions with different flow rates and power. Therefore, all of the external heat absorbed by the turbomachinery were made adjustable according to the fraction that the reactor power fluctuates from the datum point set to be AR's [REDACTED] MW [42]. Once all of the components with their respective parameters and representative equations have been created, the model was allowed to run iteratively and was observed to converge. During the simulation, the FSV was adjusted to provide the reactor pressure which would result in the desired chamber stagnation pressure of 68.046 atm [3]. Once the chamber stagnation pressure stabilized, the other states were observed to stabilize as well. This dynamic throttling is seen in the Simulink plot of the chamber pressure in Figure 5.12 where the x-axis is the iteration number. Some of the states exhibited larger error than others when comparing them to AR's states. Due to this, the respective component parameters calculated from AR's raw data were adjusted in order to obtain the values of the states in AR's model to be within 1% error. This discrepancy can likely be attributed to AR using more sophisticated codes for their model.

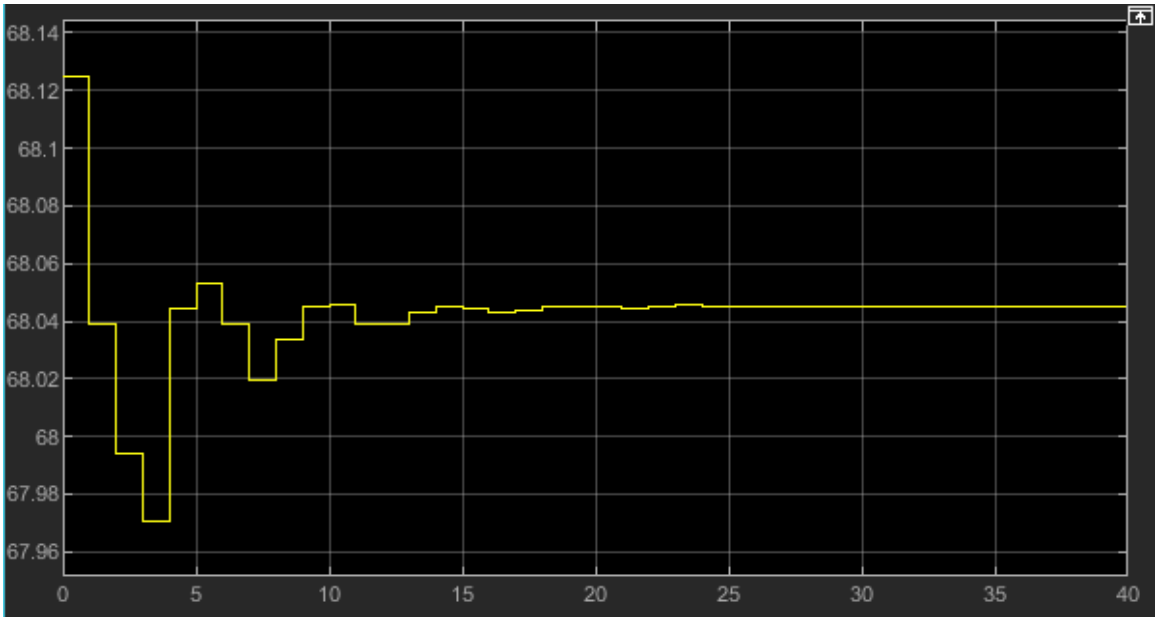

Figure 5.12: Simulink Model Chamber Pressure Convergence

The Simulink model's state outputs were extracted and compared with AR's values in Table 5.12. Each state number corresponds with the number in Figure 5.1. It should be noted that AR did not provide state values for state 12, therefore, this state was not compared. The states 15 and 16 exhibited larger errors than the rest of the states and have been marked red in Table 5.12. State 17 in the AR model could not be matched because the flows from states 16 and 14 cannot thermodynamically provide those values unless there was additional heat provided. Furthermore, state 16 does not resemble the output of a throttling valve and its values suspiciously exactly match the values of state 17. The throttling process in the Simulink model of this valve incorporated a 15% enthalpy loss in order to match state 17 which can be attributed to external effects. At this point, it is assumed that the data in state 16 is flawed and the percent error of this state is ignored. Despite this, the AR model is still valid since the state that is effected is only state 16 which

does not bleed to other states (state 17 follows thermodynamic principles). The mass flow rate in states 15 and 16 corresponds to that of the turbine bypass valve and is larger than 1%. This is due to the fact that with small mass flow rates, any deviation is magnified causing a large error where in fact, the mass flow rate difference between the Simulink model and the AR data is only 0.033 kg/s. This is the same mass flow rate increase as seen in all states which can be attributed to the fact that the nozzle throat and exit diameters provided by AR did not reflect the 386:1 area ratio which was used in the back calculation of the throat diameter. Furthermore, the ratio of specific heats was taken as a weighted average between the chamber and exit conditions to better capture the behavior of the entire flow. Lastly, it is possible that the AR model considers other nuances that were not considered in this research. Table 5.13 shows other general engine parameters extracted from the Simulink model and compares them with the AR data. At close examination, the Simulink model agrees with AR's data within 1% error resulting in this model passing the first validation test.

Table 5.12: State Comparison with AR Data

	AR Data			Simulink Model Data			Comparison		
Fluid State	**P (atm)**	**T (K)**	***ṁ* (kg/s)**	**P (atm)**	**T (K)**	***ṁ* (kg/s)**	**P % error**	**T % error**	***ṁ* % error**
1	1.293	20.556		1.292	20.555		0	0	0.253
2							0.172	0.023	0.253
3							0	0.091	0.253
4							0.083	0.533	0.253
5							0.02	0.279	0.253
6							0.088	0.067	0.253
7	[REDACTED]			[REDACTED]			0	0.533	0.253
8							0.006	0.092	0.253
9							0.011	0.025	0.253
10							0.594	0.198	0.253
11							0.237	0.306	0.47
12							--	--	--
13							0.237	0.25	0.425
14							0.082	0.024	0.425
15							0.237	0.25	**1.426**
16							**0.899**	**10.15**	**1.426**
17							0.238	0.344	0.245
18	89.07	277.22		89.11	277.42		0.041	0.073	0.253
19	68.05	2650		68.05	2649.5		0.001	0.017	0.253

Table 5.13: General Parameter Comparison with AR Data

Parameter	**AR Values**	**Simulink Model Values**	**% error**
Reactor Power	[REDACTED] MW	[REDACTED] MW	0.233
Main Flow Power	[REDACTED] MW	[REDACTED] MW	0.254
Moderator Element Power	[REDACTED] MW	[REDACTED] MW	0.012
Control Drum Power	[REDACTED] MW	[REDACTED] MW	0.254
Regen Nozzle Power	[REDACTED] MW	[REDACTED] MW	0.355
Boost Turbopump RPM	[REDACTED] RPM	[REDACTED] RPM	0.075
Main Turbopump RPM	[REDACTED] RPM	[REDACTED] RPM	0.129
Vacuum Thrust	[REDACTED] kN	[REDACTED] kN	0.015
Vacuum Isp	[REDACTED] s	[REDACTED] s	0.350

The second validation test involves changing the engine geometry, power level, and mass flow rate and then comparing it with NERVA's historical data. Although NERVA does not offer as many details as the AR model, the major states are still available to compare. The NERVA engine derivative that was used for this comparison is the PEWEE class dual TPA expander cycle from NASA's DRA 5 for which available specifications are shown in Table 5.14 [16] [18].

Table 5.14: General Parameters for PEWEE Reference Engine

Parameter	Value	
Chamber Temperature	2790	K
Chamber Pressure	68.064	atm
Thrust	111.206	kN
Specific Impulse	906	s
Mass Flow Rate	12.5	kg/s
Area Ratio	300:1	--
Exit Diameter	1.87	m
Reactor Main Flow Power	503	MW
Reactor Element Lengths	0.89	m

The chamber stagnation pressure did not change from the AR design, however, the nozzle geometry and the chamber stagnation temperature changed. No information was given on the turbomachinery or the cooling lines of this engine. The Simulink model engine nozzle parameters were changed to those in Table 5.12 and the required chamber stagnation temperature was set to be 2790 K [18] instead of 2650 K from the AR design [3]. The fuel was changed to the dispersed (U,Zr)C fuel and the thermal conductivity was changed accordingly [63]. Everything else including duct dimensions, the fraction of the amount of

heat transferred into the turbomachinery, and neutron and gamma ray attenuation adjustments were kept the same. It is expected that the percent errors in this validation will be higher than those in the previous since not much information is known. The chamber pressure convergence is shown in Figure 5.13 which took much longer to achieve than the AR model likely due to the initial conditions remaining unchanged. Table 5.15 shows the Simulink model results compared with the PEWEE engine from NASA's DRA 5. The highest percent error was the amount of heat deposited into the propellant. This error may be attributed to the gamma ray and neutron attenuation and to the likely difference in the fuel element channels and geometry which may be different for the PEWEE design than the AR design.

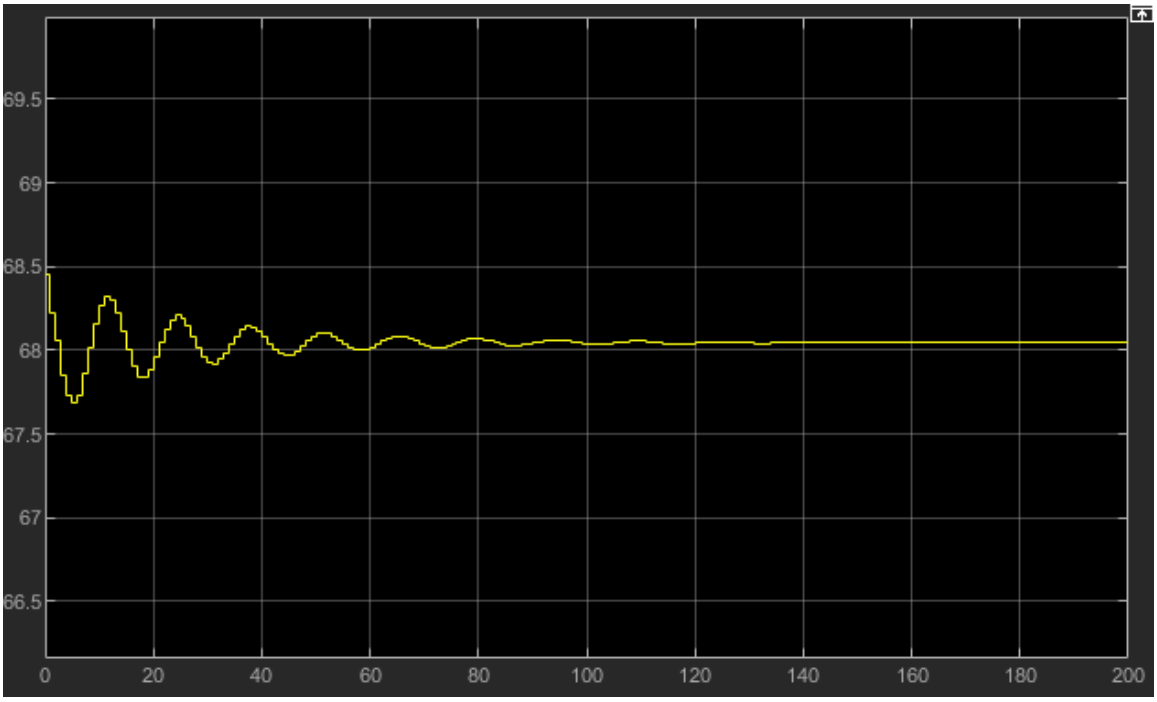

Figure 5.13: PEWEE Simulink Model Chamber Pressure Convergence

Table 5.15: General Parameter Comparison for PEWEE Reference Engine [18]

Parameter	NERVA PEWEE-1 Values	Simulink Model Values	% error
Chamber Temperature	2790.0 K	2789.5 K	0.018
Chamber Pressure	68.064 atm	68.046 atm	0.027
Thrust	111.206 kN	111.253 kN	0.043
Isp	906.000 s	912.886 s	0.760
Mass Flow Rate	12.500 kg/s	12.427 kg/s	0.585
Reactor Main Flow Power	503.000 MW	509.971 MW	1.386

In order to further check the validity of this model, it is important to make sure that no parameter approached infinity or diverged from the norm in any other way. Tables 5.16 and 5.17 show the same states and parameters for the PEWEE engine validation as do Tables 5.11a and 5.11b for the AR validation. In these values, the flow rate of the propellant went down, however, the heat deposited into the propellant went up. This is due to the fact that the exit temperature is higher at 2790 K for the PEWEE design [18] than the 2650 K of the AR design [3]. It is also noticed that the pressure losses inside the ducts are lower. Further, the length of the nozzle did not change nor the thickness of the cooling channels within the nozzle. Since the exit diameter is smaller, the hydrogen velocity becomes higher, thus increasing the heat transfer from the plume as evidenced by equations 4.34a and 4.34c (as flow velocity increases with the other parameters being constant, the Reynolds number increases and thus the overall convective heat transfer coefficient increases). The higher specific impulse and lower mass flow rate may be attributed to the fact that hydrogen's ratio of specific heats decreases as its temperature increases (refer to Appendix A, Figure A.1.4). As it appears, no parameter exhibited unpredictable or divergent behavior. In

conclusion to Chapter 5, the Simulink NTP engine model based on the Aerojet Rocketdyne's values has been created and validated.

Table 5.16: Simulink Model Fluid States

	Simulink Model AR Parameters			**Simulink Model PEWEE Parameters**		
Fluid State	**P (atm)**	**T (K)**	$\dot{m}$ **(kg/s)**	**P (atm)**	**T (K)**	$\dot{m}$ **(kg/s)**
1	1.292	20.556		1.293	20.556	12.427
2				2.922	21.721	12.427
3				190.232	43.61	12.427
4				189.584	43.852	4.069
5				183.459	94.47	4.069
6				179.571	163.885	4.069
7				189.731	43.852	8.358
8				184.644	249.448	8.358
9				177.393	393.817	8.358
10				176.238	313.703	12.427
11				175.658	313.833	0.425
12				87.829	309.705	0.425
13				175.658	313.833	9.595
14				100.61	284.055	9.595
15				175.658	313.833	2.407
16				100.885	309.407	2.407
17				100.243	289.63	12.002
18	89.109	277.426		87.499	290.968	12.427
19	68.045	2649.53		68.046	2789.5	12.427

Table 5.17: Simulink Model General Parameters

Parameter	**Simulink AR**	**Simulink PEWEE**
Reactor Power	[REDACTED] MW	560.949 MW
Main Flow Power	[REDACTED] MW	509.971 MW
Moderator Element Power	[REDACTED] MW	46.149 MW
Control Drum Power	[REDACTED] MW	4.829 MW
Regen Nozzle Power	[REDACTED] MW	2.856 MW
Boost Turbopump RPM	[REDACTED] RPM	15863.198 RPM
Main Turbopump RPM	[REDACTED] RPM	55791.923 RPM
Vacuum Thrust	[REDACTED] kN	111.253 kN
Vacuum Isp	[REDACTED] s	912.886 s

CHAPTER 6

SEEDED HYDROGEN PROPELLANT

The information provided by Aerojet Rocketdyne's NTP engine model was used to create a simulation of the engine which matched their parameters within 1% error. It was validated doubly by using AR values and by changing the engine physical geometry and steady state operation values to match the NERVA derived engine PEWEE-1 which also matched this engine to within 3% error. The highest errors encountered during the validation of the model to AR's parameters were at state 16 which was considered an unreliable data point as explained in Chapter 5. The highest error from the PEWEE validation was the reactor power which may be attributed to different reactor and fuel element geometry and attenuation coefficient. Based on these results, it may be concluded that the NTP engine Simulink model is valid and the next step would be to modify this model to incorporate seeded propellant elements and revalidate it to AR's values at 0% seed.

The flow diagram for the NTP engine utilizing seeded hydrogen propellant is shown in Figure 6.1 along with the added fluid states 20 through 26. The first part of this

chapter will deal with examining each added component for seeded propellant while the second part will focus on the revalidation and results. The considered seeds are argon, krypton, and xenon for which basic properties and prices [64] are shown in Table 6.1 with hydrogen as a comparison [65]. Detailed property graphs for these seeds are shown in Appendix A.2 through A.4. The maximum seed mass concertation was chosen to be slightly above 60% of the mass of the propellant, beyond which the specific impulse begins to resemble that of highly efficient chemical rocket engines. Since the seeds are heavy noble gases, the molar concentration will be significantly lower than the mass concentration: 6% for argon, 3% for krypton, and 2% for xenon. This large difference between the molar and mass concentration percentages is the key in preserving the lower viscosity and higher thermal conductivity of hydrogen while lowering its specific heat capacity. The effects of this will be seen primarily in the flow through the reactor in section 6.1.5.

Table 6.1: Seed and Hydrogen General Properties

	Argon (Ar)	**Krypton (Kr)**	**Xenon (Xe)**	**Hydrogen (H_2)**
Atomic Number	18	36	54	1
Atomic Weight (amu)	39.88	83.798	131.293	2.0016
Gas Constant [J/(kg*K)]	208.475	99.2148	63.324	4153.68
Critical Temperature (K)	83.8058	209.48	289.733	32.938
Critical Pressure (atm)	47.9941	54.5275	57.6561	12.6899
Density at Boiling Point (kg/m^3)	1395.4	2413	2942	70.99
Cost Per Kilogram	$0.50	$16	$1200	$3.66

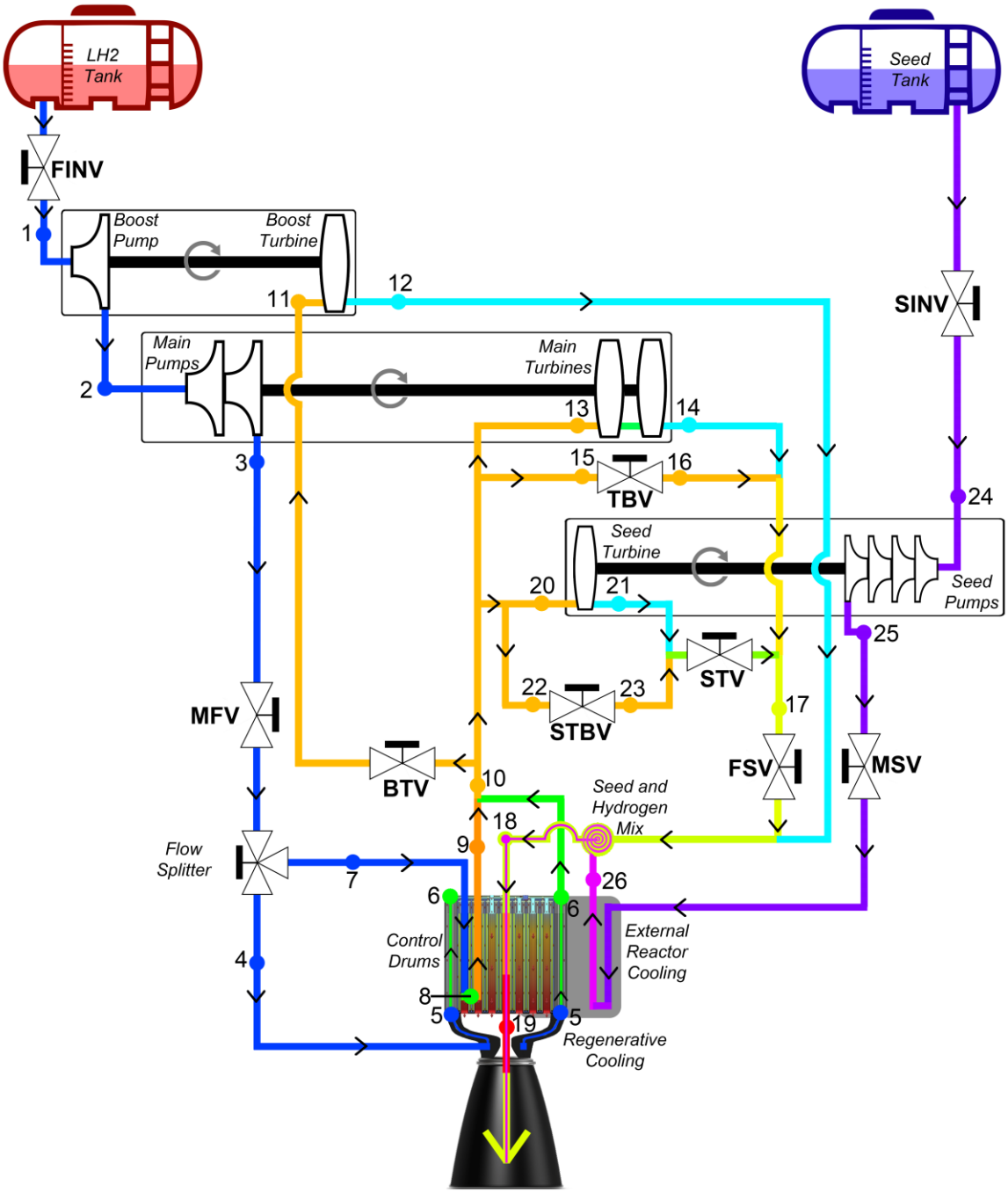

Figure 6.1: NTP Engine with Seeded Hydrogen Flow Schematic (Adapted from AR PBM 3.0 [3])

Table 6.2: NTP Engine with Seeded Hydrogen State Legend

1	Pre-Boost Pump	**14**	Post-Main Turbines
2	Pre-Main Pumps	**15**	Pre-Turbine Bypass Valve
3	Maximum Pressure (Propellant is Supercritical)	**16**	Post-Turbine Bypass Valve
4	Pre-Regenerative Cooling	**17**	Post-Turbine and Post-Bypass Valve Flows Mix
5	Post-Regenerative Cooling	**18**	Pre-Reactor State
6	Post-Control Drum Cooling	**19**	Chamber State
7	Pre-Moderator Element Cooling	**20**	Pre-Seed Turbine
8	Bottom of Moderator Element	**21**	Post-Seed Turbine
9	Post-Moderator Element Cooling	**22**	Pre-Seed Turbine Bypass Valve
10	Mixture of Post-Cooling Lines	**23**	Post-Seed Turbine Bypass Valve
11	Pre-Boost Turbine	**24**	Pre-Seed Pumps
12	Post-Boost-Turbine	**25**	Post-Seed Pumps
13	Pre-Main Turbines	**26**	Post External reactor Cooling (Seed is Supercritical)

6.1 Seed Enabling Components

All components that have been examined in Chapter 5 were left unchanged and additional seed components have been added without affecting the engine operation with pure hydrogen. Therefore, as a validation for section 6.2, the target would be to compare the seeded model states with the unseeded pure hydrogen model of Chapter 5. Figure 6.1 shows these additional components which were organized in such a way as to minimize the effect that they have on pure hydrogen operation. Table 6.2 briefly describes the additional states. The primary purpose for this is for easy incorporation into a physical system. From Chapter 5, Table 5.2 shows that there is significant mass flow through the TBV in states 15 and 16. This mass flow was used to power a turbine which would only

run the pumps required to pressurize the seed line flowing from the seed tank. To counter any expected pressure losses, the output of the seed pumps was set to be 120 atm. This pressurized seed line then flows on the outside of the reactor surface through channels providing some cooling and also absorbing some heat in order for the seed to transition into a supercritical state. According to multiple sources, supercritical fluids are readily miscible with negligible diffusion time if the two flows are turbulent [25] [26] [41]. After flowing through these channels, the supercritical seed then mixes with the main hydrogen flow and proceeds as a supercritical mixture through the reactor and out the nozzle.

6.1.1 Seed Tank

The pressure of the seed tank was kept to be the same as that of hydrogen. However, due to the considerably smaller volume of this tank, it is possible to pressurize this tank further and reduce the number of seed pumps required. Since the boiling and freezing point of heavy noble gases are close together, this tank would need to be monitored for any temperature divergence. However, the liquid range of hydrogen for the same pressure is narrower and the temperature ranges that the considered seeds require are higher and will not be as taxing on the cryocoolers. Table 6.3 shows the temperature range of the seed tank for each considered seed with hydrogen as a reference and Appendix A Figures A.2.1, A.3.1, and A.4.1 show the vapor pressure of argon, krypton, and xenon respectively. [65]

Table 6.3: Seed and Hydrogen Tank Temperature Ranges

	Liquid Temperature Range at **2.0414 atm** (K)
Argon (Ar)	83.860 to 94.667
Krypton (Kr)	115.91 to 129.68
Xenon (Xe)	161.63 to 178.57
Hydrogen (H_2)	14.037 to 23.050

6.1.2 Seed Pumps

Due to pressure losses in the duct that connects the seed tank to the seed pumps (this duct was assumed to be the same 4 m length as that of the hydrogen duct), similar to the pump system of hydrogen, a boost pump will be incorporated as a precaution for cavitation. However, unlike the pump system for hydrogen, this boost seed pump will have to operate within a very wide range of flow rates and at relatively even efficiency within that range. Furthermore, for system simplicity, this boost seed pump will be connected to the same shaft as the main seed pumps and operate at the same rotational velocity. This same even efficiency requirement will be relevant for all of the main seed pumps which will result in a series of 3 main seed pumps following the boost seed pump. The design parameters of the pumps for each seed will be the same for versatility. This means that any of the examined seeds may be put into the seed tank and the seed pumps will be compatible with it. Some of the parameters may be adjusted during further research to cater to a specific seed if so desired. The seed pumps were designed by using the pump equations 5.1 through 5.8. Table 6.4 shows the physical and performance parameters for each pump and Appendix F shows the performance graphs of each pump for each seed.

Table 6.4: Seed Pump Parameters

Parameter	**Argon**		**Krypton**		**Xenon**	
ω	131000 to 24000	RPM	114000 to 21000	RPM	108000 to 20000	RPM
Boost Seed Pump						
Pressure Head	50.2983	m	28.7516	m	23.4658	m
$NPSH_a$	2.3981	m	1.6188	m	1.4147	m
$NPSH_r$	2.3755	m	1.5644	m	1.3738	m
n_s	2.5	--	2.5	--	2.5	--
Diameter	0.0256	m	0.0256	m	0.0256	m
Main Seed Pump 1						
Pressure Head	283.346	m	158.0081	m	129.8279	m
$NPSH_a$	50.704	m	28.3068	m	23.7063	m
$NPSH_r$	51.065	m	28.7727	m	23.9899	m
n_s	0.704	--	0.704	--	0.704	--
Diameter	0.0327	m	0.0327	m	0.0327	m
Main Seed Pump 2						
Pressure Head	318.128	m	177.7283	m	145.6351	m
$NPSH_a$	318.1284	m	183.6182	m	150.053	m
$NPSH_r$	316.3067	m	186.8929	m	152.2692	m
n_s	0.6425	--	0.6425	--	0.6425	--
Diameter	0.0327	m	0.0327	m	0.0327	m
Main Seed Pump 3						
Pressure Head	396.751	m	180.6544	m	147.5694	m
$NPSH_a$	616.5447	m	355.625	m	292.2146	m
$NPSH_r$	572.7986	m	335.0843	m	276.06	m
n_s	0.6425	--	0.6425	--	0.6425	--
Diameter	0.0327	m	0.0327	m	0.0327	m

6.1.3 Seed Turbine

The purpose of the seed turbine is to drive the seed pumps as these pumps must run on a separate shaft with a separate rotating velocity from the main pumps and turbines

depending on the desired seed amount. The working fluid going through the seed turbine is the residual hydrogen not used to flow through the boost and main turbines. The input flow conditions of the seed turbine will be the same as those for the main turbines with the output flow pressure higher than that of the main turbine output to ensure no backflow. Two sets of isenthalpic throttle valves will be used to ensure that the final output state pressure is slightly higher than that of the main turbine output. This setup is shown in the Figure 6.1 seeded hydrogen flow schematic.

The seed turbine was designed by using the gas turbine equations 5.10a through 5.13 as well as the compressible flow equations 4.1 and 4.2. The stagnation pressure ratio of this turbine was set to the combined stagnation pressure ratio of the main turbines (a value of 1.741). Just like the main turbines, the mass flow rate through the seed turbine is a function of constant specific work and the required work. The required work of each seed is shown in Figure 6.2. The design point was at the maximum seed amount where the mass flow rate of hydrogen is the least. The efficiency curve was chosen so that the hydrogen mass flow rate through the seed turbine does not exceed 75% of the residual mass flow to allow for some flow through the turbine bypass valve in order to keep it operational [62].

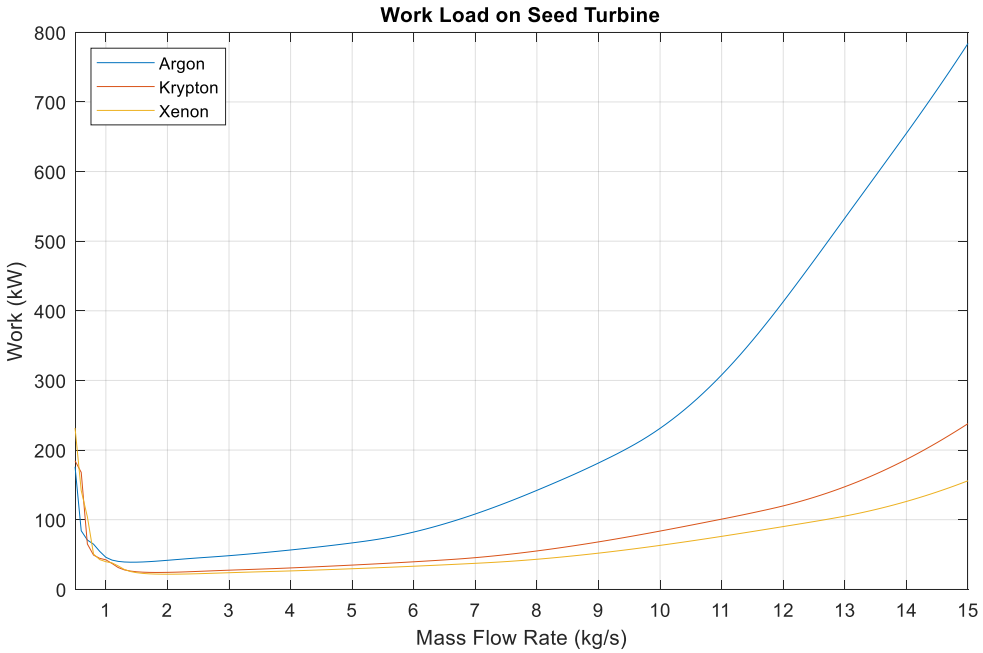

Figure 6.2: Seed Turbine Required Work

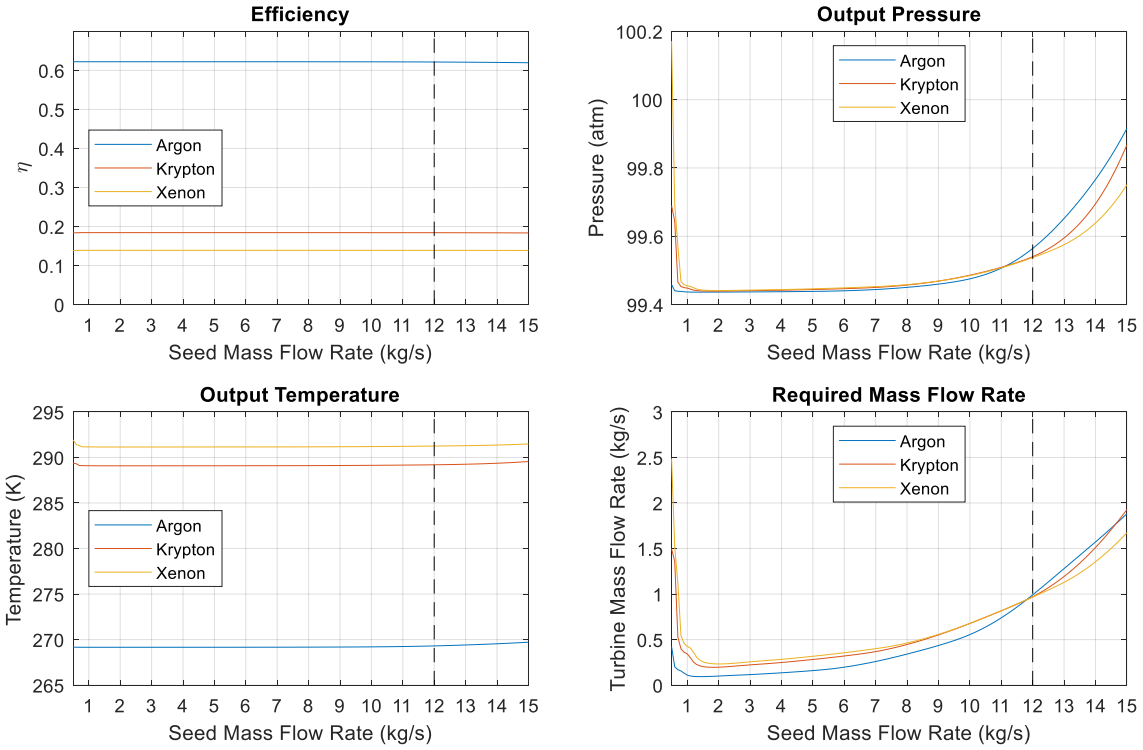

Figure 6.3: Seed Turbine Performance

The performance of this design is shown in Figure 6.3 with assumed constant inlet conditions of the AR specified state 13. The black dashed line represents the design point with the valid turbine operation to the left of it. On the right side of the design point, the graphs show that as the seed amount increases further, the required hydrogen mass flow rate through the seed turbine exceeds the maximum design mass flow rate. However, it will still be possible to push the seed percent mass even further until the system can no longer provide the required hydrogen mass flow rate through the seed turbine or the seed flow rate is so high that it begins to boil from excessive pressure losses within the tank duct before reaching the boost pump. Higher seed concentrations may be examined in future research. Furthermore, at very low seed concentrations, the efficiency of the pumps approaches zero which results in a minimum amount of seed for the system to be operational. This value is within the range of 0.75kg/s to 1 kg/s of seed mass flow rate or 5% to 7.4% mass concentration. The size of this turbine, blade angles, and other physical parameters will be examined and determined in future research. These parameters are not critical to the equations used thus far. Table 6.5 shows the summary of the physical and performance parameters of the seed turbine at the design point. The total work that the seed turbine is required to provide as a function of seed mass flow rate is shown in Figure 6.4.

Table 6.5: Seed Turbine Parameters at the Design Point *(Given values from* [42] *have been redacted)*

Parameter	Argon	Krypton	Xenon
ω	131000 to 24000 RPM	114000 to 21000 RPM	108000 to 20000 RPM
PR_0	[REDACTED]	[REDACTED]	[REDACTED]
η_{turb}	0.6215 --	0.1842 --	0.1390 --
T_{in}	[REDACTED]	[REDACTED]	[REDACTED]
P_{in}	[REDACTED]	[REDACTED]	[REDACTED]
T_{out}	269.3000 K	289.2000 K	291.3000 K
P_{out}	99.5600 atm	99.5400 atm	99.5400 atm
$\dot{W}_{turb}$	413.1000 kW	119.8000 kW	90.1100 kW
$\dot{Q}_{in,external}$	0.0000 kW	0.0000 kW	0.0000 kW
d_{in}	0.0300 m	0.0300 m	0.0300 m
d_{out}	0.0425 m	0.0425 m	0.0425 m

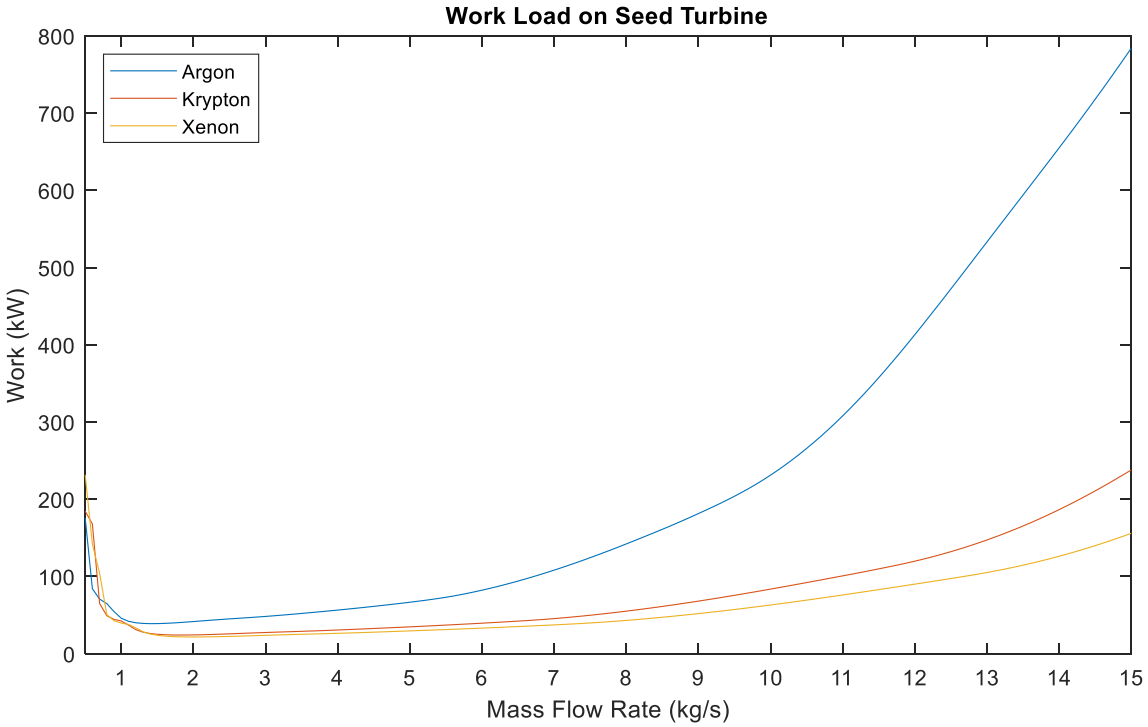

Figure 6.4: Total Work Required from Seed Turbine

6.1.4 Reactor Pressure Shell Surface Cooling (Seed Preheating)

The primary purpose of the seed channels running around the surface of the reactor pressure shell is to preheat the seed in order for it to transition into the supercritical phase before mixing with supercritical hydrogen. No information was given on the surface temperature of the reactor or the temperature distribution inside the reactor. Therefore, the control drums will be used as the heat source as they already have a temperature distribution T_{CD}. The heat transfer from the control drums to the reactor surface is assumed to be driven by radiative heat transfer to space from the reactor surface as well as the heat transfer to the seed channels. The reactor pressure shell and reflector materials are assumed to be aluminum and beryllium respectively which is consistent with NERVA reactor designs [66]. No information was given about the reactor shell material by AR. The thermal conductivity of beryllium and aluminum is similar at around $210\ \frac{W}{mK}$ [67]. By solving equation 6.1 for the reactor surface temperature T_S iteratively with a grid spacing of ΔL corresponding to differential seed channel surface area ΔA_s, the reactor surface temperature was found. Future research will address the temperature distribution inside the reactor, throughout the control drums, and out to the reactor pressure shell surface with higher fidelity.

$$\frac{2\pi K \Delta L}{\ln\left(\frac{d_o}{d_i}\right)}(T_{CD} - T_S) = \pi d_o \Delta L \sigma \varepsilon\left(T_S^4 - T_{space}^4\right) + \hbar \Delta A_s (T_S - T_{seed}) \tag{6.1}$$

The seed will enter into lines on top of the reactor pressure shell surface close to the turbomachinery, run through to the bottom of the reactor, make a 180 degree turn, and

run back up to the top of the reactor pressure shell surface. This layout is illustrated in Figure 6.5. Throughout all of this flow, the seed is absorbing the heat coming from the reactor while also losing pressure as seen in Figure 6.6 which refers to argon at maximum seed concentration. Unlike the sharp pressure drop in a 180-degree bend as seen in the moderator element (refer to Figure 5.11), this pressure drop is rather even throughout the flow. This is due to the fact that the seed is transitioning from a liquid into a supercritical fluid with high density, high viscosity, and relatively low velocity. However, this velocity is still capable of producing a Reynolds' number of over 10^7 resulting in a fully turbulent flow. Thus, the majority of the pressure drop is due to the flow viscosity rather than flow velocity. Due to the lower specific heat capacity of krypton and xenon relative to argon, but similar mass flow rates, their resulting temperatures after leaving the seed preheating channels are over their critical temperatures even though they have higher values. The temperature and pressure distributions of krypton and xenon at maximum seed concentrations are shown in Appendix I. Table 6.6 shows the physical parameters of the seed preheating channels. Furthermore, as the seed concentration increases, the hydrogen flow rate decreases, thus the control drum temperatures rise from those in Figure 5.9 to those in Figure 6.7. [65]

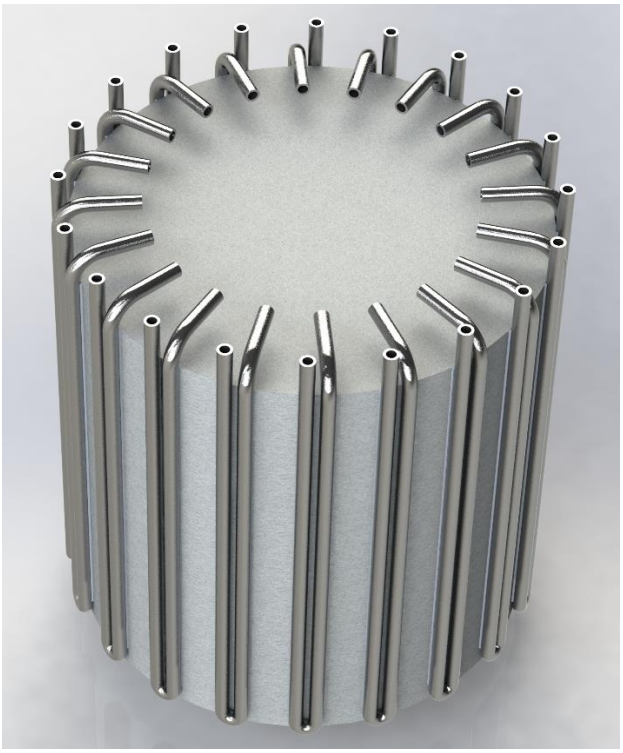

Figure 6.5: Seed Preheating Lines

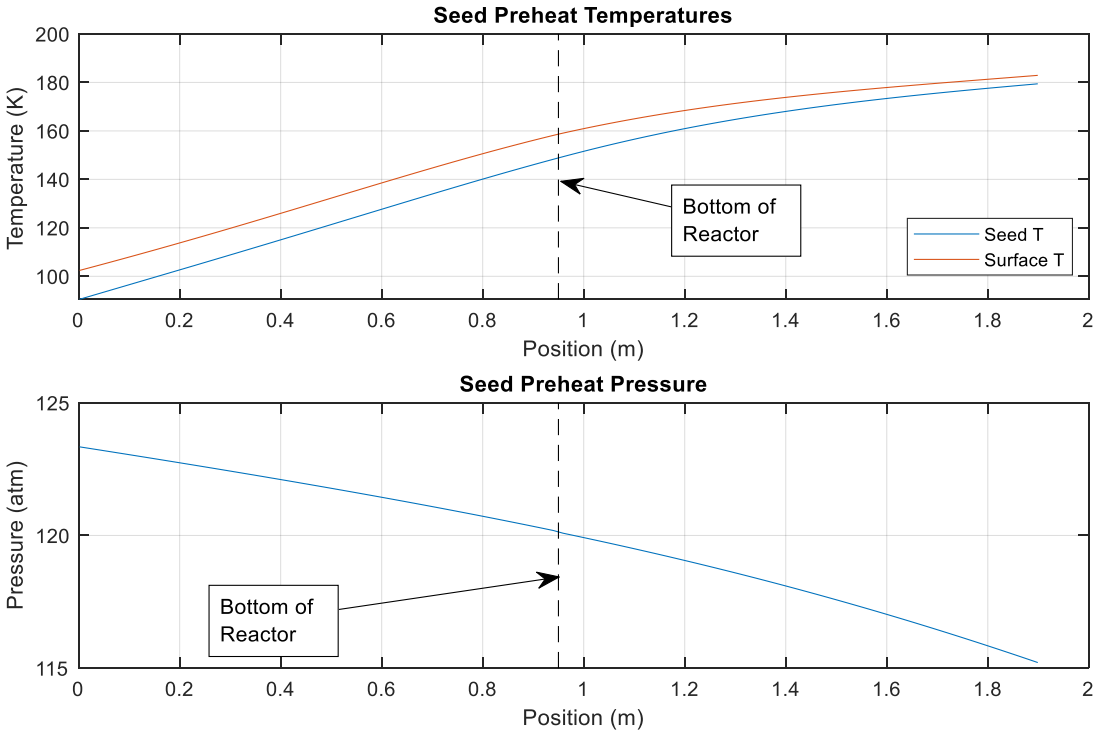

Figure 6.6: Argon Preheating Temperature and Pressure at Maximum Concentration

Table 6.6: Seed Preheating Line Parameters

Parameter	Value	
Total Length	1.9	m
Number of Lines	20	--
Internal Diameter	0.02	m
Roughness	3×10^{-5}	m
Curvature Radius	0.04	m
Curvature Angle	180	deg

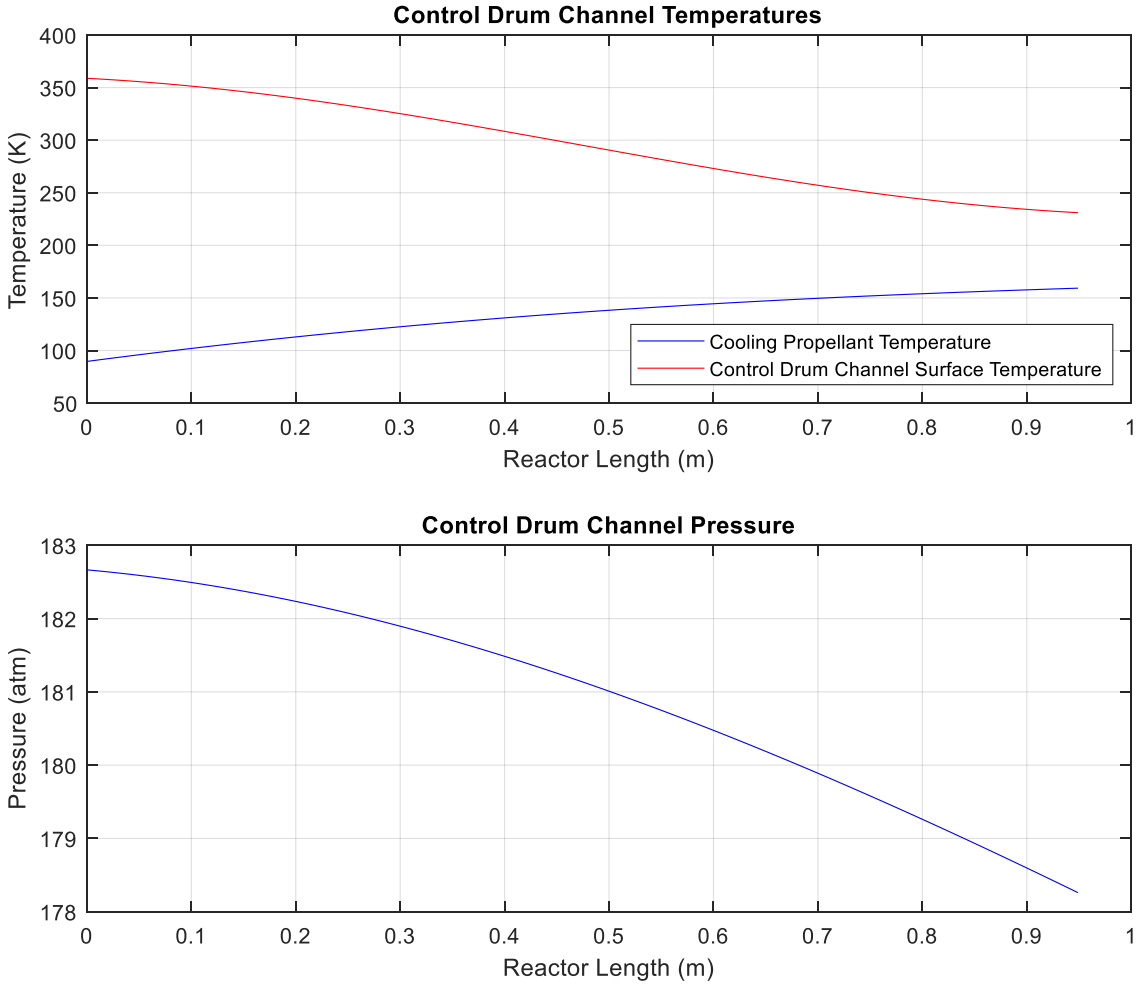

Figure 6.7: Hydrogen Control Drum Temperature and Pressure Distributions at Maximum Seed Concentration

Once the seed has exited the preheating channels, it mixes with hydrogen by the process of turbulent diffusion which is assumed to occur instantaneously with the process explained in more detail in Chapter 2. Future research will examine turbulent diffusion in supercritical fluids. This mixture has its own critical temperature and pressure. Due to the lack of experimental data, pseudo critical temperature and pseudo critical pressure have been graphed as a function of seed mass percentage via lever rule [41] in Figure 6.8.

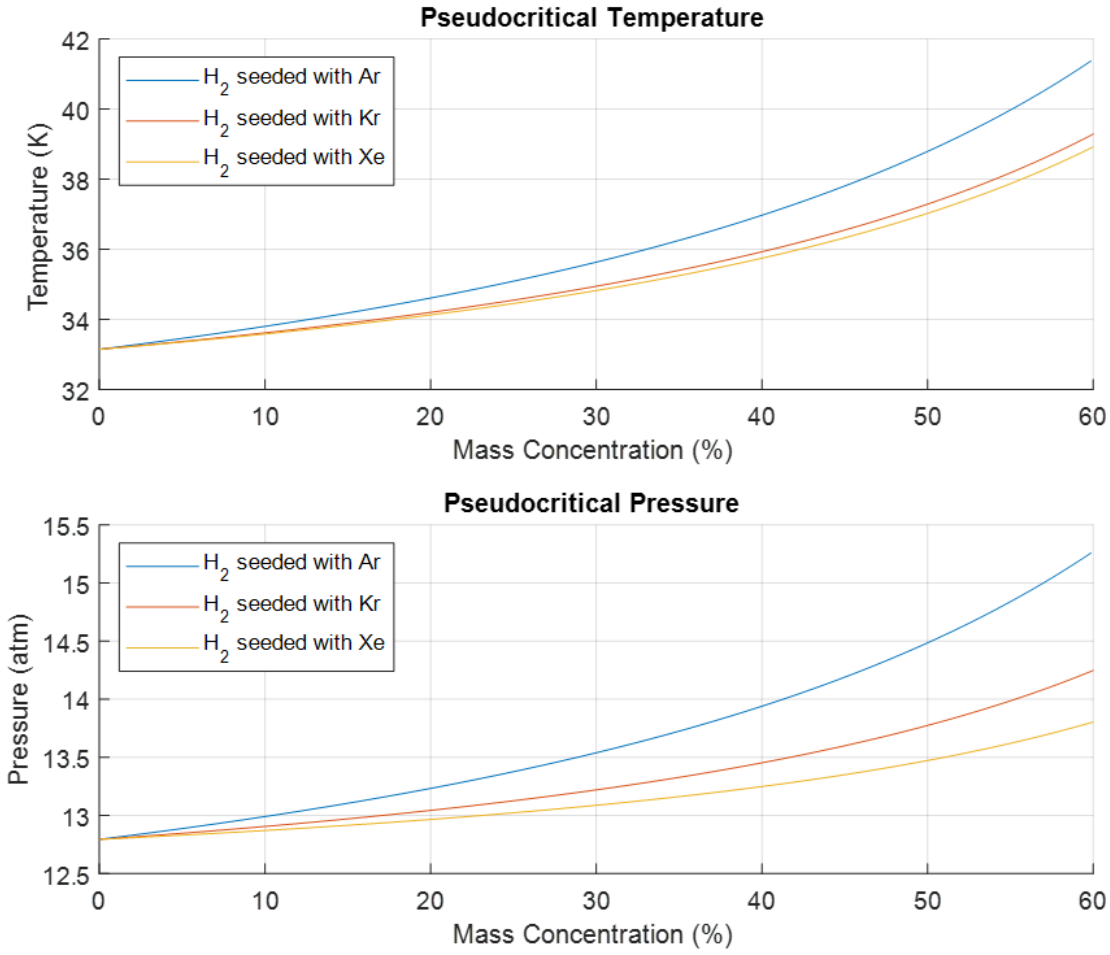

Figure 6.8: Seeded Hydrogen Pseudocritical Temperature and Pressure

6.1.5 Main Reactor Modification

The main heating of the seeded hydrogen occurs inside the reactor fuel element channels. Since this propellant is now a mixture, the fluid properties will change according to the mixture concentration. In Chapter 4, various mechanisms by which the properties of a mixture can be calculated were examined and will be used in the modification of the main reactor. From the fluid exit temperature and pressure drop equations 4.16 and 4.21b respectively, the main parameters of concern are the viscosity, thermal conductivity, density, and specific heat capacity. The viscosity and thermal conductivities are dependent on the molar concentration of the seed in the propellant as shown in equations 4.18b and 4.19 respectively. The density and specific heat capacity, on the other hand, are dependent on the mass concentration of the seed as shown in equations 4.10 and 4.17a respectively. Figure 6.9 shows how these four parameters change with respect to the mass concentrations of the respective seeds at the average reactor temperature and pressure of 1500 K and 77 atm respectively. Three dimensional plots at discretized seed concentrations are shown in Appendix G for all three considered seeds.

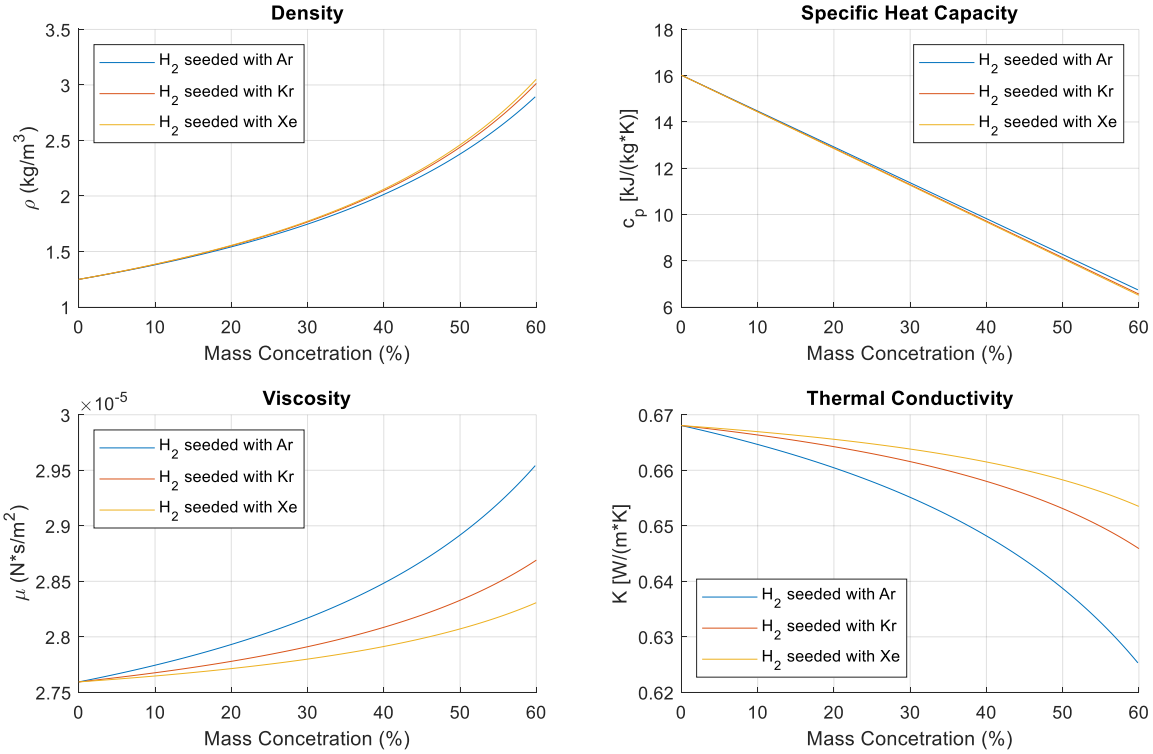

Figure 6.9: Seeded Hydrogen Properties at 1500 K and 77 atm

The neutron and gamma ray attenuation coefficient will be modified to incorporate the fact that heavy noble gases do a poor job of neutron scattering and absorb much less gamma radiation than hydrogen [68]. Furthermore, krypton and xenon have higher absorption cross sections than hydrogen [69] which may present an issue with the neutron population inside the reactor which will be addressed in future research. The reactor geometry will not be modified, however, the constraints and requirements which will be used to dictate the amount of flow and reactor power will be modified and discussed in section 6.3. Once heated, the flow proceeds to the nozzle where it follows the same calculations as for the pure hydrogen model but with the modified fluid properties as discussed.

Even though a simple comparison of the heat transfer and pressure drops through the flow can be completed for a constant mass flow rate, this comparison will not be valid as the mass flow rate itself changes in the engine because it is dependent on the mixture properties as evidenced in the maximum mass flow through the nozzle throat equation 4.6. Therefore, the Simulink model will be employed to provide a thorough analysis and comparison among pure hydrogen and various seed concentrations which will be explored in section 6.3.

6.2 Validation

The modified model was validated by setting the seed amount to 0% and allowing it to operate with only pure hydrogen flowing through it. The results were compared with both the original AR state data (Table 6.7) and the pure hydrogen model state data (Table 6.8) from Chapter 5. The results generally agree with both data sets except for the previously discussed issue with state 15 and 16 in Chapter 5 where the values in question are marked in red. The mass flow rate in these states appears to be somewhat higher, and because of the relatively small flow rate, the percent error appears higher. However, this error is within 3% of AR values. State 17's error increased due to lower pressure. This lower pressure is due to the fact that the duct from the main turbines was extended to allow for the duct from the seed turbine to mix into the main flow. Increasing the length of a duct increases the pressure loss which is what is seen as a result in state 17. Although this increases the error, it further validates the accuracy of the model. The other parameters such as specific impulse, thrust, and reactor power are compared with the original AR data

and the pure hydrogen model data in Tables 6.9 and 6.10 respectively with the data in question from states 15 and 16 marked in red.

	AR Data			Simulink Model Data			Comparison		
Fluid State	**P (atm)**	**T (K)**	***ṁ* (kg/s)**	**P (atm)**	**T (K)**	***ṁ* (kg/s)**	**P % error**	**T % error**	***ṁ* % error**
1	1.293	20.556		1.292	20.56		0	0	0.2684
2	[REDACTED]			[REDACTED]			0.0192	0.003	0.2684
3							0.1372	0.004	0.2684
4							0.3101	0.004	0.2683
5							0.2587	0.328	0.2683
6							0.2588	0.357	0.2683
7							0.0862	0.004	0.2683
8							0.1562	0.182	0.2683
9							0.2261	0.122	0.2683
10							0.1825	0.168	0.2684
11							0.1825	0.223	0.2676
12							--	--	--
13							0.4014	0.168	0.2685
14							0.4107	0.237	0.2685
15							0.4014	0.168	**2.2311**
16							0.2752	**10.06**	**2.2311**
17							0.5994	0.267	0.2685
18	89.07	277.22		89.16	277.9		0.0961	0.245	0.2684
19	68.05	2650		68.06	2650		0.016	0.018	0.2684

Table 6.8: Validation Against Pure Hydrogen Model Data

	Pure Hydrogen Model Data			Seeded Model Data			Comparison		
Fluid State	**P (atm)**	**T (K)**	**(kg/s)**	**P (atm)**	**T (K)**	**(kg/s)**	**P % error**	**T % error**	**% error**
1	1.293	20.56		1.293	20.56		0.0101	0	0.0122
2	[REDACTED]			[REDACTED]			0.117	0.0336	0.0122
3							0.1241	0.521	0.0122
4							0.1986	0.521	0.0149
5							0.2025	0.2253	0.0149
6							0.2493	0.1962	0.0149
7							0.0926	0.521	0.0144
8							0.1351	0.182	0.0144
9							0.3091	0.2552	0.0144
10							0.3486	0.253	0.0122
11							0.0537	0.253	0.0233
12							0.4575	0.3778	0.0233
13							0.5295	0.253	0.4158
14							0.0451	0.4979	0.4158
15							0.5295	0.253	**1.906**
16							0.7268	0.2602	**1.906**
17							0.7474	0.4524	0.0143
18	89.14	276.8		89.16	277.9		0.02	0.398	0.0122
19	68.05	2650		68.06	2650		0.0173	0.0001	0.0122

Table 6.9: Validation Against Original AR Data (Other Parameters)

Parameter	**AR Values**	**Simulink Seeded Hydrogen Model Data (0% Seed Concentration)**	**% Error**
Reactor Power	[REDACTED] MW	[REDACTED] MW	0.239
Main Flow Power	[REDACTED] MW	[REDACTED] MW	0.266
Moderator Element Power	[REDACTED] MW	[REDACTED] MW	0.0257
Control Drum Power	[REDACTED] MW	[REDACTED] MW	0.056
Regen Nozzle Power	[REDACTED] MW	[REDACTED] MW	0.354
Boost Turbopump RPM	[REDACTED] RPM	[REDACTED] RPM	0.071
Main Turbopump RPM	[REDACTED] RPM	[REDACTED] RPM	0.128
Vacuum Thrust	[REDACTED] kN	[REDACTED] kN	0.019
Vacuum Isp	[REDACTED] s	[REDACTED] s	0.350

Table 6.10: Validation Against Pure Hydrogen Model Data (Other Parameters)

Parameter	**Simulink Pure Hydrogen Model Data**	**Simulink Seeded Hydrogen Model Data (0% Seed Concentration)**	**% Error**
Reactor Power	[REDACTED] MW	[REDACTED] MW	0.0050
Main Flow Power	[REDACTED] MW	[REDACTED] MW	0.0121
Moderator Element Power	[REDACTED] MW	[REDACTED] MW	0.0530
Control Drum Power	[REDACTED] MW	[REDACTED] MW	0.1677
Regen Nozzle Power	[REDACTED] MW	[REDACTED] MW	0.0019
Boost Turbopump RPM	[REDACTED] RPM	[REDACTED] RPM	0.0046
Main Turbopump RPM	[REDACTED] RPM	[REDACTED] RPM	0.0008
Vacuum Thrust	[REDACTED] kN	[REDACTED] kN	0.0034
Vacuum Isp	[REDACTED] s	[REDACTED] s	0.0003

The engine specific impulse, thrust, and reactor heat were also compared with both the original AR data and the pure hydrogen Simulink model in Tables 6.7 and 6.8 respectively. Figure 6.10 shows that the model converged. After this, the engine performance will be analyzed at various levels of argon concentration only. Krypton and xenon do not have readily available viscosity and thermal conductivity properties in CoolProp [46] which results in the necessity of invoking a MATLAB function that does table look up. This function drastically increases the amount of time that the simulation must run resulting in these seeds being left for future research. Furthermore, argon is more readily available and much cheaper than these other seeds. Like the pure hydrogen model, the Simulink report of this model is available upon request.

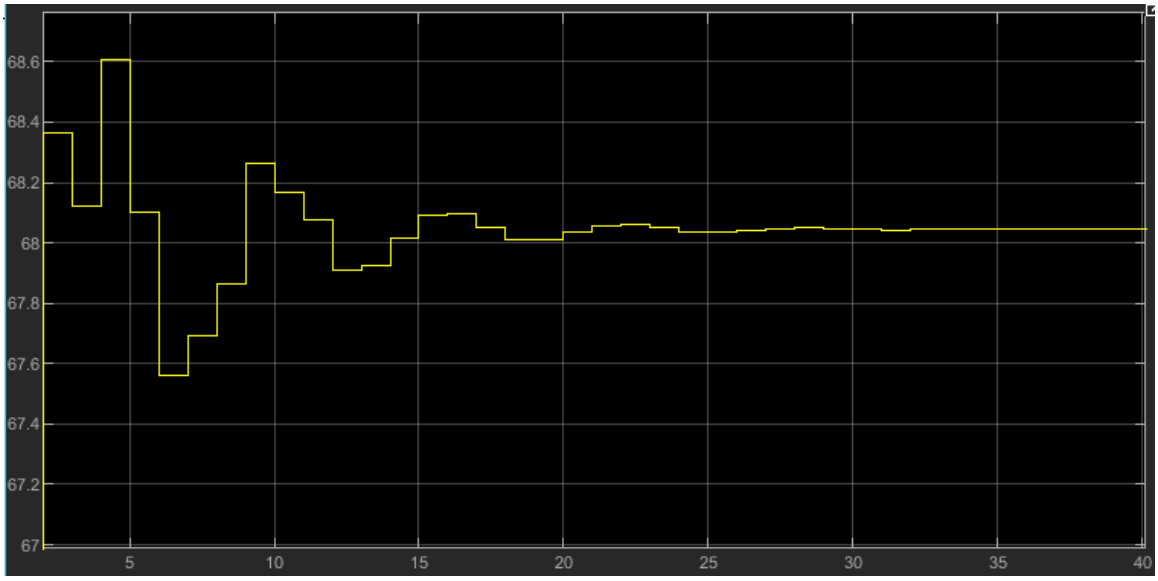

Figure 6.10: Seeded Hydrogen Convergence at 0% Seed

6.3 Engine Performance Results

As the various argon concentrations were examined, it became quickly evident that the upper limiting factor on the amount of argon introduced into the engine was the

available flow rate of hydrogen through the seed turbine to power it. The secondary upper limiting factor was the diameter and length of the seed duct from the seed tank to the seed boost pump. However, this limit was reached after the hydrogen availability for the seed turbine was reached resulting in hydrogen availability for the seed turbine to be the limit on the maximum argon concentration.

The lower argon concentration limit was around 0.6 kg/s below which the seed pump efficiency approached 0% as seen in the pump graphs in Appendix F. The argon operational lower and upper limits are shown in Table 6.11. Limits beyond these may be examined in future studies by modifying the seed duct diameters and lengths as well as the seed pumps' efficiency curves. Figure 6.11 shows the overall mass flow rates of hydrogen, argon, and the combination of the two. It is important to observe that the hydrogen mass flow rate decreases as the seed mass flow rate increases and the total mass flow rate increases with increased seed mass flow rates. This will result in the specific impulse decreasing and will be addressed later.

Table 6.11: Upper and Lower Argon Concentration Limits

Chamber Pressure Capped at 68 atm				
	Molar (%)	**Mass (%)**	**Seed ṁ**	**H_2 ṁ**
Ar Min	0.250	4.732	0.624	12.566
Ar Max	6.000	55.848	10.317	8.156
Chamber Pressure No Limit				
	Molar (%)	**Mass (%)**	**Seed ṁ**	**H_2 ṁ**
Ar Min	0.250	4.732	0.637	12.829
Ar Max	5.6000	54.035	11.197	9.525

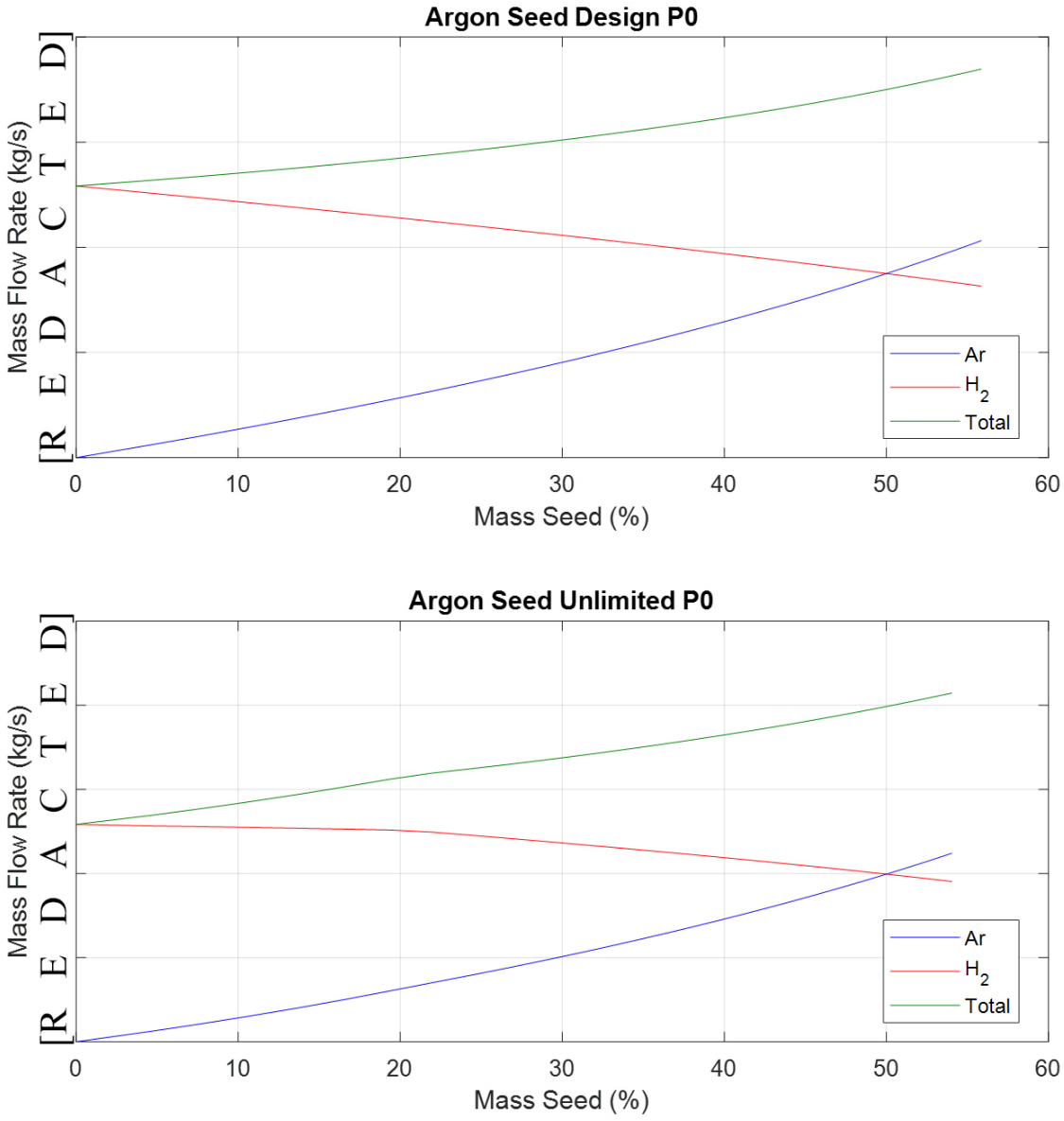

Figure 6.11: Seeded Propellant Mass Flow Rates

From examining the pressures of states with only hydrogen flow present after the main pumps (states 4 through 17) and while keeping the main feed pressure from the MFV as well as the chamber pressure the same, it is apparent that the addition of argon into this engine reduces pressure drops and the stagnation pressures at these states rise as a result as seen in Figure 6.12. The pressure produced by the main pumps was forced to be the same

as the design pressure by varying the rotational velocity. States 20 through 23 were not examined as their mass flow rates change to provide the power necessary for powering the seed pumps. These states are also not part of the original AR design.

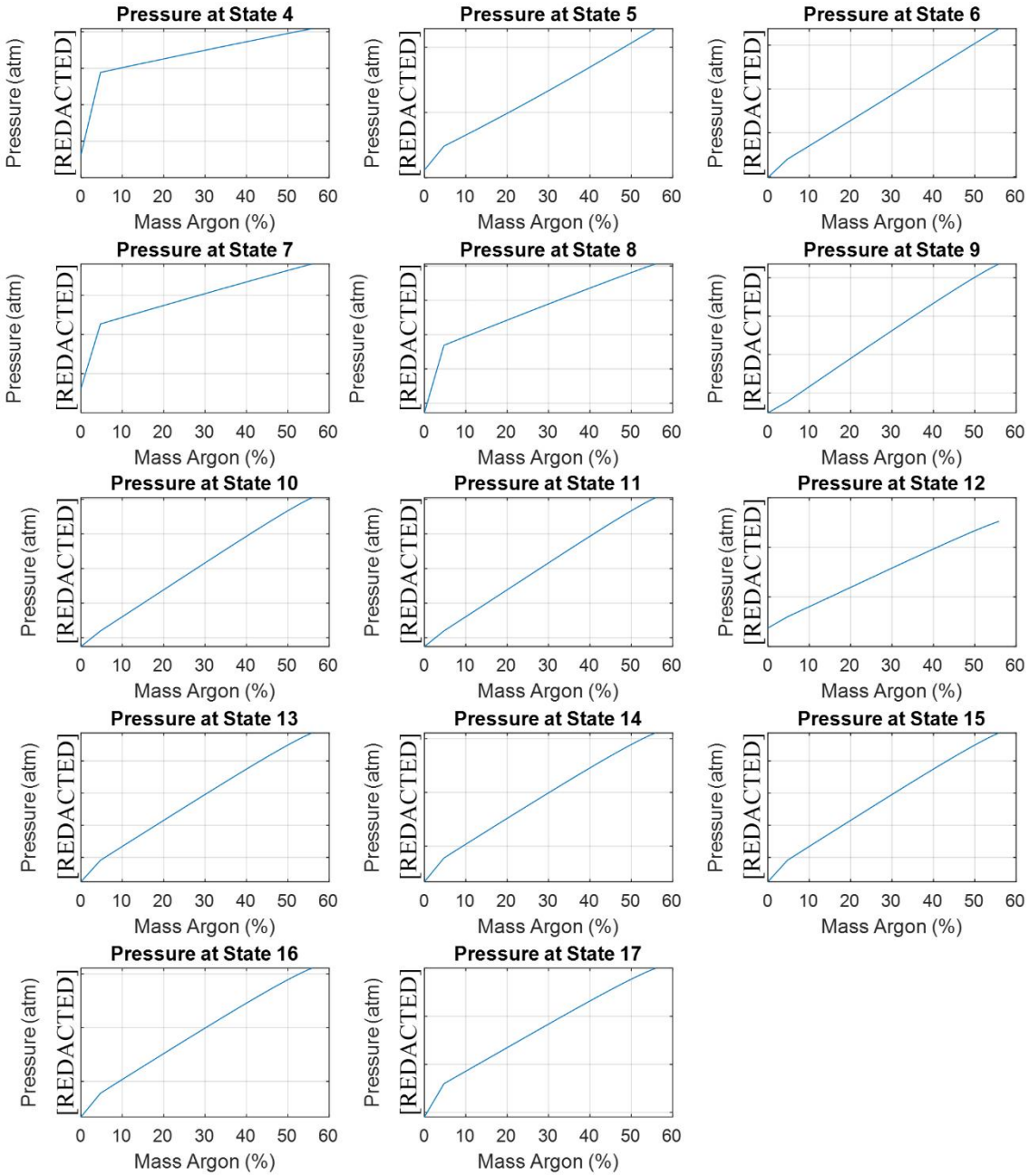

Figure 6.12: Pressures of Hydrogen States

These lower pressure drops thus provide the answer to the 3rd follow up question to the overarching question of this thesis:

3rd Follow Up Research Question:

How does adding a seed affect the internal engine pressure losses?

ANS: The addition of the seed reduces these pressure losses overall.

Pressure losses, in general, are primarily affected by the velocity of the fluid which is reduced as the density is increased. They are also affected by the fluid viscosity. Furthermore, with a constant chamber stagnation pressure of state 19, the required stagnation pressure of the fluid before entering the reactor at state 18 initially falls due to densification, but later increases as the increased viscosity dominates as seen in Figure 6.13. The viscosity curve of the seeded propellant was shown in Figure 6.9.

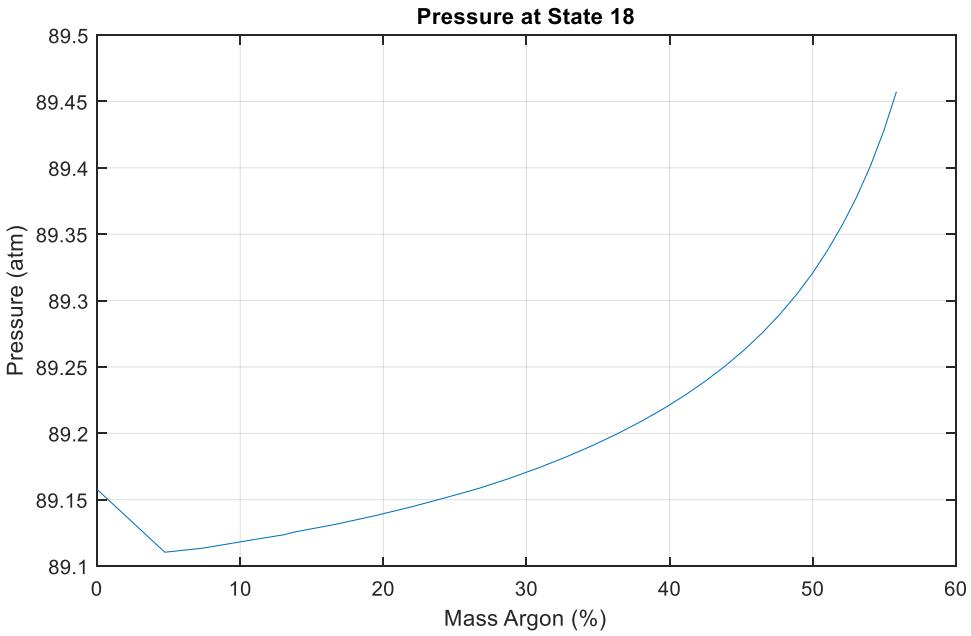

Figure 6.13: Pressure at State 18

It was unclear during the initial analytical analysis of the pressure drops in Chapter 4 if the increased overall mass flow rate and increased viscosity of the propellant would counteract the increased density. Figure 6.12 demonstrates that the increased viscosity and increased mass flow rate do indeed counteract the effect of densification likely due to the extreme temperature rise inside the reactor. However, the required pressure before the seeded propellant enters the reactor is increased only by about 0.35 atm. This nuance was possible to observe due to the fine grid size of 1mm of the model. This increased required pressure of state 18 is far outweighed by the increased available pressure from state 17 shown in Figure 6.12. However, due to the increased mass flow rate of argon, the higher argon concentrations also yield an increased pressure drop in the seed ducts as seen in the seed preheating outlet state 26 Figure 6.14.

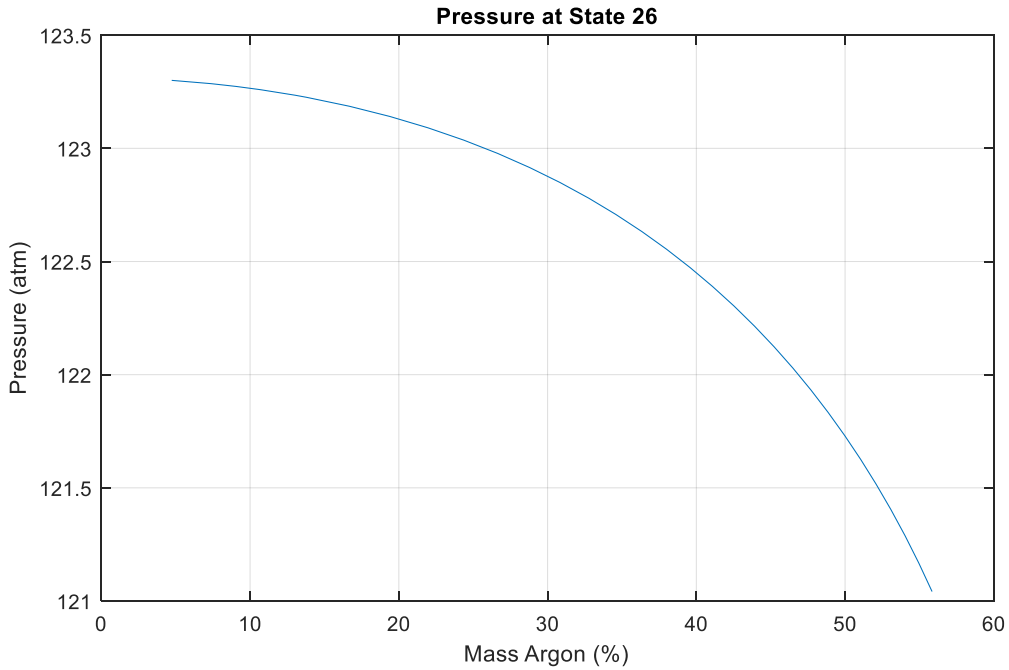

Figure 6.14: Pressure at State 26

By utilizing the increased available pressure of state 17 achieved by the reduced pressure drops, it is possible to bring up the chamber stagnation pressure while setting the design reactor power as a limit and thus produce more thrust as seen in Figure 6.15. The reactor limit does not allow for the utilization of the maximum fuel temperature which results in a propellant with slightly higher density leading to lower pressure drops inside the reactor.

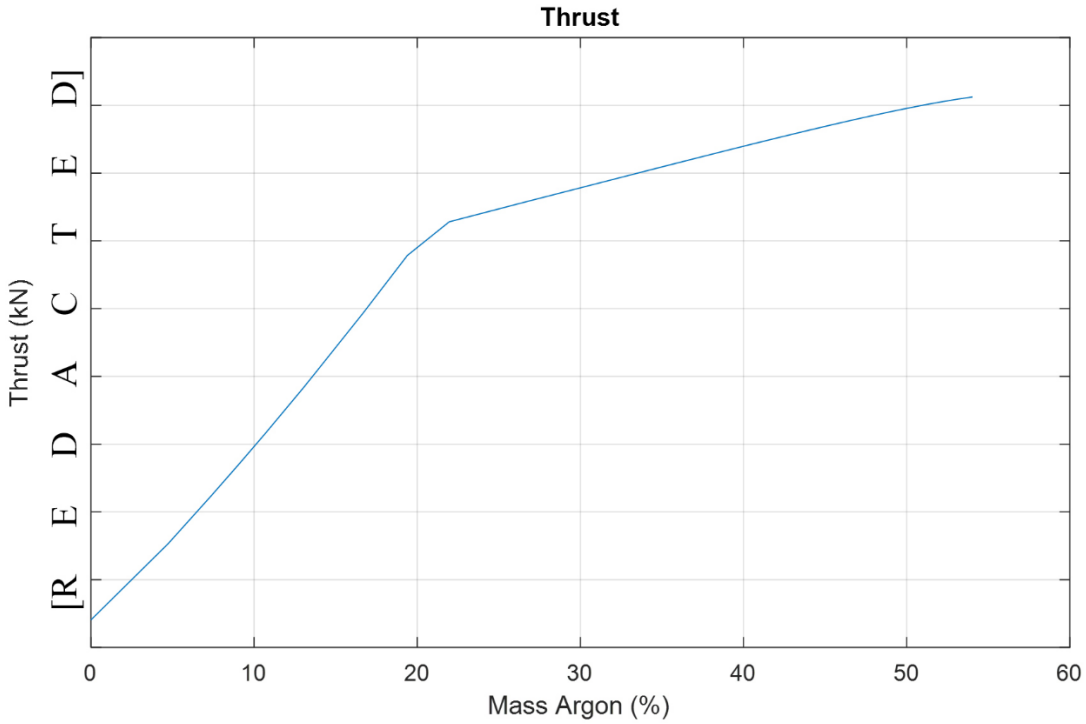

Figure 6.15: Increased Thrust While Utilizing Lessened Pressure Drops

On the other hand, it is possible to reduce the amount of pressure head produced by the main pumps and allocate the excess hydrogen to perform other work, thus preserving the same chamber pressure and thrust. Examples of this include powering the seed turbine to allow for a wider range of seed concentrations or run an electric generator to name a couple of possibilities.

Increased heat transfer capabilities of the seeded propellant were observed. By keeping the maximum fuel temperature the same as the AR design, the reactor outlet temperature was observed to rise. Moreover, the total heat provided by the reactor was observed to fall with direct correlation to the seed concentration. Both the reactor outlet temperature and the reactor power for the case of constant chamber pressure are shown in Figure 6.17 where these relationships can be observed.

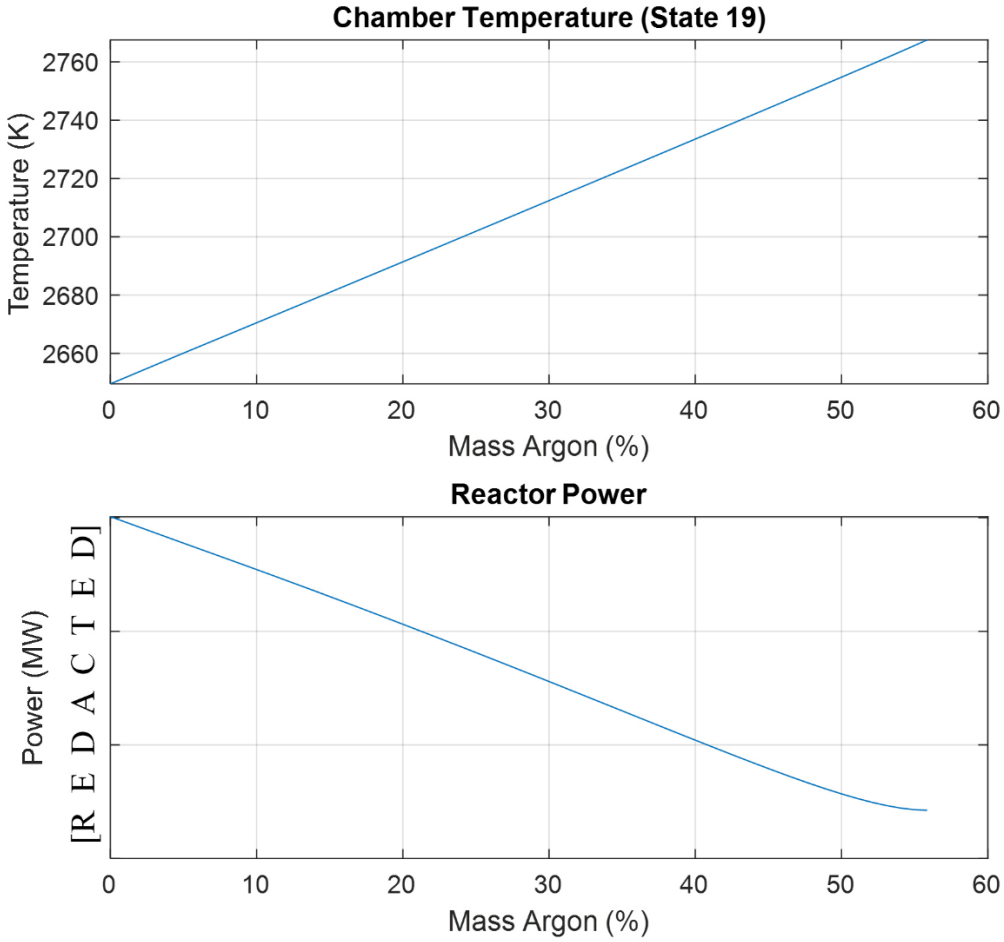

Figure 6.16: Reactor Power and Chamber Temperature at Design Chamber Pressure

Figure 6.17 shows the increased chamber pressure due to the utilization of the lesser pressure drops, the reactor power, and chamber temperature for this case. Here, it should

be observed how the reactor power is initially constant for reasons discussed previously and how the chamber temperature rises slowly initially, but then faster as the reduced specific heat capacity dominates over the increased mass flow rate due to the increased chamber pressure.

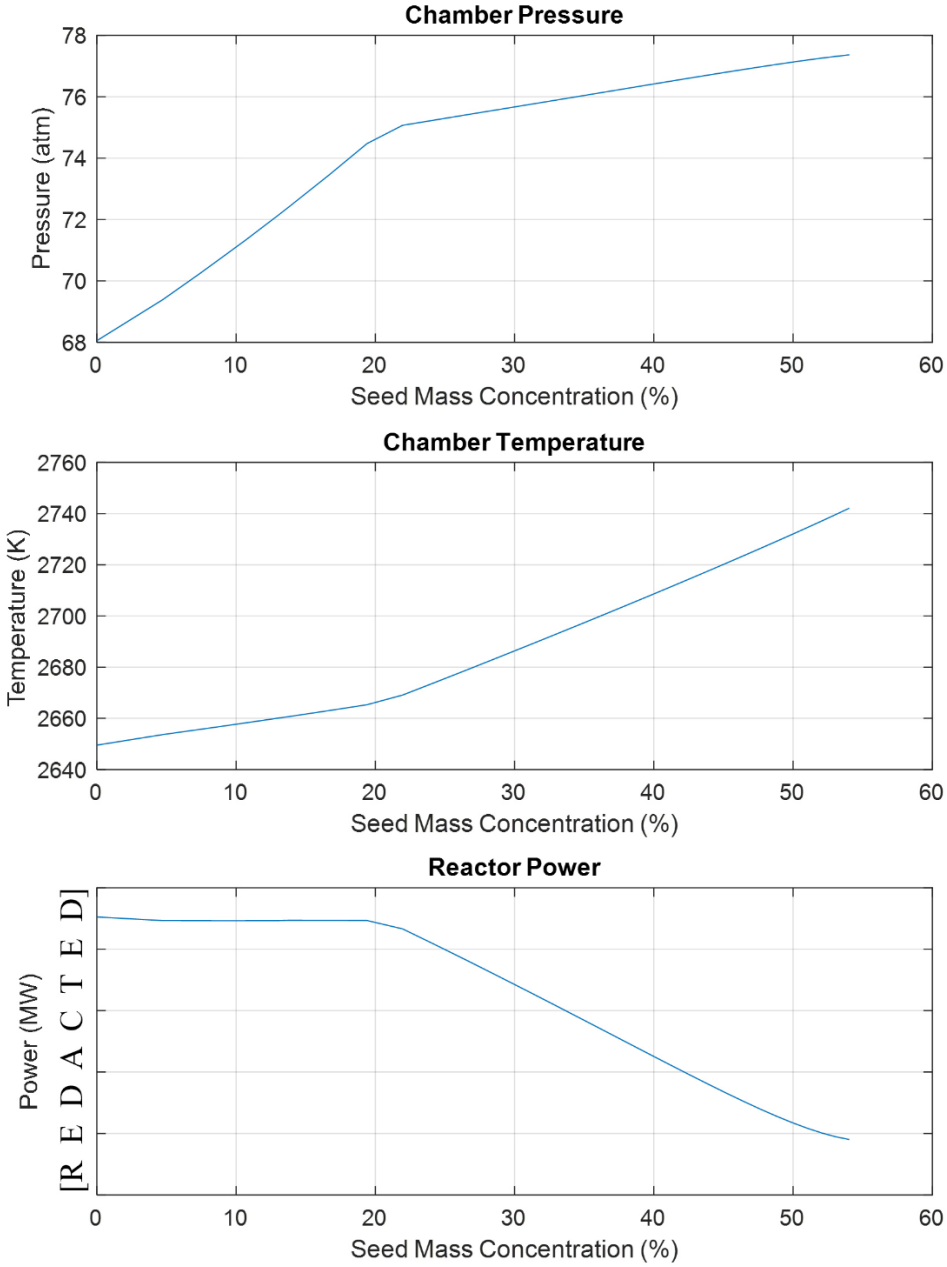

Figure 6.17: Reactor Power and Chamber Temperature at Unlimited Chamber Pressure

Seeding hydrogen comes at the expense of reduced specific impulse due to the heavier net molecular weight of the exhaust plume. Even though the chamber temperature increases, this increase is not enough to keep the specific impulse as high as for pure hydrogen. Furthermore, the specific impulse will remain the same with negligible differences for the considered chamber pressures as shown in Figure 6.18.

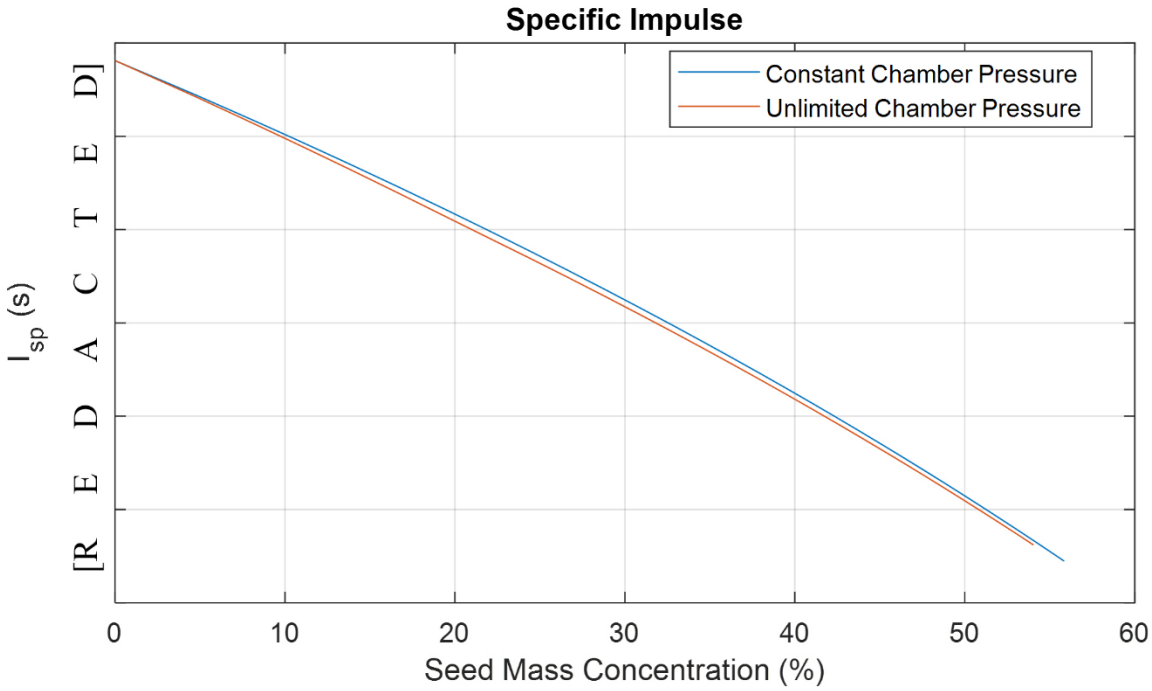

Figure 6.18: Decreased Specific Impulse

The differences between the reactor maximum fuel temperature, the surface temperature, and the fluid temperature decreased. This is demonstrated in the comparison of the temperature distribution of the pure hydrogen and seeded hydrogen flow through the reactor shown in Figures 5.7 and 6.19 respectively for the design chamber pressure.

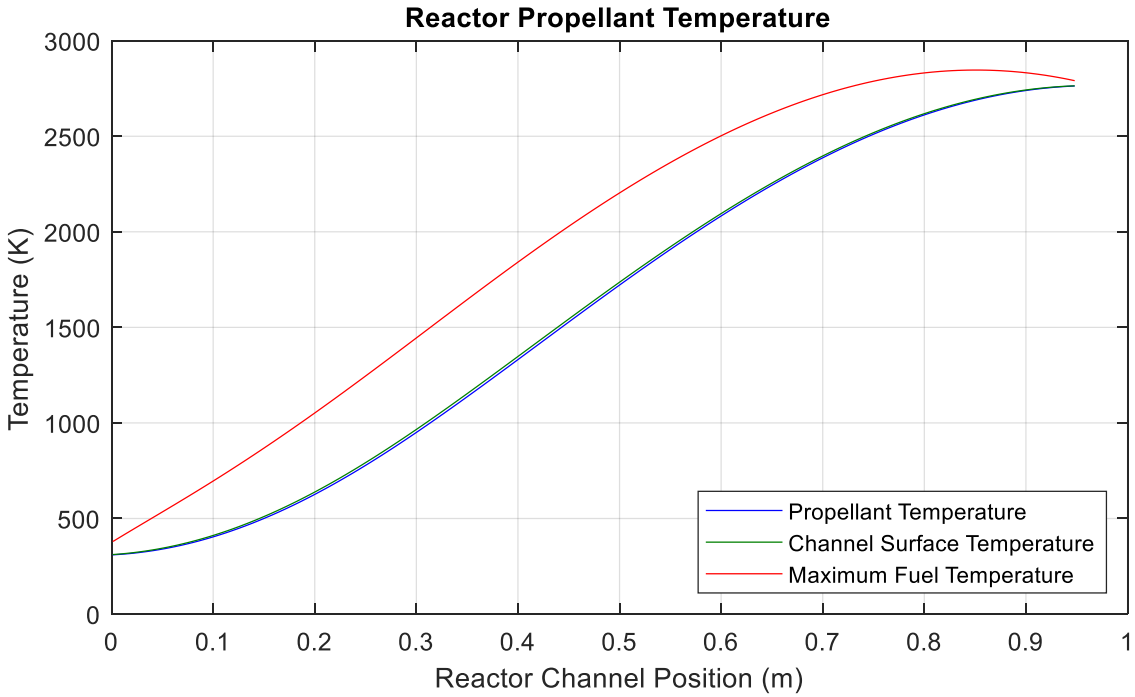

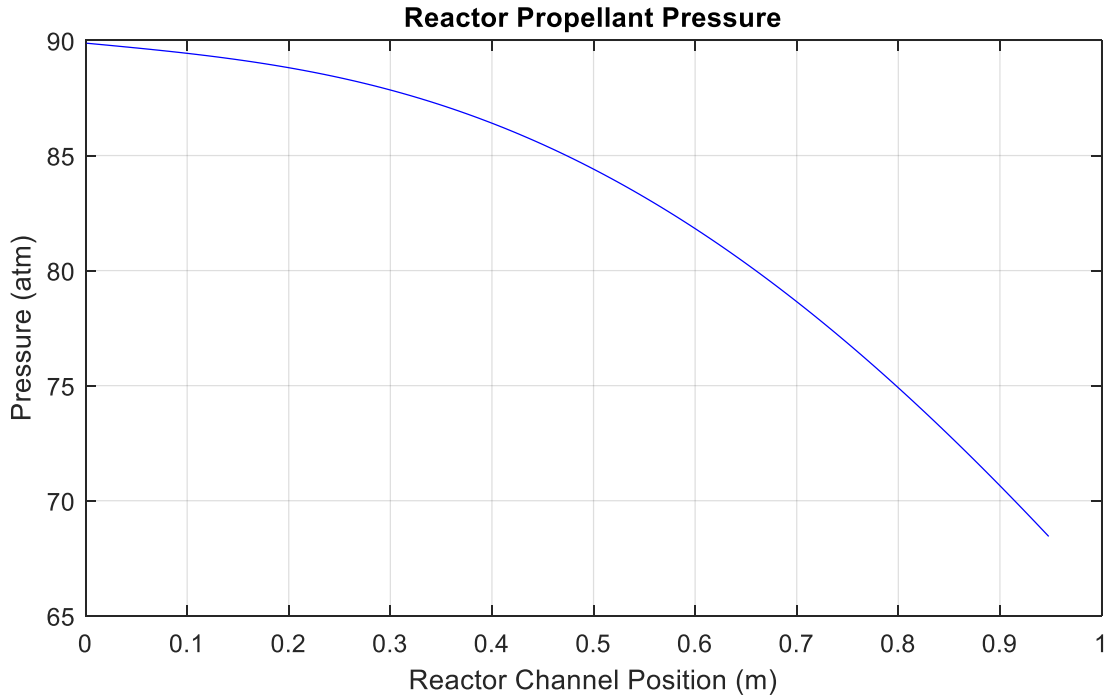

Figure 6.19: Reactor Temperature and Pressure (Seeded Hydrogen)

The increased chamber temperature; decreased reactor power; and decreased differences between the maximum fuel, channel surface, and fluid temperatures answer the 2nd follow up research question to the overarching question:

2nd Follow Up Research Question:

How is convective heat transfer affected by the addition of the seed?

ANS: The addition of a seed improves convective heat transfer and thus results in a lower reactor power and higher chamber temperature for a given thrust level.

The heavy noble gasses, including argon, have a very low specific heat capacity. Specific heat capacity, as discussed in Chapter 4, is a function of mass concentration of each substance in a mixture. Due to the high mass difference between heavy noble gases and hydrogen, the reduction in specific heat capacity is amplified and outweighs the effects of the decreased fluid thermal conductivity and increased mass flow rate. This more effective heat transfer allows raising the chamber stagnation temperature (state 19) while keeping the maximum fuel temperature constant as was shown in Figures 6.17, 6.18, and 6.19.

The validated pure hydrogen model was modified with additional components specifically designed to work with the heavy noble gases: argon, krypton, and xenon. These components had minimal interference with the pure hydrogen operation as evidenced by

the validation performed at 0% seed. Argon had readily available properties for viscosity and thermal conductivity and it was the seed that was examined at various levels. By varying the seed amount and plotting the data extracted at various states, some key observations were made.

These observations include that the overall mass flow rate increases thus decreasing the specific impulse. However, even though the mass flow rate increases, the specific heat capacity decreased so much that the reactor power still decreased despite the mass flow increase. Moreover, the difference between the bulk propellant and channel surface temperatures inside the reactor decreased as a result from the increased convective heat transfer resulting in an increased chamber temperature. Furthermore, the pressure drops within the ducts and lines decreased as a result of the hydrogen mass flow rate decreasing allowing for a flow of lower velocity.

All of these observations affect the engine performance, however, the parameters affected do not show the effect on the vehicle performance and the mission itself. In order to answer the remaining research questions, a systems level approach must be taken which would analyze how seeded propellant affects the entire system. This will involve analyzing the balance between the volume occupied by hydrogen and seed inside the propellant tanks as well as the associated vehicle mass with seed concentration variation and the effect it has on the performance of the reaction control and orbital maneuvering systems.

CHAPTER 7

VEHICLE ANALYSIS

Understanding the performance of the engine running seeded hydrogen is not enough to determine if it is beneficial or not for the vehicle as a whole and will not answer the 1st follow up research question. In order to do this, a vehicle mission analysis must be performed. This will involve analyzing the total vehicle mass, the total vehicle volume, and the total change in velocity that the vehicle can provide primarily utilizing Tsiolkovsky's Rocket Equation. The latter will be treated as the dominant parameter as it will shorten the trip time between destinations and reduce the effects of space radiation on the crew, thus reducing the risk of adverse human health effects from space travel. All other parameters will remain secondary. Like the analysis of engine performance in Chapter 6, the considered seed will be argon. Krypton and xenon will be explored in future research.

The vehicle performance while utilizing Aerojet Rocketdyne's engine parameters and changes in velocity must be analyzed first in order to establish a baseline which will then be used as the datum point of comparison. The total trip time to Mars and back to Earth is 358 days – slightly less than a year. Although this travel time is good, it will still

require astronauts to spend half a year travelling in deep space each way in a radiation filled environment. Any decrease in travel time will decrease potential health issues that these astronauts could experience. In order to decrease the travel times, the changes in velocity for each burn event must increase. These burn events include: Earth departure burn or Trans Mars Injection (TMI), Mars Orbit Insertion (MOI), Mars departure burn or Trans Earth Injection (TEI), and Earth Orbit Insertion (EOI). By the principles of orbital mechanics, higher changes in velocities during departure burns will require higher changes in velocities during arrival or orbit insertion burns. This quickly results in diminishing returns in terms of correlating the propellant mass expelled to the change in velocity.

AR has performed a vehicle analysis while assuming an 875 second Isp for the main engines and a 470 second Isp for the orbital maneuvering system (OMS) which uses the same hydrogen from the main propellant tank. The OMS flows through the moderator elements of the reactor during standby mode and utilizes the residual heat to produce additional thrust, albeit with a lower Isp. A reaction control system (RCS) is also used for attitude changes and corrections which had a calculated specific impulse of 316 seconds. All of the changes in velocities had a 4% flight performance reserve. The current AR vehicle design is shown as a CAD model in Figure 7.1 with its initial masses, changes in velocities, and changes in masses shown in Tables 7.1, 7.2, and 7.3 respectively. [4] [43]

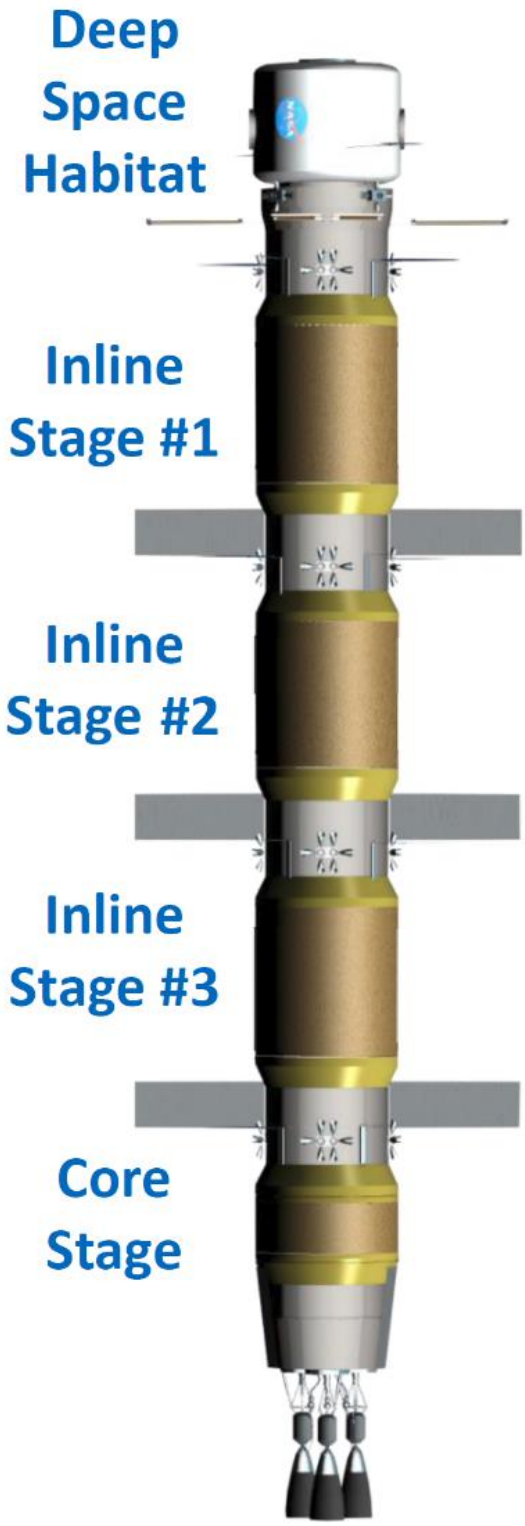

Figure 7.1: Vehicle CAD [43]

Table 7.1: Initial Vehicle Physical Parameters [4] [43]

Parameter	Given/Calculated Values
Deep Space Habitat Mass	47111 kg
Total Inline Stage Dry Mass	32088 kg
Inline Stage OMS Propellant	16108.575 kg
Total Inline Stage Reserved Propellant	7137 kg
Total Inline Stage Propellant Mass	83283 kg
Total Inline Stage Propellant Volume	1277.705161 m^3
Total Inline Stage Expendable Mass	9117 kg
Core Stage Dry Mass	26180 kg
Core Stage OMS Propellant	5369.525 kg
Core Stage Reserved Propellant	1075.92 kg
Core Stage Propellant Mass	13449 kg
Core Stage Propellant Volume	205.2484544 m^3
Core Stage Expendable Mass	3000 kg

Table 7.2: Changes in Velocities [4] [43]

Change In Velocities	Given/Calculated Values	Time
Launch to NRHO	115 m/s	-- --
NRHO to LDHEO	100 m/s	-- --
Trans Mars Injection	622 m/s	354 s
Mars Orbit Injection	1668 m/s	823 s
Plane Changes	250 m/s	-- --
Trans Earth Injection	1352 m/s	479 s
Earth Orbit Injection	581 m/s	181 s
LDHEO to NRHO	70 m/s	-- --

Table 7.3: Changes in Masses [4] [43]

Change in Mass	**Main Propellant**	**RCS\Expendables**
Launch to NRHO	5683.6 kg	916.721 kg
LDHEO to NRHO	4674.4 kg	6692.8 kg
Trans Mars Injection	14874 kg	-- --
Mars Orbit Injection	33606 kg	-- --
Plane Changes	9367.6 kg	-- --
Trans Earth Injection	21744 kg	-- --
Earth Orbit Injection	8210.4 kg	-- --
NRHO to LDHEO	1752.5 kg	4507.48 kg

The changes in velocity shown in Table 7.1 that the main engines provide is for the minimum required specific impulse of 875 seconds which does not reflect the current engine performance specific impulse of 893.8 seconds. However, the changes in masses reported in Table 7.3 do reflect the anticipated values as the total propellant mass that will flow through the engines will be the same. Furthermore, since this engine is nuclear, start up and shut down states require propellant flow to be present in order to prevent a reactor meltdown. These masses were not reported in Table 7.3, however, the deficiency between the initial physical masses presented in Table 7.1 and those reported to be used to produce thrust in Table 7.3 is the mass of the propellant used for this purpose. This required mass flow rate is a function of the neutronics and power level of the reactor as well as the time that the reactor was operating at full power. The relation between these parameters is provided in equation 7.1 with the neutronics constants shown in Table 7.4. As stated by AR, the propellant will flow through the reactor until the reactor reaches a power level of

7 kW. At this point, the decay heat from the fission fragments will be radiated away into space or rejected by other means [43].

In order to accommodate the startup and shutdown procedures and obtain a rough value for the mass used, the total cool down mass calculated by integrating equation 7.1 between the time of shut down initiation and reactor power level of 7 kW was doubled. This is likely an overestimation of the propellant necessary to accommodate cooling the reactor during power increase events due to the fact that decay heating is not an issue at this state. Furthermore, it was assumed that the engine does not generate thrust during the startup and shut down states. This will result in longer travel times than the system would otherwise provide. Therefore, the actual results would be better than the calculations. However, since this analysis will be uniform for all seed concentrations including the case of 0% seed concentration, the general trends are expected to be the same.

$$P_{sd}(t) = P_{fp}\left\{\frac{\rho}{\rho-\beta}\exp\left(\frac{\rho-\beta}{\Lambda}t\right) - \frac{\beta}{\rho-\beta}\exp\left(\frac{-\rho\lambda}{\rho-\beta}t\right) + 0.1104\left[t^{-0.2436} - \left(t_{fp}+t\right)^{-0.2436}\right]\right\} \quad (7.1)$$

Table 7.4: Neutronics Constants [43]

Constant	**Symbol**	**Given/Calculated Values**
Fission Yield	β	0.0065 --
Decay Constant	λ	0.0764 s^{-1}
Prompt Neutron Lifetime	Λ	6×10^{-5} s
Reactivity	ρ	-0.01377 \$

The values used in the calculations for the changes in velocity with respect to the seed concentration were those provided by the Simulink model which present an Isp at 0%

seed concentration slightly below the AR reported value. Therefore, the datum point for the changes in velocities will be slightly higher than those reported in Table 7.1. At the current state of the engine and vehicle design, the changes in velocities provided by the OMS and RCS are not entirely certain and may fluctuate in future design iterations. However, based on the values provided by AR, some estimates of the vehicle performance during the utilization of seeded hydrogen propellant have been made. An upper limit (best case) for the vehicle performance was set by keeping the masses of both the RCS and OMS propellants the same, while a lower limit (worst case) for the vehicle performance was set by keeping the changes in velocity provided by both the RCS and OMS thrusters the same. The propellant utilized by the OMS thrusters was assumed to be pure hydrogen just as in the datum design. A preliminary analysis which assumed an 800 K chamber temperature and 10 atm chamber pressure in the OMS [43] was performed for utilizing the noble gas seeds. The results were not good as the calculated Isp for argon, krypton, and xenon were 97.7s, 67.46s, and 53.90s respectively. This produced vehicle masses which were over the datum point by over 200%, and therefore, were not used.

Figure 7.2 shows the overall change in velocity provided by the main engines during the four main burn events using constant chamber pressure (not utilizing the pressure gains obtained from seeded hydrogen) and Figure 7.3 shows the percent increase in this change in velocity. The worst case scenario calculated a maximum of a 34.28% mass and volume increase for the pure hydrogen utilized by the OMS. Due to the fact that the OMS propellant shares the same tank as the main propellant and the density of the hydrogen utilized by the OMS was kept constant, the maximum decrease in the volume

available for the main propellant (hydrogen and the seed) was calculated to be 9.44%. This resulted in less propellant usable by the main engines which reduced the total change in velocity provided by the vehicle.

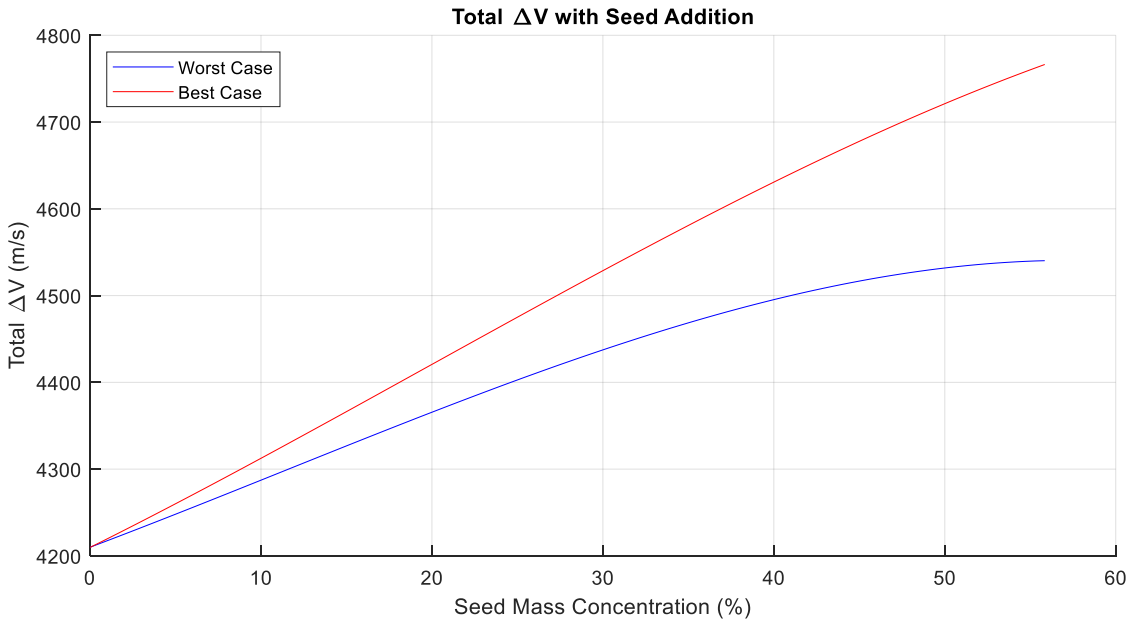

Figure 7.2: Total Change in Velocity with Seed Addition

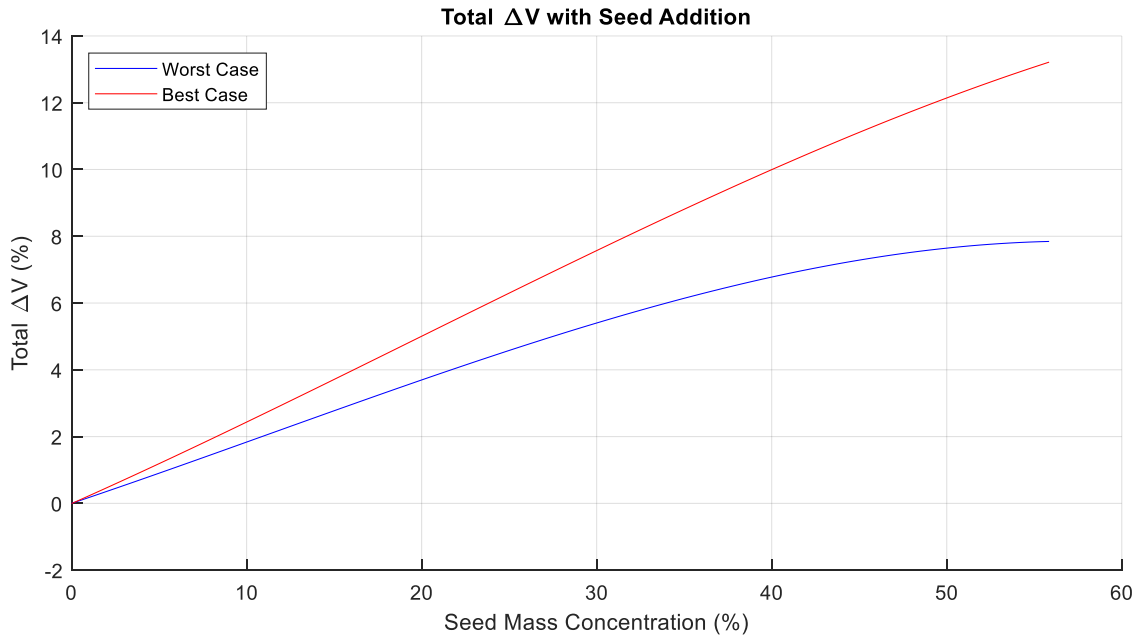

Figure 7.3: Increase in the Change in Velocity with Seed Addition

It was found that due to the increased vehicle mass and constant thrust, the time it took to complete a burn and achieve a specified change in velocity increased. Since the reactor power decreased as the seed concentration increased but the time that each burn took increased, the hydrogen allocated for the engine cool down initially decreased until reaching a seed mass concentration of 49.98% for the worst case scenario. At this point, the mass of this cool down hydrogen decreased by 7.6%. Afterwards, the mass of the hydrogen allocated for cool down increased until reaching the maximum operational seed mass concentration of 55.85%. At this point, the mass of this cool down hydrogen was 6.68% below the datum point. Similarly, the same analysis was performed for the best case scenario and Figure 7.4 summarizes this behavior while Figure 7.5 shows the volume variation of the main propellant (hydrogen and seed). Unsurprisingly, the main propellant

volume for the best case scenario remained relatively constant due to the lack of mass and volume variation from the RCS and OMS thruster systems.

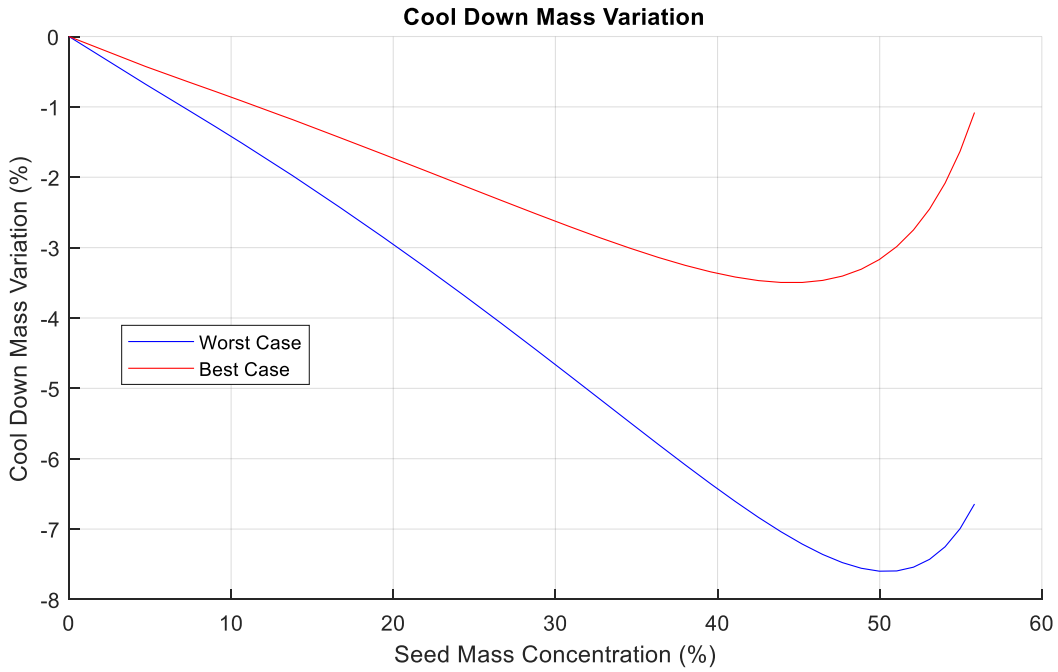

Figure 7.4: Cool Down Mass Variation

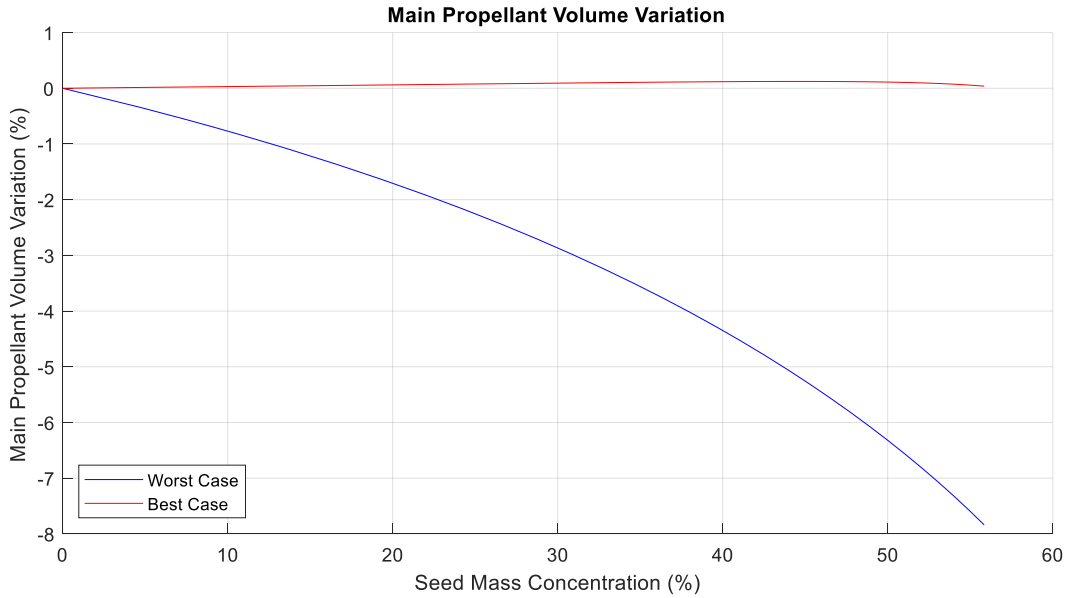

Figure 7.5: Main Propellant Volume Variation

The worst case scenario also calculated a maximum 36.37% increase in the RCS propellant mass. Nonetheless, the change in velocity still increased with the addition of the noble gas seed. Furthermore, no differences in the total changes in velocity were recorded between the case of keeping the chamber pressure the same as the AR design and the utilization of the lesser pressure drops throughout the engine. These increased chamber pressures, as discussed in Chapter 6, yielded higher thrust and higher mass flow rate but did not affect vehicle performance other than very slight changes in the trajectories.

Even with the vehicle mass the same, the differences in the trajectory remain nearly identical in four hours after the burn as shown in Figures 7.6 and 7.7 for Earth and Mars departure trajectories respectively. This reveals that there is no real advantage to the utilization of the higher chamber pressures provided by the lesser pressure drops. However, these lesser pressure drops can still be utilized to put less strain on the turbomachinery and initially pressurize the propellant to lower pressures. Further, it can be noticed in these figures that the trajectory curve changes significantly between the datum and maximum seed burns.

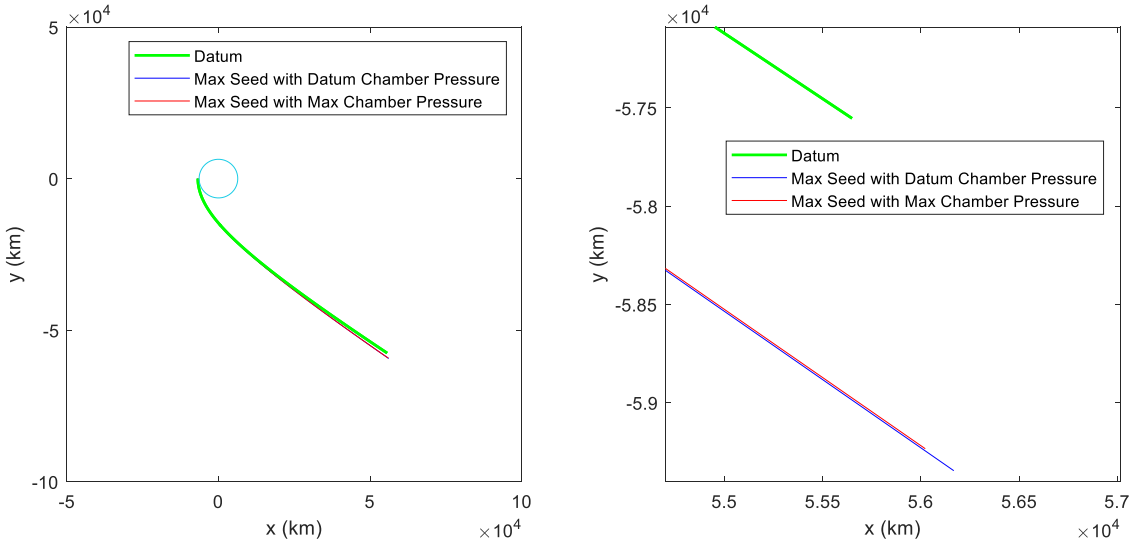

Figure 7.6: Earth Departure Trajectories: Datum and Maximum Chamber Pressures [70]

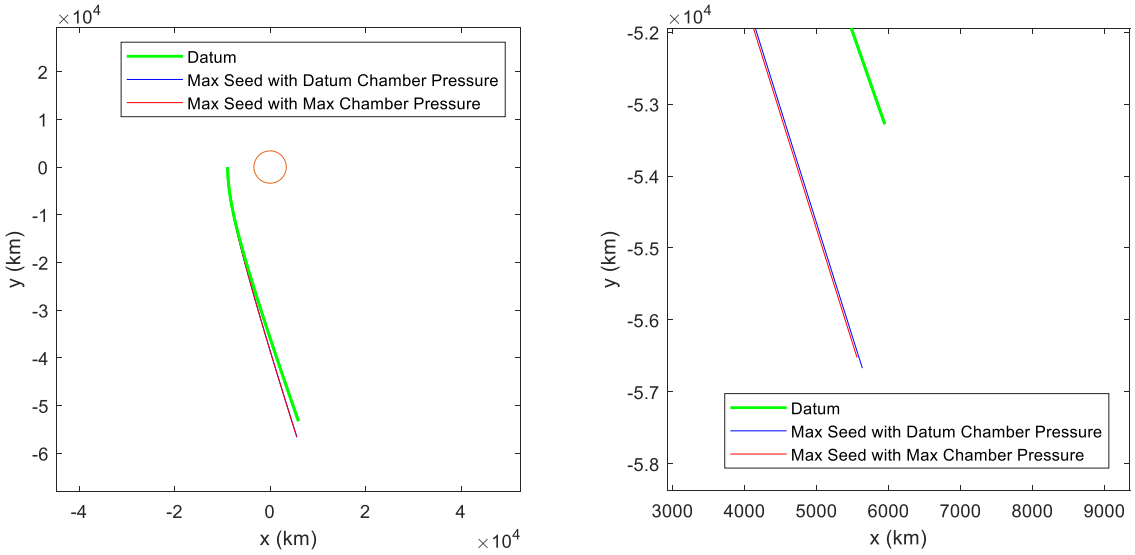

Figure 7.7: Mars Departure Trajectories: Datum and Maximum Chamber Pressures [70]

Figures 7.8 and 7.9 show the trajectories for the other seed levels 4 hours after the burn events for the Earth departure and Mars departure trajectories respectively. Close examination of Figure 7.8 (the longer red curves represent higher changes in velocities corresponding to higher seed concentrations) reveals that after a certain seed amount, the

trajectory curve starts to regress back, however, this could also be attributed to rounding errors since the results are so close together.

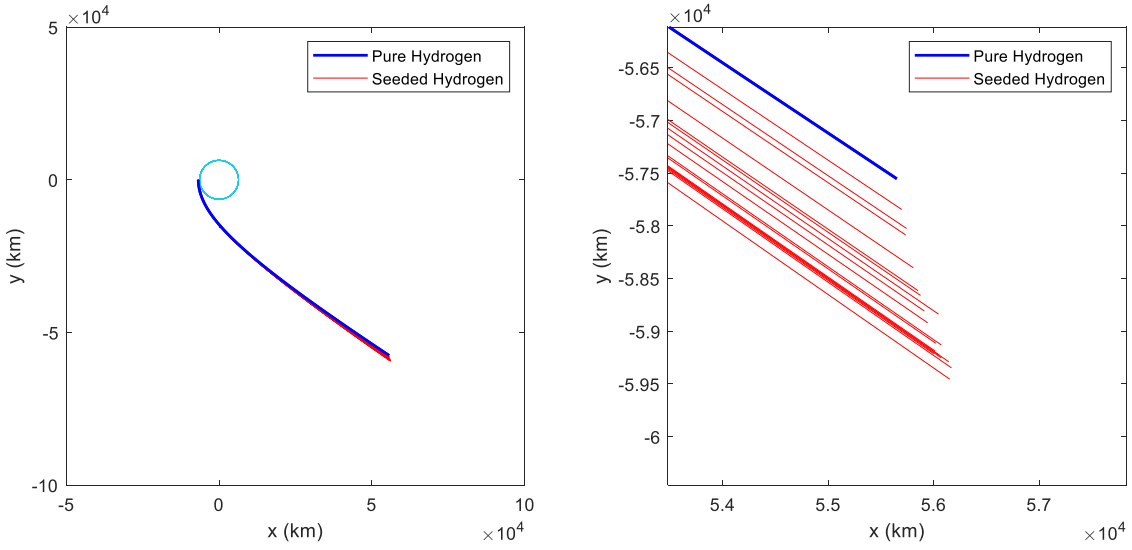

Figure 7.8: Earth Departure Trajectories for Various Seed Concentrations [70]

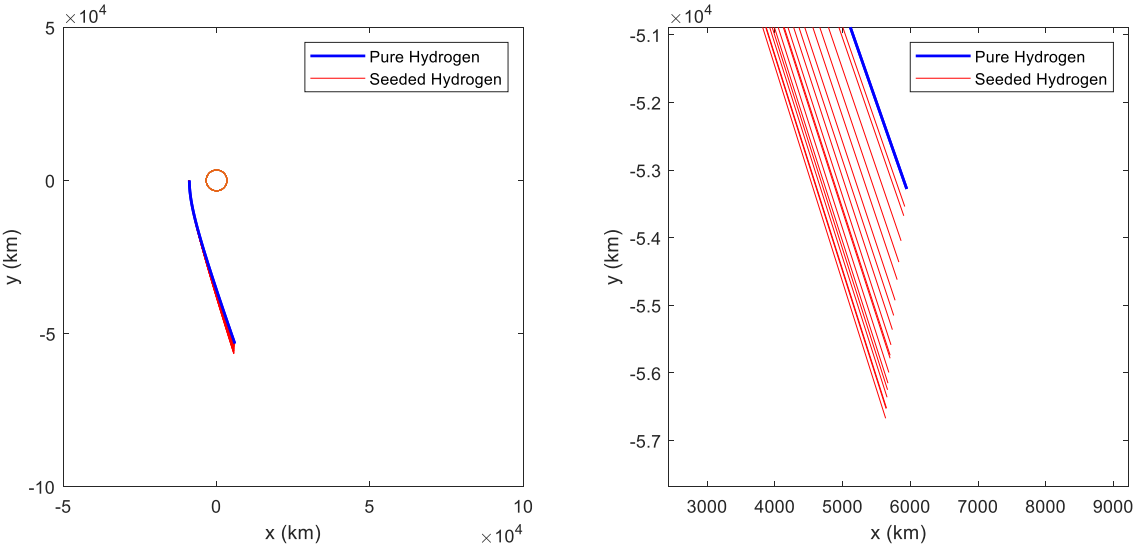

Figure 7.9: Mars Departure Trajectories for Various Seed Concentrations [70]

The density increase of the propellant is shown in Figure 7.10. At the maximum seed concentration, the increase in the bulk density of the propellant is between 79.89%

and 86.59% depending on the OMS propellant criteria. The implications of this is higher vehicle mass given a constant vehicle volume. Relating this to the research question that this thesis is attempting to answer:

1st Follow Up Research Question (Part 1):

Can seeding hydrogen provide a density increase percentage higher than 8.16% of densified hydrogen?

ANS: Yes, seeding hydrogen can indeed increase the bulk propellant density over 8.16% to between 79.89% and 86.59% depending on the OMS propellant criteria.

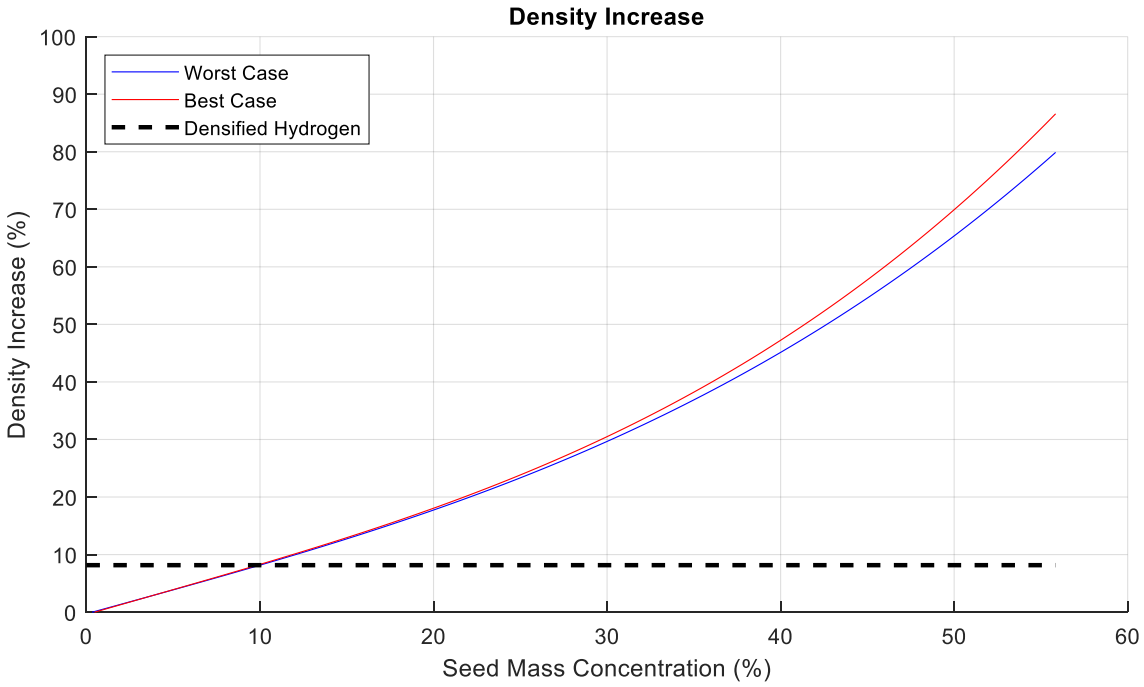

Figure 7.10: Seeded Hydrogen Density Increase

To compare the performance between seeded hydrogen and densified hydrogen, the entirety of the hydrogen propellant in the vehicle (including OMS) was replaced by densified hydrogen (it is densest at 14K and the datum 2 atm). The resulting overall changes in velocity were compared with the values that seeded non-densified hydrogen provided. Figures 7.11 and 7.12 show that seeded non-densified hydrogen can certainly outperform densified hydrogen even when it is chilled down to fractions of a degree above its freezing point. The worst and best case scenario of seeded hydrogen will outperform densified hydrogen when the seed mass concentration exceeds 36.67% and 25.39% respectively.

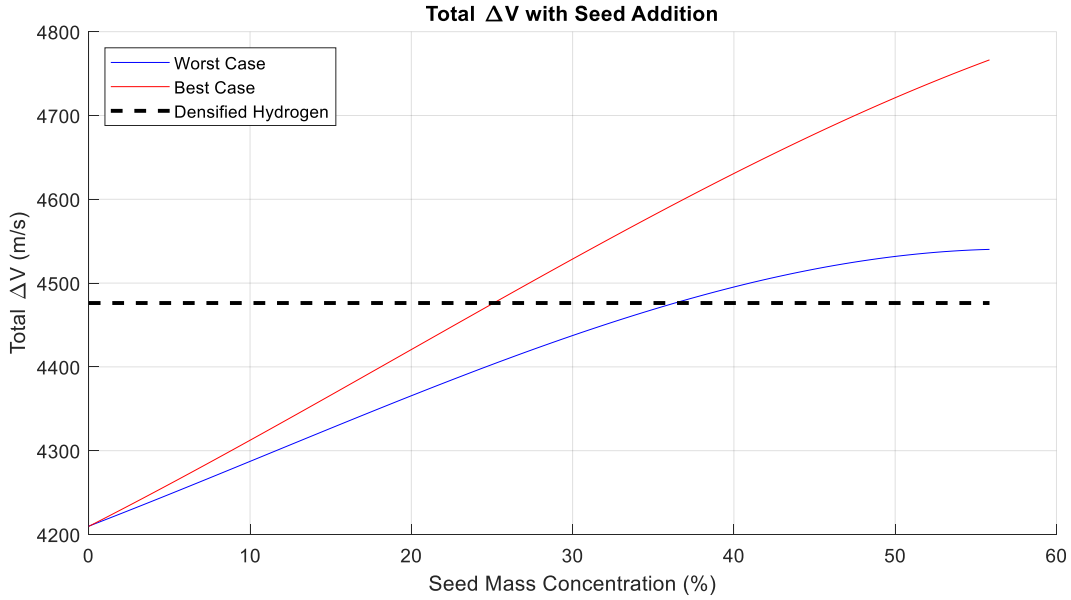

Figure 7.11: Comparing Change in Velocity of Densified Hydrogen and Seeded Hydrogen

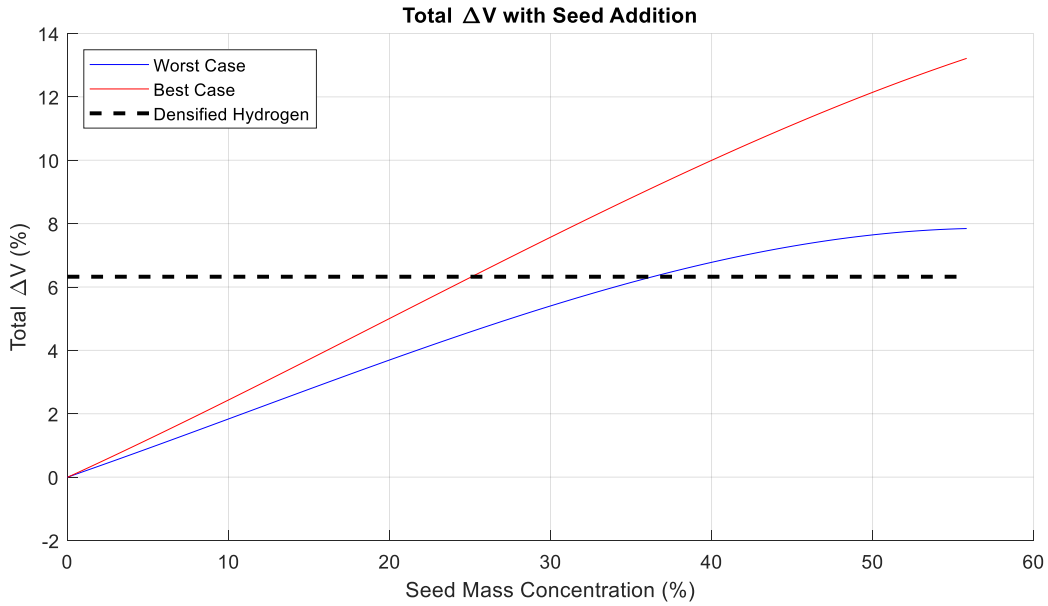

Figure 7.12: Comparing Increase in the Change in Velocity of Densified Hydrogen and Seeded Hydrogen

Relating this back to the thesis questions, the second part of the first follow up question asks:

1st Follow Up Research Question (Part 2):

Can seeding hydrogen yield higher overall change in velocity than densified hydrogen?

ANS: Yes, the worst and best case scenario of seeded hydrogen will outperform densified hydrogen when the seed mass concentration exceeds 36.67% and 25.39% respectively.

A preliminary analysis on the effect of seeding densified hydrogen was done and the change in velocity graph of Figure 7.13 as well as the increase in the change in velocity graph of Figure 7.14 show these results while comparing them to the datum. These figures show that the change in velocity is always increasing with higher seed mass concentration but with diminishing returns. However, the worst case scenario exhibits a maximum favorable seed mass concentration of around 53% beyond which the change in velocity starts decreasing with increased seed mass concentration. Analyzing densified hydrogen flow through this engine will be a topic for future research as it is expected that pump performance will be impacted. Nevertheless, a quick vehicle analysis while assuming the same engine performance with densified hydrogen shows that seeding densified hydrogen will increase vehicle performance even further.

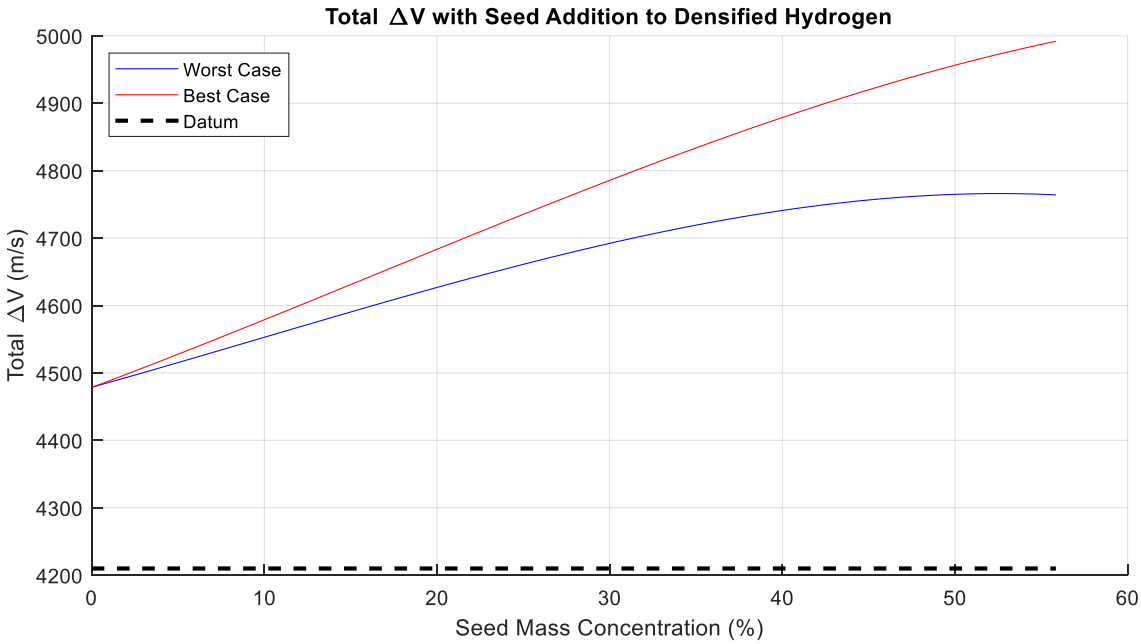

Figure 7.13: Change in Velocity of Densified Seeded Hydrogen

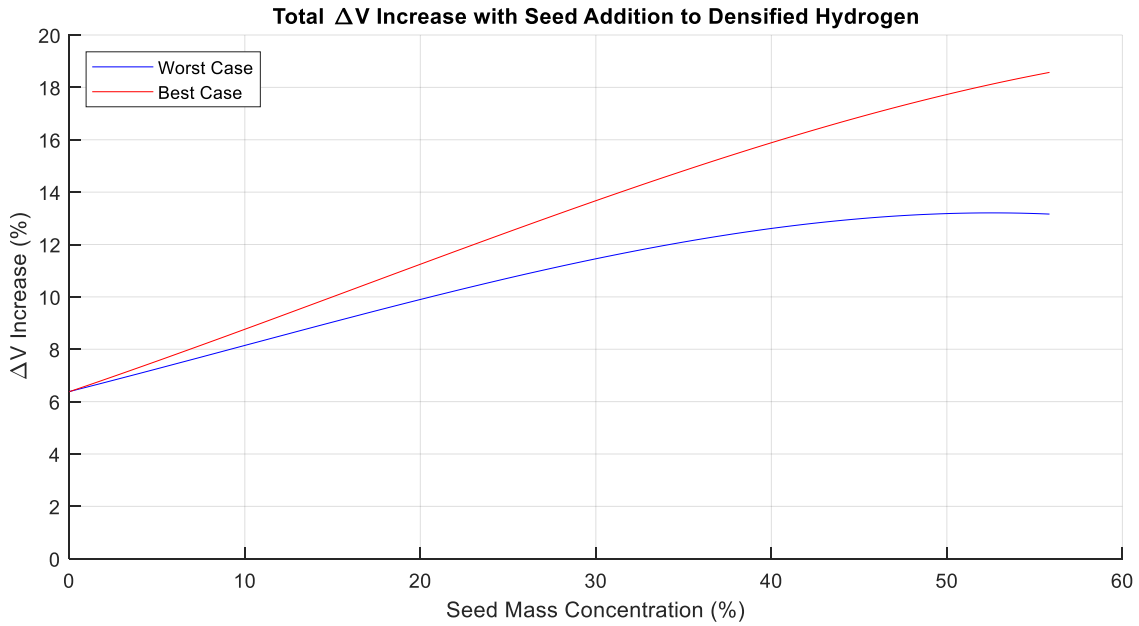

Figure 7.14: Increase in the Change in Velocity of Densified Seeded Hydrogen

The change in velocity is the primary factor, other than the location of the planets, which affects travel time. This is the key parameter of interest that will dictate the health of the astronauts travelling onboard this vehicle. Using patch conics, the estimated travel times were calculated by first setting the departure and arrival dates for both Earth to Mars and Mars to Earth trips and then modifying the change in velocity for each trip to obtain the travel times. Doing so for varying levels of seeded non-densified hydrogen resulted in the total trip time savings curves of Figure 7.15 with the worst and best case maximum seed concentrations yielding net savings of 21.59 and 32.45 days respectively. The travel trajectories for the worst case at 50% seed mass concentration are shown in Figures 7.16 and 7.17 for Earth to Mars and Mars to Earth respectively.

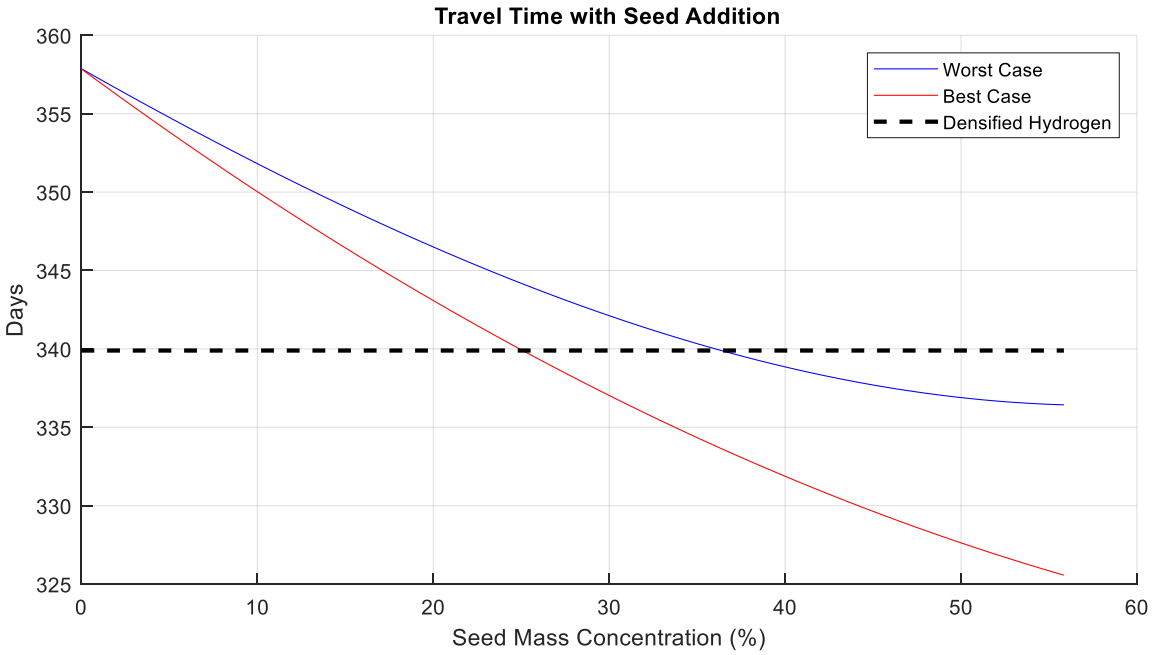

Figure 7.15: Comparing Total Travel Time of Seeded Non-Densified Hydrogen with Densified Hydrogen

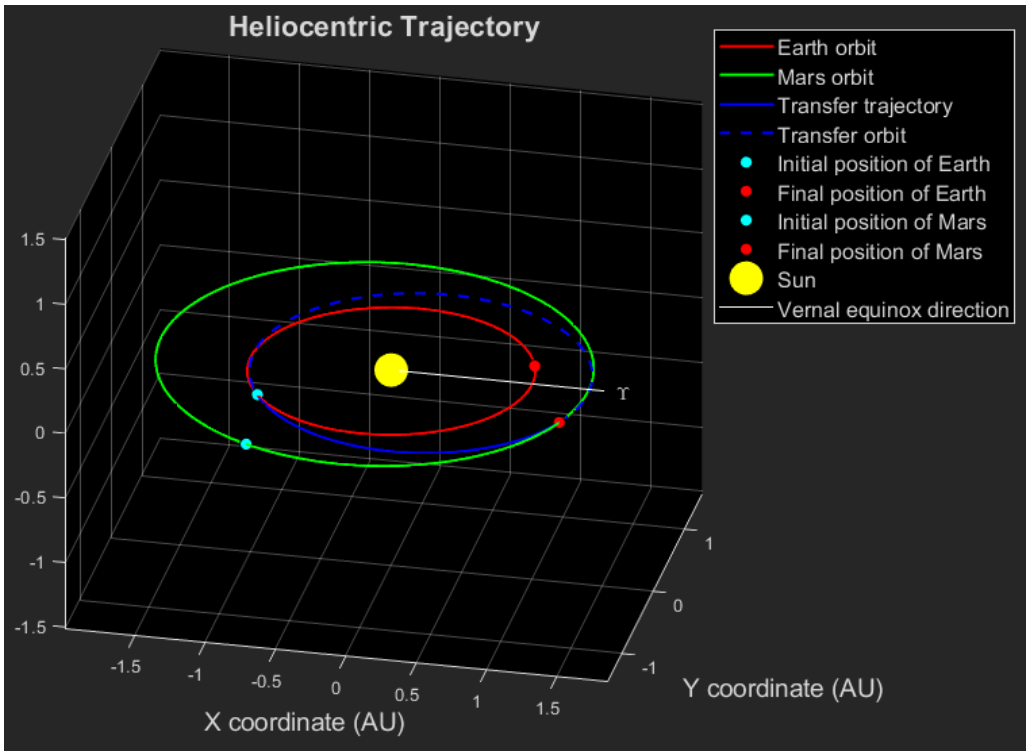

Figure 7.16: 50% Seed Mass Concentration, Worst Case, Earth to Mars Trajectory [71]

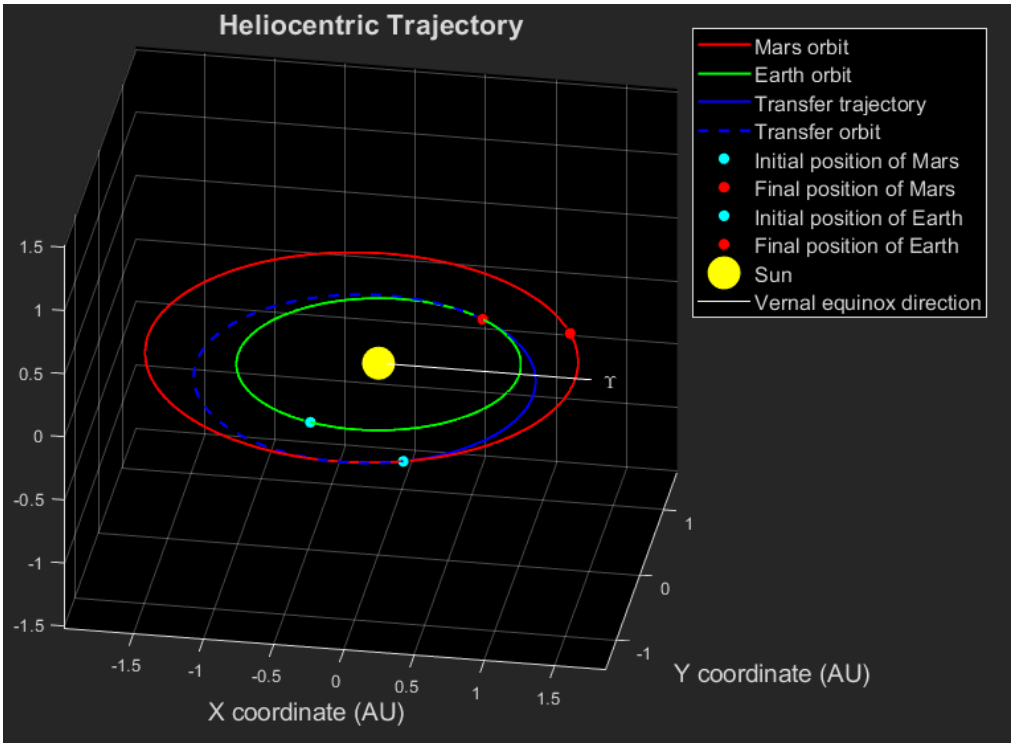

Figure 7.17: 50% Seed Mass Concentration, Worst Case, Mars to Earth Trajectory [71]

Extending this to seeded densified hydrogen yields the preliminary time savings curves shown in Figure 7.18 where the worst and best case total time savings at maximum seed concentration are 32.32 days and 41.66 days respectively. The switch to densified hydrogen (at 14K and 2 atm) immediately grants 18.22 days of saved total travel time. These values may change as future research examines the impact of densified hydrogen on the engine.

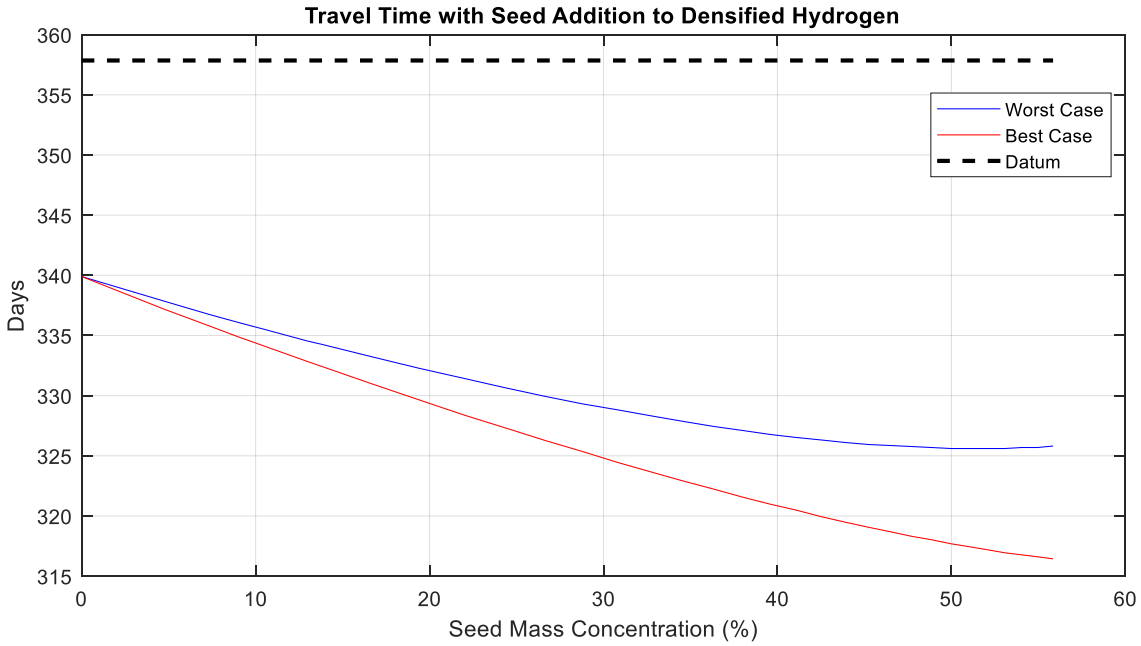

Figure 7.18: Total Travel Time with Seeded Densified Hydrogen

Even though both seeded hydrogen and seeded densified hydrogen provide increased vehicle performance and decreased total travel time, the addition of the seed increased the overall vehicle mass substantially by up to 46.53% while keeping the same volume in the case of non-densified seeded hydrogen. Densified seeded hydrogen exhibited a further mass increase of up to 41.25%. However, the vehicle mass did not change greatly among the worst and best case scenarios. This is demonstrated in Figures 7.19: Vehicle Mass for Seeded Non-Densified Hydrogen, Figure 7.20: Increase in Vehicle Mass for Seeded Non-Densified Hydrogen, Figure 7.21: Vehicle Mass for Seeded Densified Hydrogen, and Figure 7.22: Increase in Vehicle Mass for Seeded Densified Hydrogen.

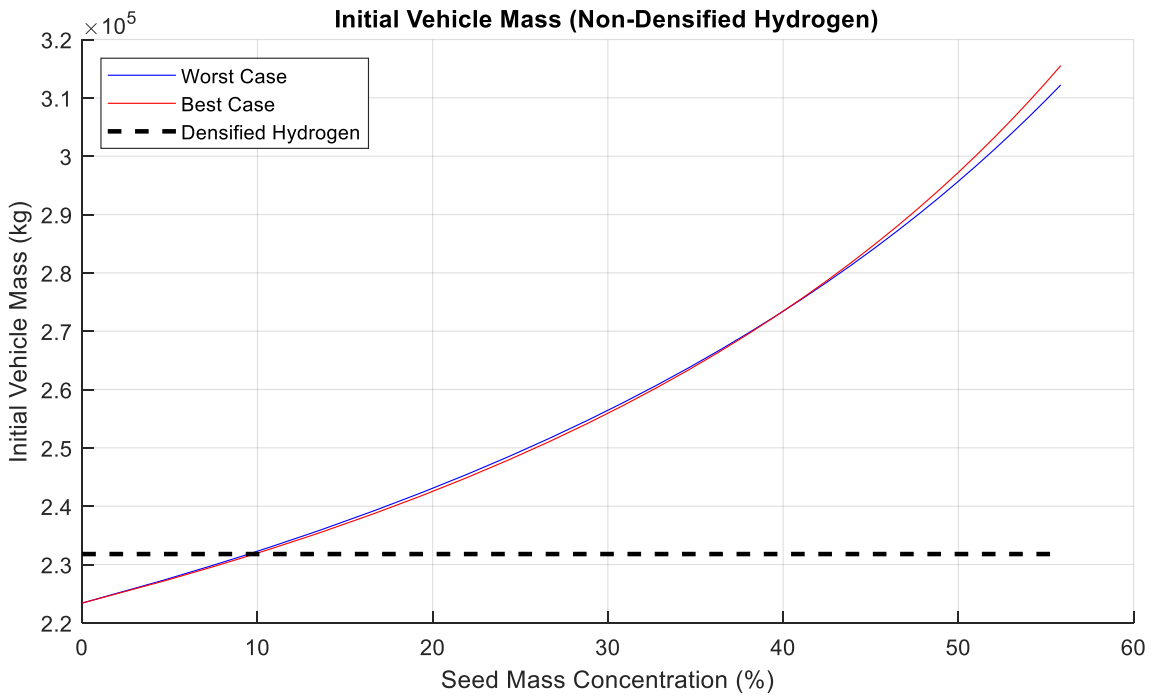

Figure 7.19: Initial Vehicle Mass for Seeded Non-Densified Hydrogen

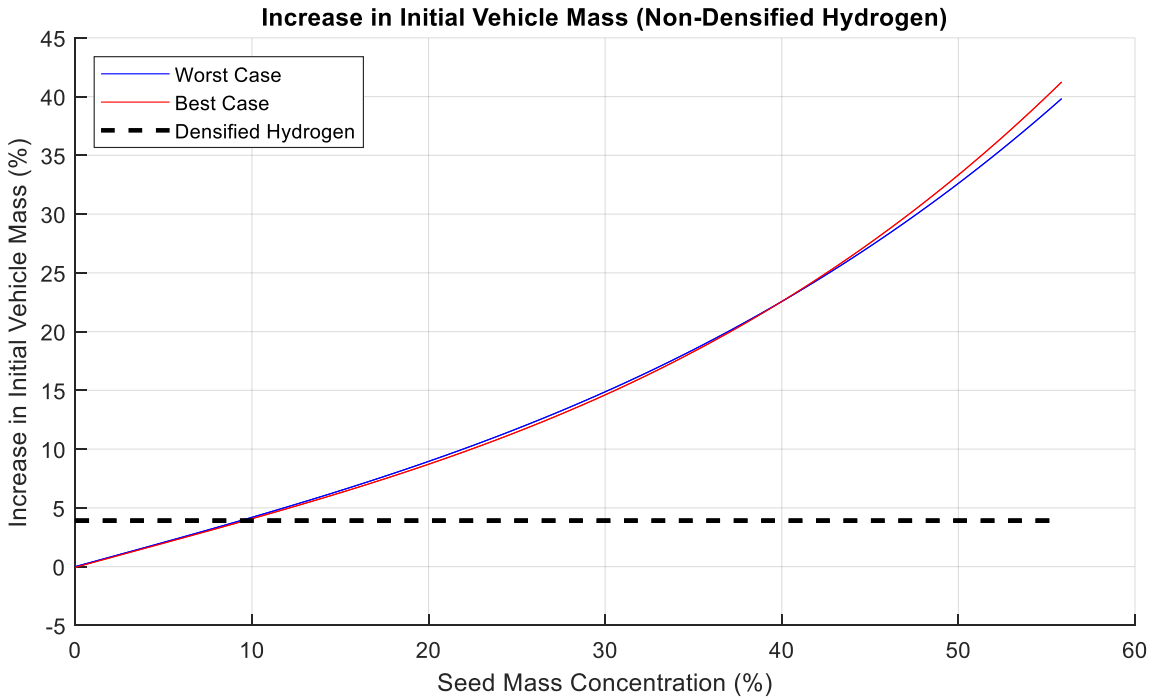

Figure 7.20: Increase in the Initial Vehicle Mass for Seeded Non-Densified Hydrogen

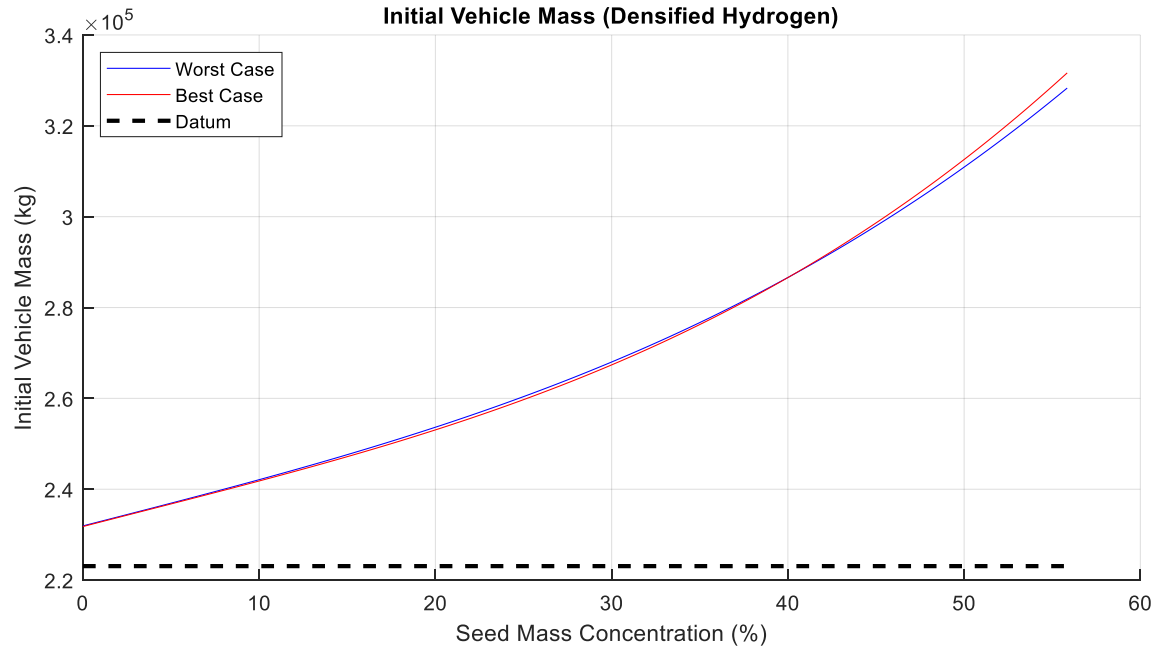

Figure 7.21: Initial Vehicle Mass for Seeded Densified Hydrogen

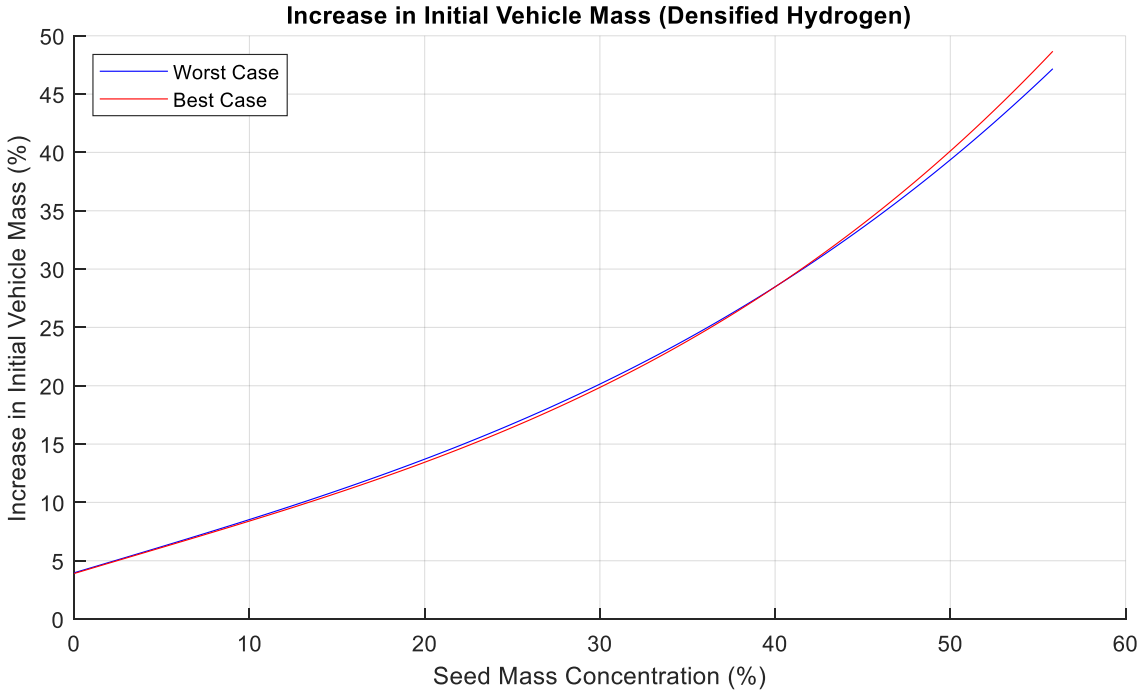

Figure 7.22: Increase in the Initial Vehicle Mass for Seeded Densified Hydrogen

According to this analysis, if cryocoolers that are able to keep hydrogen densified at around 14 K are available, then a decrease in travel time is possible with minimal increase in mass at 0% seed concentration. However, if these cryocoolers are not available and/or decreased travel time is still available with the ability to accommodate the higher mass increase of the vehicle, then seeded propellant will be able to satisfy these requests.

Tying all of this back to the overarching question of this thesis:

The Overarching Research Question:

How does the addition of an inert noble gas, a seed, into the hydrogen propellant affect the engine performance as well as the overall vehicle performance and architecture and whether this will be better than simply densifying pure hydrogen propellant?

ANS: Adding a heavy noble gas impurity, a seed, to hydrogen (densified or not) will increase the vehicle's ability to provide substantial change in velocity for a given volume if the mass constraints are lifted. Further, the required reactor power will be less for a given nozzle geometry. However, all of this comes at the cost of lower specific impulse and considerably higher vehicle mass.

Utilizing densified hydrogen will have a prominent effect on the change in velocity while increasing the seed concentration will increase that effect. Furthermore,

the addition of a seed alleviates the strain on the turbomachinery and will not require the high pressures associated with pure hydrogen to overcome the pressure loses caused by its low density. The reactor power will also be reduced and thus providing the potential for a smaller and lighter reactor. The convective heat transfer of the mixture is also increased and allows for higher chamber temperatures while keeping the maximum fuel temperature the same as for pure hydrogen. However, all of this comes at the cost of lower specific impulse and substantially higher vehicle mass.

CHAPTER 8

CONCLUSION

8.1 Thesis Conclusions

This thesis has shown the advantages and disadvantages of injecting heavy noble gases (seeds) into the hydrogen propellant, also known as seeding, in a nuclear thermal propulsion system. The propulsion system was chosen to be Aerojet Rocketdyne's (AR) April 4th, 2019 version of the NTP engine [42]. This system was modelled in MATLAB's Simulink and validated to AR's values as well as to some of the key parameters of the Nuclear Engine for Rocket Vehicle Application (NERVA) program. This model was modified to include the turbomachinery needed to add the capability of injecting the seed into the hydrogen propellant. Furthermore, a model of AR's Mars vehicle architecture was modelled in a MATLAB code to examine the effects of seeded propellant on vehicle performance through orbital mechanics and changes in velocities.

The results answered the main question asked at the end of the literature review in Chapter 2: How does the addition of an inert noble gas, a seed, into the hydrogen propellant

affect the engine performance as well as the overall vehicle performance and architecture and whether this will be better than simply densifying pure hydrogen propellant?

To answer this question, a few other questions had to be answered first: (1a) Can seeding hydrogen provide a higher density increase percentage, (1b) Can seeding hydrogen yield better overall change in velocity than densified hydrogen, (2) How is convective heat transfer affected by the addition of the seed, and (3) How does adding a seed affect the internal engine pressure losses?

These questions were answered in reverse order and provided the following answers:

(3) How does adding a seed affect the internal engine pressure losses?

The addition of the seed decreases the pressure losses experienced by hydrogen when it flows by itself. However, due to the increased viscous effects and increased mass flow rate, the pressure losses inside the reactor channels are increased. This increased pressure loss is overcome and exceeded by the summation of the reduced pressure losses exhibited in the hydrogen only duct flows prior to this. These decreased pressure losses can then be used to increase the chamber pressure and, in turn, increase the engine's thrust.

(2) How is convective heat transfer affected by the addition of the seed?

The heavy noble gas seeds have extremely low specific heat capacities when compared to hydrogen. This results in lower required reactor power to increase the seeded propellant's temperature by the same amount as pure hydrogen. Furthermore, with

increased viscous effects coupled with the lowered specific heat capacity, the seeded propellant more effectively promotes heat transfer from the parts of the core not in direct contact with the fluid. The result is the reduction of the maximum fuel temperature for the same propellant outlet temperature. By forcing the maximum fuel temperature to be the same as that in the case of pure hydrogen, the seeded propellant outlet temperature becomes higher than pure hydrogen while still benefiting for the decreased reactor power.

(1a) Can seeding hydrogen provide a higher density increase percentage?

The highest densification achieved was between 79.89% and 86.59% whereas the densification of pure hydrogen was only 8.16%.

(1b) Can seeding hydrogen yield better overall change in velocity than densified hydrogen?

AR's Mars vehicle architecture MATLAB code showed that seeded propellant and densified hydrogen performance can be expected to be similar between 25.39% and 36.1% seed mass concentration. Beyond these values, seeded propellant shows increased performance. However, the downside of this is increased vehicle mass by up to a maximum of 41.25% due to the lower specific impulse provided by the seeded propellant. Seeding densified hydrogen was also analyzed which resulted in even further performance increase but up to 48.67% vehicle mass increase.

Thus, the addition of a heavy noble gas into hydrogen does increase overall engine and vehicle performance by reducing pressure losses, increasing thrust, decreasing reactor power, and increasing the overall change in velocity of the vehicle. However, this comes

at the cost of lowered specific impulse which results in vehicle mass increase of up to 41.25%. When compared to densified hydrogen, the vehicle performance at around 30% seed mass concentration was about the same. Beyond this seed concentration, the performance increased to provide up to a 32-day savings on a round trip to Mars. However, the best case for gaining the most vehicle performance would be to seed the densified hydrogen which could be capable of providing a reduction of up to 41 days on a round trip to Mars.

8.2 Future Research

Based on the literature review (Chapter 2), this thesis is the first known attempt to examine the effects of seeding hydrogen propellant in a nuclear thermal propulsion (NTP) engine system. Although the results from the previous section are significant, much more research must be conducted to prove the viability of seeded hydrogen in these engines and the Mars transfer vehicle.

The next step in this research topic would be to introduce higher fidelity in the radial direction of the reactor in the Simulink model as well as examining the neutron flux distribution to observe the effects that the seed will have on the neutronics. It was mentioned that argon has similar cross section properties to hydrogen, therefore negligible effects are expected [68]. However, krypton and xenon have larger cross sections implying that these effects may be observable and may deserve some consideration [69]. The higher fidelity in the radial direction of the reactor by the use of Bessel functions will provide insight on to how the radial thermal distribution will affect the surface temperature of the

reactor shell and, in turn, provide more accurate results for determining if the exit temperature of the seed inside the preheating seed channels will indeed be over the critical temperature of the selected species.

Examining the engine performance with densified hydrogen will also be part of this next step in future research. Since densified hydrogen will flow at a different flow rate than non-densified hydrogen, pump performance is expected to be affected. Due to this, it is possible that a different pump selection will be made and that the engine performance could change. However, large changes in the engine performance are not expected. After addressing the pump selection, this engine will be outfitted again with the capability of seeding the hydrogen flow and examining the engine performance as well as the vehicle performance in a similar way that was addressed in Chapters 6 and 7 of this thesis. This research will also consider more up-to-date design versions of the Aerojet Rocketdyne NTP based engine and update the engine parameters accordingly. Should more information become available about the material properties such as the thermal conductivity of the fuel and nozzle material, it will be incorporated into the Simulink model.

Future experimental research will examine the diffusivity of supercritical noble gases into supercritical hydrogen while both species are in turbulent flow. Although complete and a negligible time of mixing has been confirmed by an expert as well as other sources [25] [26] [41], experimental studies must still be conducted to prove that though the two species are completely miscible, the time it takes for complete diffusivity is negligible in an engine apparatus. If the length of time proves to be considerable, then a

mixing component should be considered in the area where the supercritical seed stream is injected into the supercritical hydrogen stream.

This thesis has assumed that the critical point of the hydrogen-noble gas mixture is within 5% of the pseudocritical point. This is another area for future research to examine experimentally since the actual critical points of any substance or mixture are obtained by experimental procedures. However, previous research discussed in the literature review has pointed to the use of the pseudocritical point as a valid approximation of the actual critical point of a mixture composed of hydrogen and mono-atomic fluids to within 5% of the true value [41]. If, however, experimental research finds that this approximation is inaccurate and that the mixture is not supercritical when it flows through the reactor, then further research would be required to analyze the structure of the non-supercritical mixture and if there are any critical areas which would provide significant changes to the current analysis.

APPENDIX A

Fluid Properties

A.1 Hydrogen

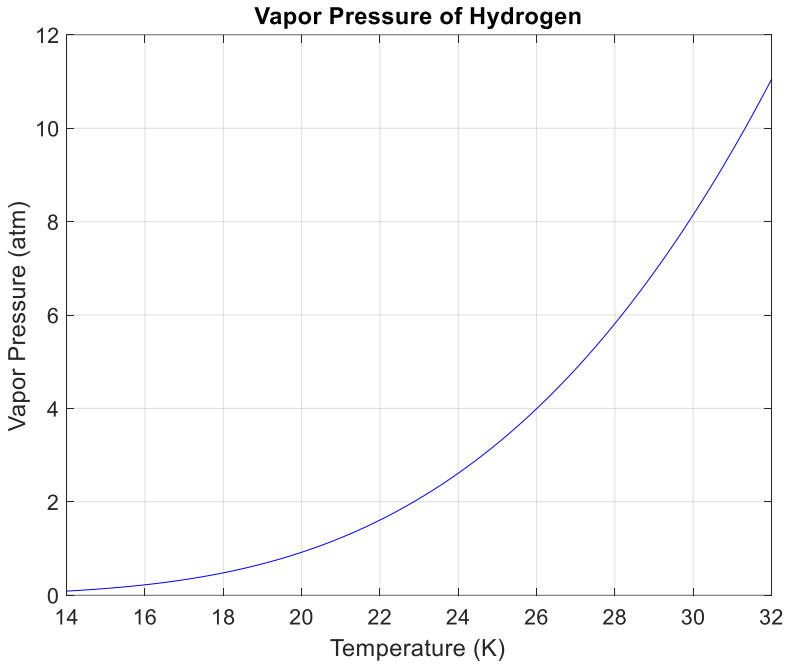

Figure A.1.1: Vapor Pressure of Hydrogen

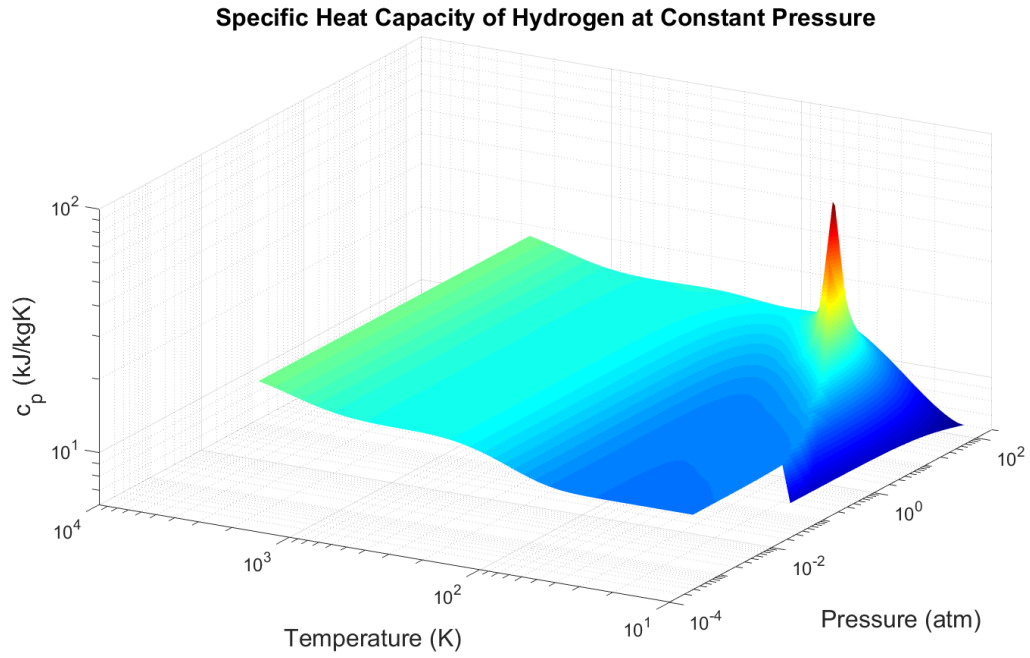

Figure A.1.2: c_p of Hydrogen

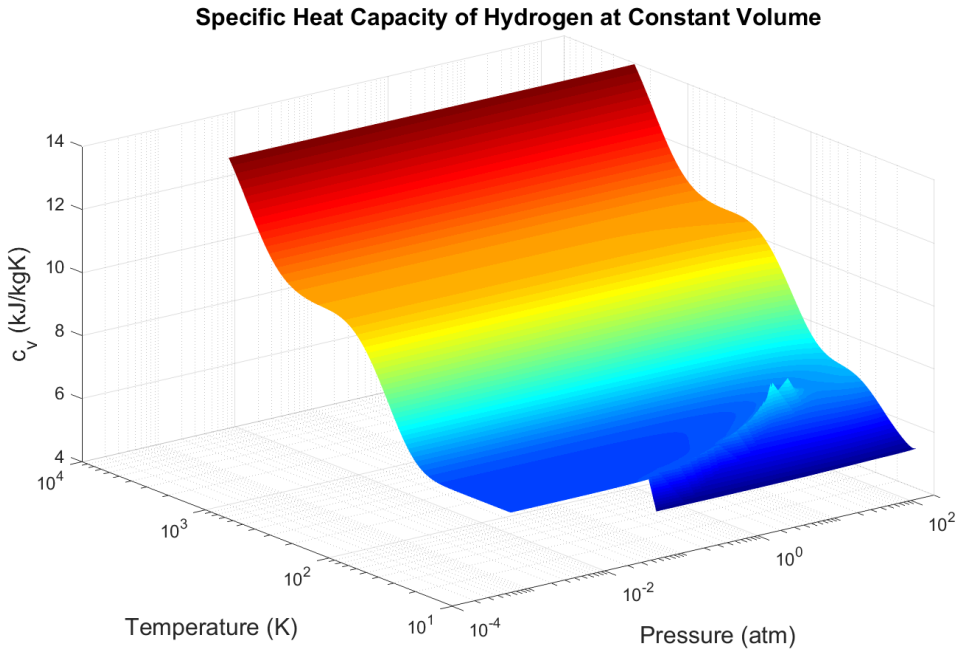

Figure A.1.3: c_v of Hydrogen

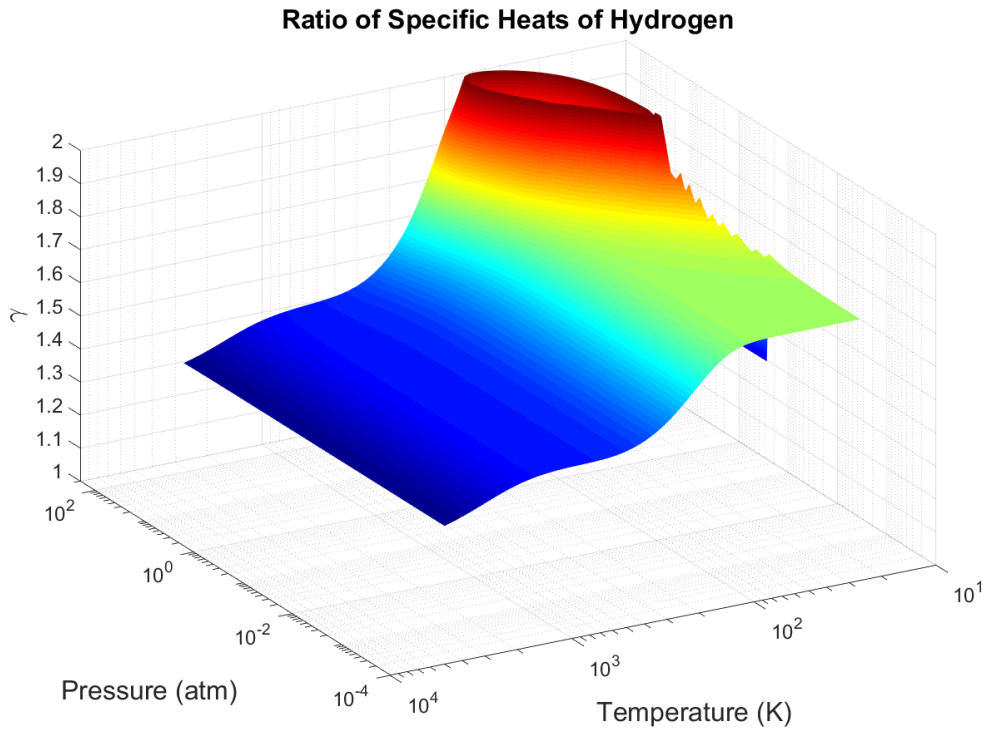

Figure A.1.4: Ratio of Specific Heats of Hydrogen

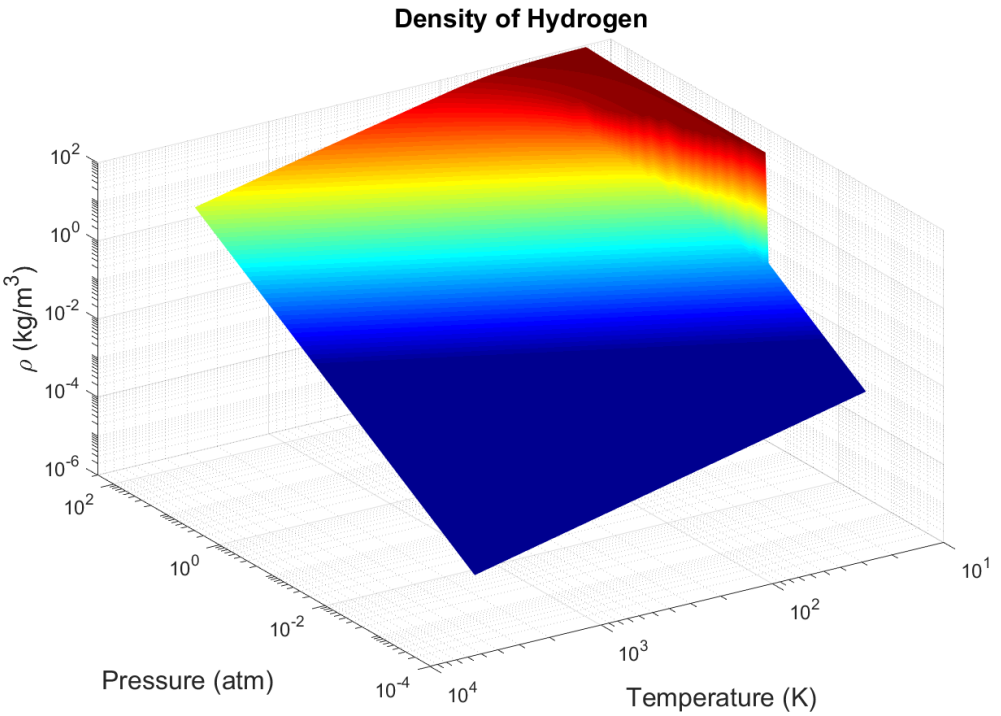

Figure A.1.5: Density of Hydrogen

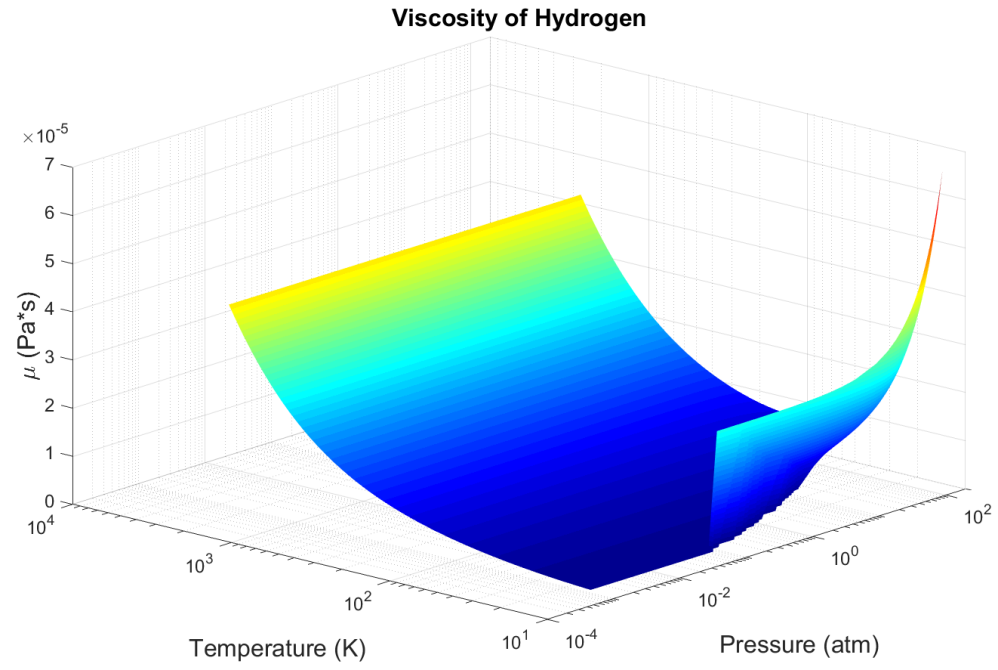

Figure A.1.6: Viscosity of Hydrogen

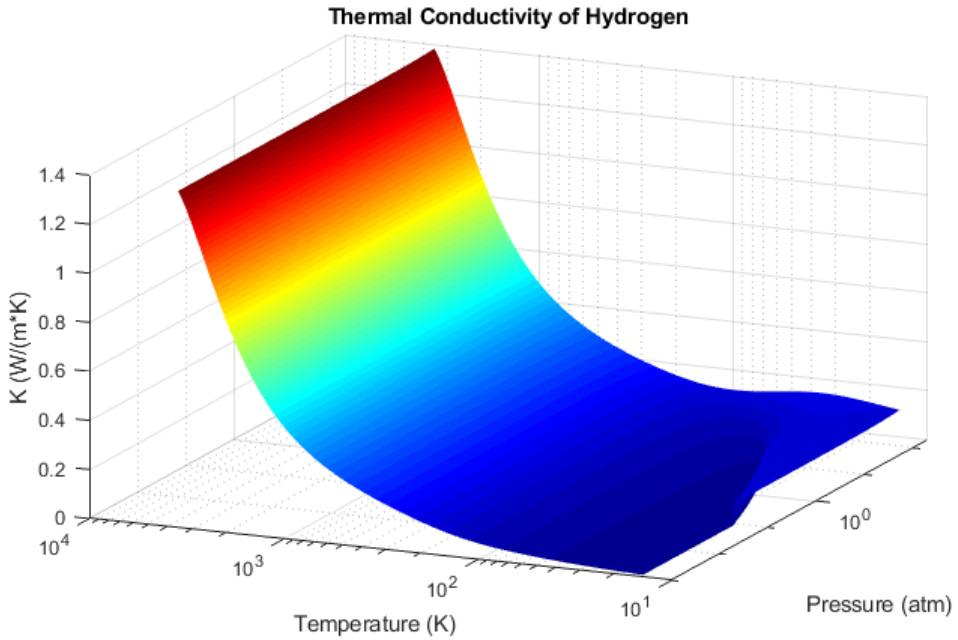

Figure A.1.7: Thermal Conductivity of Hydrogen

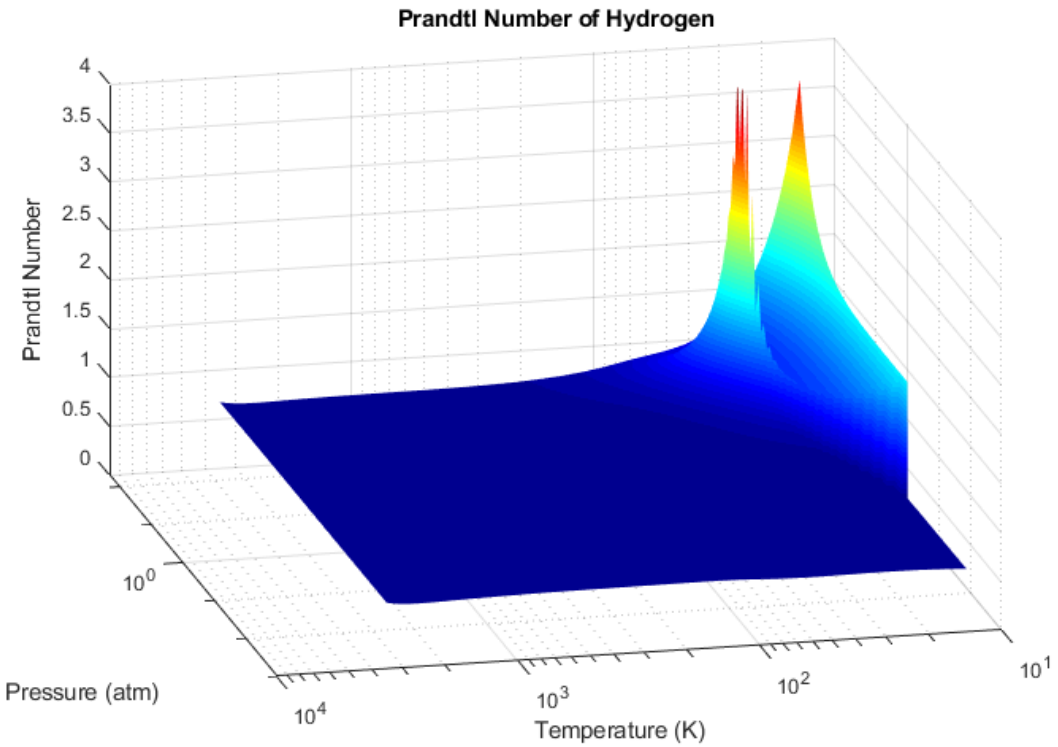

Figure A.1.8: Prandtl Number of Hydrogen

A.2 Argon

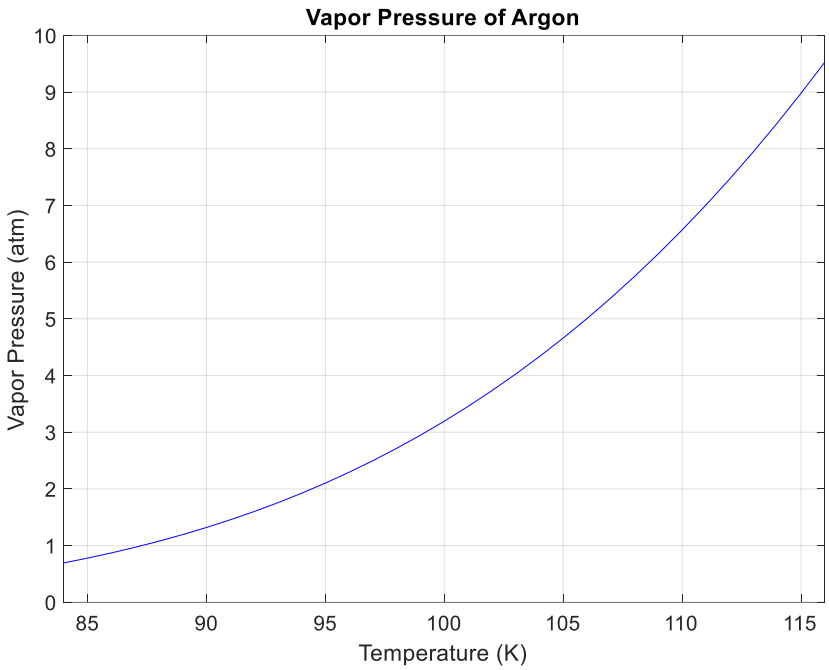

Figure A.2.1: Vapor Pressure of Argon

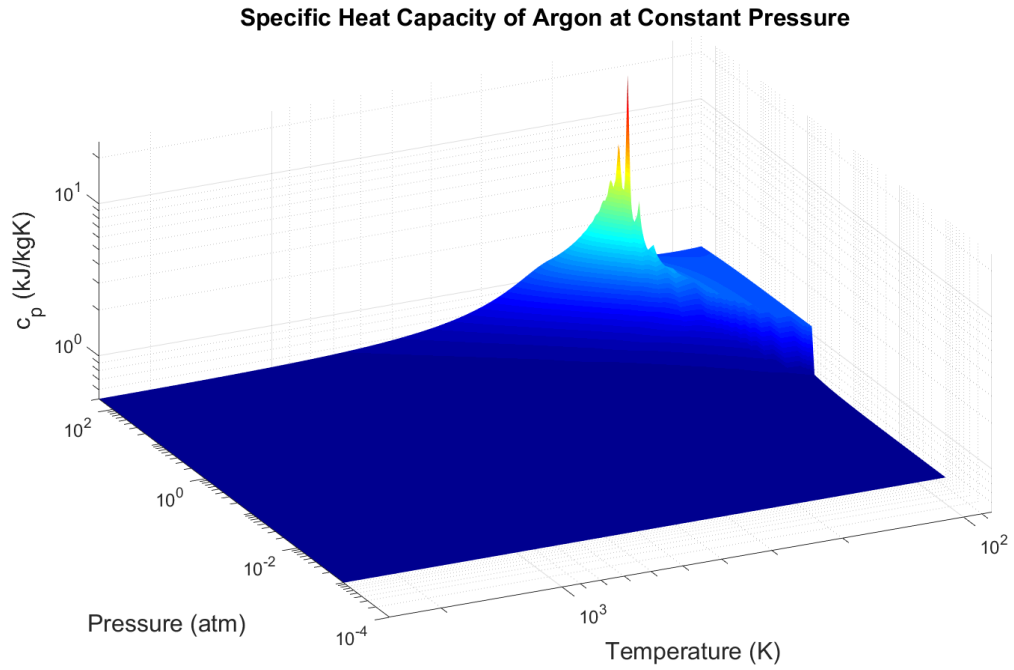

Figure A.2.2: c_p of Argon

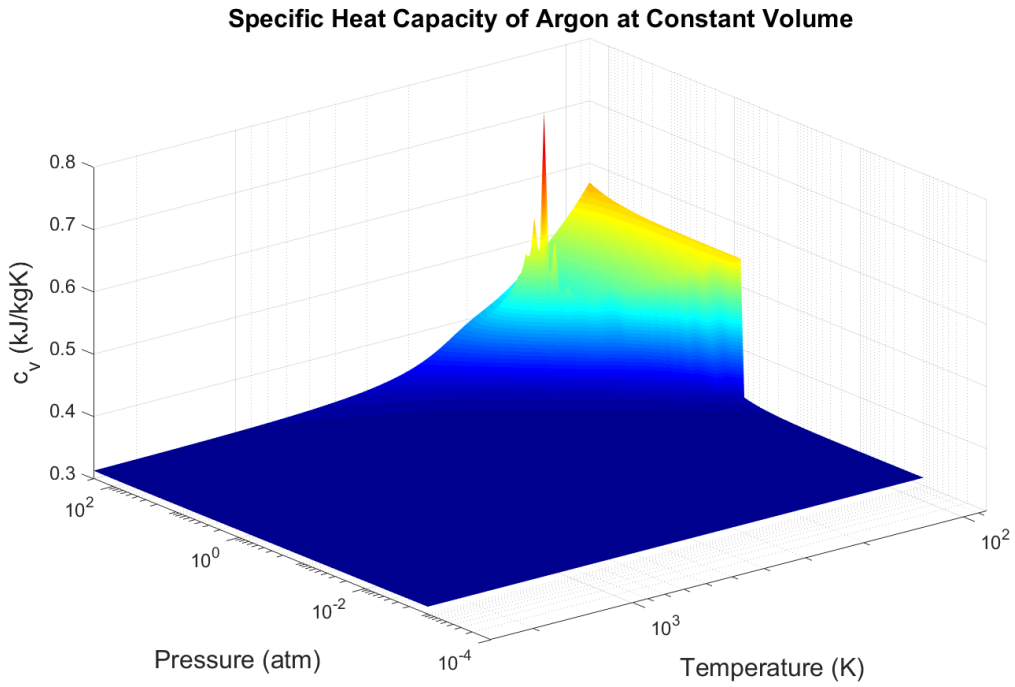

Figure A.2.3: c_v of Argon

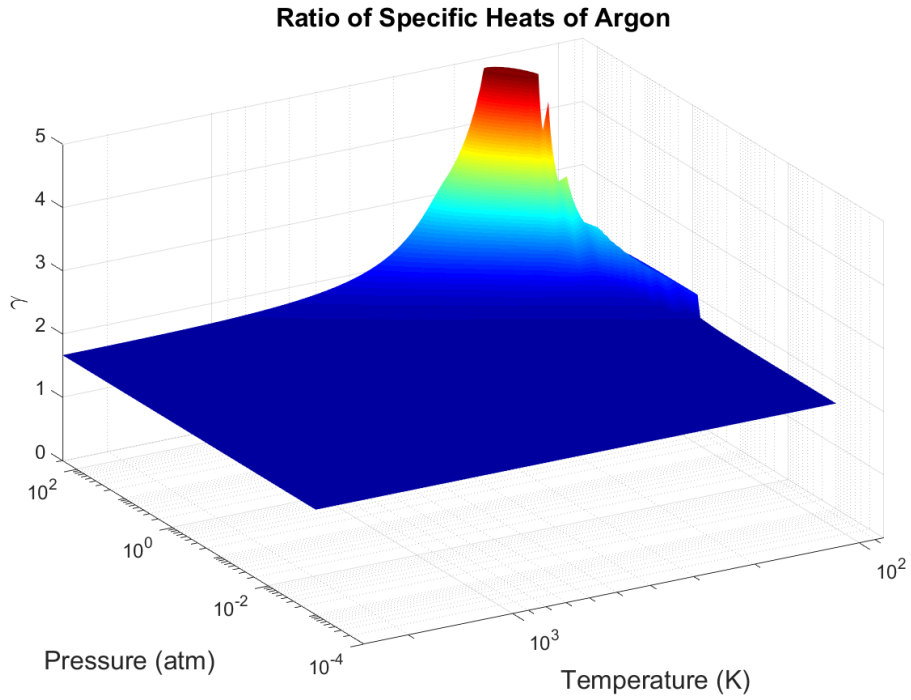

Figure A.2.4: Ratio of Specific Heats of Argon

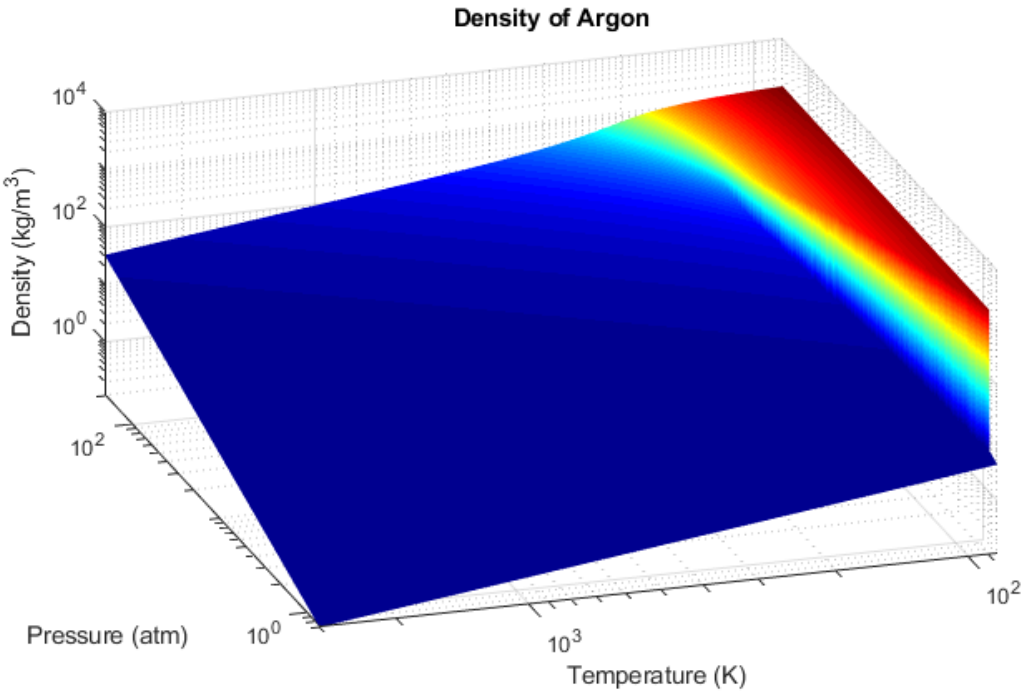

Figure A.2.5: Density of Argon

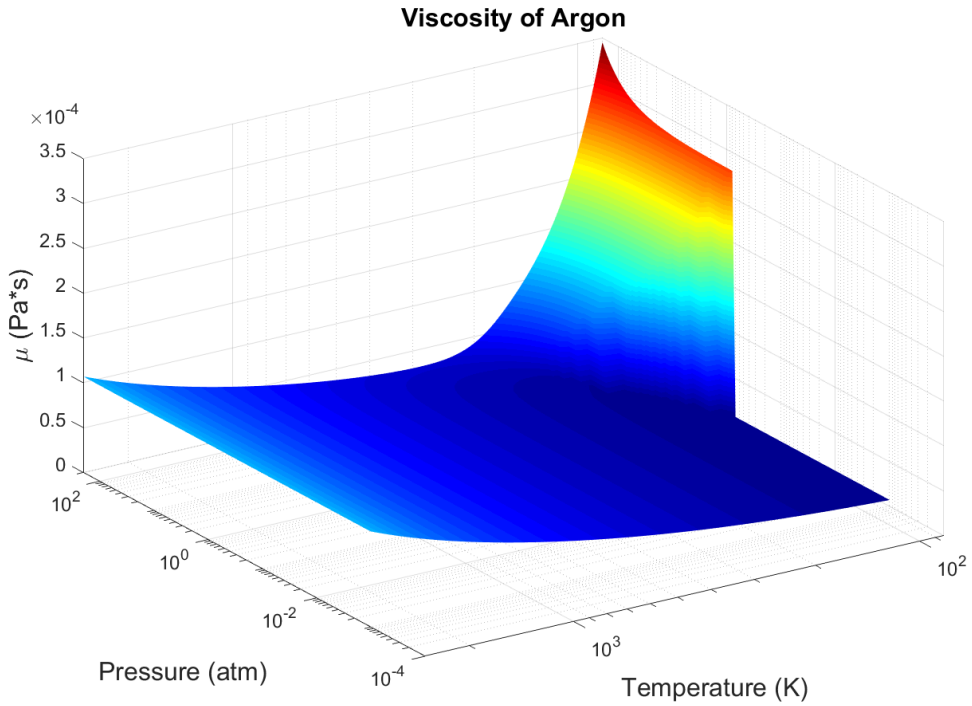

Figure A.2.6: Viscosity of Argon

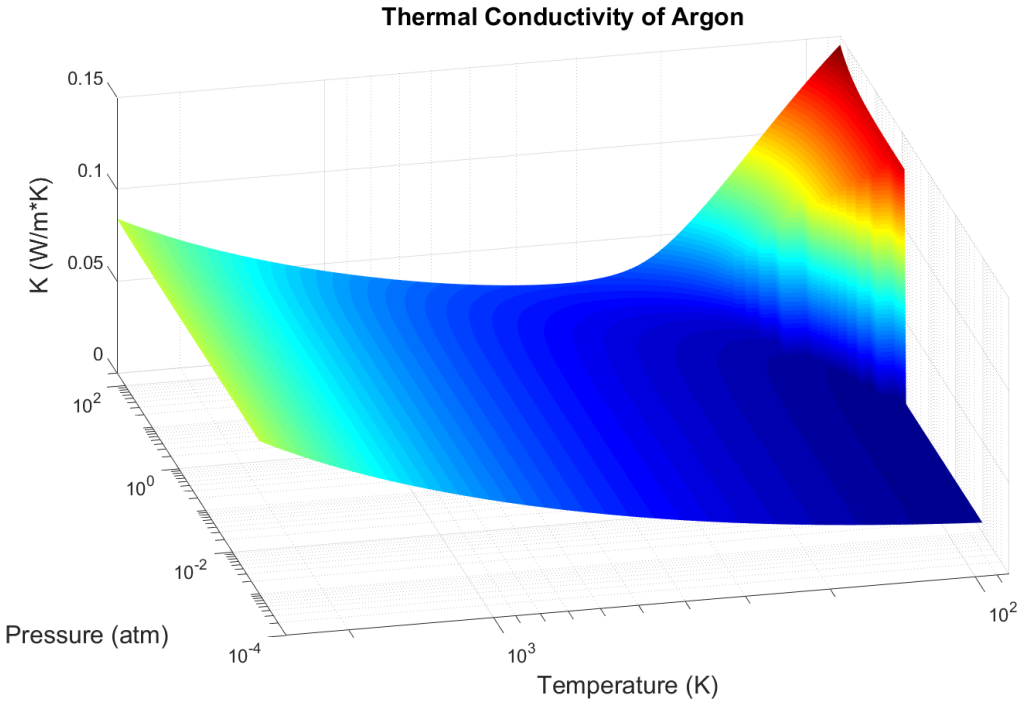

Figure A.2.7: Thermal Conductivity of Argon

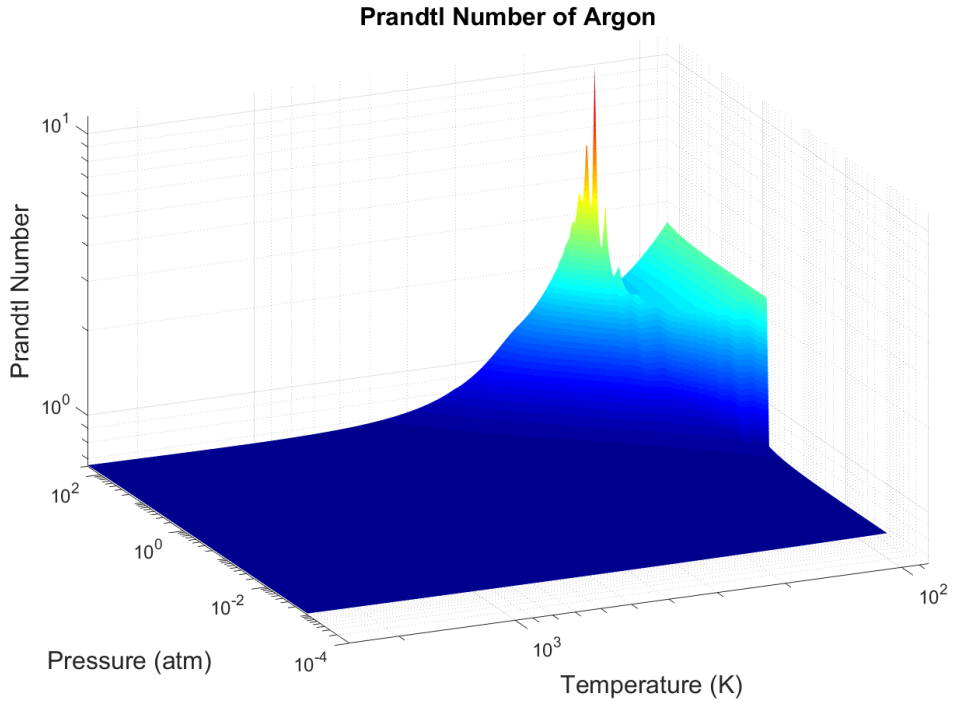

Figure A.2.8: Prandtl Number of Argon

A.3 Krypton

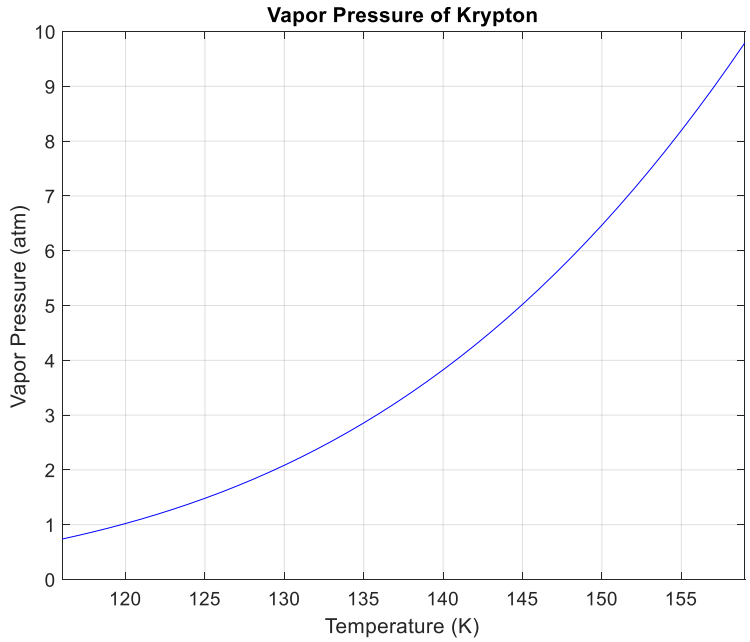

Figure A.3.1: Vapor Pressure of Krypton

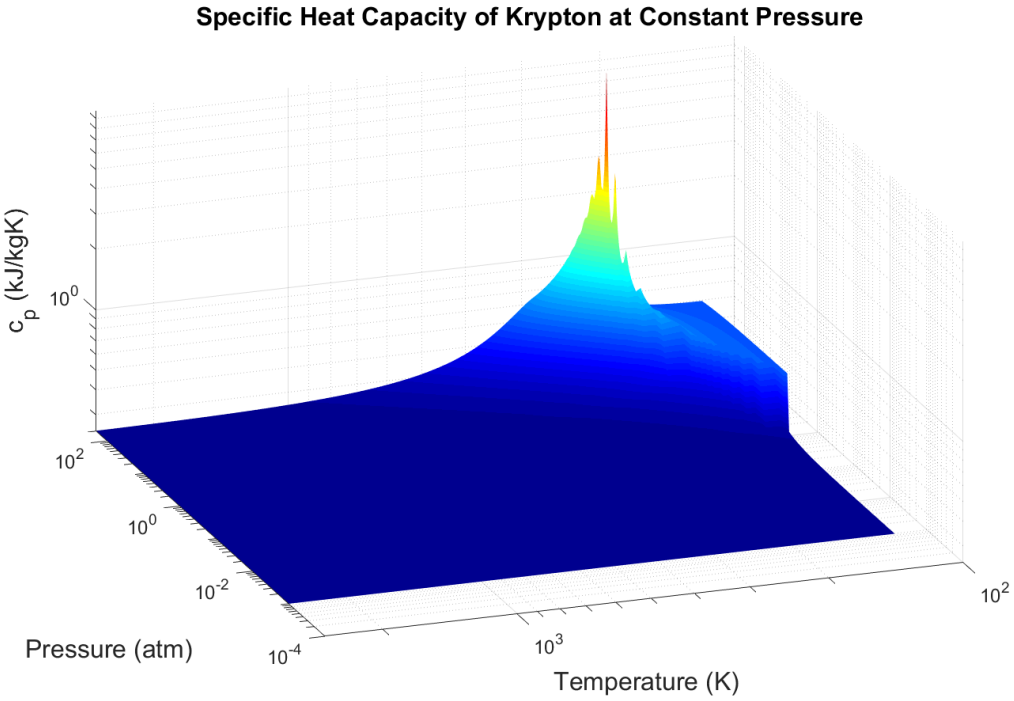

Figure A.3.2: c_p of Krypton

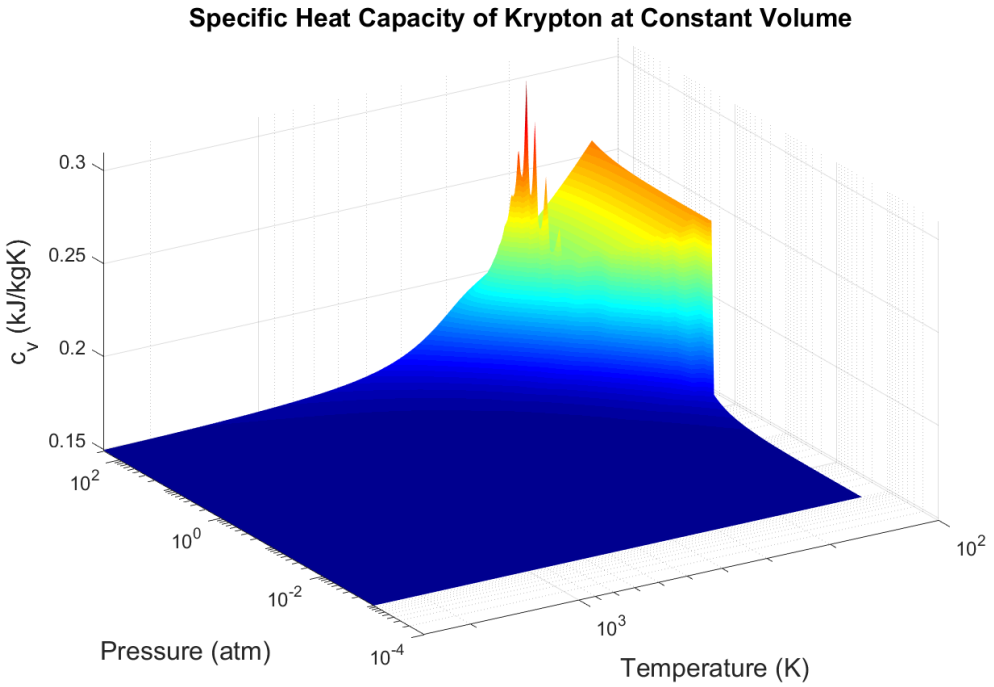

Figure A.3.3: c_v of Krypton

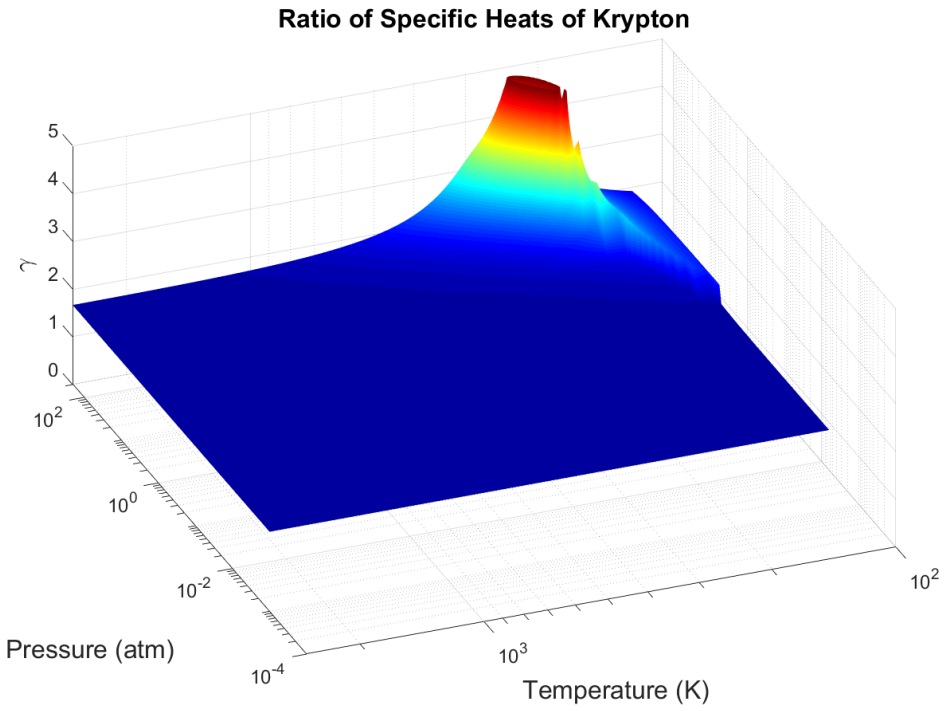

Figure A.3.4: Ratio of Specific Heats of Krypton

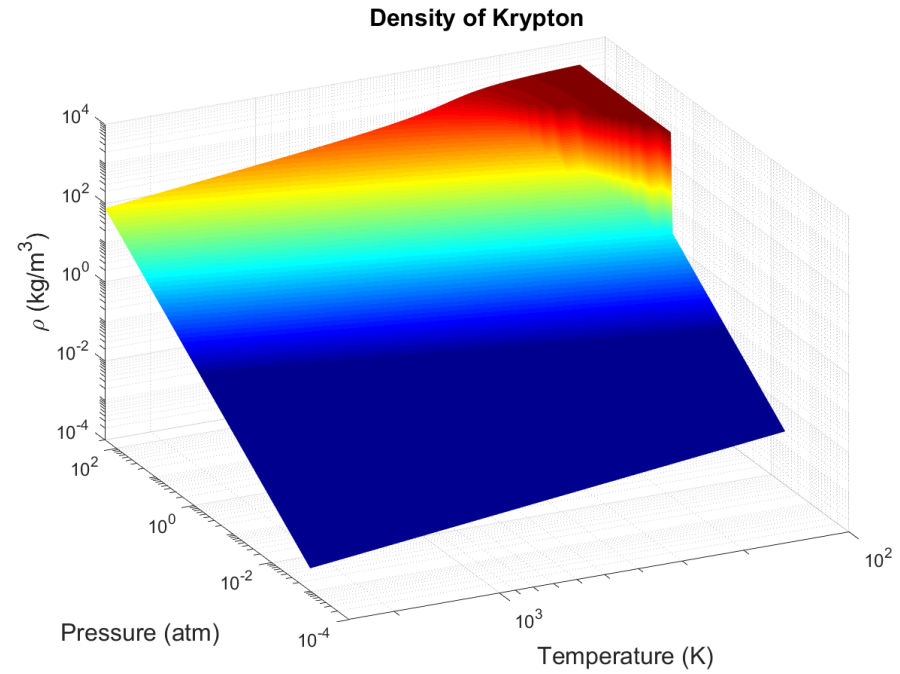

Figure A.3.5: Density of Krypton

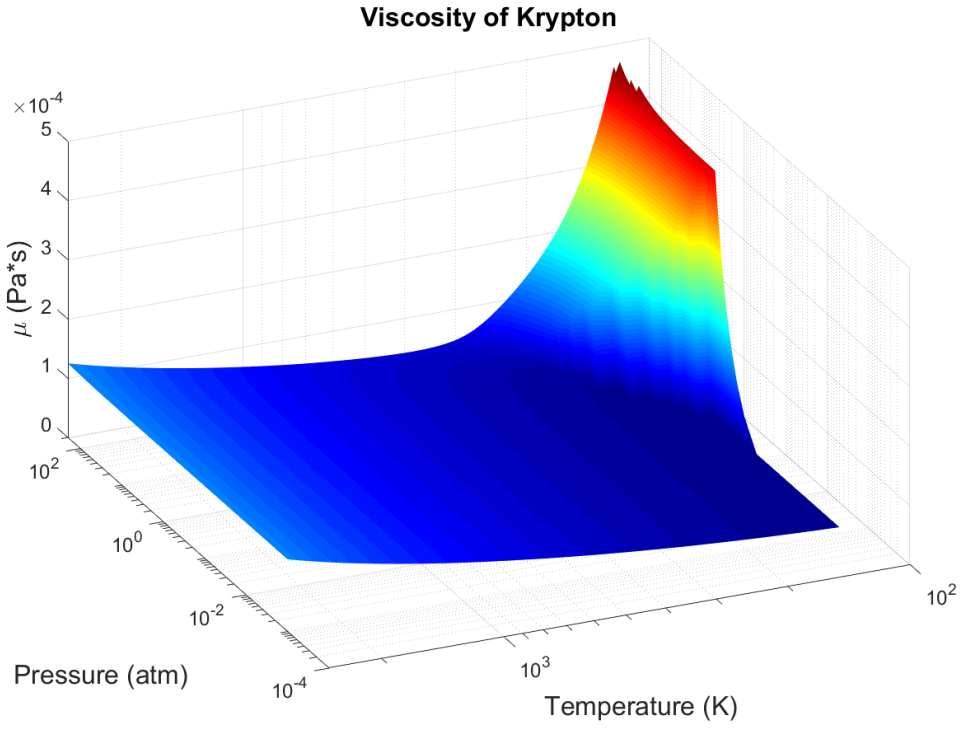

Figure A.3.6: Viscosity of Krypton

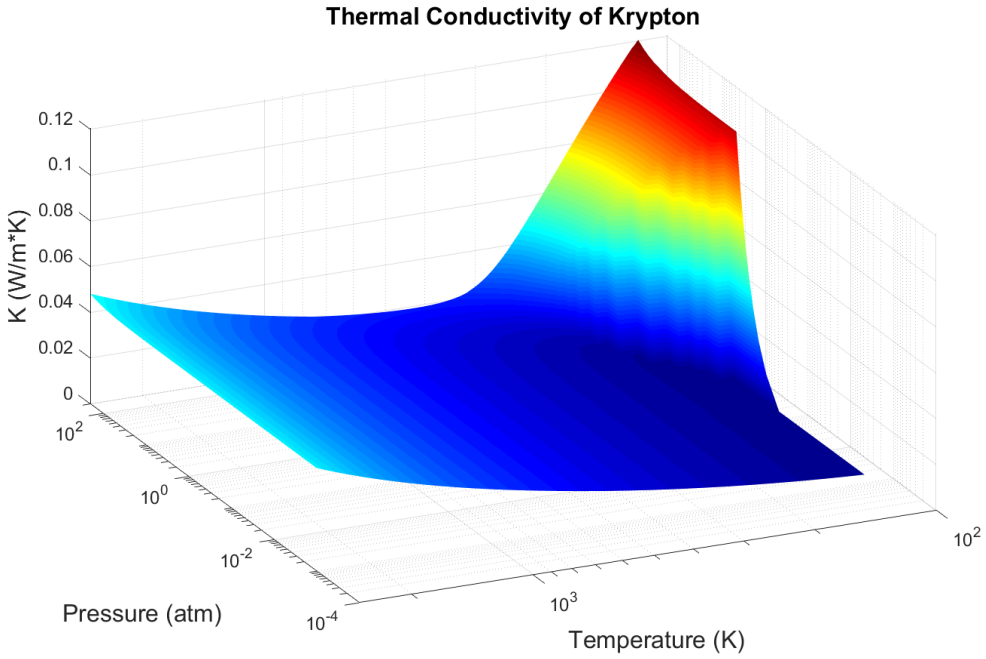

Figure A.3.7: Thermal Conductivity of Krypton

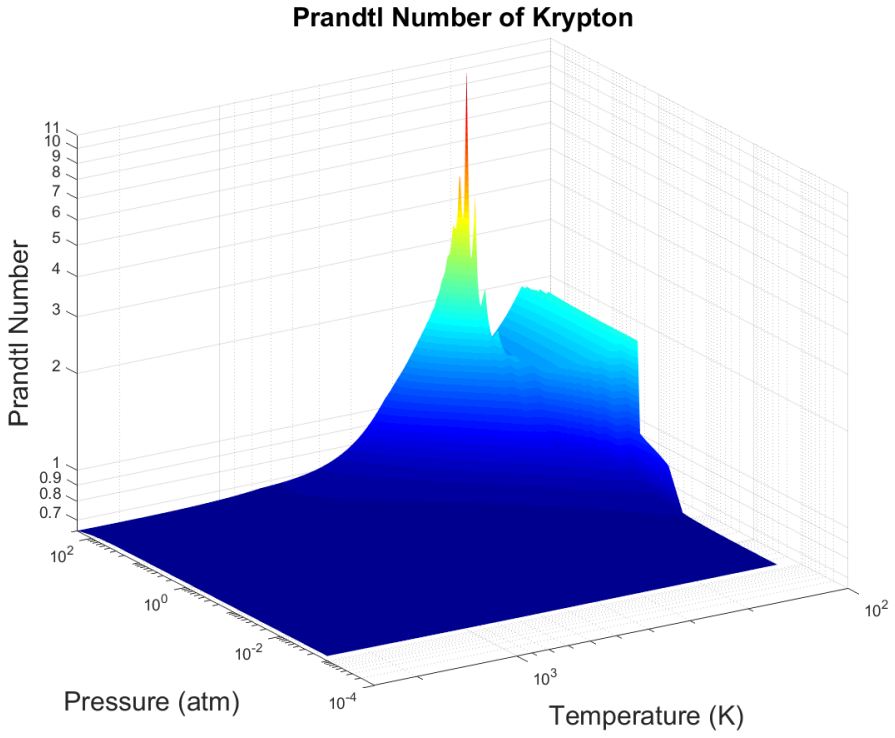

Figure A.3.8: Prandtl Number of Krypton

A.4 Xenon

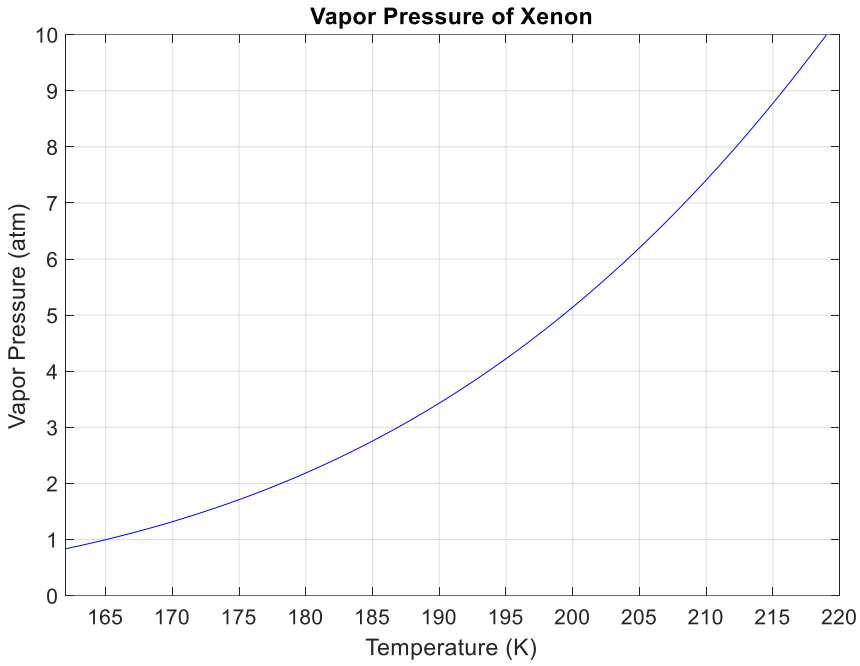

Figure A.4.1: Vapor Pressure of Xenon

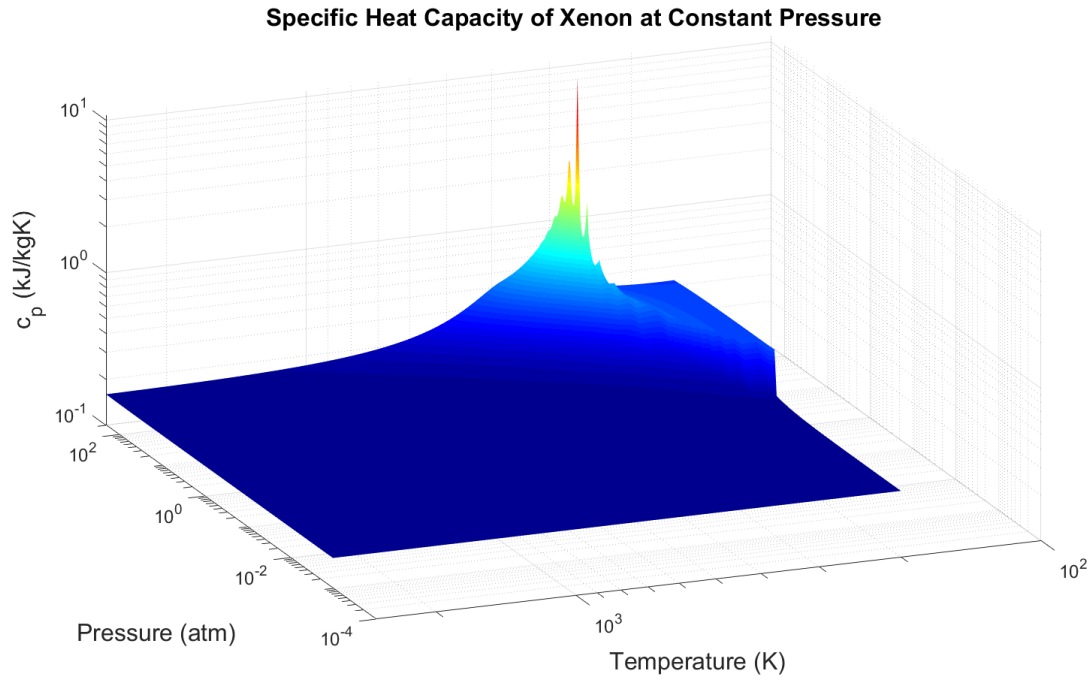

Figure A.4.2: c_p of Xenon

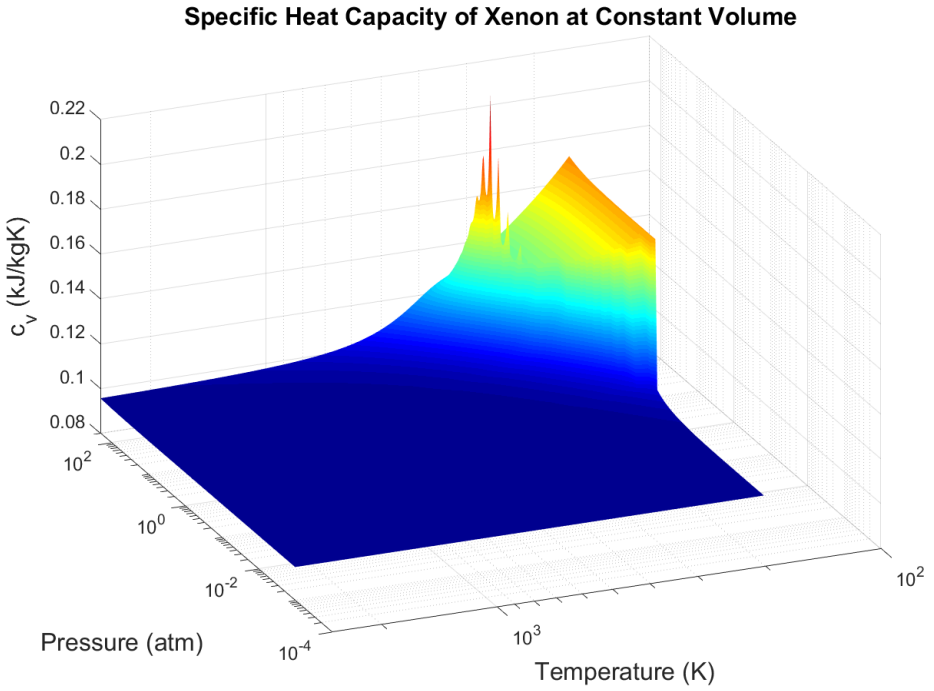

Figure A.4.3: c_v of Xenon

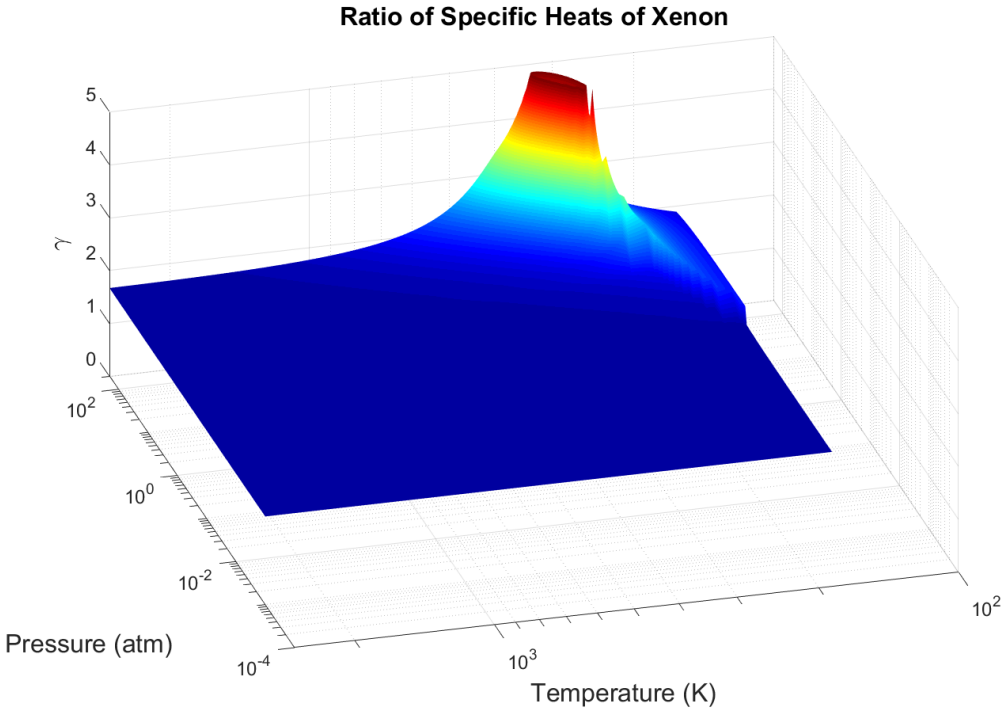

Figure A.4.4: Ratio of Specific Heats of Xenon

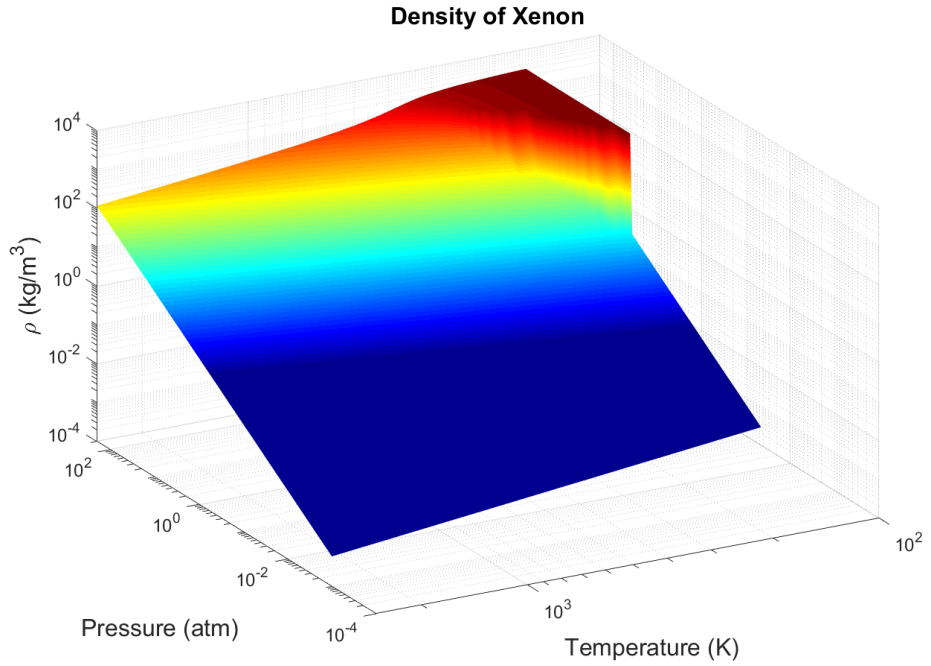

Figure A.4.5: Density of Xenon

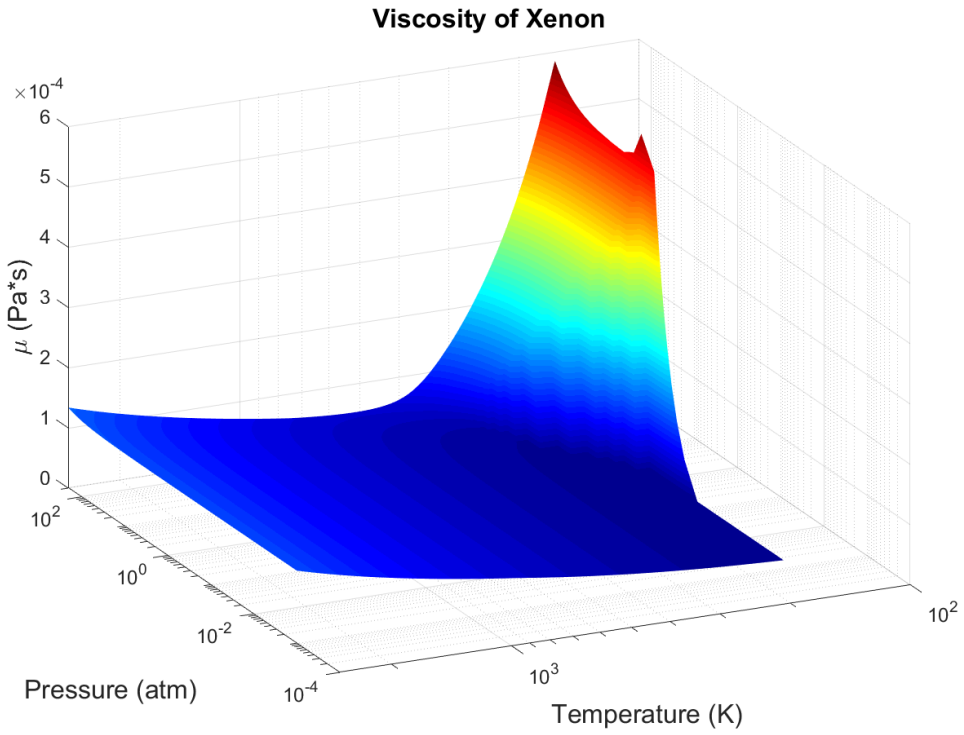

Figure A.4.6: Viscosity of Xenon

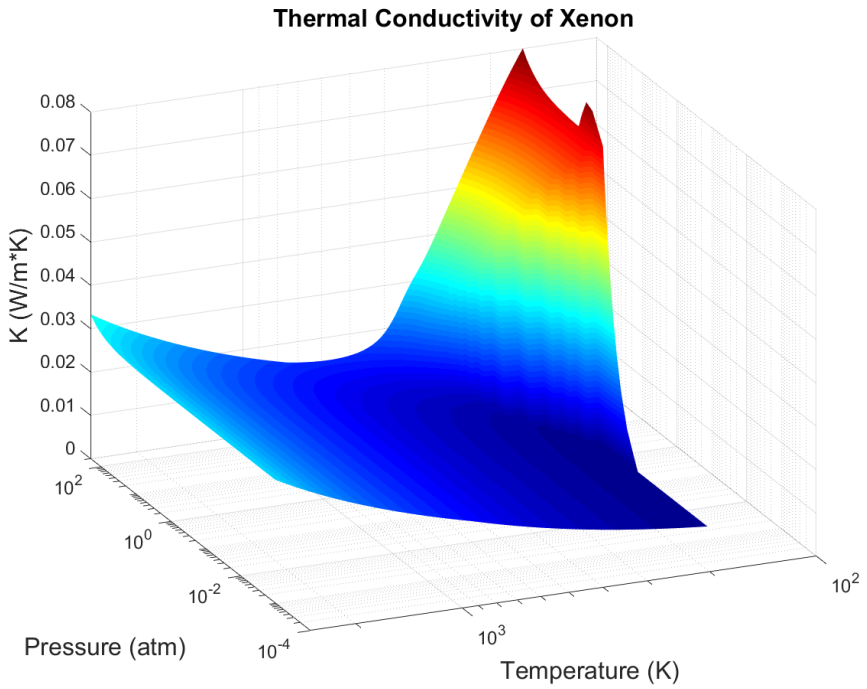

Figure A.4.7: Thermal Conductivity of Xenon

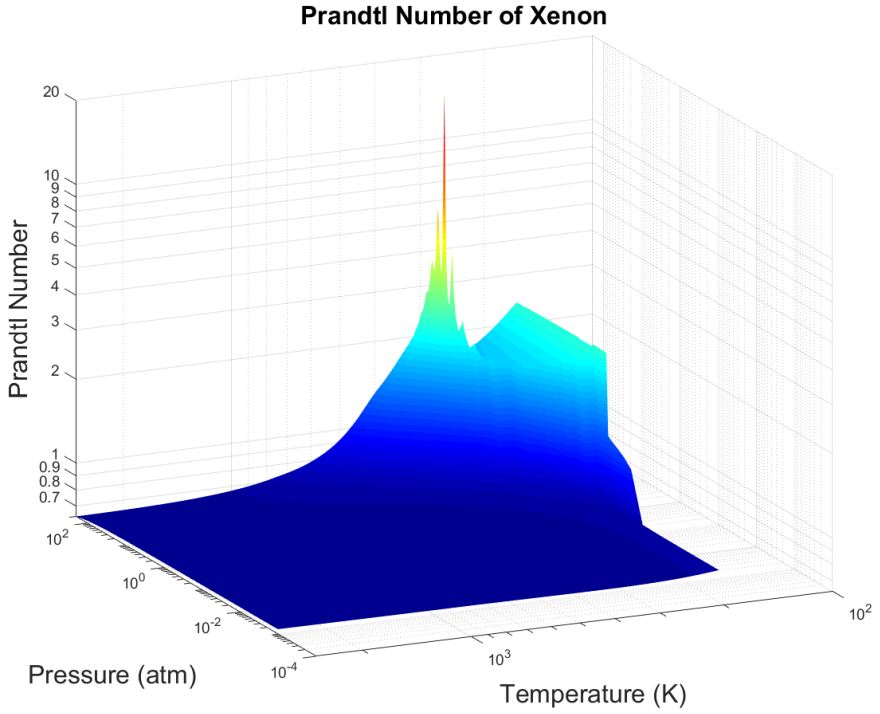

Figure A.4.8: Prandtl Number of Xenon

APPENDIX B

Turbine Analysis

In Chapter 2, a case was presented for running pure hydrogen through the turbines inside of seeded hydrogen. The first reason for this is to avoid solid particles of the seed forming inside the ducts where hydrogen is below the freezing point of the seed fluid. The second reason is the reduced mechanical work potential of the seeded hydrogen which will be explored here. By utilizing equations 5.15a through 5.18 and performing an analysis on finding the required efficiency of the turbine and predefined inlet and outlet conditions of state 13 and state 14 respectively of the Aerojet Rocketdyne engine model, the graph of turbine efficiency versus seed mass concentration is presented in Figure B.1. The mass flow rate through the turbine was kept at 77.42% of the total flow rate through the engine (shown in Figure B.2) with all other conditions the same as shown in Table B.1. It is clear that a higher efficiency turbine would be required to accommodate the addition of the seed. This is why the seed was chosen to be added into the hydrogen flow after it has run through all of the turbomachinery. Furthermore, the seed would not need to be pressurized to the same pressure as the hydrogen before running through the turbomachinery, thus, reducing the amount of work that the seed turbine would have to produce.

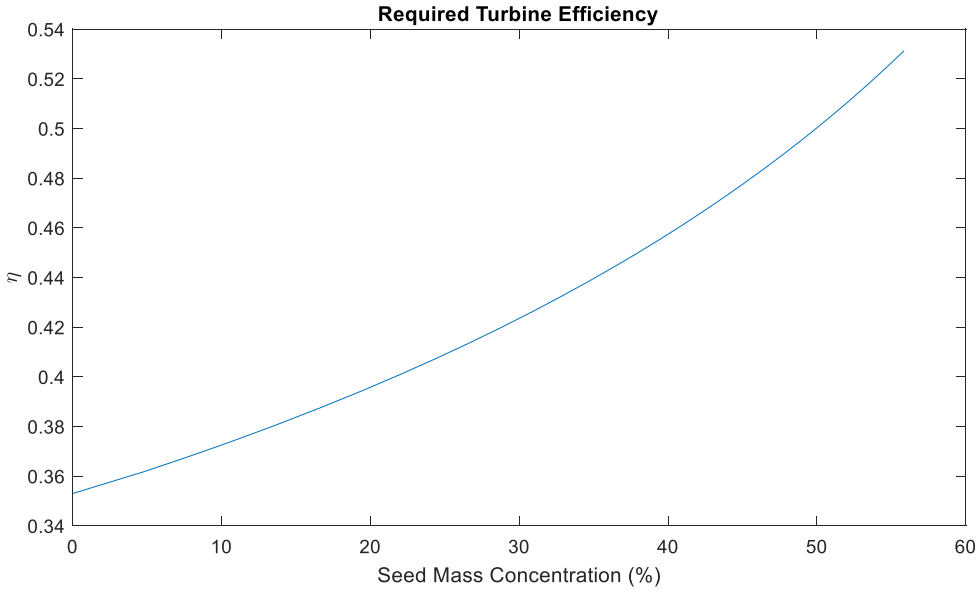

Figure B.1: Required Turbine Efficiency

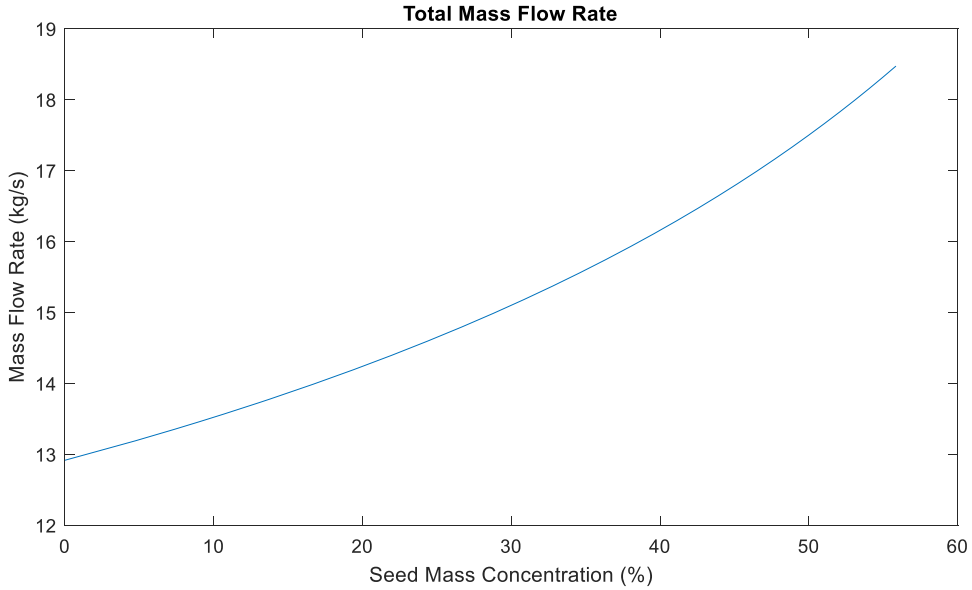

Figure B.2: Total Mass Flow Rate

APPENDIX C

Correspondence with Dr. Martyn Poliakoff

Dennis Nikitaev <dn0038@uah.edu>

Supercritical Fluid Miscibility

4 messages

Dennis Nikitaev <dn0038@uah.edu>Fri, Jun 21, 2019 at 1:58 PM To: martyn.poliakoff@nottingham.ac.uk

Hello Dr. Poliakoff,

I am conducting research on mixing supercritical hydrogen and supercritical argon for a nuclear thermal rocket engine at the University of Alabama in Huntsville. I had a question about the miscibility of supercritical fluids. I read on wikipedia that any supercritical fluid is completely miscible with another supercritical fluid but I cannot find a citable source. Could you please provide a recommendation?

I would really appreciate it if you could help and I really admire your videos on YouTube! Thank you,

Dennis Nikitaev

Graduate Research Assistant University of Alabama in Huntsville Dennis.Nikitaev@uah.edu

702-287-6852

Von Braun Research Hall M40

Martyn Poliakoff <Martyn.Poliakoff@nottingham.ac.uk> Thu, Jun 27, 2019 at 4:54 PM To: Dennis Nikitaev <dn0038@uah.edu>

Dear Dennis,

Thank you for your message. The short answer to your question is that supercritical fluids are gases therefore they are inherently miscible. This does not mean that they will mix well if they are not properly stirred or agitated. I am also slightly confused by your statement

about supercritical hydrogen and helium because the critical pressures are 13 and 2.3 bar respectively so the gases in standard lab cylinders are well above their critical pressures.

Best wishes Martyn

[Quoted text hidden]

Dennis Nikitaev <dn0038@uah.edu>Thu, Jun 27, 2019 at 4:59 PM To: Martyn Poliakoff <Martyn.Poliakoff@nottingham.ac.uk>

Hello Dr. Poliakoff,

Thank you for your reply. The gas is argon, not helium. The flow is expected to be turbulent when argon is injected into hydrogen. This flow will be at around 88 bar. Hydrogen will be at 300 K and argon will be at 350 K when this happens.

Thank you,

Dennis

[Quoted text hidden]

--

[Quoted text hidden]

Martyn Poliakoff <Martyn.Poliakoff@nottingham.ac.uk> Thu, Jun 27, 2019 at 5:13 PM
To: Dennis Nikitaev <dn0038@uah.edu>

Hi! Of course they will mix.

[Quoted text hidden] [Quoted text hidden]

APPENDIX D

MATLAB Functions

D.1 Thoma parameter look up [17]

```
function [sigma] = thoma_fun(n_s,S_s)

n_s_range=[0.1,0.2,0.3,0.4,0.5,0.6,0.7,0.8,0.9,1,2,3,4];
sigma_range=flipud([0.01;0.02;0.03;0.04;0.05;0.06;0.07;0.08;0.09;0.1;0.2;0.3;0.
4;0.5]);
S_s_range=[0.175 0.331    0.5      0.673    0.844    1        1.17     1.35
         1.524    1.682    3.37     5.028    6.65
           0.203   0.396  0.6      0.809    1        1.201    1.394    1.595
         1.805    2        3.979    5.918    7.877
           0.255   0.489  0.74     1            1.238        1.476    1.725
         1.973    2.234    2.455    5        7.37     9.809
           0.346   0.679  1.018    1.35     1.693    2.016    2.36     2.7
         3.024    3.352    6.693    9.958    13.25
           0.58    1.137  1.69     2.266    2.819    3.371    3.971    4.495
         5.078    5.617    11.19    16.75    22.25
           0.63    1.234  1.805    2.432    3.052    3.641    4.254    4.877
         5.509    6.119    12.14    18.18    25
           0.69    1.347  1.99     2.667    3.353    3.975    4.674    5.324
         6.014    6.681    13.26    19.76    30
           0.758   1.489  2.229    2.96     3.661    4.422    5.167    5.886
         6.649    7.309    14.65    22.25    40
           0.854   1.667  2.48     3.328    4.132    5        5.784    6.658
         7.49     8.268    16.51    25       60
           0.976   2.252  2.864    3.764    4.713    5.671    6.598    7.516
         8.544    9.51     18.83    30       100
           1.154   2.787  3.371    4.487    5.57     6.689    7.897    8.939
         10.12    11.24    25       40       180
           1.422   2.822  4.225    5.5          6.952        8.365    9.671
         11.06    12.47    13.68    30       60       400
           1.918   3.861  5.613    7.5          9.492        11.37    13.31
         15.14    17.06    18.72    40       100      700
           3.147   6.178  9.249    12.52    15.48    18.58    22.25    25       30
40       60       180      1000];
sigma_fun=@(SIGMA) interp2(n_s_range,sigma_range,S_s_range,n_s,SIGMA,'makima')-
S_s;
sigma=fzero(sigma_fun,mean(sigma_range));

end
```

D.2 Pressure Losses within Ducts, Lines, and Channels

```
function [P_out,m_dot_out,T_out] =
pipe_pressure_loss(resolution,P_in,d,m_dot,roughness,T_in,iteration,P_old)

import py.CoolProp.CoolProp.PropsSI
%coder.extrinsic('warning')
%mu=coder.nullcopy(zeros(size(P_in)));
%rho=coder.nullcopy(zeros(size(P_in)));
P_atm=101325;

if iteration==1
    rho=PropsSI('D','T',T_in,'P',P_in*P_atm,'Hydrogen');
    mu=PropsSI('V','T',T_in,'P',P_in*P_atm,'Hydrogen');
    v=m_dot/(pi*(d/2)^2*rho);
    Re=4*m_dot/(pi*mu*d)
    if Re<5000
        f=64/Re;
    else

f=0.094*(roughness/d)^0.225+0.53*roughness/d+88*(roughness/d)^0.44*Re^(-
1.62*(roughness/d)^0.134);
        %f_fun=@(f) 1/sqrt(f)+2*log10(roughness/(3.7*d)+2.51/(Re*sqrt(f)));
        %f=fzero(f_fun,0.01);
    end
    P_out=(P_in*P_atm-f*rho/2*v^2/d*resolution)/P_atm;
    if P_out<0
        error('Negative Pressure 1st iteration')
    end
    h=PropsSI('H','T',T_in,'P',P_out*P_atm,'Hydrogen');
else
    rho=PropsSI('D','T',T_in,'P',P_old*P_atm,'Hydrogen');
    mu=PropsSI('V','T',T_in,'P',P_old*P_atm,'Hydrogen');
    v=m_dot/(pi*(d/2)^2*rho);
    Re=4*m_dot/(pi*mu*d);
    if Re<5000
        f=64/Re;
    else

f=0.094*(roughness/d)^0.225+0.53*roughness/d+88*(roughness/d)^0.44*Re^(-
1.62*(roughness/d)^0.134);
        %f_fun=@(f) 1/sqrt(f)+2*log10(roughness/(3.7*d)+2.51/(Re*sqrt(f)));
        %f=fzero(f_fun,0.01);
    end
    DP=f*rho/2*v^2/d*resolution/P atm;
    P_out=P_old-DP;
```

```
    if P_out<0
        error('Negative Pressure')
    end
    h=PropsSI('H','T',T_in,'P',P_out*P_atm,'Hydrogen');
end


T_out=PropsSI('T','H',h,'P',P_out*P_atm,'Hydrogen');

m_dot_out=m_dot;
end
```

D.3 Boost Turbine

```
function [P0_out,T0_out,N_thermal] =
Boost_turbine(T0_in,P0_in,Work_required,Q_env,w_rad,m_dot_in,n,P_ratio)
import py.CoolProp.CoolProp.PropsSI
P_atm=101325;
options = optimset('Display','off');


para_ratio=0;

s0_in_para=PropsSI('S','T',T0_in,'P',P0_in*P_atm,'parahydrogen');
s0_in_h=PropsSI('S','T',T0_in,'P',P0_in*P_atm,'Hydrogen');
h0_in=para_ratio*PropsSI('H','T',T0_in,'P',P0_in*P_atm,'parahydrogen')+(1-
para_ratio)*PropsSI('H','T',T0_in,'P',P0_in*P_atm,'hydrogen');
    P0_out=P0_in/P_ratio;
    para_ratio=0.002;
    h0_out=(Q_env-Work_required+m_dot_in*h0_in)/m_dot_in;
    h0_out_s_para=PropsSI('H','S',s0_in_para,'P',P0_out*P_atm,'parahydrogen');
    h0_out_s_h=PropsSI('H','S',s0_in_h,'P',P0_out*P_atm,'hydrogen');
    h0_out_s=para_ratio*h0_out_s_para+(1-para_ratio)*h0_out_s_h;
    N_thermal=(Work_required/m_dot_in)/(h0_in-h0_out_s);
    %T0_out=T0_in-T0_in*N*(1-(1/P_ratio)^((gamma-1)/gamma));

T0_out=para_ratio*PropsSI('T','P',P0_out*P_atm,'H',h0_out,'parahydrogen')+(1-
para_ratio)*PropsSI('T','P',P0_out*P_atm,'H',h0_out,'hydrogen');
```

D.4 Nozzle Temperature

```
function [T_N_out,T_N_in,T_new] =
Temp_dist_nozzle(T_previous,h_convective_cooling,h_convective,As_in,As_out,m_do
t,Cp,thickness,d,T_inside,K_nozzle,resolution)
%T(1)=T_N_out, T(2)=T_N_in, T(3)=T_solved
options = optimset('Display','off');
 T_fun=@(T) [T(1)-(T(1)-T_previous)*exp(-
h_convective_cooling*As_out/(m_dot*Cp))-T(3);

(2*pi*K_nozzle*resolution/(h_convective*As_in*log((d+thickness*2)/d))*T(1)+T_in
side)/(2*pi*K_nozzle*resolution/(h_convective*As_in*log((d+thickness*2)/d))+1)-
T(2);
        (T(3)-exp(h_convective_cooling*As_out*(T_previous-
T(3))/(h_convective*As_in*(T_inside-T(2))))*T_previous)/(1-
exp(h_convective_cooling*As_out*(T_previous-
T(3))/(h_convective*As_in*(T_inside-T(2)))))-T(1)];
T_guess=[T_previous+0.0001   T_previous+0.0001   T_previous+0.0001];
T_solved=fsolve(T_fun,T_guess,options)
T_N_out=T_solved(1);
T_N_in=T_solved(2);
T_new=T_solved(3);

end
```

D.5 Nozzle Exit Pressure

```
function [Pe] = Nozzle_Pe(m_dot,Te,Pe_s,Ae,Me)
import py.CoolProp.CoolProp.PropsSI
P_atm=101325;
Pe_s=Pe_s;
%Pe_fun=@(P) ((1-
mf_para_H2(Te,abs(P)))*PropsSI('D','T',Te,'P',abs(P)*P_atm,'Hydrogen')^-
1+mf_para_H2(Te,abs(P))*PropsSI('D','T',Te,'P',abs(P)*P_atm,'parahydrogen')^-
1)^-1-m_dot/(Ae*((1-
mf_para_H2(Te,abs(P)))*PropsSI('A','T',Te,'P',abs(P)*P_atm,'Hydrogen')+mf_para_
H2(Te,abs(P))*PropsSI('A','T',Te,'P',abs(P)*P_atm,'parahydrogen'))*Me);
Pe_fun=@(P) PropsSI('D','T',Te,'P',abs(P)*P_atm,'Hydrogen')-
m_dot/(Ae*PropsSI('A','T',Te,'P',abs(P)*P_atm,'Hydrogen')*Me);
Pe=abs(fzero(Pe_fun,Pe_s));

end
```

APPENDIX E

Nozzle Thermal Equation Derivation

This appendix provides the derivation of equations E.1 and E.2. E.3 is a basic equation for the exit temperature of a fluid inside a duct. These three equations must be solved simultaneously to provide the temperatures on the inside and outside of the nozzle as well as the temperature of the fluid inside the cooling channels given the temperature of the plume inside the nozzle. The subscript *c* refers to the coolant inside the coolant channels, subscript *p* refers to the plume, subscript *o* refers to the outside of the nozzle incident to the coolant flow, and subscript *in* refers to the inside of the nozzle incident to the plume flow. T_i and T_e are the temperatures of the coolant that enter and exit the position inside the coolant channels that these three equations were solved respectively.

$$T_o = \frac{T_e \exp\left[\hbar_p A_{s_i}\left(T_p - T_i\right) + \hbar_c A_{s_o}(T_e - T_{in})\right] - T_{in}}{\exp\left[\hbar_p A_{s_i}\left(T_p - T_i\right) + \hbar_c A_{s_o}(T_e - T_{in})\right] - 1} \tag{E.1}$$

$$T_i = \frac{2\pi KLT_o + T_p \hbar_p A_{s_i}\, ln\left(\frac{d + 2t_n}{d}\right)}{2\pi KL + \hbar_p A_{s_i}\, ln\left(\frac{d + 2t_n}{d}\right)} \tag{E.2}$$

$$T_e = T_o - (T_o - T_{in})\exp\left(-\frac{\hbar_c A_{s_o}}{\dot{m} c_p}\right) \tag{E.3}$$

This derivation begins by taking the heat transfer from the plume to the inside of the nozzle (E.4) and equating it to the heat transfer from the inside of the nozzle to the outside of the nozzle (coolant channel surface) (E.5). The goal is to solve for the temperature of the inside of the nozzle with the algebraic simplification steps detailed in equations E.6a through E.6d. In these equations, *K* is the thermal conductivity of the nozzle material and *L* is the length of the "slice" of the nozzle under consideration. In the engine

analysis, this length was arbitrarily chosen to be 1 mm to provide high resolution and a finite number of iterations. This derivation is independent of this value.

$$\dot{Q} = \hbar_p A_{s_i}(T_p - T_i) \tag{E.4}$$

$$\dot{Q} = 2\pi KL \frac{T_i - T_o}{\ln\left(\frac{d + 2t_n}{d}\right)} \tag{E.5}$$

$$2\pi KL \frac{T_i - T_o}{ln\left(\frac{d + 2t_n}{d}\right)} = \hbar_p A_{s_i}(T_p - T_i) \tag{E.6a}$$

$$T_i - T_o = \frac{\hbar_p A_{s_i}}{2\pi KL} ln\left(\frac{d + 2t_n}{d}\right) T_p - \frac{\hbar_p A_{s_i}}{2\pi KL} ln\left(\frac{d + 2t_n}{d}\right) T_i \tag{E.6b}$$

$$T_o + \frac{\hbar_p A_{s_i}}{2\pi KL} ln\left(\frac{d + 2t_n}{d}\right) T_p = T_i \left[1 + \frac{\hbar_p A_{s_i}}{2\pi KL} ln\left(\frac{d + 2t_n}{d}\right)\right] \tag{E.6c}$$

$$T_i = \frac{T_o + \frac{\hbar_p A_{s_i}}{2\pi KL} ln\left(\frac{d + 2t_n}{d}\right) T_p}{1 + \frac{\hbar_p A_{s_i}}{2\pi KL} ln\left(\frac{d + 2t_n}{d}\right)} \tag{E.6d}$$

$$T_i = \frac{2\pi KL T_o + T_p \hbar_p A_{s_i} ln\left(\frac{d + 2t_n}{d}\right)}{2\pi KL + \hbar_p A_{s_i} ln\left(\frac{d + 2t_n}{d}\right)} \tag{E.6e}$$

Equation E.6e is equation E.2 and this finishes the derivation. The next derivation involves setting the heat transferred from the plume (E.4) equal to the heat absorbed by the coolant (E.7) and solving for the temperature of the outside of the nozzle (surface temperature of the coolant channels). The steps for the algebraic simplification are provided in equations E.8a through E.8e.

$$\dot{Q} = \hbar_c A_{s_o} \frac{T_{in} - T_e}{\ln\left(\frac{T_o - T_e}{T_o - T_{in}}\right)} \tag{E.7}$$

$$\hbar_p A_{s_i}(T_p - T_i) = \hbar_c A_{s_o} \frac{T_{in} - T_e}{\ln\left(\frac{T_o - T_e}{T_o - T_{in}}\right)} \tag{E.8a}$$

$$\exp\left[\ln\left(\frac{T_o - T_e}{T_o - T_{in}}\right)\right] = \exp\left[\frac{-\hbar_c A_{s_o}(T_e - T_{in})}{\hbar_p A_{s_i}(T_p - T_i)}\right] \tag{E.8b}$$

$$T_o - T_e = T_o \exp\left[\frac{\hbar_c A_{s_o}(T_{in} - T_e)}{\hbar_p A_{s_i}(T_p - T_i)}\right] - T_{in} \exp\left[\frac{-\hbar_c A_{s_o}(T_e - T_{in})}{\hbar_p A_{s_i}(T_p - T_i)}\right] \tag{E.8c}$$

$$T_o = \frac{T_e - T_{in} \exp\left[\frac{-\hbar_c A_{s_o}(T_e - T_{in})}{\hbar_p A_{s_i}(T_p - T_i)}\right]}{1 - \exp\left[\frac{-\hbar_c A_{s_o}(T_e - T_{in})}{\hbar_p A_{s_i}(T_p - T_i)}\right]} = \frac{T_e - T_{in} \frac{\exp\left[-\hbar_c A_{s_o}(T_e - T_{in})\right]}{\exp\left[\hbar_p A_{s_i}(T_p - T_i)\right]}}{1 - \frac{\exp\left[-\hbar_c A_{s_o}(T_e - T_{in})\right]}{\exp\left[\hbar_p A_{s_i}(T_p - T_i)\right]}} \tag{E.8d}$$

$$T_o = \frac{T_e \exp\left[\hbar_p A_{s_i}(T_p - T_i) + \hbar_c A_{s_o}(T_e - T_{in})\right] - T_{in}}{\exp\left[\hbar_p A_{s_i}(T_p - T_i) + \hbar_c A_{s_o}(T_e - T_{in})\right] - 1} \tag{E.8e}$$

Equation E.8e is equation E.1 and this finishes the derivation. Equation E.3, like all the other equations that were used in this derivation, was taken from an engineering heat transfer textbook [45], therefore, its derivation is not shown.

APPENDIX F

Seed Pump Performance Graphs

F.1 Argon

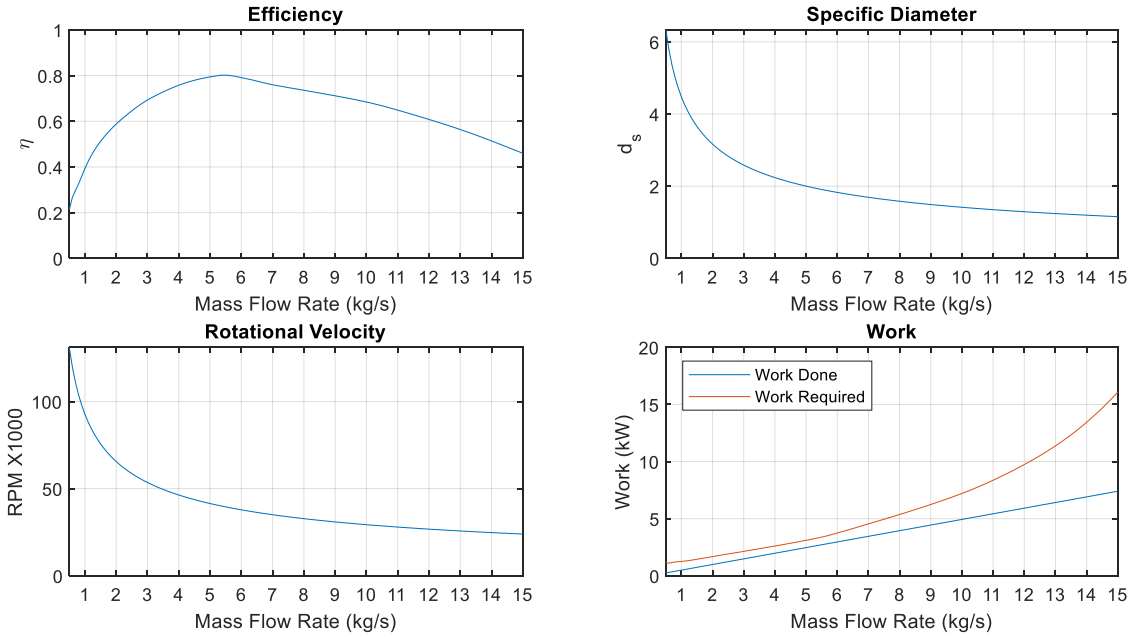

Figure F.1.1: Boost Seed Pump with Argon

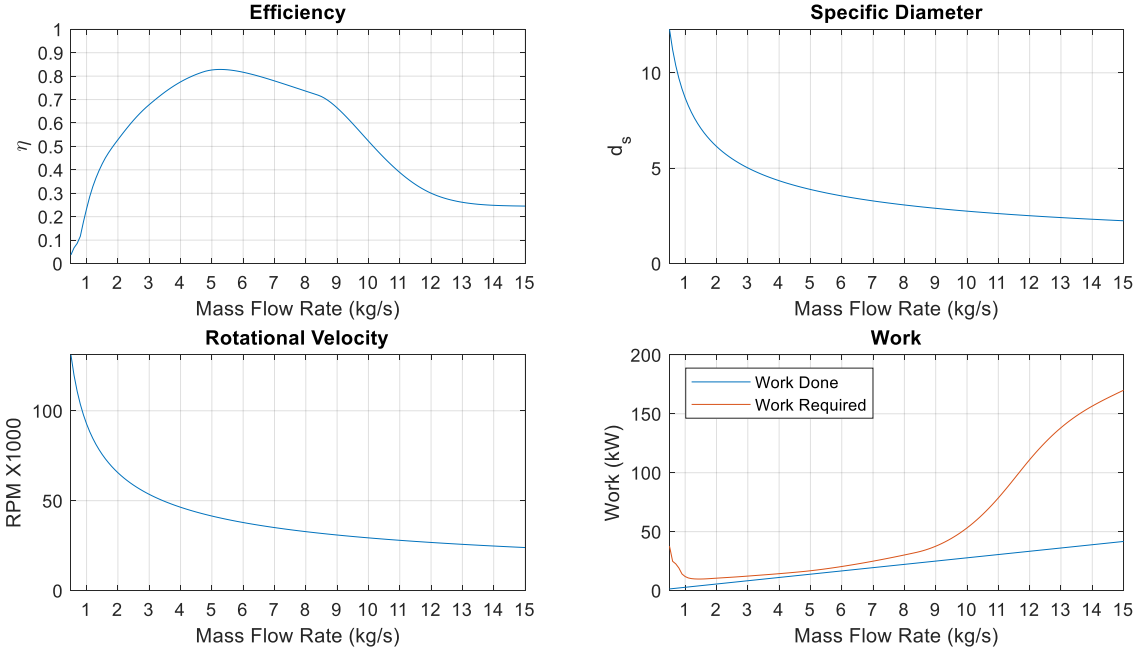

Figure F.1.2: Main Seed Pump 1 with Argon

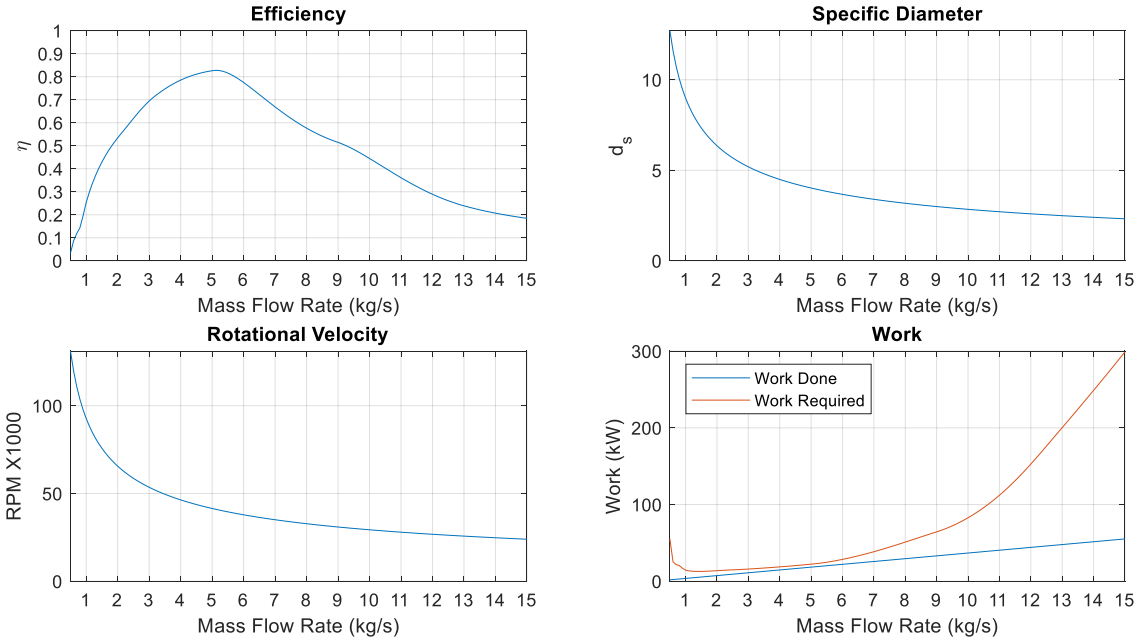

Figure F.1.3: Main Seed Pump 2 with Argon

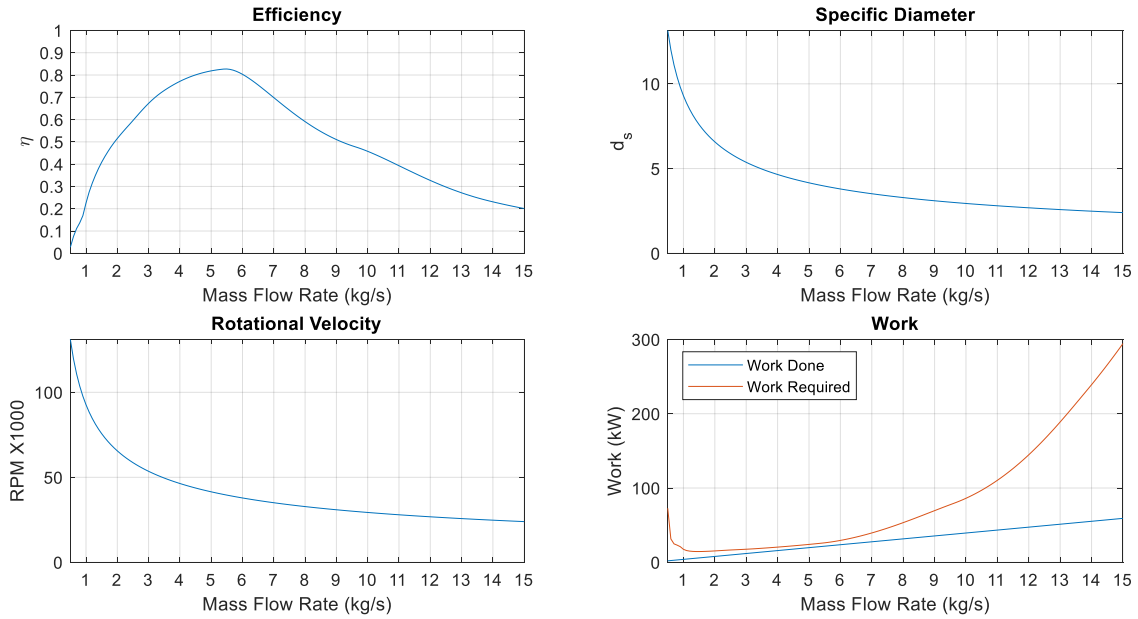

Figure F.1.4: Main Seed Pump 3 with Argon

F.2 Krypton

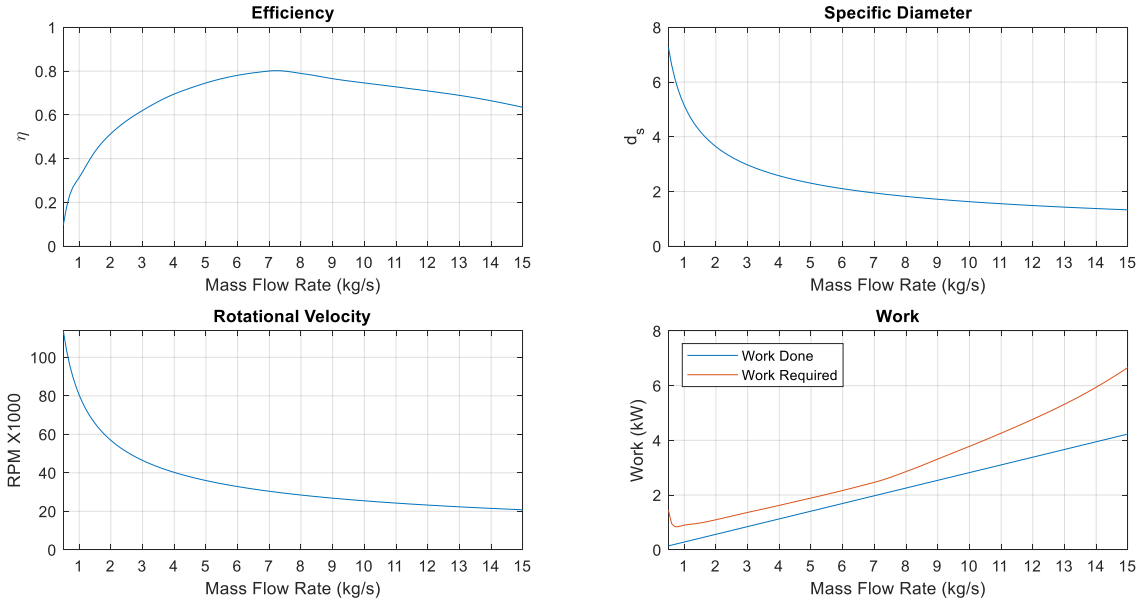

Figure F.2.1: Boost Seed Pump with Krypton

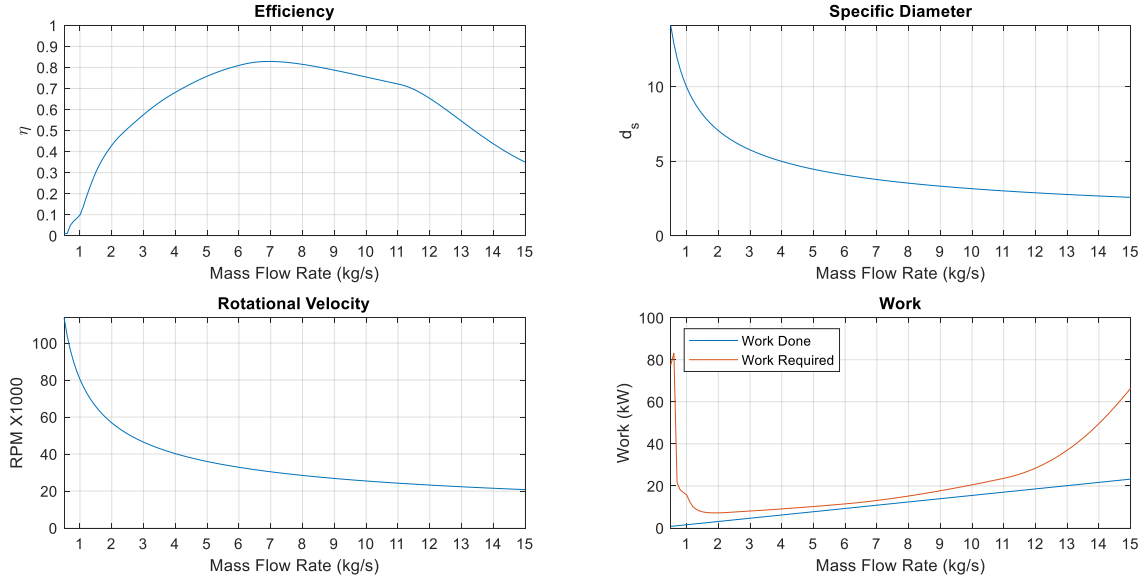

Figure F.2.2: Main Seed Pump 1 with Krypton

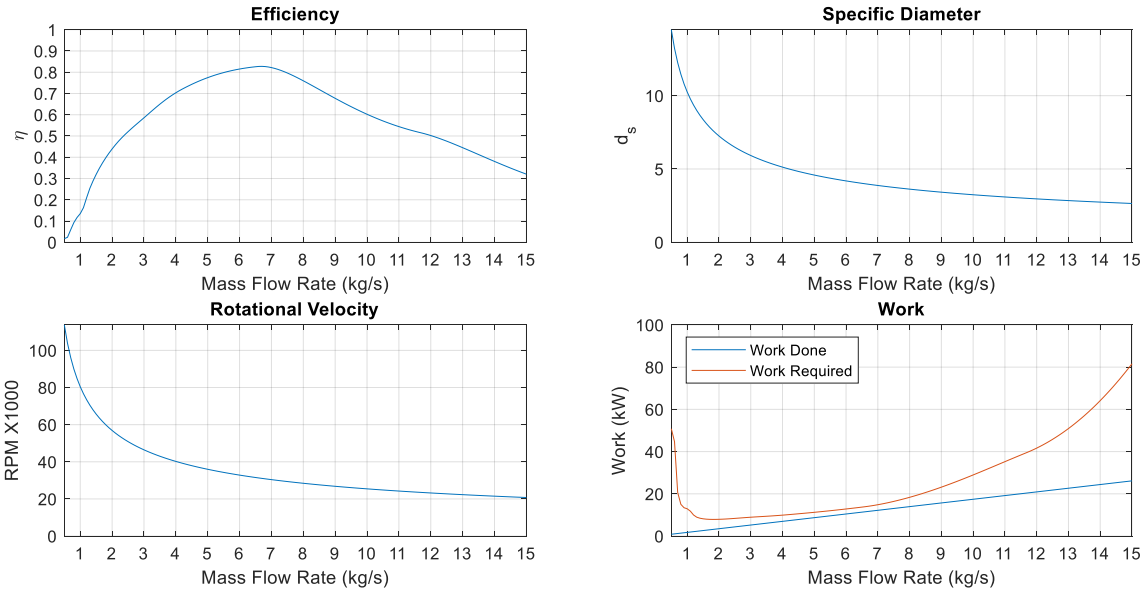

Figure F.2.3: Main Seed Pump 2 with Krypton

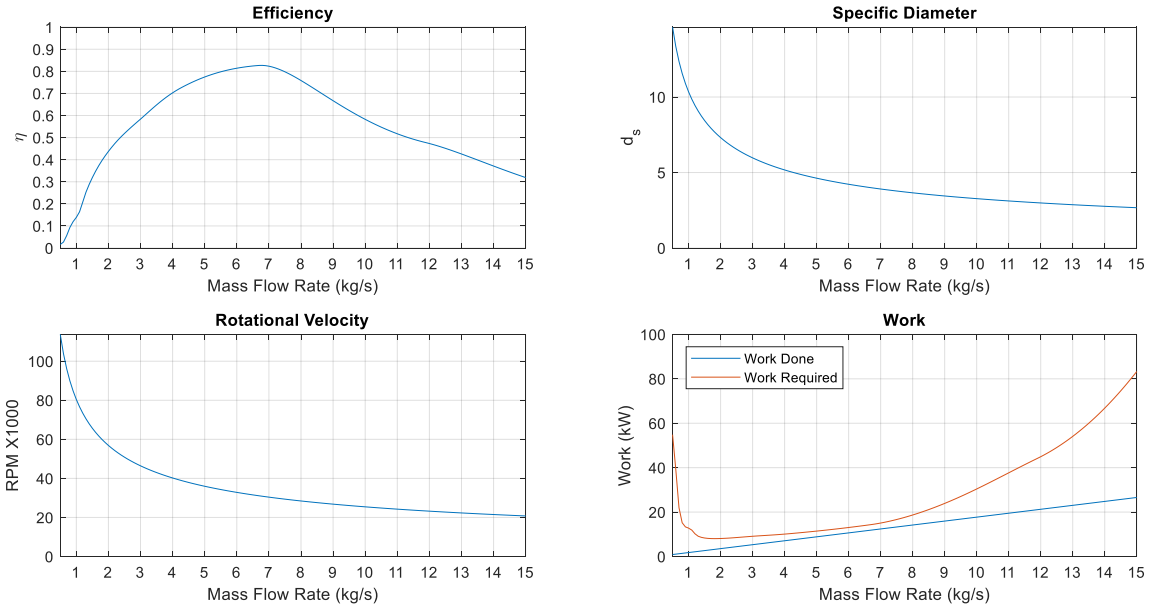

Figure F.2.4: Main Seed Pump 3 with Krypton

F.3 Xenon

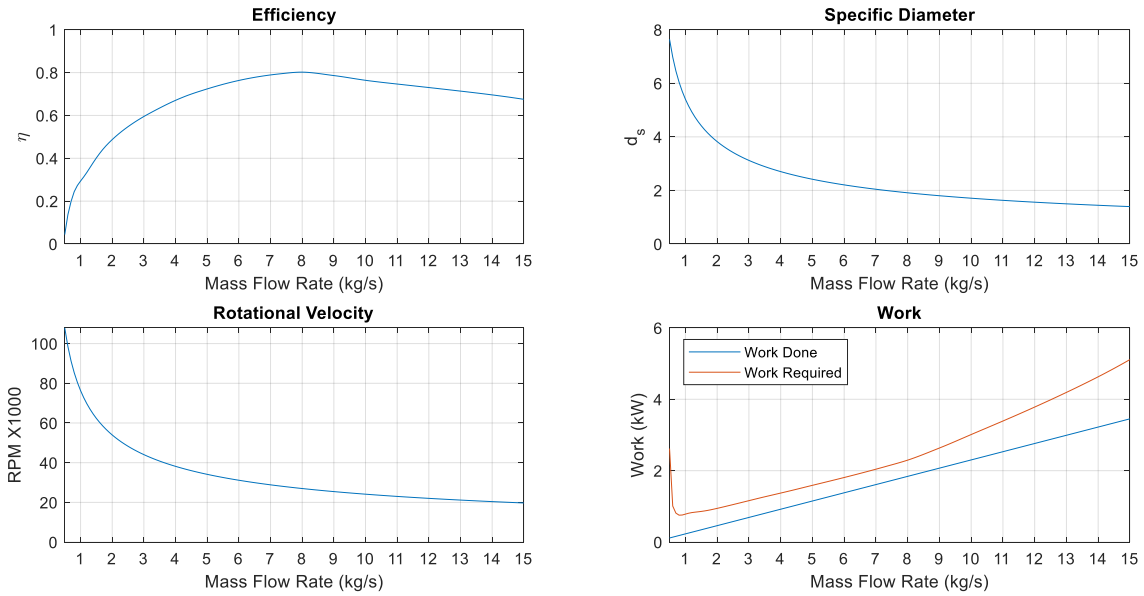

Figure F.3.1: Boost Seed Pump with Xenon

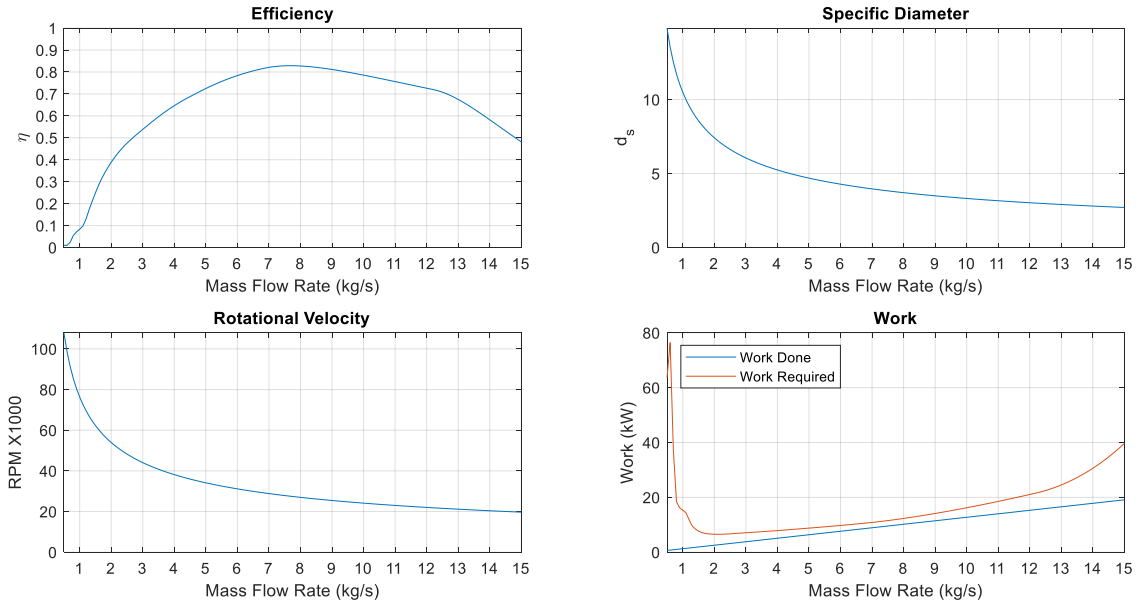

Figure F.3.2: Main Seed Pump 1 with Xenon

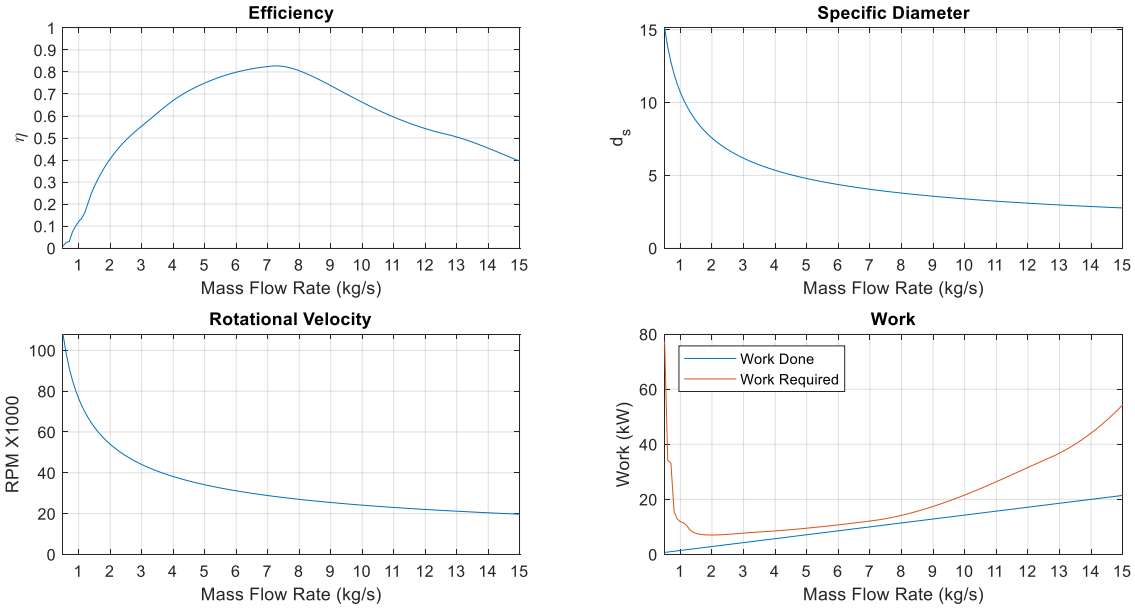

Figure F.3.3: Main Seed Pump 2 with Xenon

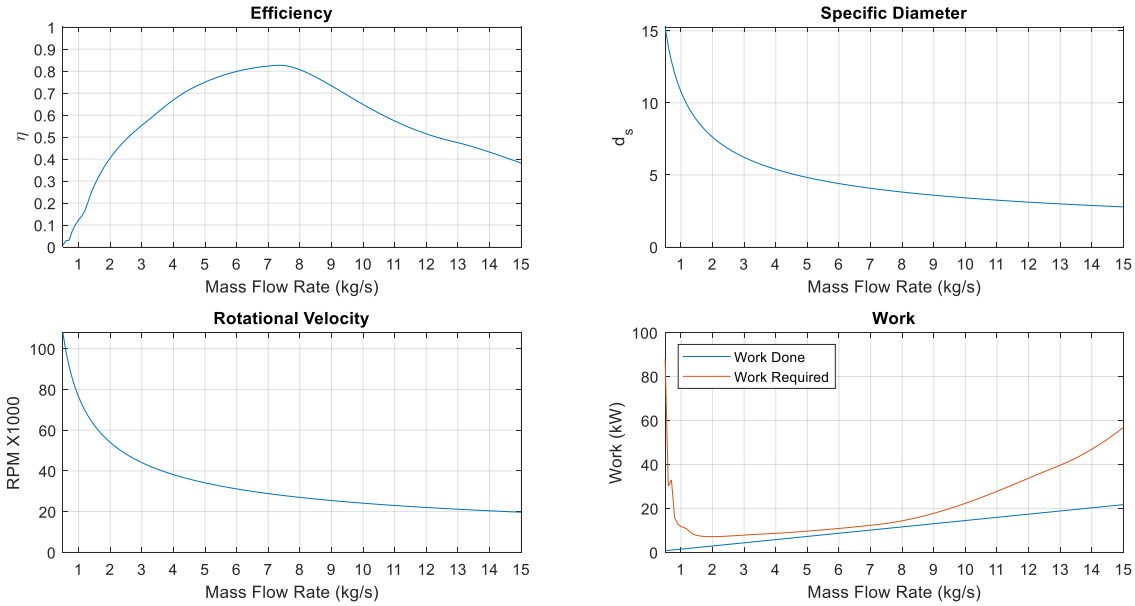

Figure F.3.4: Main Seed Pump 3 with Xenon

APPENDIX G

Seeded Hydrogen Properties

G.1 Hydrogen Seeded with Argon

G.1.1 H2 Seeded with Ar: Density at Various Concentrations

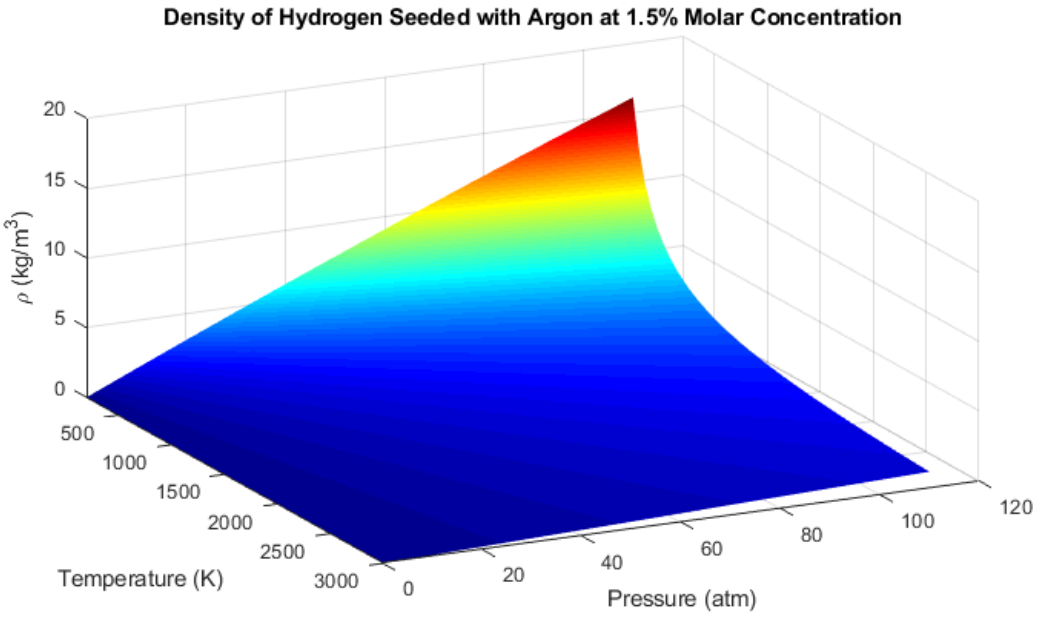

Figure G.1.1.1: Density of H_2 Seeded with Ar at 1.5% Molar Concentration

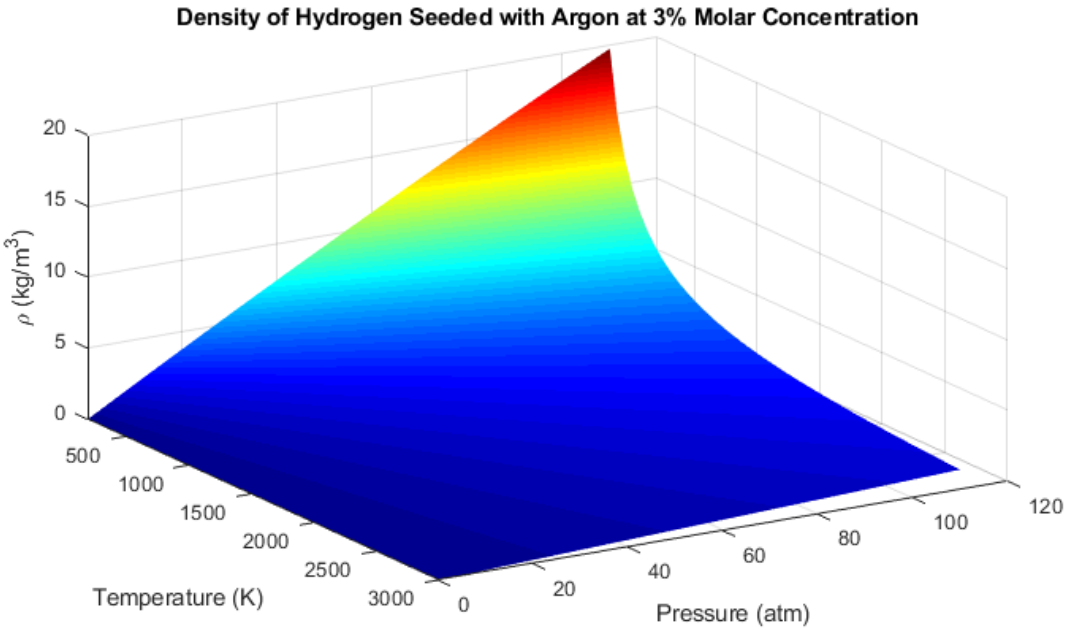

Figure G.1.1.2: Density of H_2 Seeded with Ar at 3% Molar Concentration

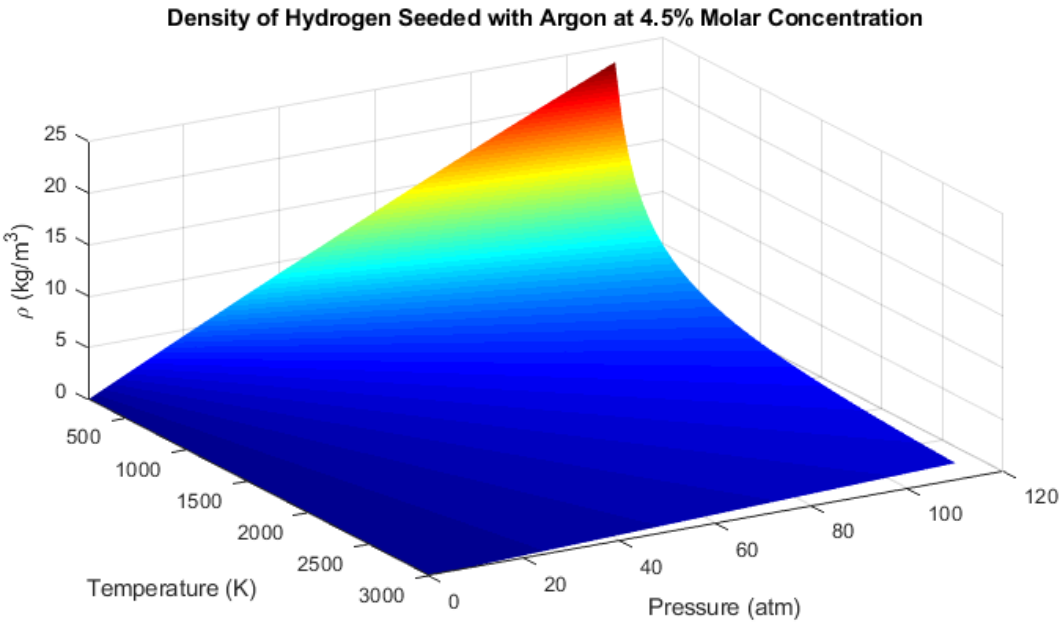

Figure G.1.1.3: Density of H_2 Seeded with Ar at 4.5% Molar Concentration

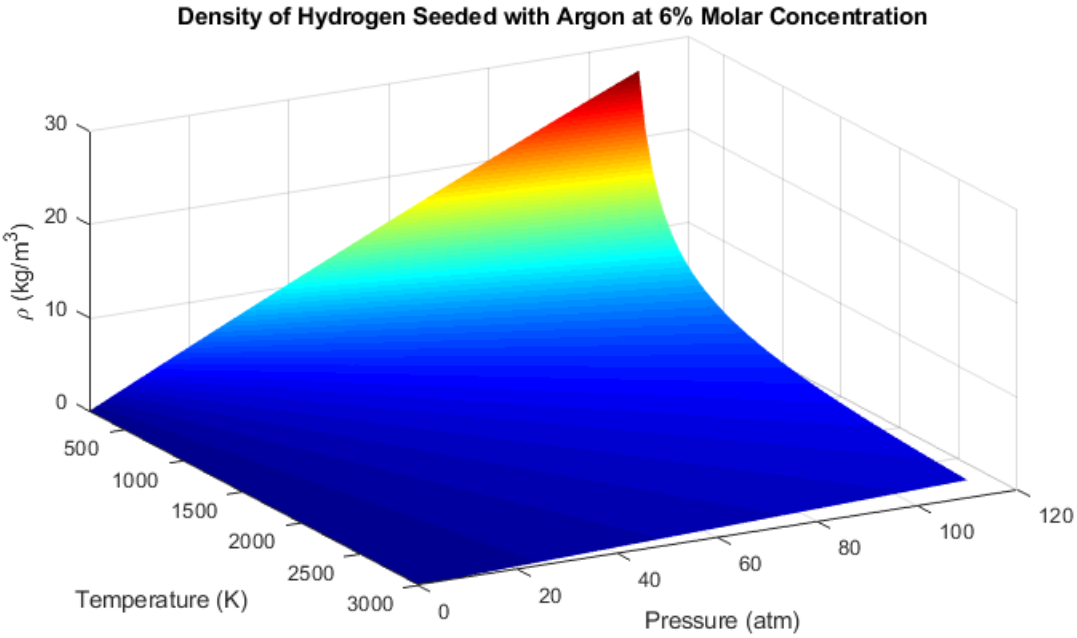

Figure G.1.1.4: Density of H_2 Seeded with Ar at 6% Molar Concentration

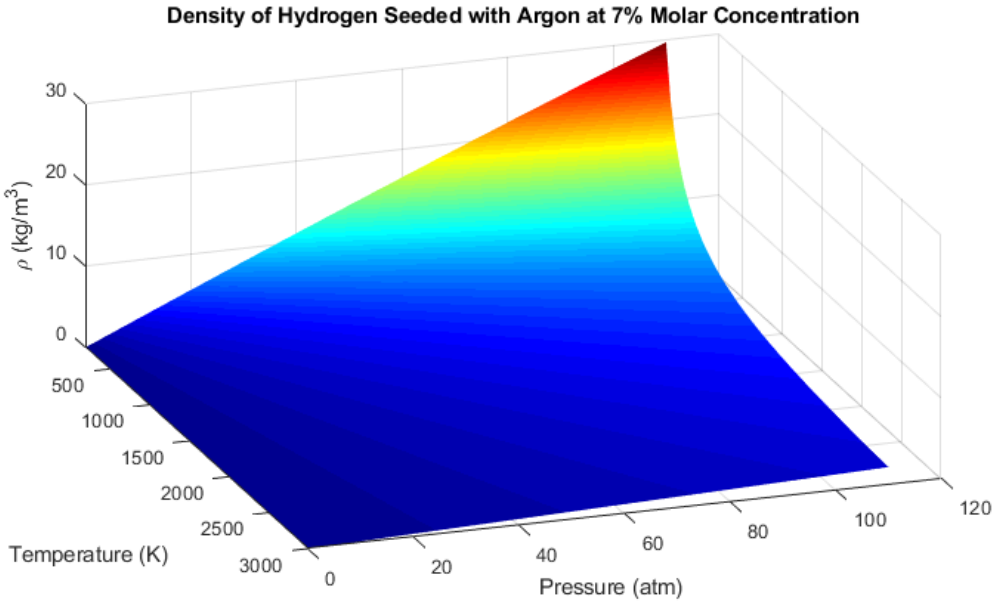

Figure G.1.1.5: Density of H_2 Seeded with Ar at 7% Molar Concentration

G.1.2 H2 Seeded with Ar: Specific Heat Capacity at Various Concentrations

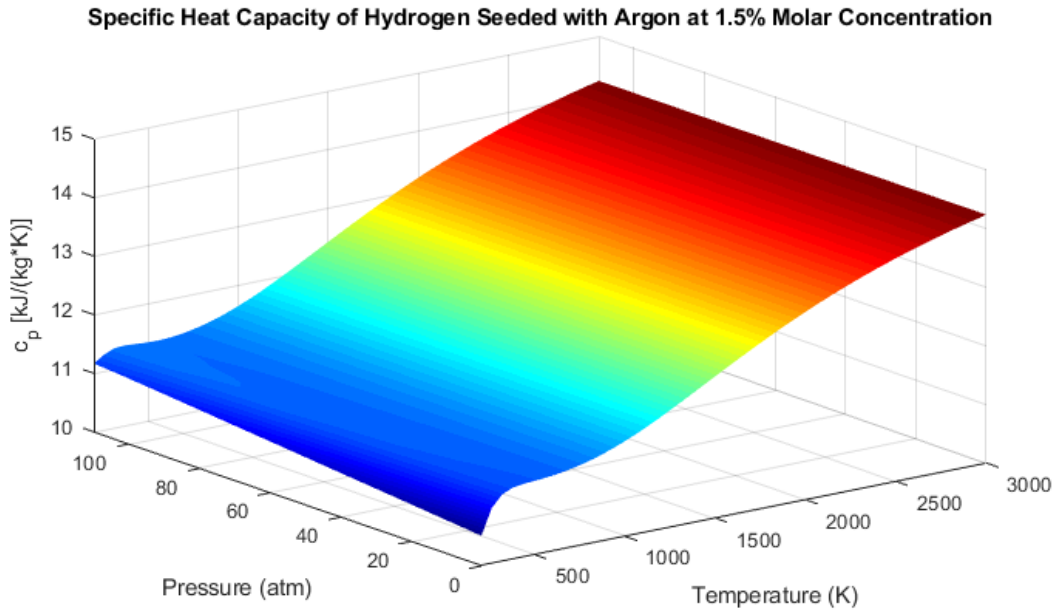

Figure G.1.2.1: Specific Heat Capacity of H_2 Seeded with Ar at 1.5% Molar Concentration

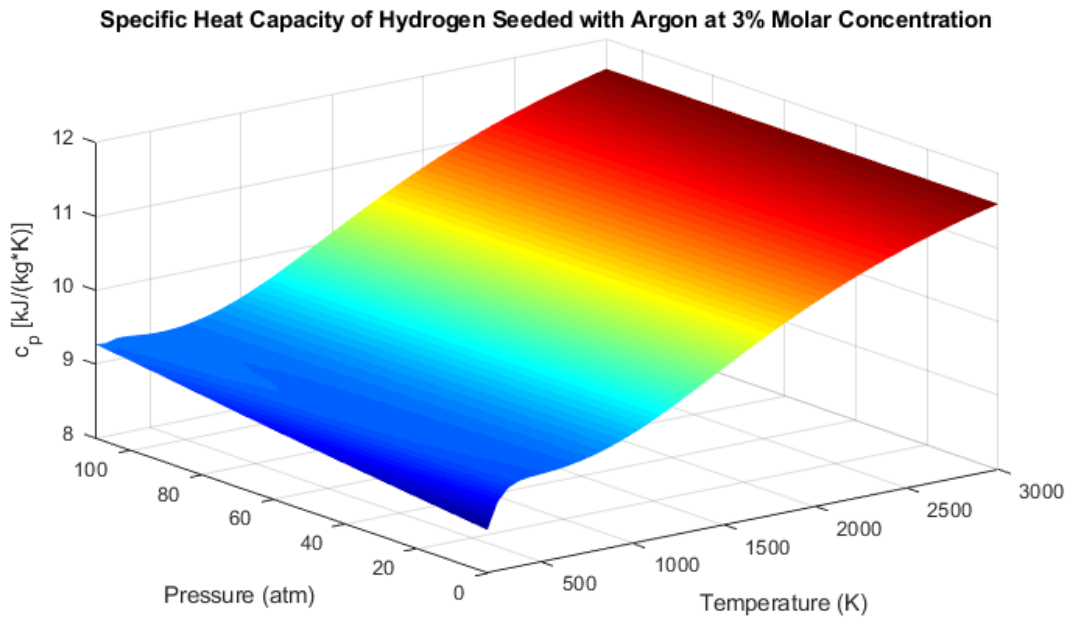

Figure G.1.2.2: Specific Heat Capacity of H_2 Seeded with Ar at 3% Molar Concentration

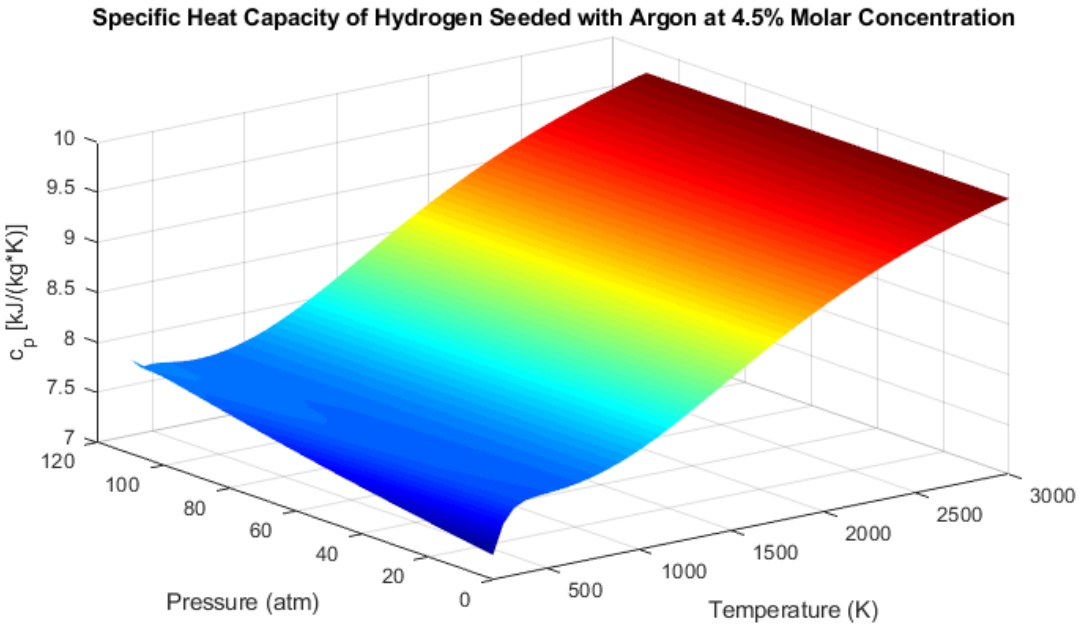

Figure G.1.2.3: Specific Heat Capacity of H_2 Seeded with Ar at 4.5% Molar Concentration

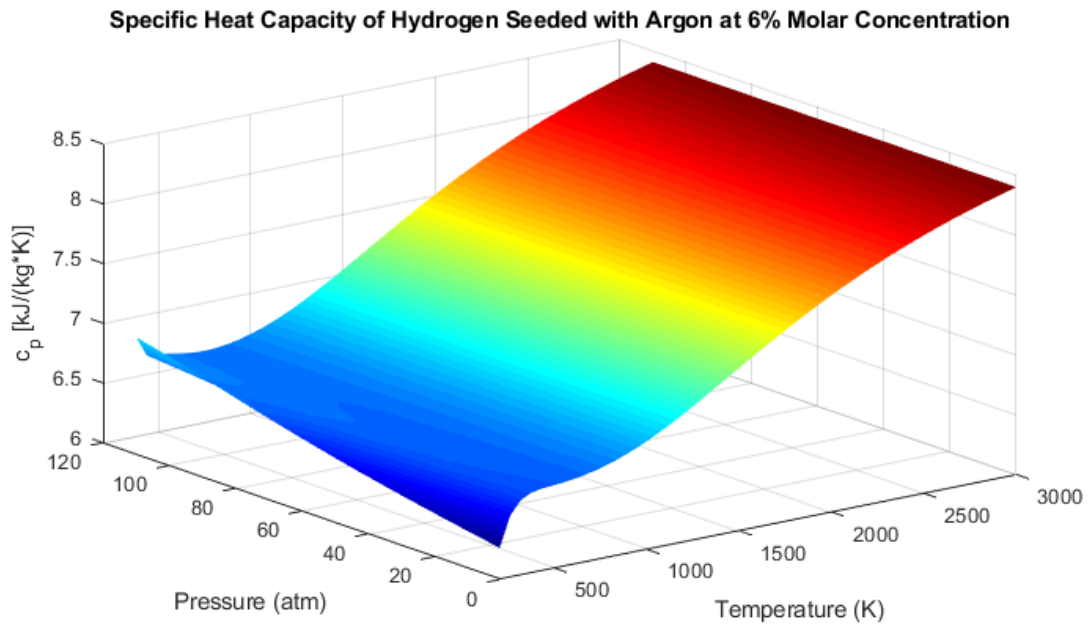

Figure G.1.2.4: Specific Heat Capacity of H_2 Seeded with Ar at 6% Molar Concentration

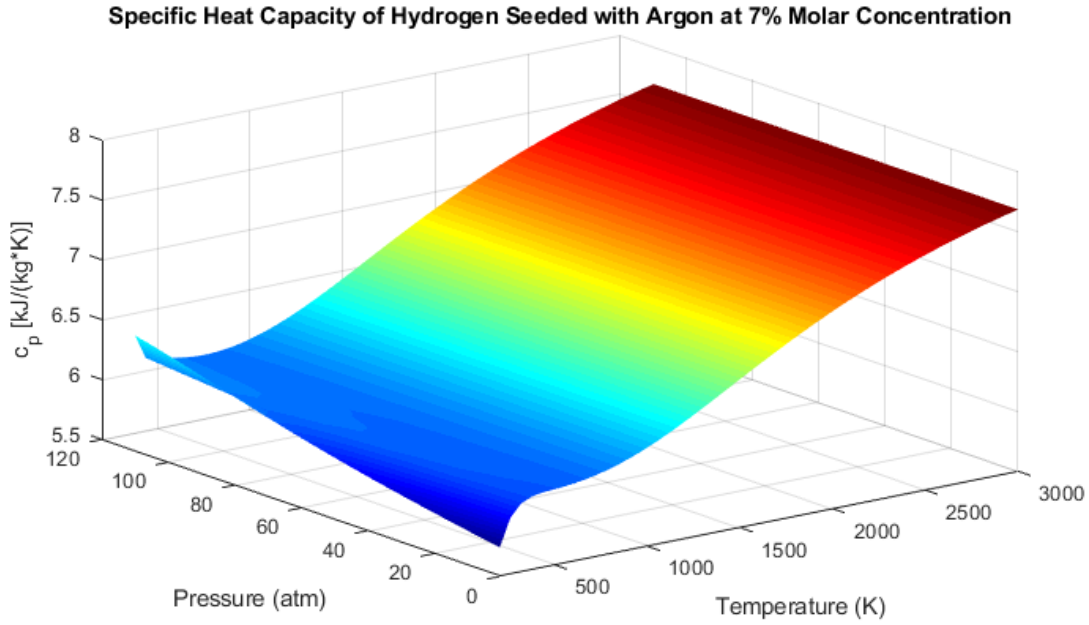

Figure G.1.2.5: Specific Heat Capacity of H_2 Seeded with Ar at 7% Molar Concentration

G.1.3 H2 Seeded with Ar: Viscosity at Various Concentrations

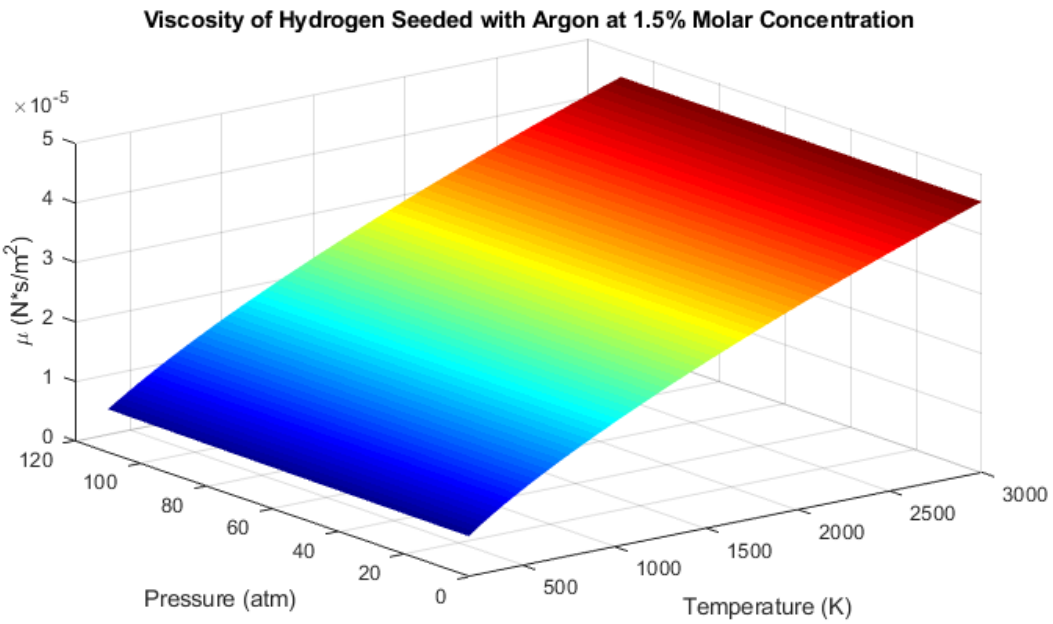

Figure G.1.3.1: Viscosity of H_2 Seeded with Ar at 1.5% Molar Concentration

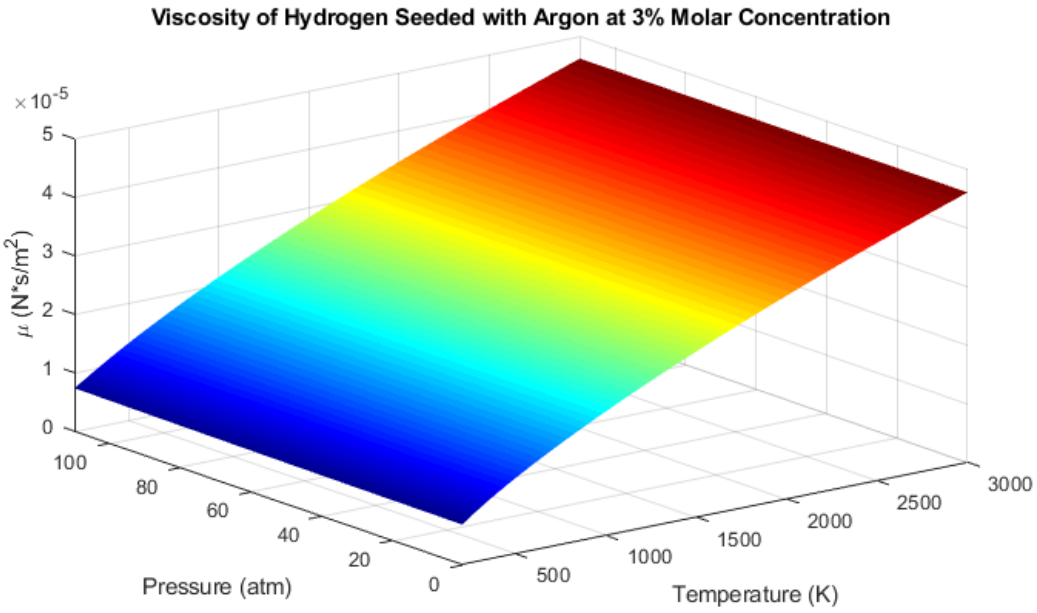

Figure G.1.3.2: Viscosity of H_2 Seeded with Ar at 3% Molar Concentration

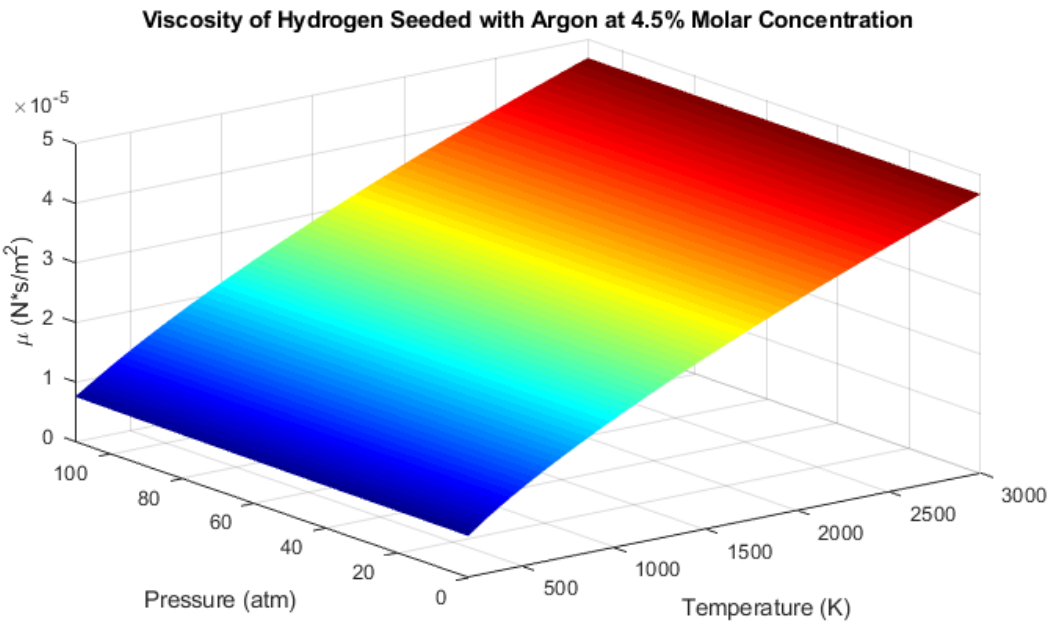

Figure G.1.3.3: Viscosity of H_2 Seeded with Ar at 4.5% Molar Concentration

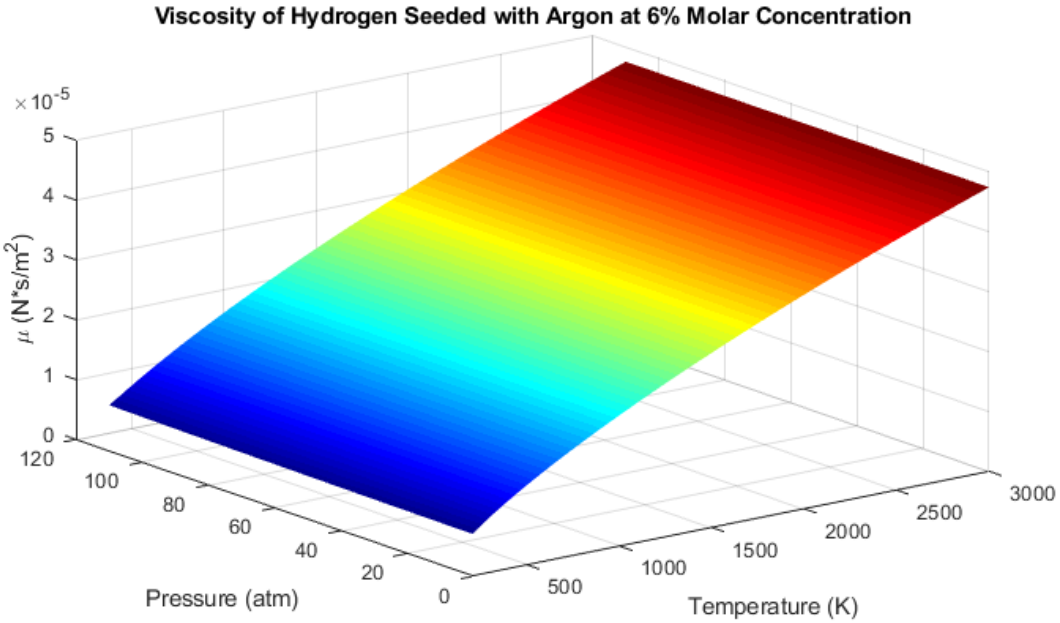

Figure G.1.3.4: Viscosity of H_2 Seeded with Ar at 6% Molar Concentration

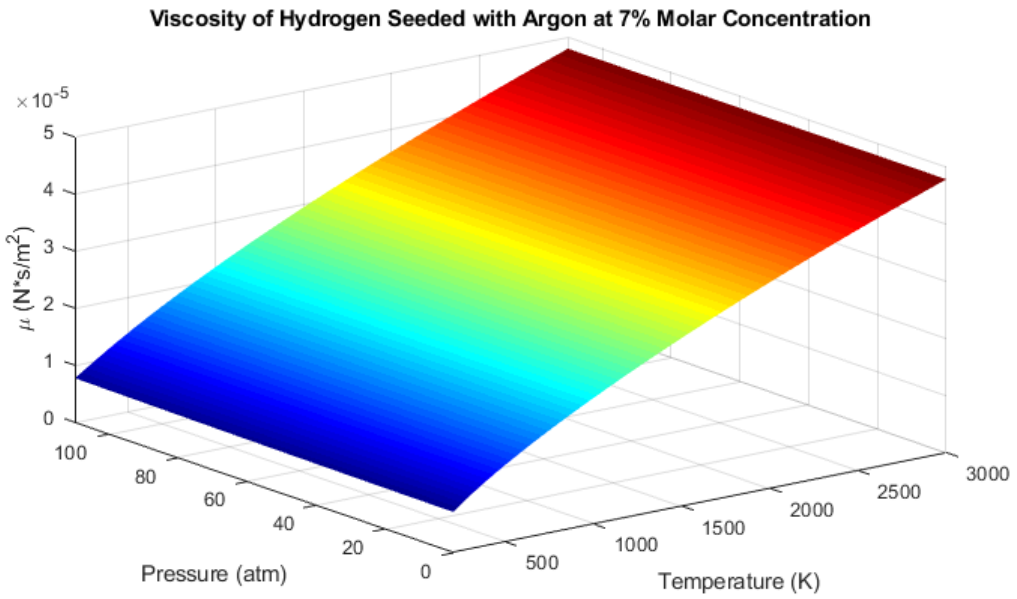

Figure G.1.3.5: Viscosity of H_2 Seeded with Ar at 7% Molar Concentration

G.1.4 H2 Seeded with Ar: Thermal Conductivity at Various Concentrations

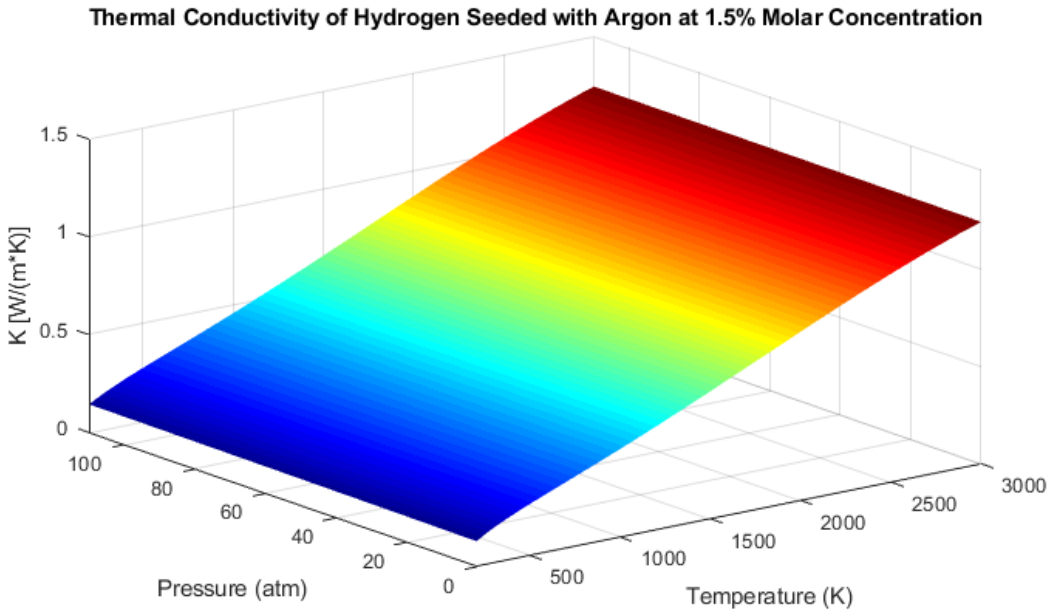

Figure G.1.4.1: Thermal Conductivity of H_2 Seeded with Ar at 1.5% Molar Concentration

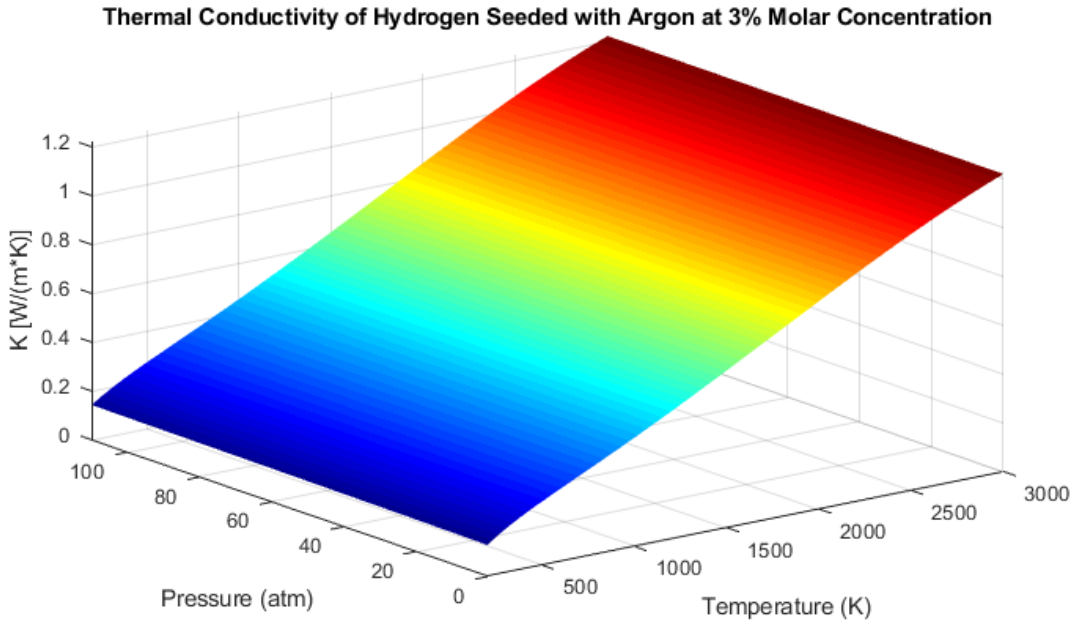

Figure G.1.4.2: Thermal Conductivity of H_2 Seeded with Ar at 3% Molar Concentration

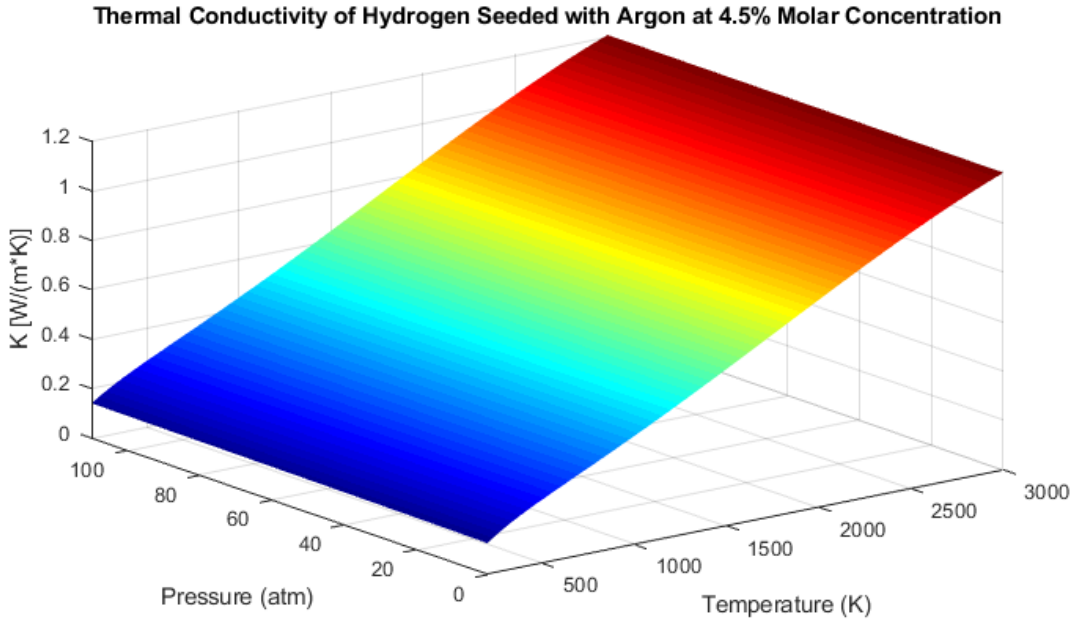

Figure G.1.4.3: Thermal Conductivity of H_2 Seeded with Ar at 4.5% Molar Concentration

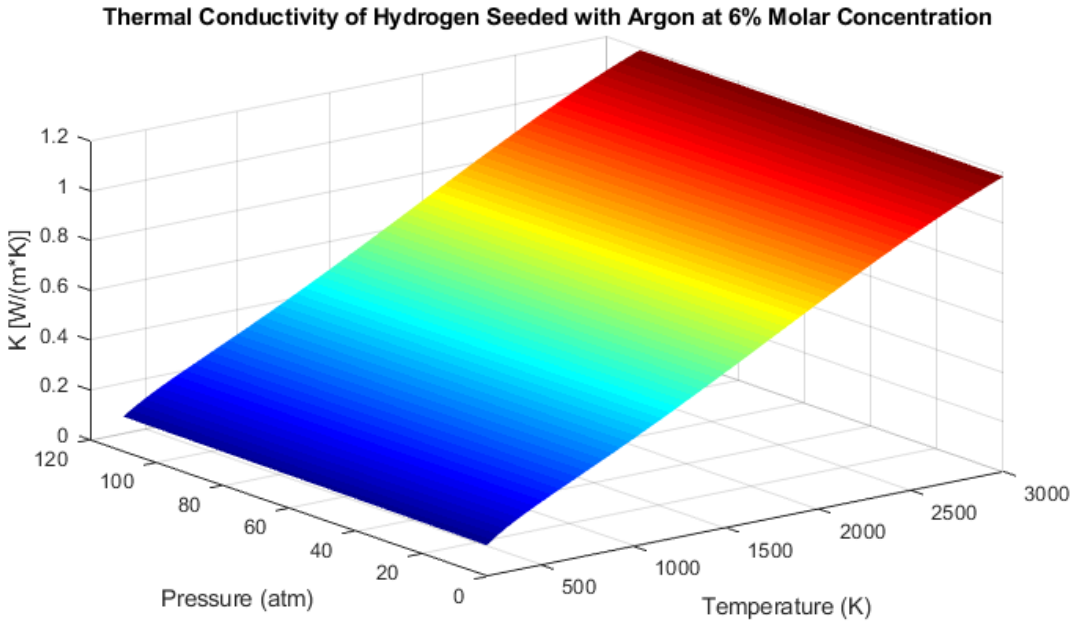

Figure G.1.4.4: Thermal Conductivity of H_2 Seeded with Ar at 6% Molar Concentration

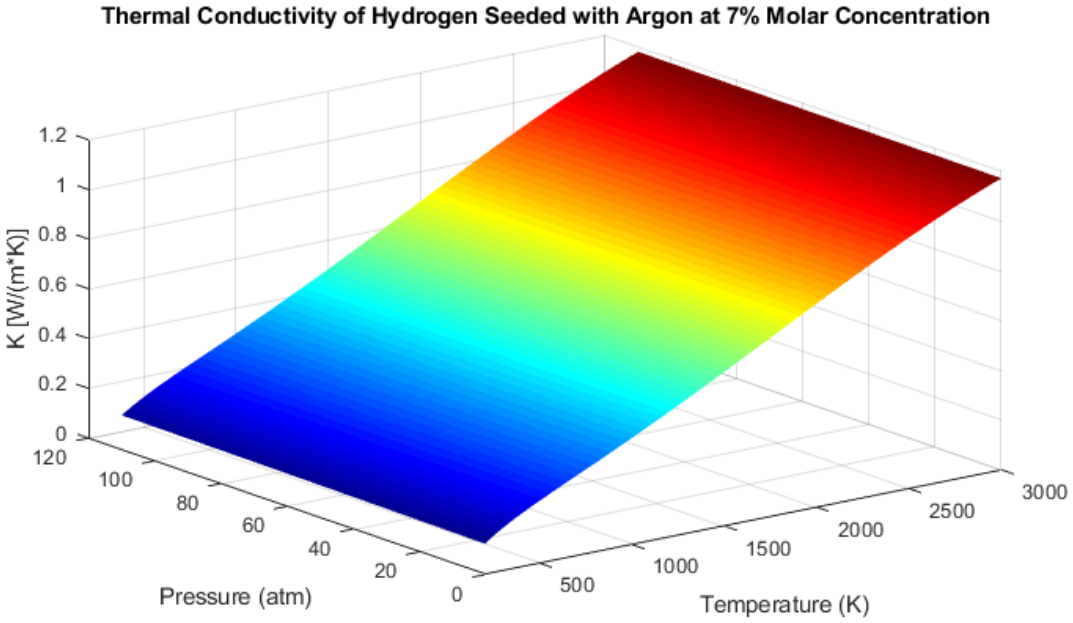

Figure G.1.4.5: Thermal Conductivity of H_2 Seeded with Ar at 7% Molar Concentration

G.2 Hydrogen Seeded with Krypton

G.2.1 H2 Seeded with Kr: Density at Various Concentrations

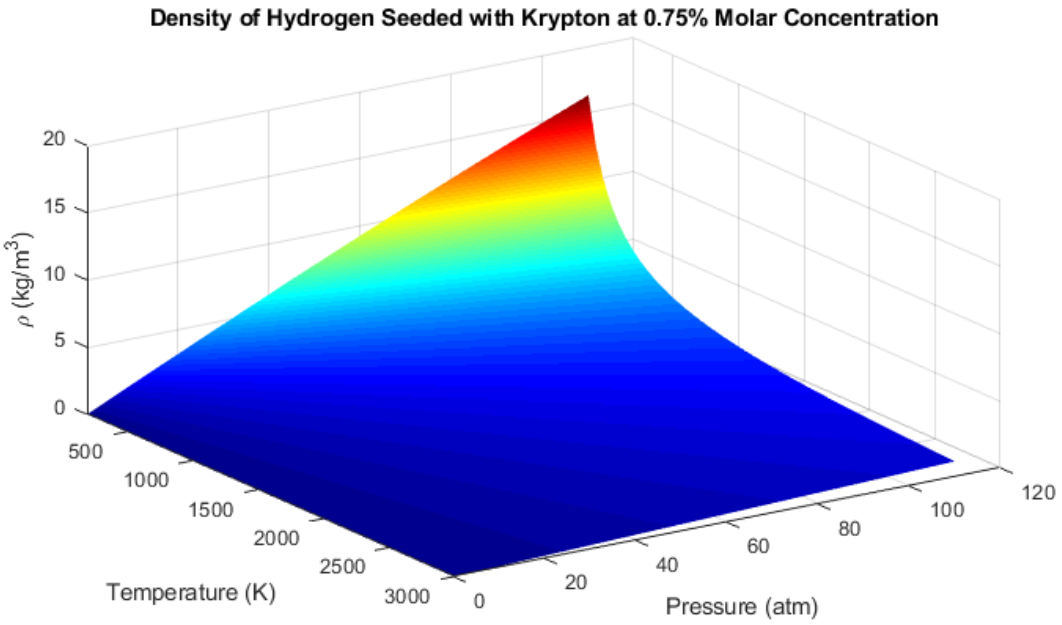

Figure G.2.1.1: Density of H_2 Seeded with Kr at 0.75% Molar Concentration

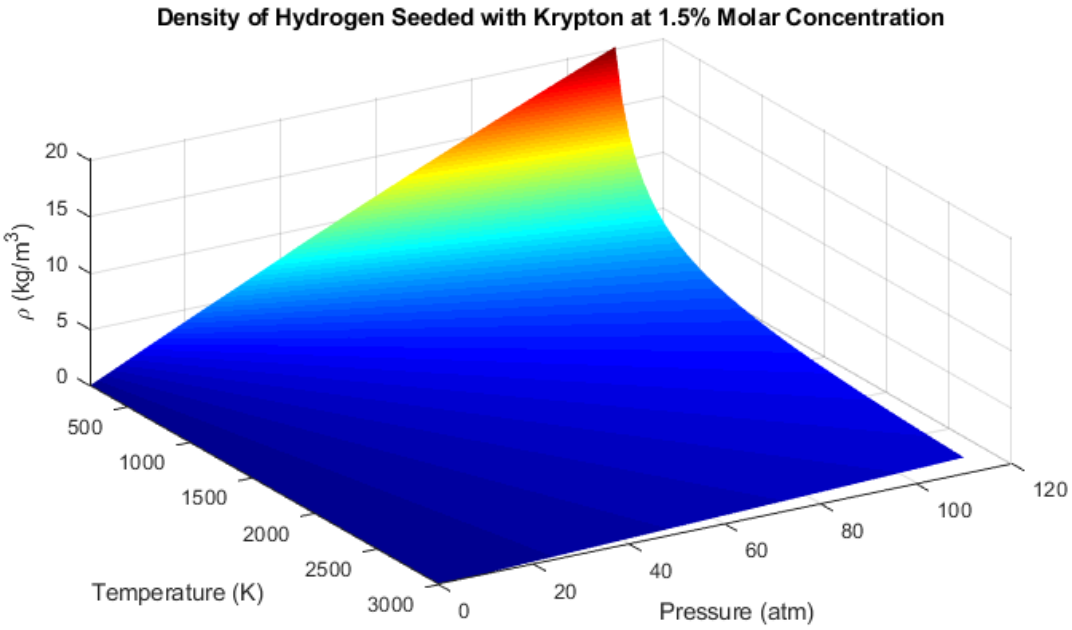

Figure G.2.1.2: Density of H_2 Seeded with Kr at 1.5% Molar Concentration

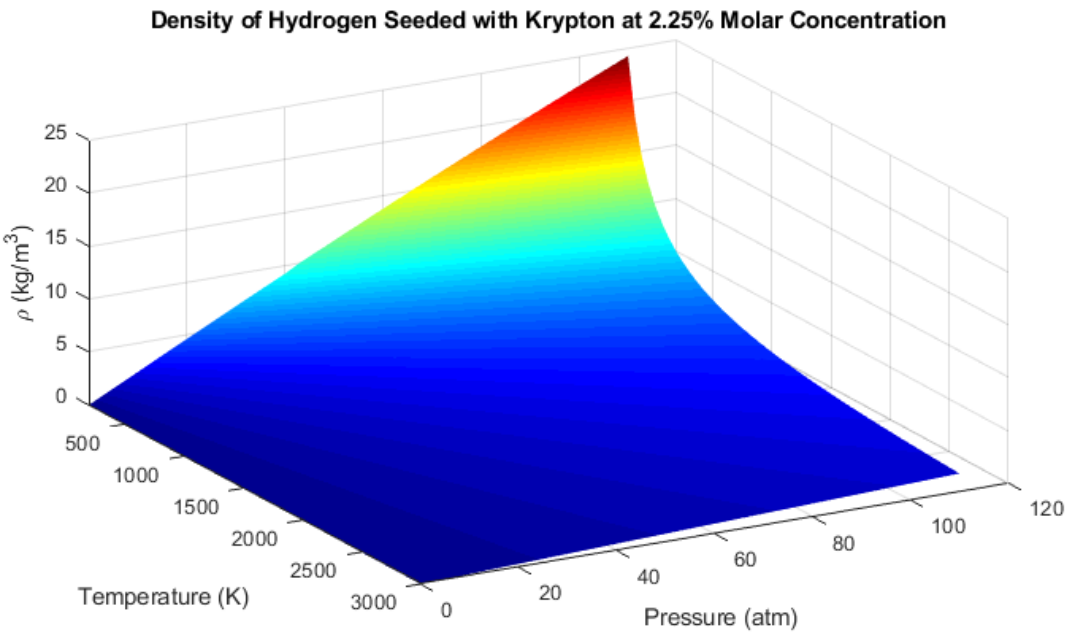

Figure G.2.1.3: Density of H_2 Seeded with Kr at 2.25% Molar Concentration

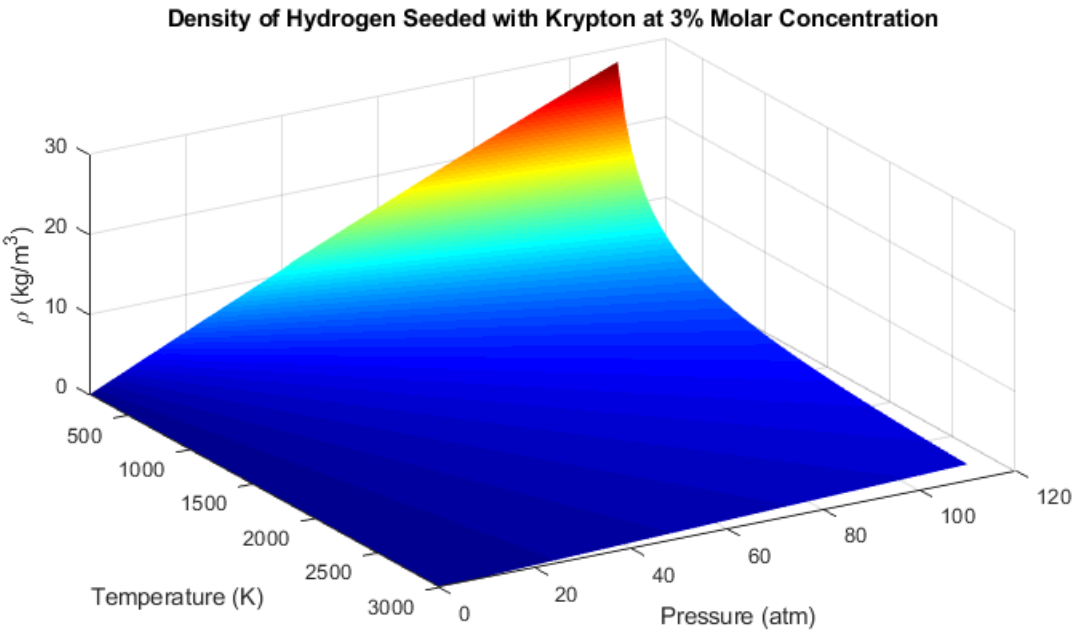

Figure G.2.1.4: Density of H_2 Seeded with Kr at 3% Molar Concentration

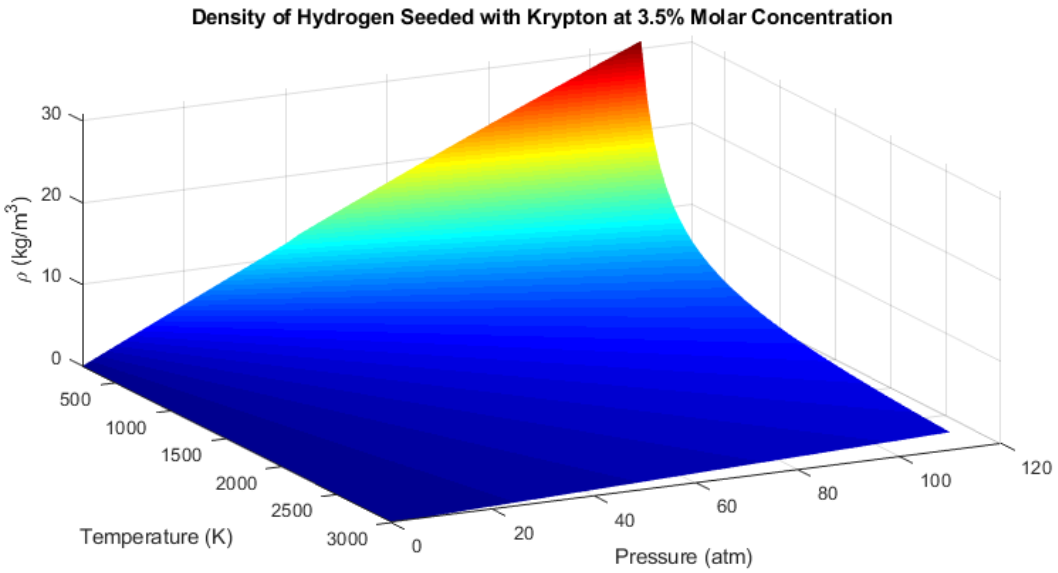

Figure G.2.1.5: Density of H_2 Seeded with Kr at 3.5% Molar Concentration

G.2.2 H2 Seeded with Kr: Specific Heat Capacity at Various Concentrations

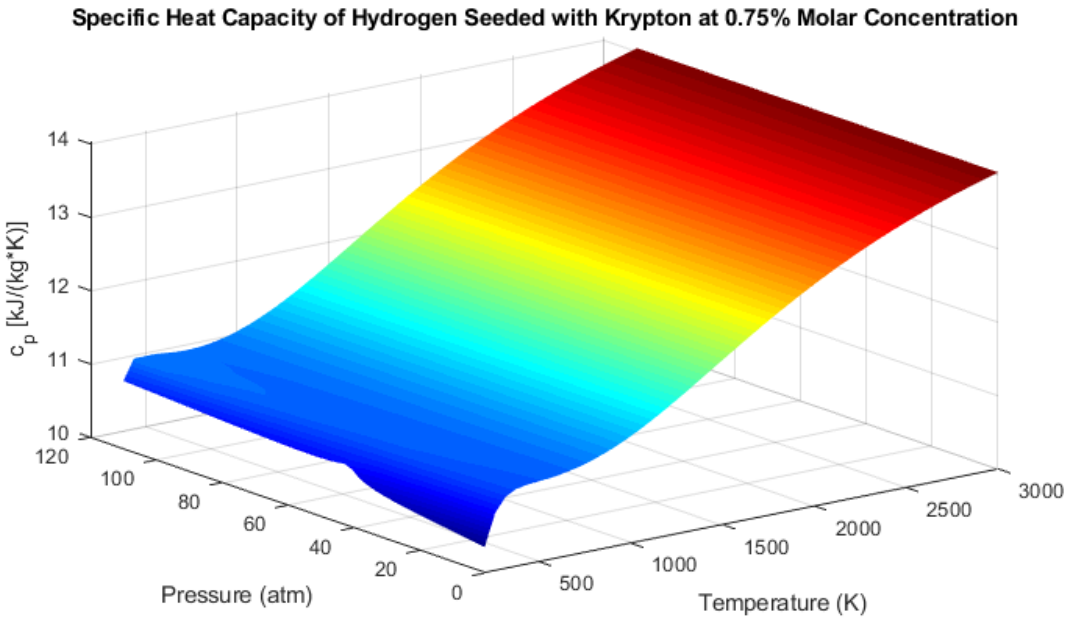

Figure G.2.2.1: Specific Heat Capacity of H_2 Seeded with Kr at 0.75% Molar Concentration

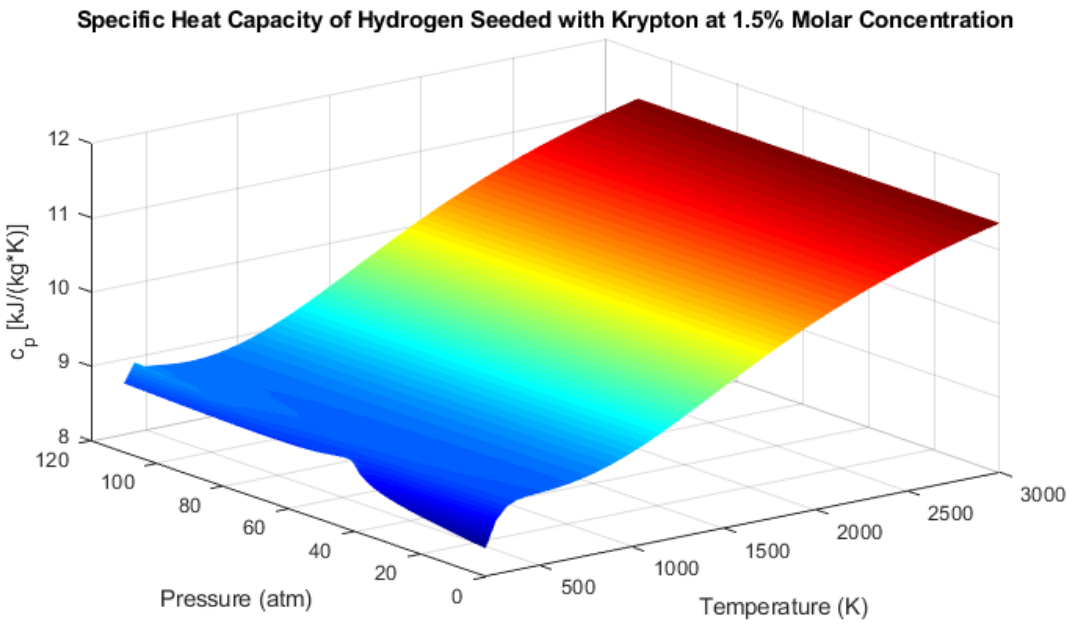

Figure G.2.2.2: Specific Heat Capacity of H_2 Seeded with Kr at 1.5% Molar Concentration

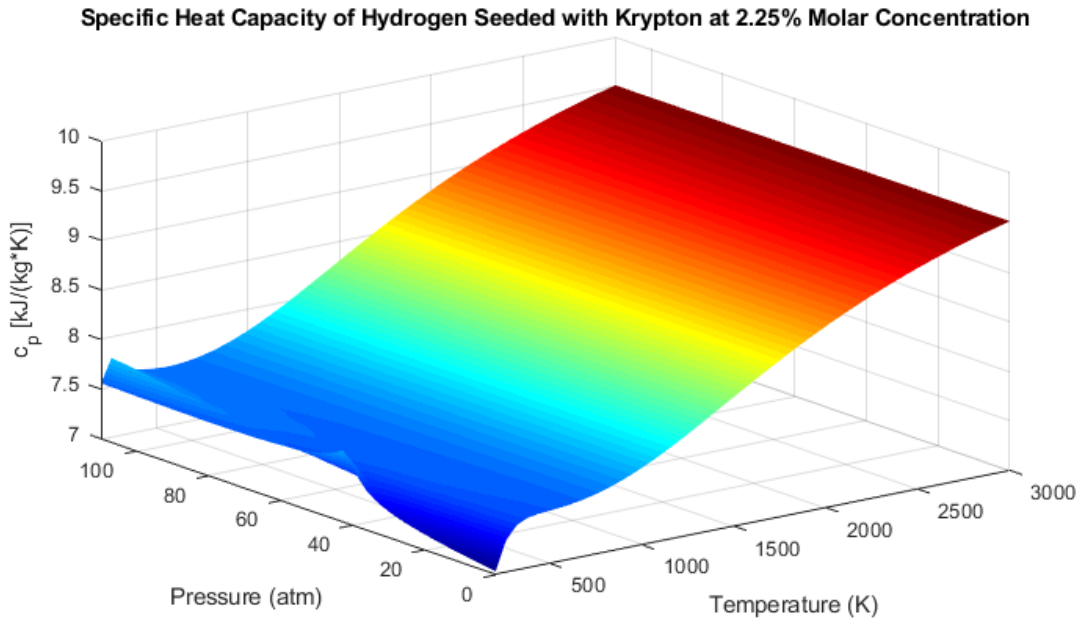

Figure G.2.2.3: Specific Heat Capacity of H_2 Seeded with Kr at 2.25% Molar Concentration

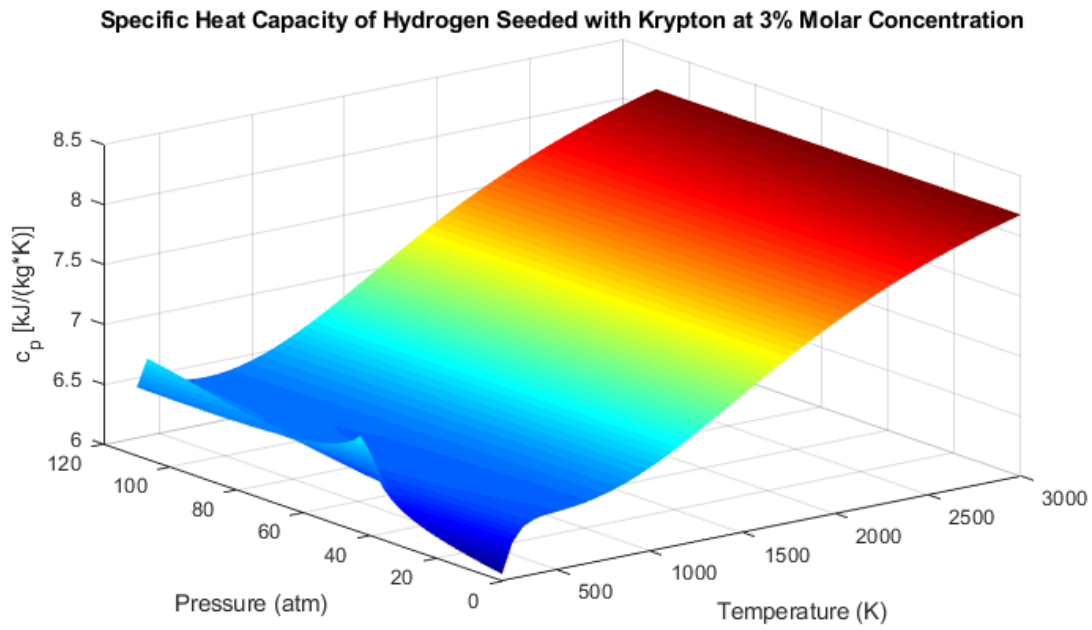

Figure G.2.2.4: Specific Heat Capacity of H_2 Seeded with Kr at 3% Molar Concentration

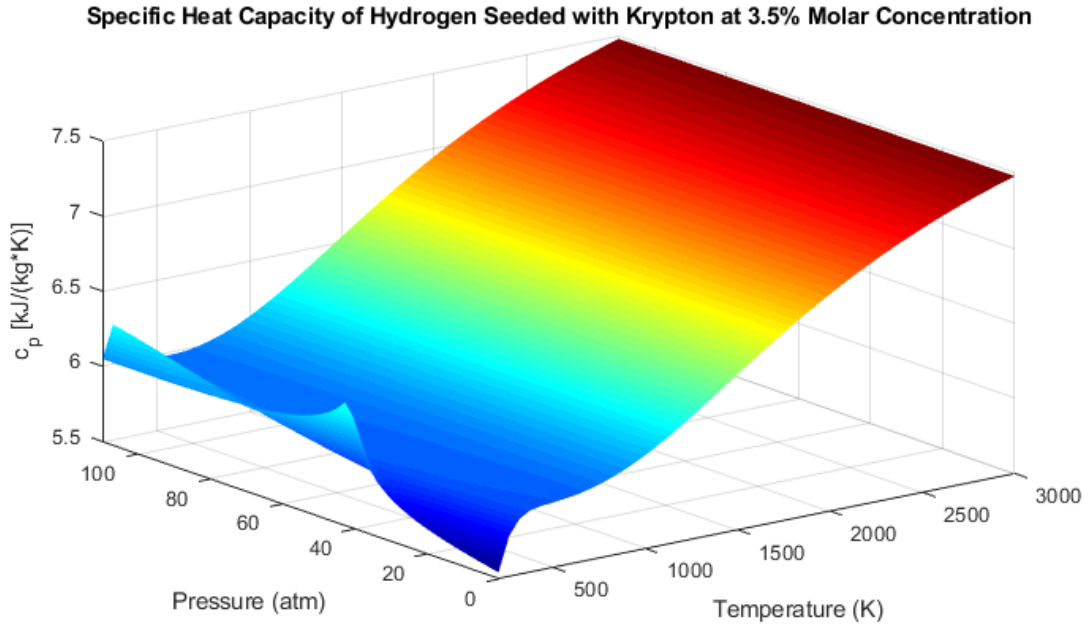

Figure G.2.2.5: Specific Heat Capacity of H_2 Seeded with Kr at 3.5% Molar Concentration

G.2.3 H2 Seeded with Kr: Viscosity at Various Concentrations

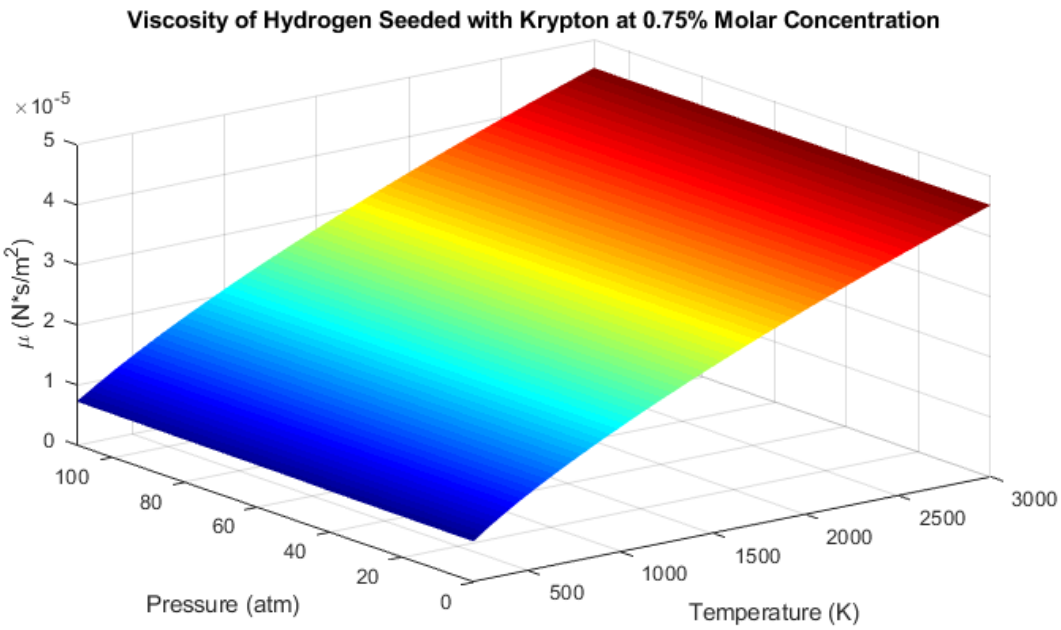

Figure G.2.3.1: Viscosity of H_2 Seeded with Kr at 0.75% Molar Concentration

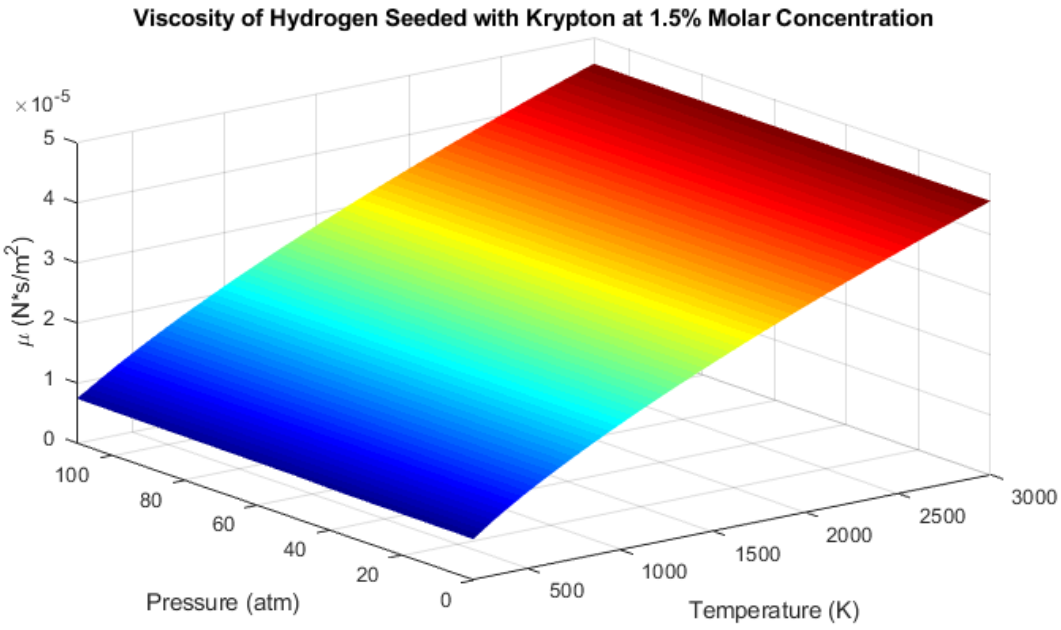

Figure G.2.3.2: Viscosity of H_2 Seeded with Kr at 1.5% Molar Concentration

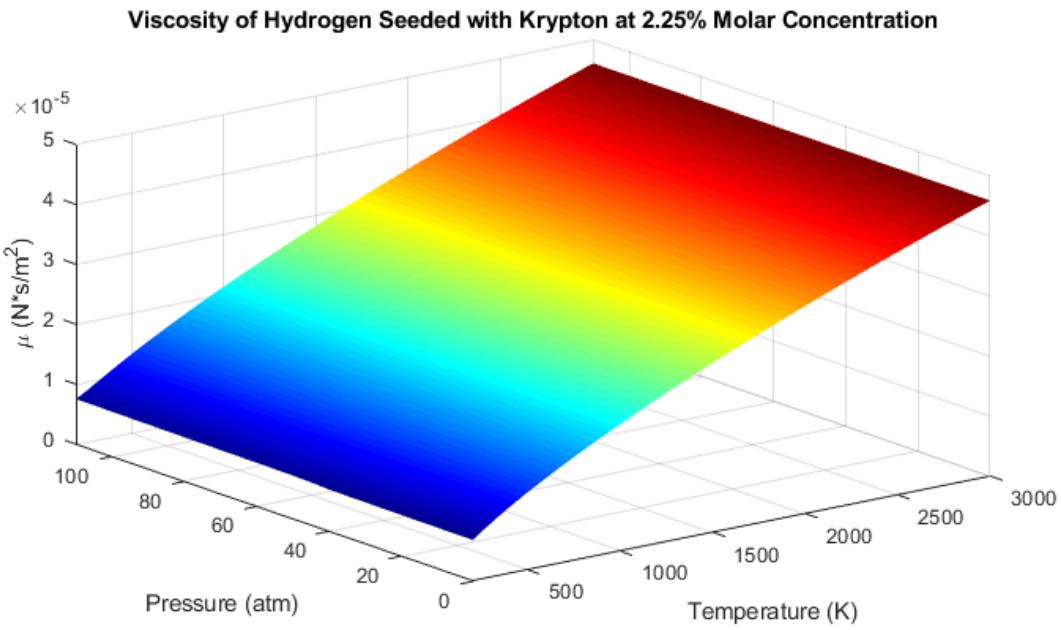

Figure G.2.3.3: Viscosity of H_2 Seeded with Kr at 2.25% Molar Concentration

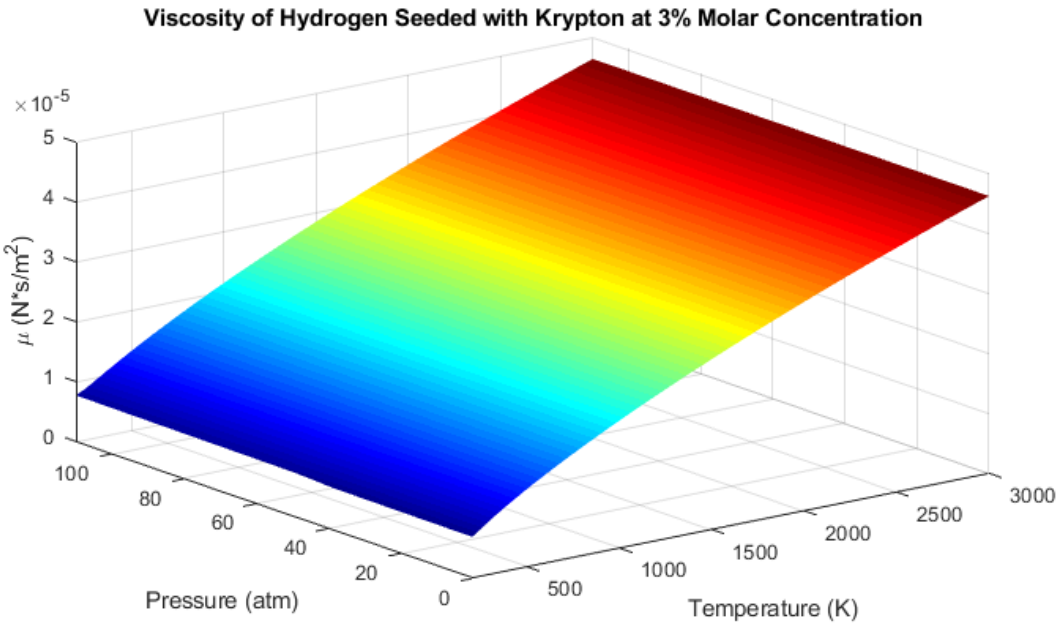

Figure G.2.3.4: Viscosity of H_2 Seeded with Kr at 3% Molar Concentration

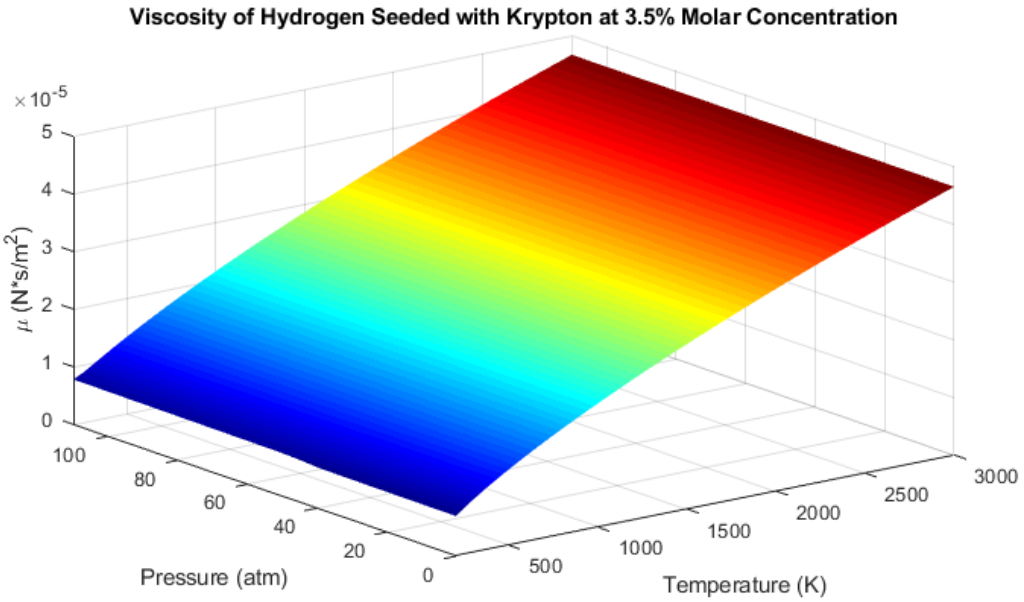

Figure G.2.3.5: Viscosity of H_2 Seeded with Kr at 3.5% Molar Concentration

G.2.4 H2 Seeded with Kr: Thermal Conductivity at Various Concentrations

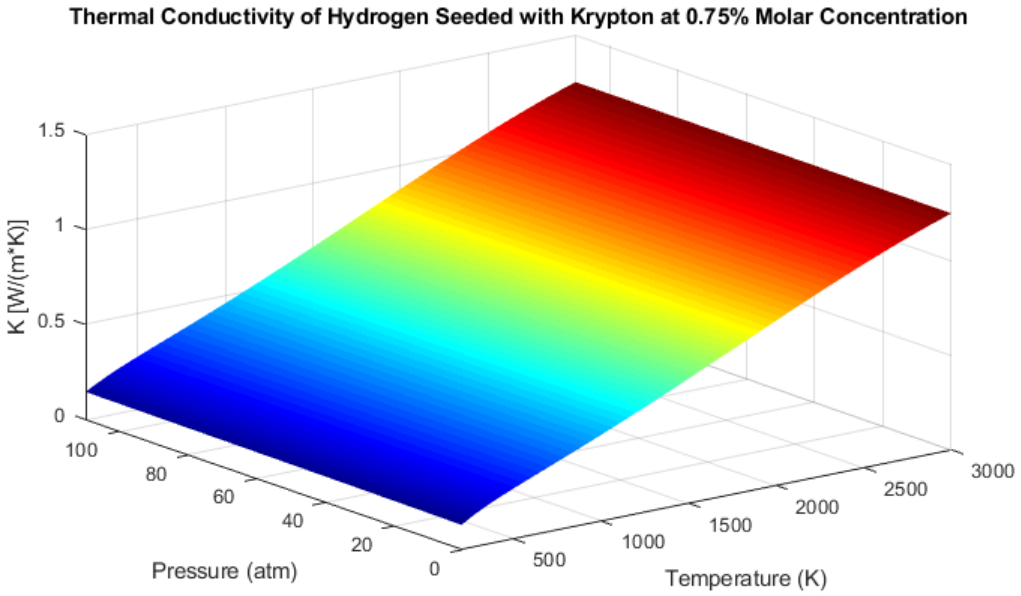

Figure G.2.4.1: Thermal Conductivity of H_2 Seeded with Kr at 0.75% Molar Concentration

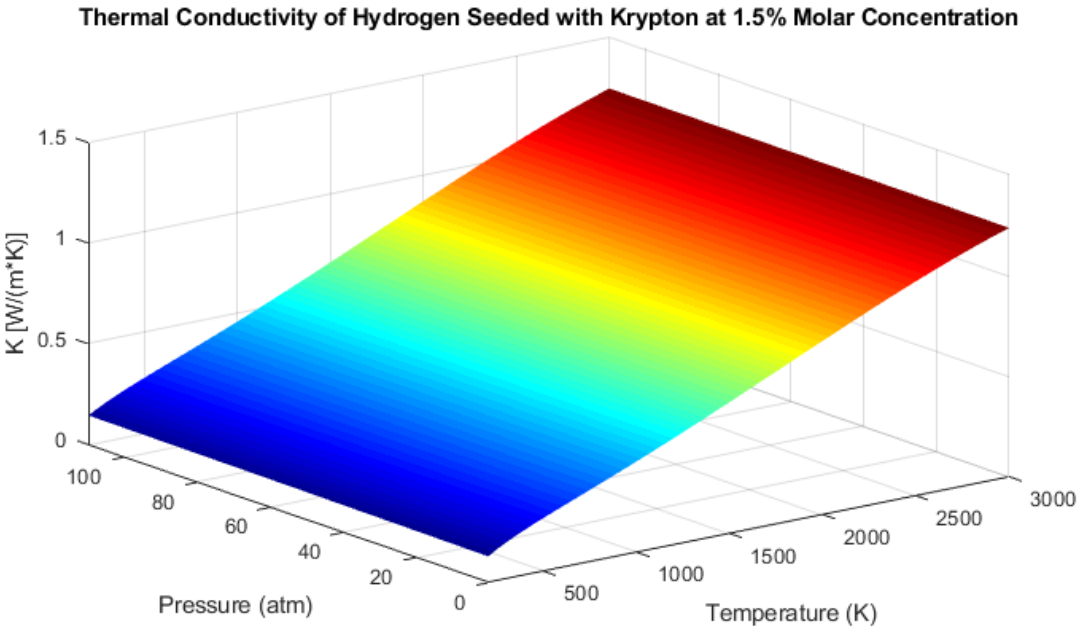

Figure G.2.4.2: Thermal Conductivity of H_2 Seeded with Kr at 1.5% Molar Concentration

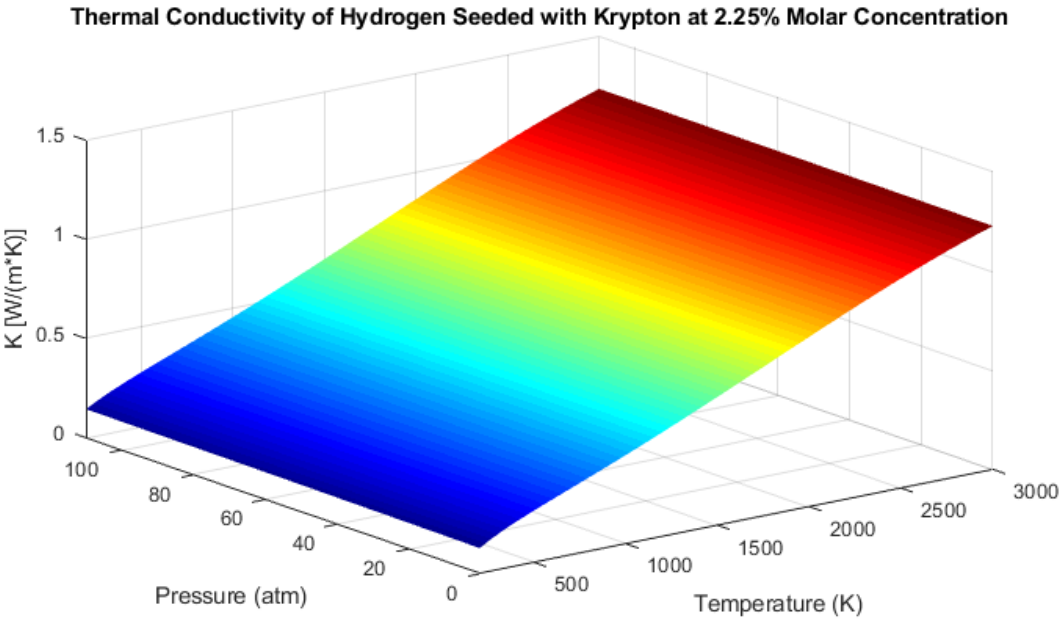

Figure G.2.4.3: Thermal Conductivity of H_2 Seeded with Kr at 2.25% Molar Concentration

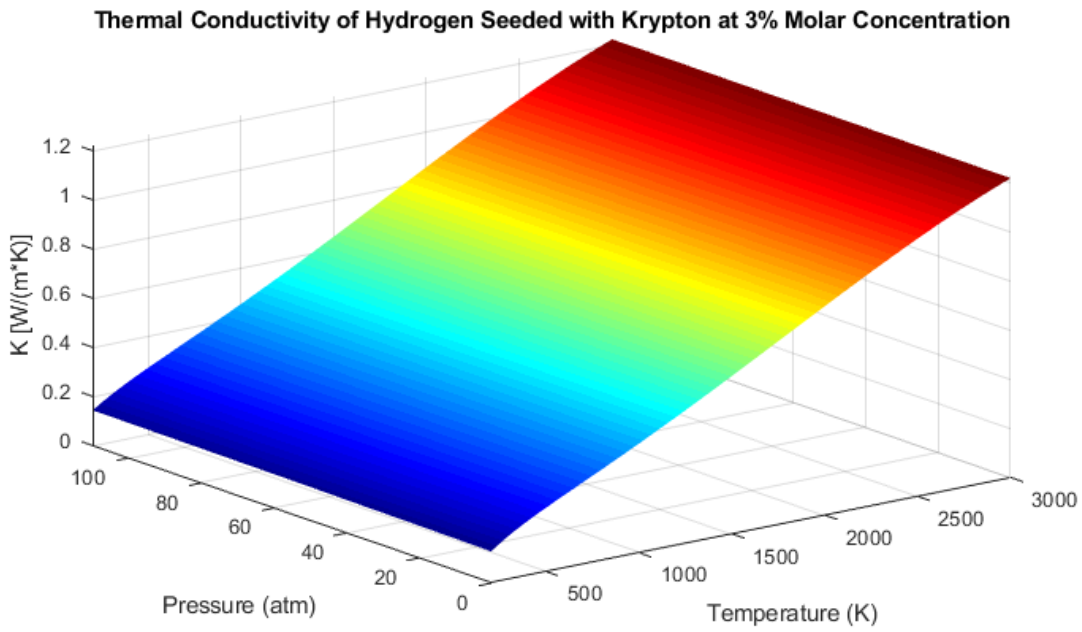

Figure G.2.4.4: Thermal Conductivity of H_2 Seeded with Kr at 3% Molar Concentration

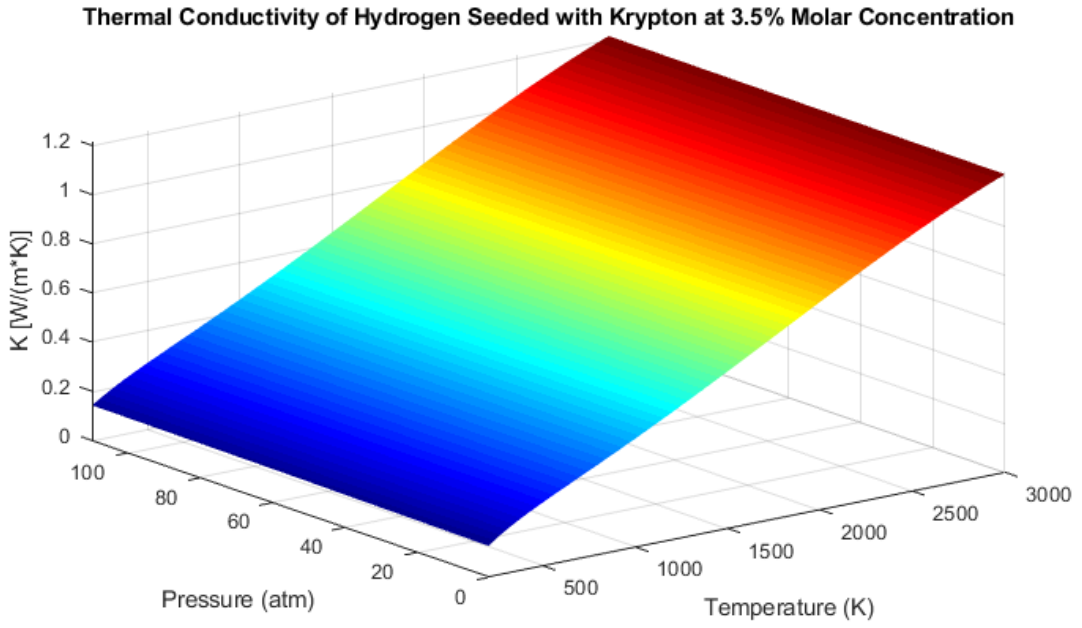

Figure G.2.4.5: Thermal Conductivity of H_2 Seeded with Kr at 3.5% Molar Concentration

G.3 Hydrogen Seeded with Xenon

G.3.1 H2 Seeded with Xe: Density at Various Concentrations

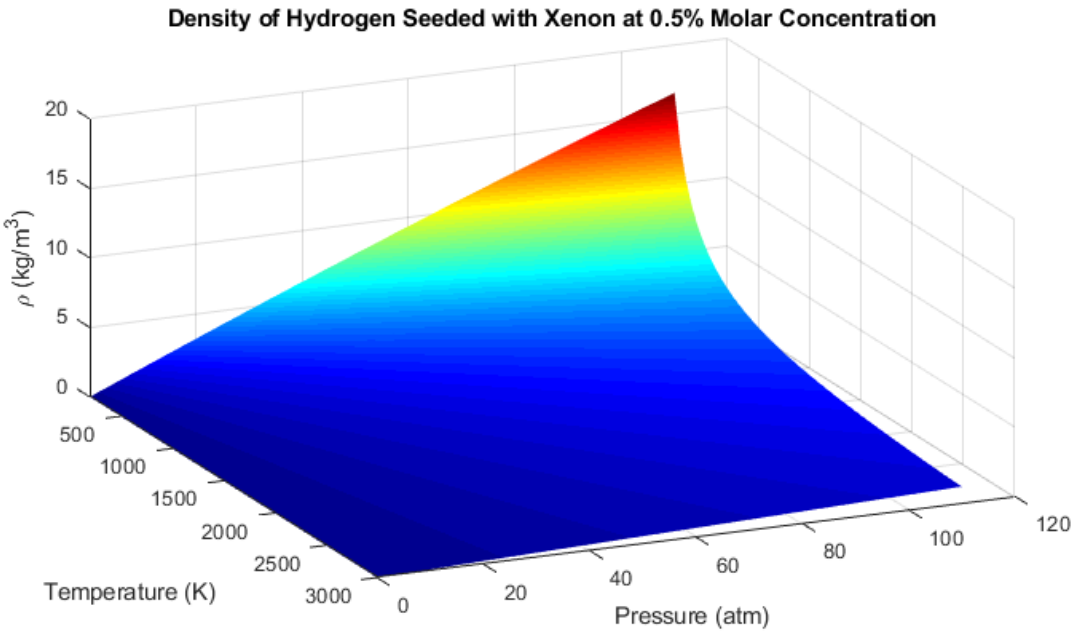

Figure G.3.1.1: Density of H_2 Seeded with Xe at 0.5% Molar Concentration

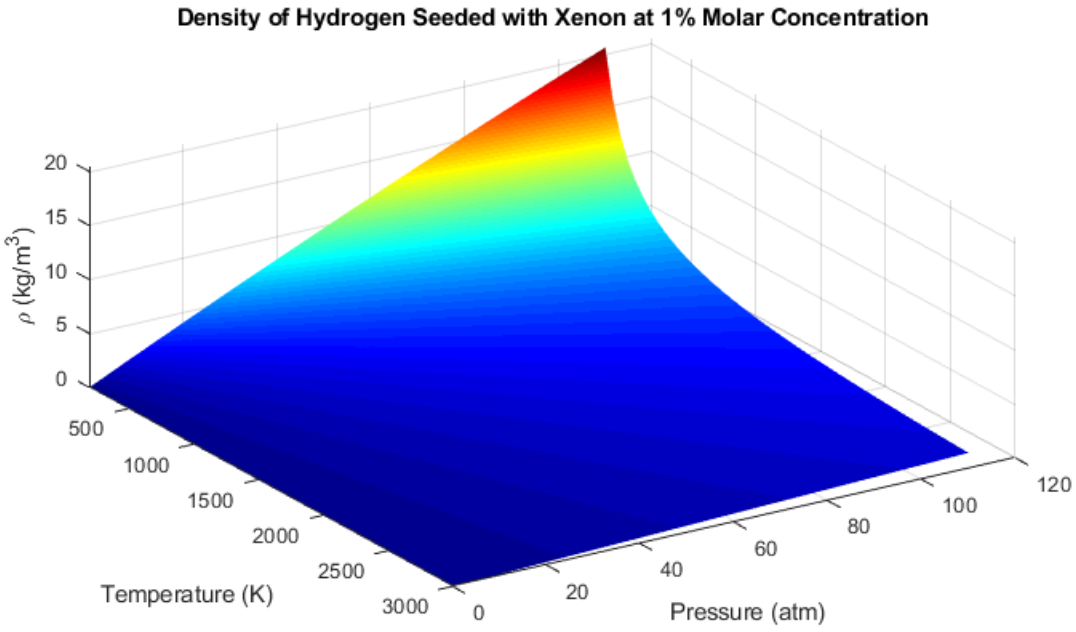

Figure G.3.1.2: Density of H_2 Seeded with Xe at 1% Molar Concentration

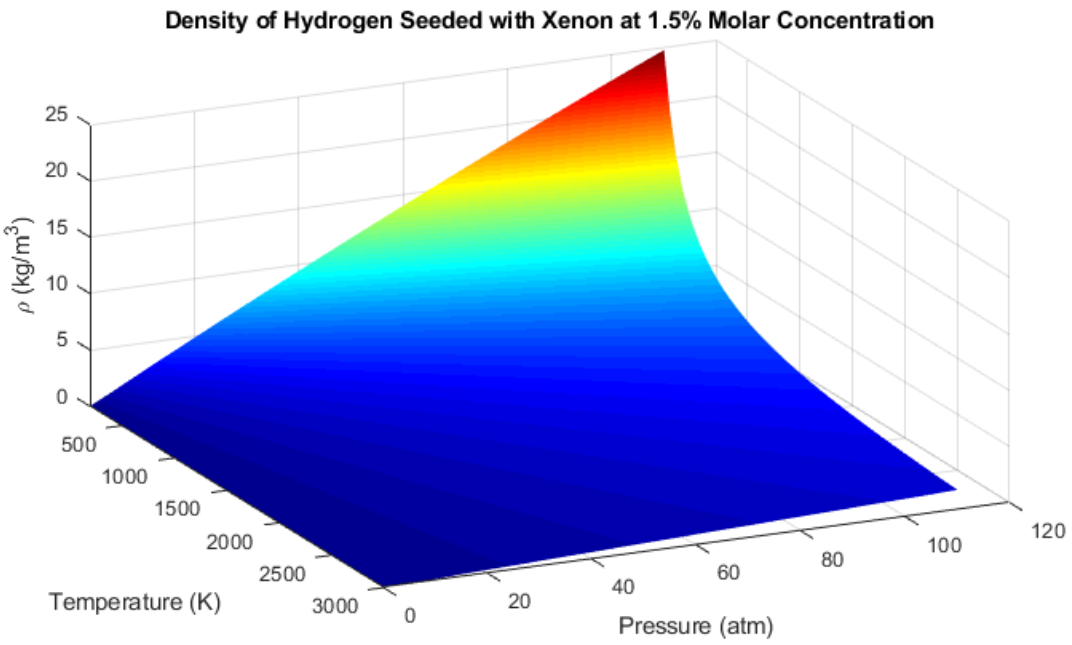

Figure G.3.1.3: Density of H_2 Seeded with Xe at 1.5% Molar Concentration

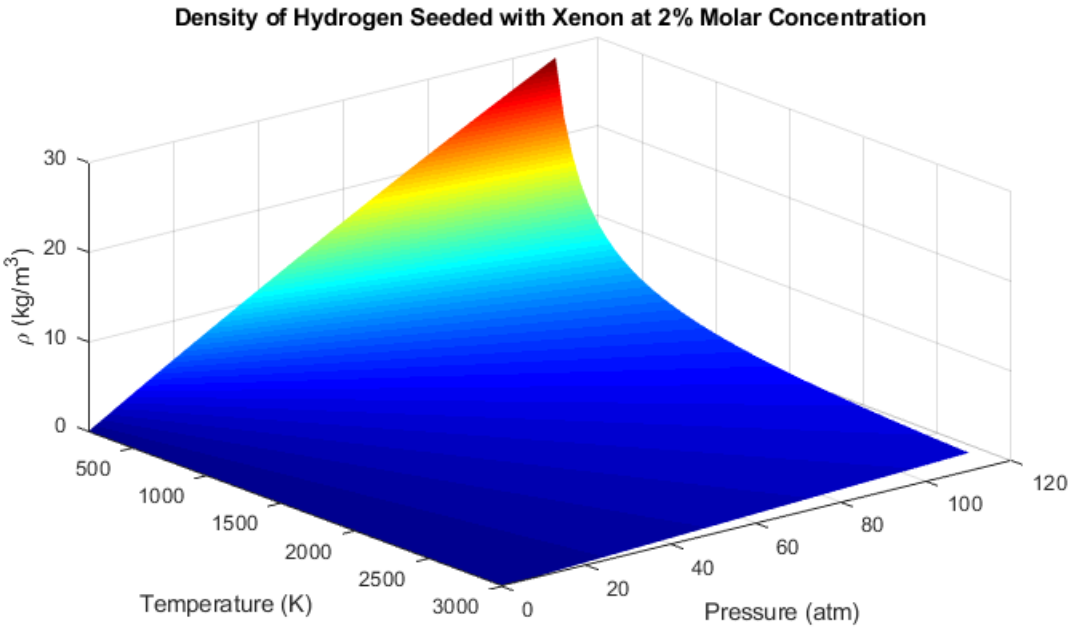

Figure G.3.1.4: Density of H_2 Seeded with Xe at 2% Molar Concentration

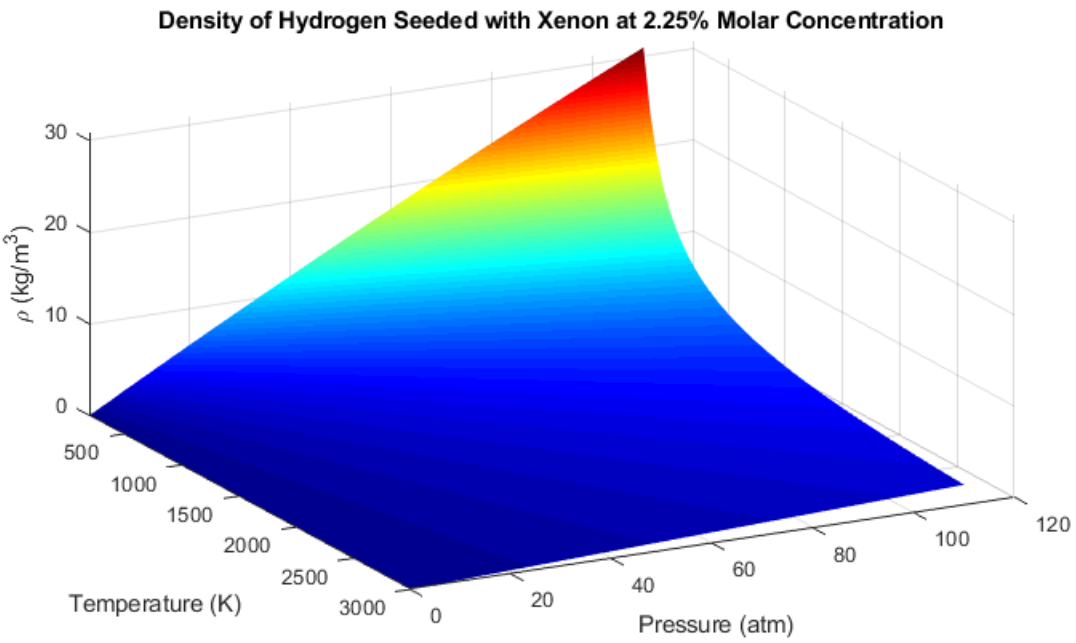

Figure G.3.1.5: Density of H_2 Seeded with Xe at 2.25% Molar Concentration

G.3.2 H2 Seeded with Xe: Specific Heat Capacity at Various Concentrations

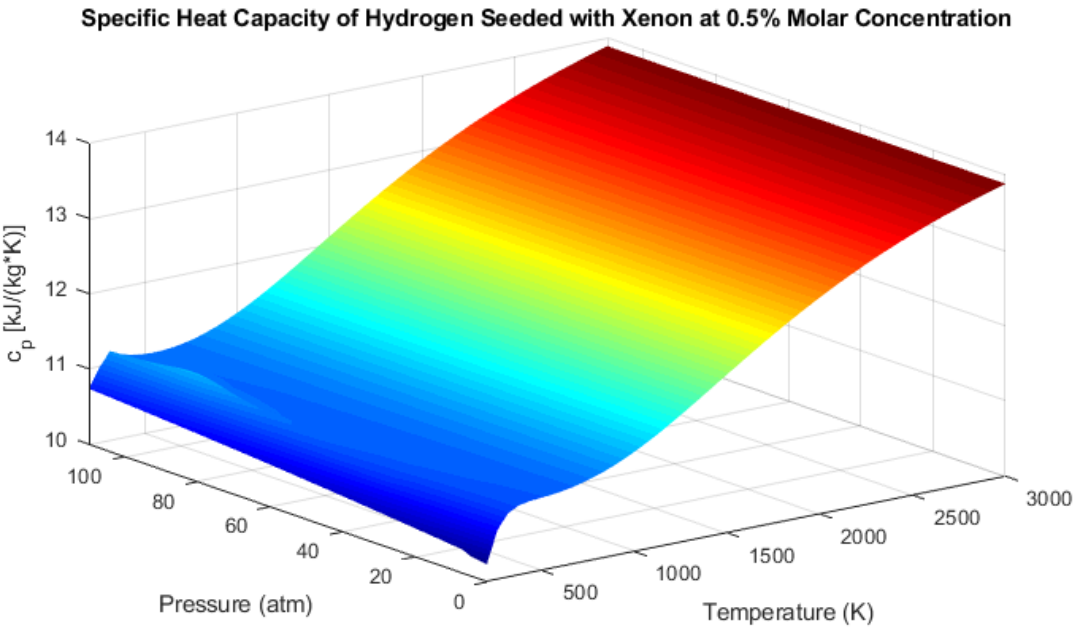

Figure G.3.2.1: Specific Heat Capacity of H_2 Seeded with Xe at 0.5% Molar Concentration

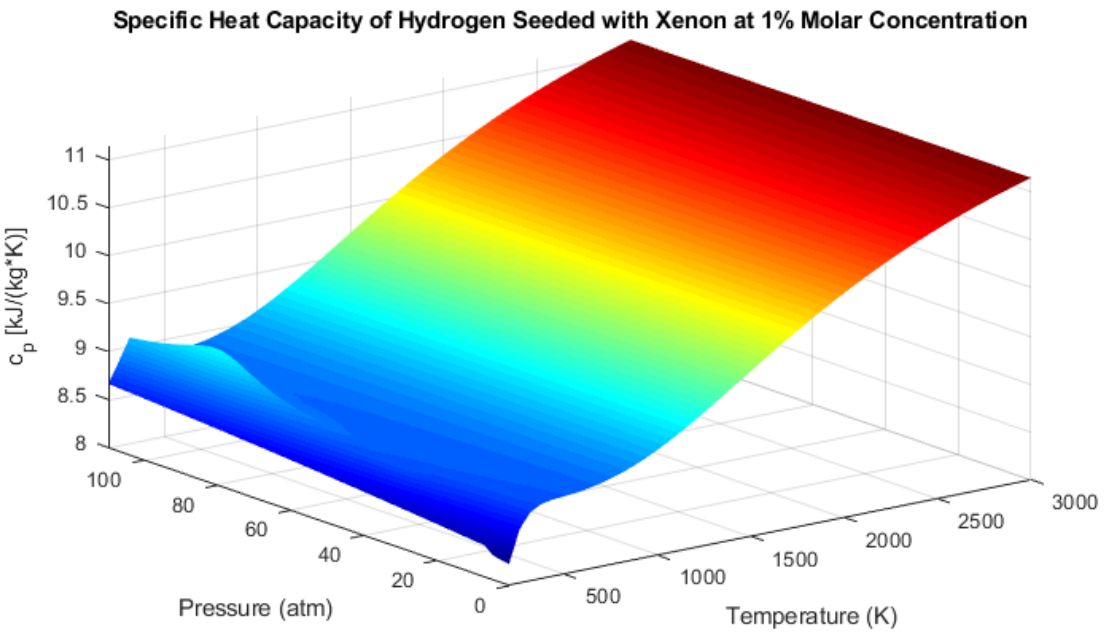

Figure G.3.2.2: Specific Heat Capacity of H_2 Seeded with Xe at 1% Molar Concentration

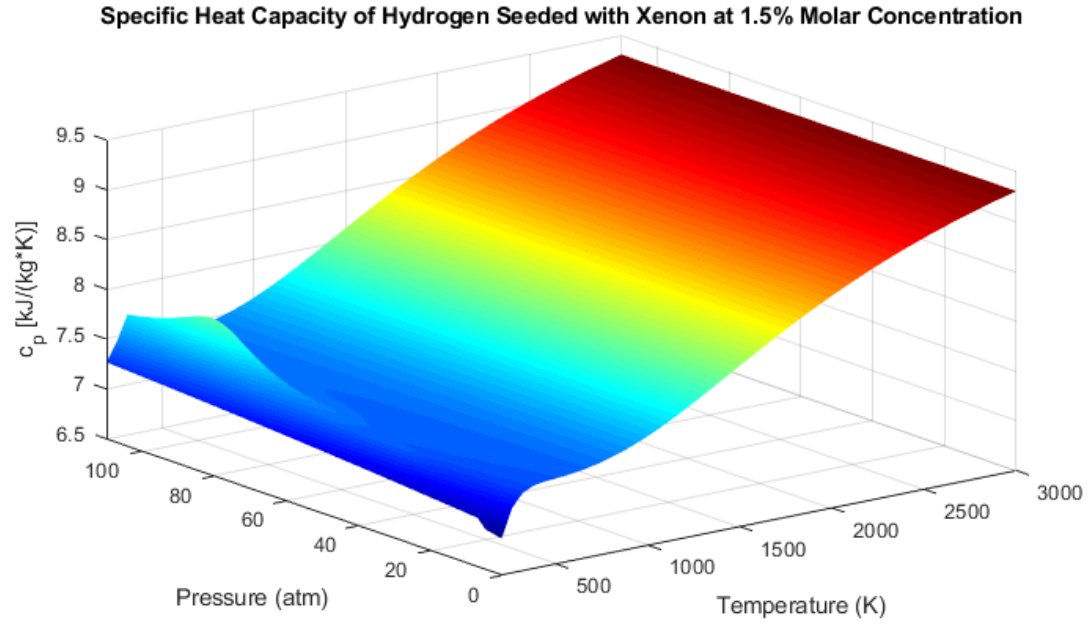

Figure G.3.2.3: Specific Heat Capacity of H_2 Seeded with Xe at 1.5% Molar Concentration

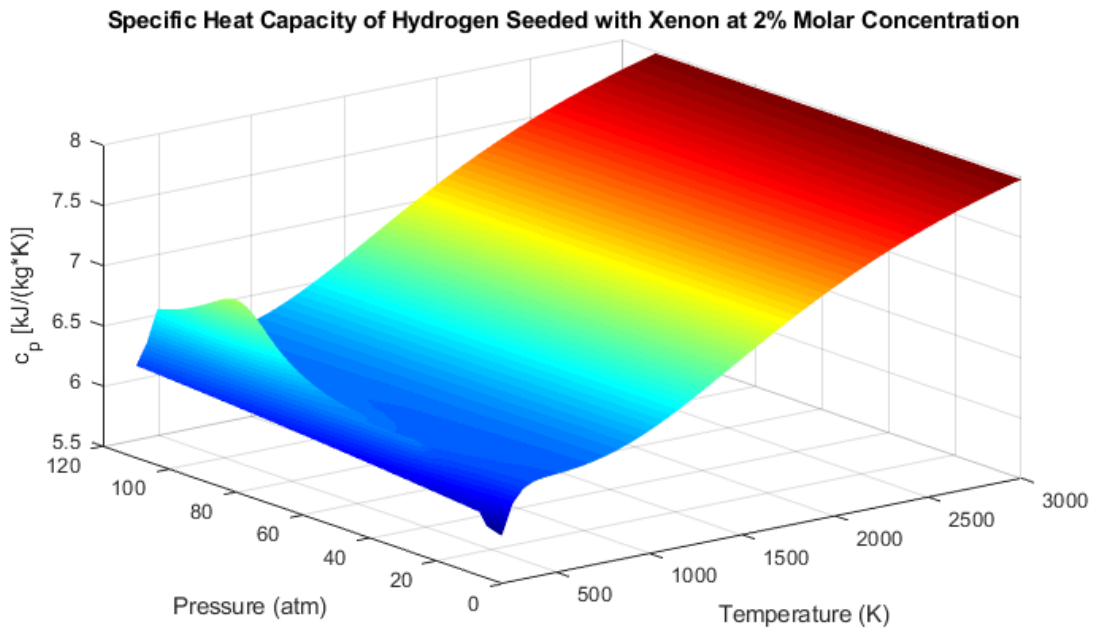

Figure G.3.2.4: Specific Heat Capacity of H_2 Seeded with Xe at 2% Molar Concentration

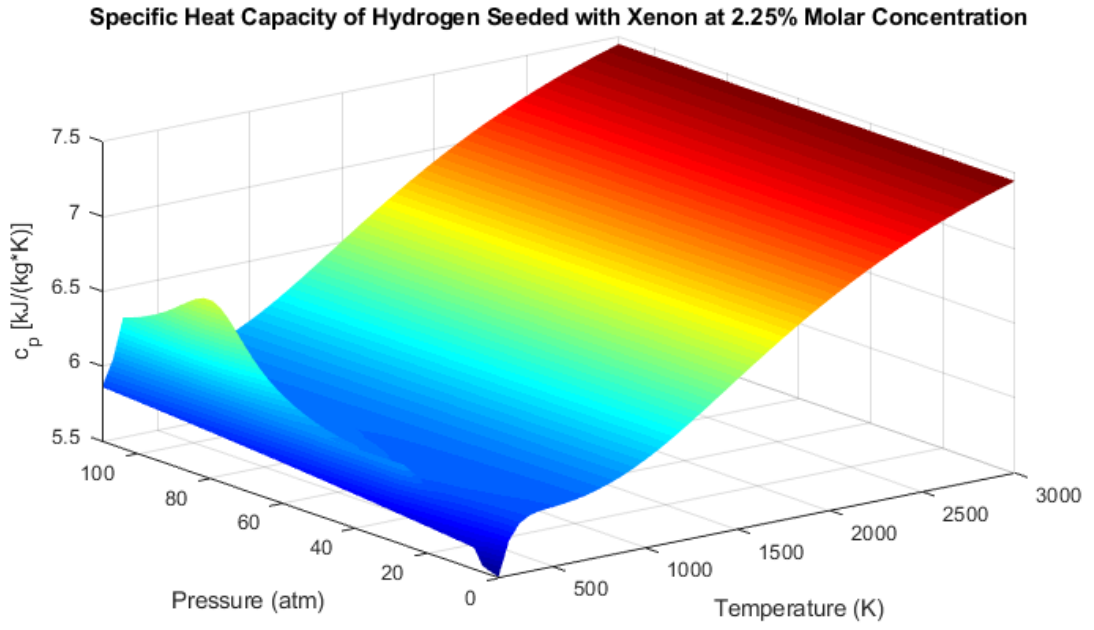

Figure G.3.2.5: Specific Heat Capacity of H_2 Seeded with Xe at 2.25% Molar Concentration

G.3.3 H2 Seeded with Xe: Viscosity at Various Concentrations

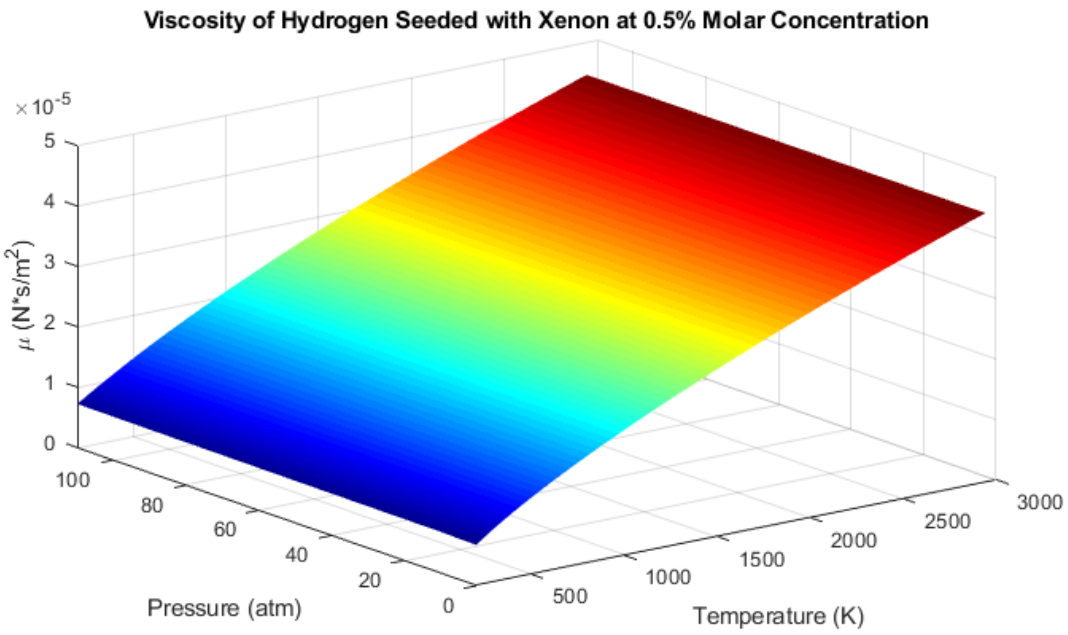

Figure G.3.3.1: Viscosity of H_2 Seeded with Xe at 0.5% Molar Concentration

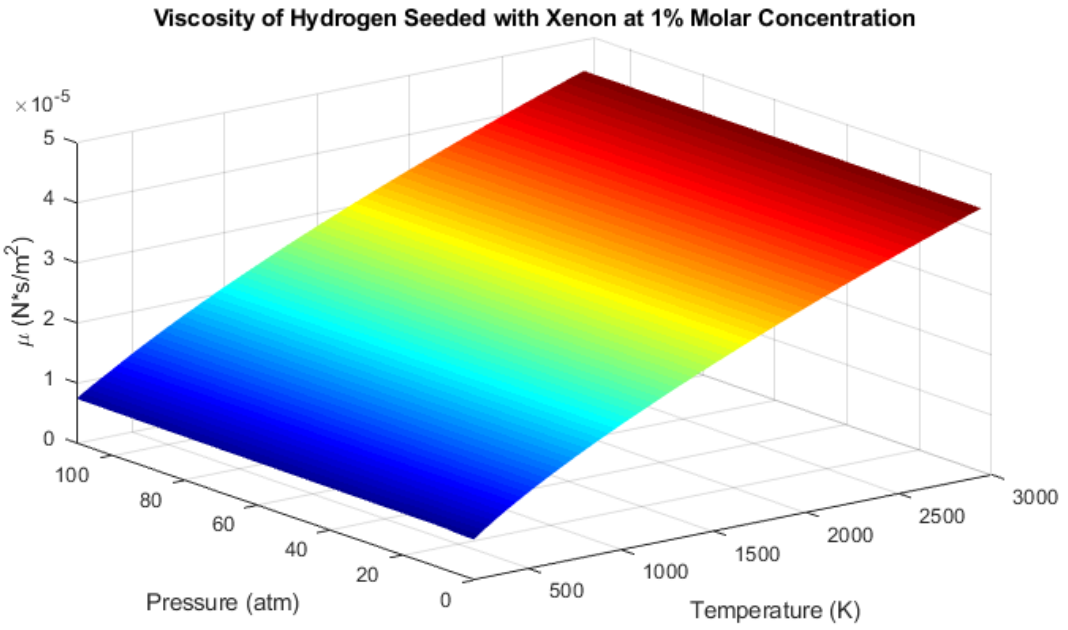

Figure G.3.3.2: Viscosity of H_2 Seeded with Xe at 1% Molar Concentration

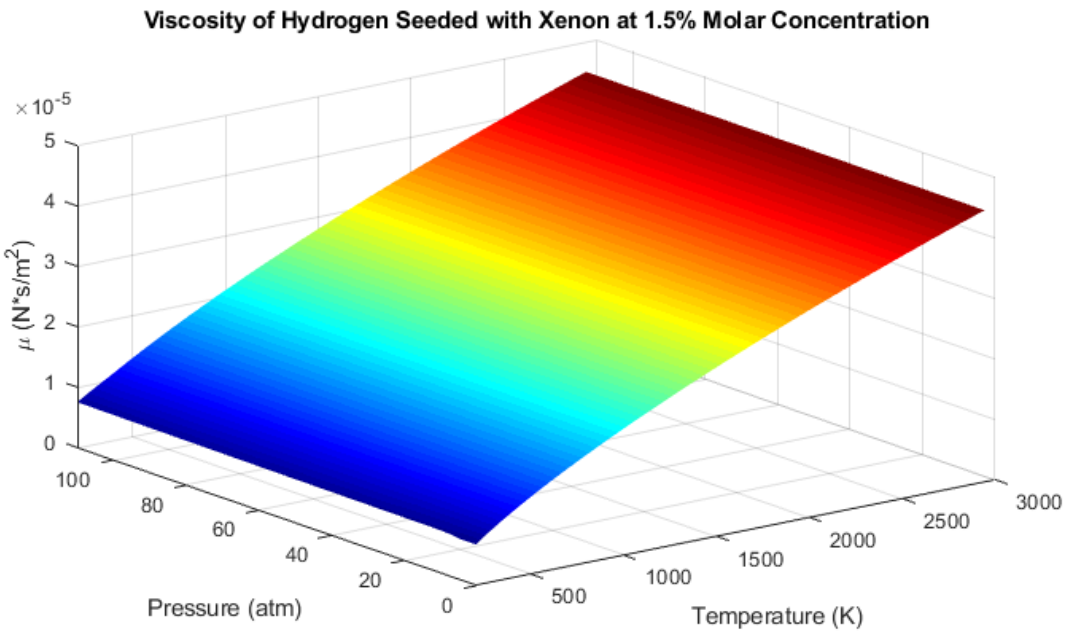

Figure G.3.3.3: Viscosity of H_2 Seeded with Xe at 1.5% Molar Concentration

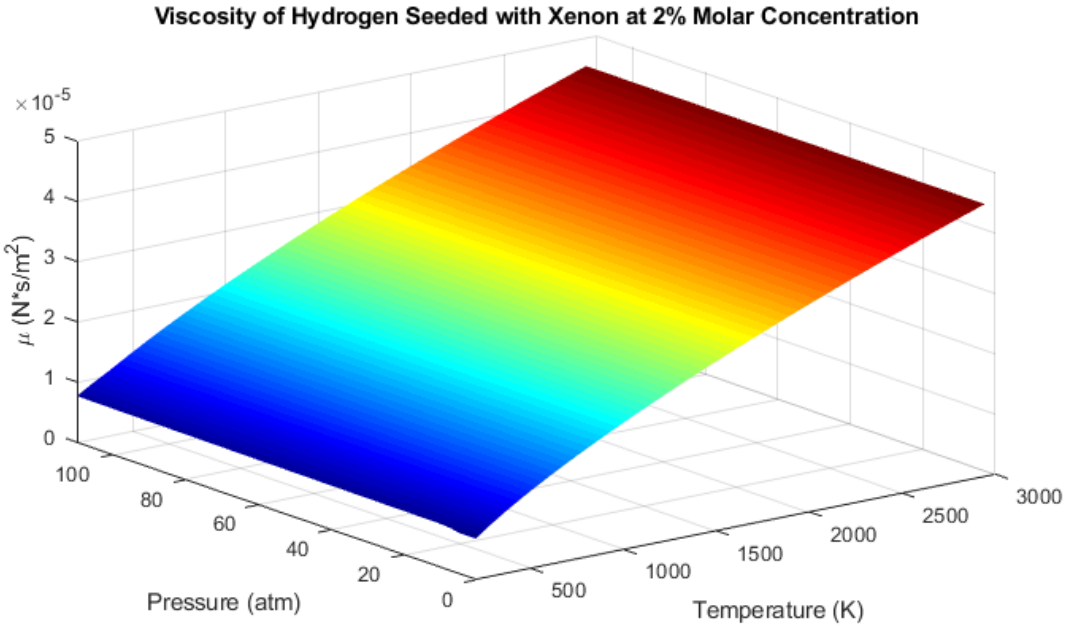

Figure G.3.3.4: Viscosity of H_2 Seeded with Xe at 2% Molar Concentration

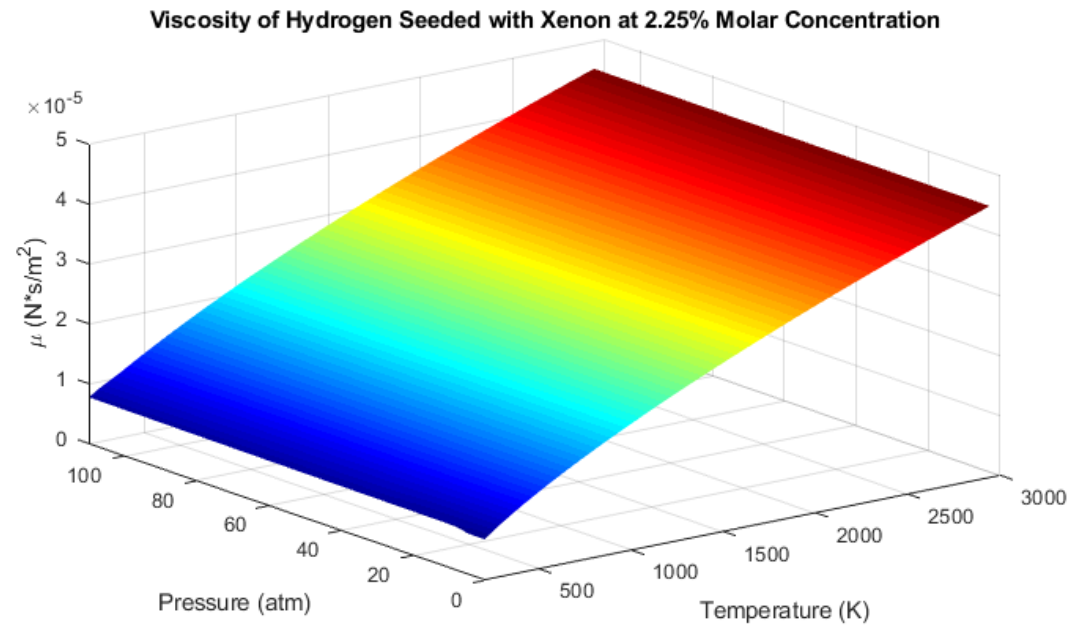

Figure G.3.3.5: Viscosity of H_2 Seeded with Xe at 2.25% Molar Concentration

G.3.4 H2 Seeded with Xe: Thermal Conductivity at Various Concentrations

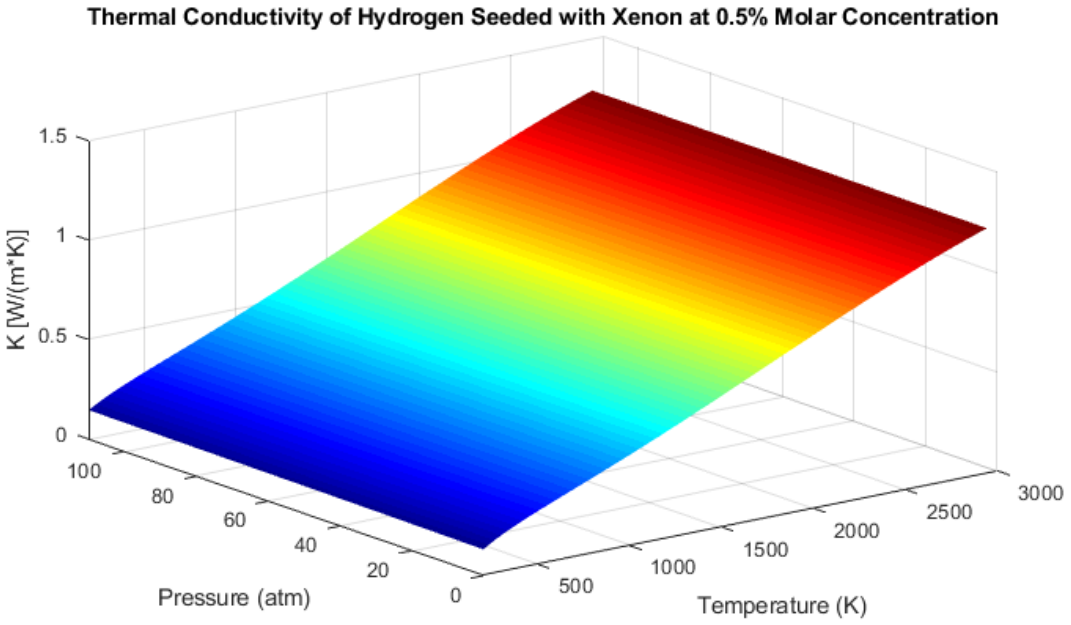

Figure G.3.4.1: Thermal Conductivity of H_2 Seeded with Xe at 0.5% Molar Concentration

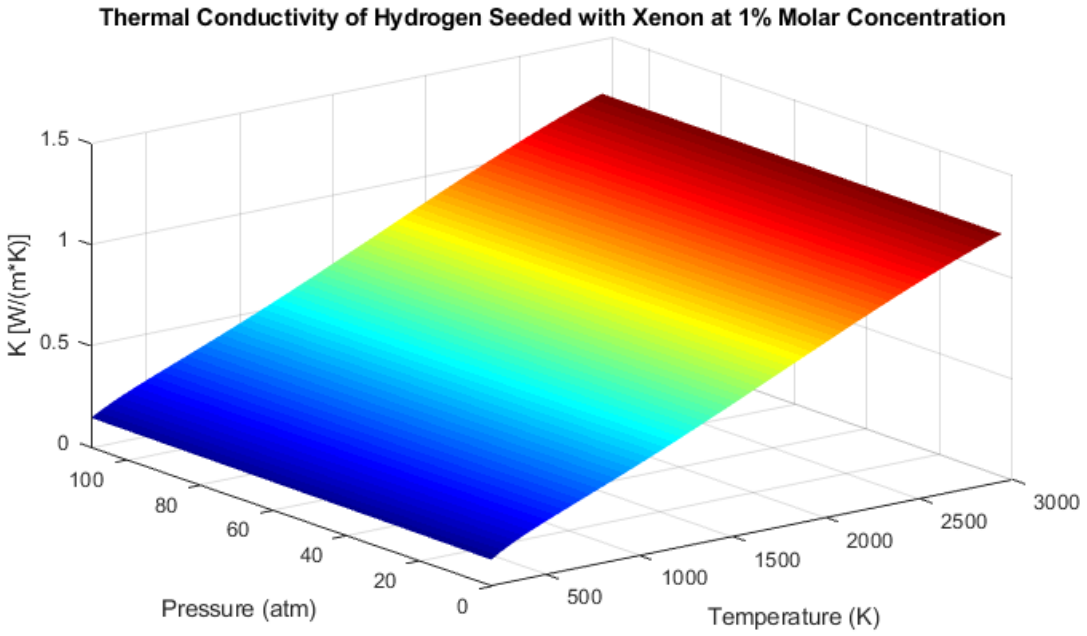

Figure G.3.4.2: Thermal Conductivity of H_2 Seeded with Xe at 1% Molar Concentration

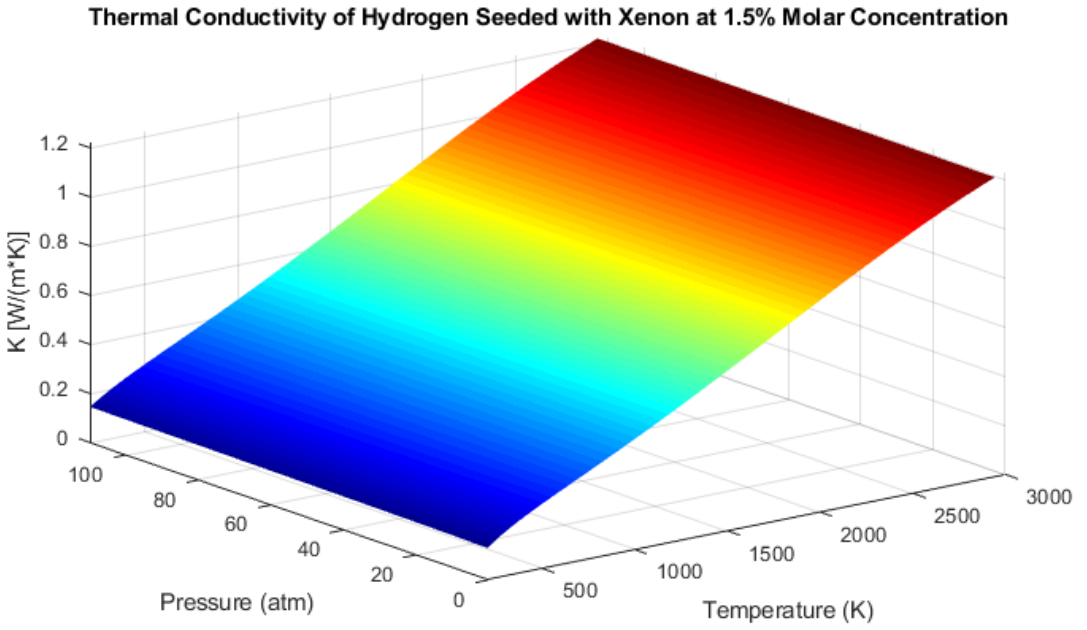

Figure G.3.4.3: Thermal Conductivity of H_2 Seeded with Xe at 1.5% Molar Concentration

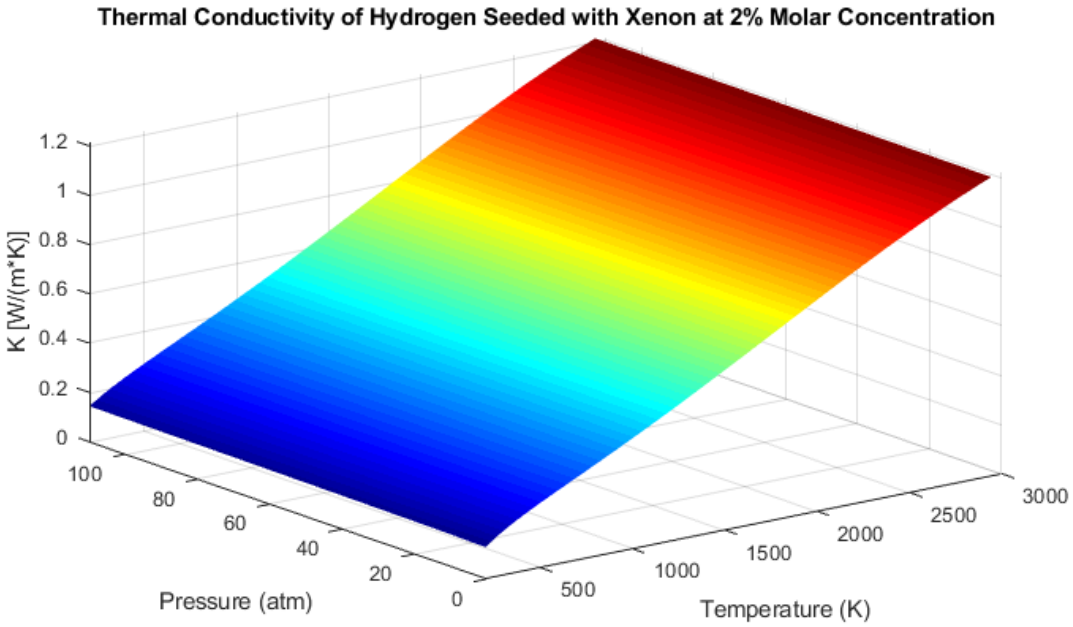

Figure G.3.4.4: Thermal Conductivity of H_2 Seeded with Xe at 2% Molar Concentration

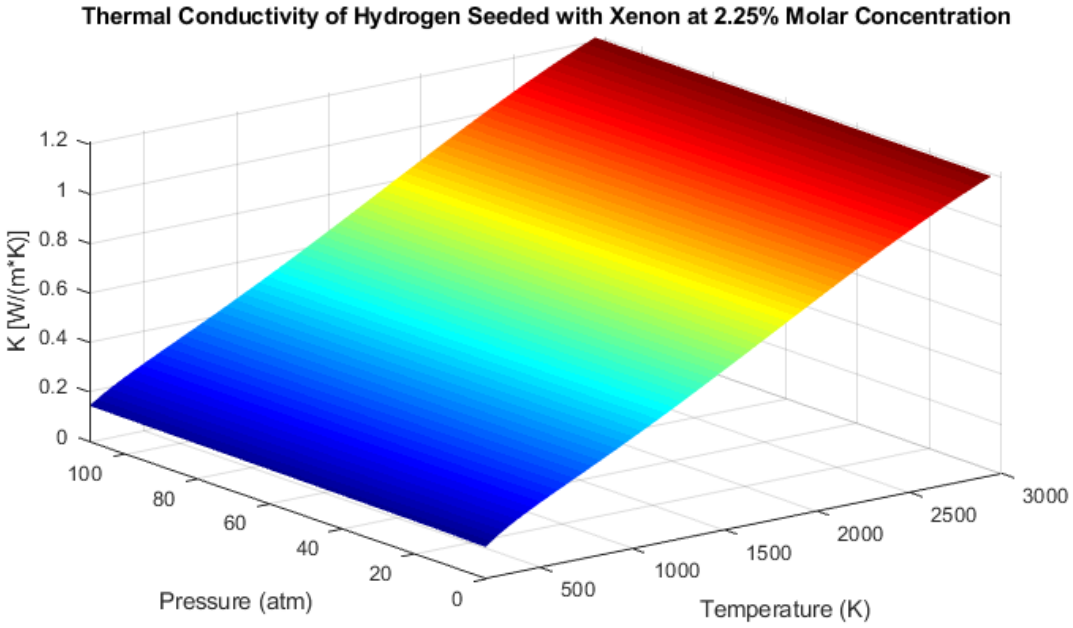

Figure G.3.4.5: Thermal Conductivity of H_2 Seeded with Xe at 2.25% Molar Concentration

APPENDIX H

Derivations

H.1 Deriving Density of a Mixture Using the Specific Volume Approach

From thermodynamics, when two species are mixed, their intensive properties can be found on a mole or mass fraction basis, based on whether the property of interest is in terms of units per mole or units per unit mass. Since density is usually given in terms of volume per unit mass and specific volume is the reciprocal of density, the mass fraction basis will be used. Furthermore, the seed amount will be in terms of molar fraction due to the fact that gas mixture composition is usually given in terms of mole fractions. The density derivation will assume liquid states for both the main lattice and seed species, and thus incompressibility.

From thermodynamics, the lever rule for specific volume per mass fraction basis is given in equation H.1.

$$v = \sum_{i=1}^{n} f_{m_i} v_i \Rightarrow \rho = \left[\sum_{i=1}^{n} f_{m_i} v_i \right]^{-1} \tag{H.1}$$

The apparent molecular weight of the mixture is defined by equation H.2.

$$mw = \sum_{i=1}^{n} f_{X_i} mw_{X_i} \tag{H.2}$$

Mass fractions are defined by equation H.3.

$$f_{m_{X_i}} = \frac{f_{X_i} mw_{X_i}}{\sum_{j=1}^{n} f_{X_j} mw_{X_j}} \tag{H.3}$$

Since only 2 species are utilized, the sum of their fractions will be equal to 1 as shown in equation H.4 where the *H* subscript is for hydrogen and the *s* subscript is for the seed.

$$f_H + f_s = 1 \Rightarrow f_H = 1 - f_s \tag{H.4}$$

In the case of seeded propellant, the mass fractions for the main lattice species and the seed will be defined by equations H.5 and H.6 respectively. Equation H.4 will also be incorporated.

$$f_{m_H} = \frac{(1 - f_s)mw_H}{(1 - f_s)mw_H + f_s mw_s} \tag{H.5}$$

$$f_{m_s} = \frac{f_s mw_s}{(1 - f_s)mw_H + f_s mw_s} \tag{H.6}$$

Putting equations H.5 and H.6 into equation H.1 results in equation H.7.

$$\frac{1}{\rho} = \frac{(1 - f_s)mw_H}{\rho_H[(1 - f_s)mw_H + f_s mw_s]} + \frac{f_s mw_s}{\rho_s[(1 - f_s)mw_H + f_s mw_s]} \tag{H.7}$$

Rearranging and solving for ρ results in the seeded density function H.8.

$$\boldsymbol{\rho = \frac{\rho_H \rho_s[(1 - f_s)mw_H + f_s mw_s]}{(1 - f_s)mw_H \rho_s + f_s mw_s \rho_H}} \tag{H.8}$$

H.2 Deriving Density of a Mixture Using the Mass Over Volume Approach

The overall propellant density will be found by using the definition of density: mass divided by volume. According to this definition, volume is equal to mass divided by density as shown in equation H.9.

$$\forall = \frac{m}{\rho} \tag{H.9}$$

Further, the sum of the volumes that each species contributes in a mixture is equal to the total volume of that mixture shown in equation H.10.

$$\forall = \sum_{i=1}^{n} \forall_i \tag{H.10}$$

Combining equations H.9 and H.10 results in equation H.11.

$$\forall = \sum_{i=1}^{n} \frac{m_i}{\rho_i} \tag{H.11}$$

The masses of each species will be expressed in terms of moles as shown in equation H.12.

$$m_X = n_X m w_X \tag{H.12}$$

By definition, a mole fraction is the number of moles of the species of interest divided by the total moles as shown in equation H.13.

$$f_X = \frac{n_X}{\sum_{i=1}^{n} n_i} \tag{H.13}$$

Equation H.13 is also used to solve for the number of moles of a specific species as shown in H.14.

$$n_X = f_X \sum_{i=1}^{n} n_i \tag{H.14}$$

Putting equation H.12 into equation H.11 will result in equation H.15.

$$\forall = \sum_{i=1}^{n} \frac{n_i mw_i}{\rho_i} \tag{H.15}$$

Applying equations H.14 and H.4 to equation H.15 will result in the general formula for the volume in terms of moles and molecular weights shown in equation H.16.

$$\forall = \sum_{i=1}^{n} \frac{f_i \sum_{k=1}^{n} (n_k)\, mw_i}{\rho_i} \tag{H.16}$$

Applying the general formula to the seeded propellant will result in equation H.17 where $\forall_s = \frac{f_s(n_s+n_H)mw_s}{\rho_s}$ and $\forall_H = \frac{(1-f_s)(n_s+n_H)mw_H}{\rho_H}$.

$$\forall = \forall_s + \forall_H = \frac{f_s(n_s + n_H)mw_s}{\rho_s} + \frac{(1 - f_s)(n_s + n_H)mw_H}{\rho_H} \tag{H.17}$$

From here, the entire equation is divided by the term relating to the volume of the main lattice species shown in equation H.18.

$$\frac{\forall}{\frac{(1 - f_s)(n_s + n_H)mw_H}{\rho_H}} = \frac{\frac{f_s(n_s + n_H)mw_s}{\rho_s}}{\frac{(1 - f_s)(n_s + n_H)mw_H}{\rho_H}} + 1 = \frac{f_s mw_s \rho_H}{(1 - f_s)mw_H \rho_s} + 1 \tag{H.18}$$

Using the fact that $\forall_H = \frac{(1-f_s)(n_s+n_H)mw_H}{\rho_H}$, equation H.18 is rearranged to solve for $\forall_H$ which is shown in equation H.19.

$$\forall_H = \frac{\forall}{\frac{f_s mw_s \rho_H}{(1-f_s)mw_H \rho_s} + 1} \tag{H.19}$$

By using the definition of density in equation H.9, it is stated that the sum of all of the masses within a volume divided by that volume equal the overall density shown in equation H.20.

$$\rho = \frac{\sum_i^n m_n}{\forall} \tag{H.20}$$

Applying equation H.20 to the seeded propellant and using equation H.9 to solve for the masses in terms of volume and density yields equation H.21.

$$\rho = \frac{m_H + m_s}{\forall} = \frac{\rho_H \forall_H + \rho_s \forall_s}{\forall} \tag{H.21}$$

Applying equation H.10 to the seeded propellant and solving for $\forall_s$ yields equation 4.22.

$$\forall = \forall_H + \forall_s \Rightarrow \forall_s = \forall - \forall_H \tag{4.30}$$

Applying equations H.22 and H.19 to equation H.21 yields equations H.23a and H.23b.

$$\rho = \frac{\rho_H \forall_H + \rho_s(\forall - \forall_H)}{\forall} = \frac{\rho_H \frac{\cancel{\forall}}{\frac{f_s mw_s \rho_H}{(1-f_s)mw_H \rho_s} + 1} + \rho_s \left(\cancel{\forall} - \frac{\cancel{\forall}}{\frac{f_s mw_s \rho_H}{(1-f_s)mw_H \rho_s} + 1} \right)}{\cancel{\forall}} \tag{H.23a}$$

$$\rho = \rho_H \frac{1}{\frac{f_s m w_s \rho_H}{(1-f_s) m w_H \rho_s} + 1} + \rho_s \left(1 - \frac{1}{\frac{f_s m w_s \rho_H}{(1-f_s) m w_H \rho_s} + 1} \right) \qquad \text{(H.23b)}$$

Equation H.23b is the density equation for the seeded propellant in liquid state. The astute reader will notice that the molar terms seen in the original formulation in equation H.17 are gone as well as the total volume terms. This equation is in terms of the molar fraction of the seed, the molecular weights, and the densities only. Further elementary algebraic manipulation will match the result seen in H.8. The assumption that the liquid propellant density can be found in terms of specific volume has been analytically and rigorously validated by using molar basis. This conclusion is shown in equation H.24.

$$\boldsymbol{\rho = \left(\frac{m_{f_s}}{\rho_s} + \frac{m_{f_H}}{\rho_H} \right)^{-1} = \frac{\rho_H \rho_s [(1-f_s) m w_H + f_s m w_s]}{(1-f_s) m w_H \rho_s + f_s m w_s \rho_H}} \qquad \text{(H.24)}$$

H.3 General Derivation of the Ideal Rocket Equation

Tsiolkovsky's ideal rocket equation explains the relationship between the amount of propellant onboard a rocket, the exit velocity of the propellant, and the change in velocity that the rocket will experience if it used all of its propellant. This equation uses the ideal rocket model which assumes that the sum of all external forces is equal to zero. In other words, the effects of gravity and air resistance are neglected.

Recall that force F is the change in momentum P with respect to time or $\frac{dP}{dt}$. Using this, it is be stated that the sum of all external forces on the rocket will equal the total change in momentum during a time interval. Equation H.25 provides the definition of force in terms of momentum in the differential form.

$$\sum_{i=1}^{n} F_i = \frac{d}{dt}\left(P_f - P_i\right) = \frac{dP}{dt} \tag{H.25}$$

It is also known that the momentum equals mass times velocity or $P = mv$. Furthermore, the initial momentum is the momentum P_i of the rocket with mass m fueled with propellent of mass dm. This rocket is travelling at an initial velocity V with respect to the observer. Therefore, P_i can be defined as seen in equation H.26.

$$P_i = (m + dm)V = mV \tag{H.26}$$

In a similar way, the final momentum P_f is also defined. By expelling the propellant of mass dm, the rocket gained or "changed" its velocity by dV. Moreover, the principle of conservation of momentum states that the sum of momentums before a collision is equal

to the sum of momentums after a collision. In this case, the "collision" is the ejection of the propellant at velocity V_e. It can then be said that the rocket became two objects where the first object is the rocket with mass m and velocity $V + dV$ and the second object is the propellant with mass dm and velocity V_e. The final momentum can then be defined as seen in equation H.27.

$$P_f = m(V + dV) + dmV_e \tag{H.27}$$

Putting equation H.26 and H.27 together will yield equation H.28.

$$d(P_f - P_i) = (m(V + dV) + dmV_e) - (m + dm)V \tag{H.28}$$

By algebraic simplification, equation H.28 reduces to H.29.

$$d(P_f - P_i) = mdV - dm(V - V_e) \tag{H.29}$$

The form of the rocket equation does not account for the velocity of the propellant with respect to the rocket v_e. However, v_e can be defined as $v_e = V - V_e$ which is found in equation H.29. Substituting v_e into equation H.28 and replacing $d(P_f - P_i)$ in equation H.25 with equation H.29 will yield equation H.30.

$$\sum_{i=1}^{n} F_i = \frac{mdV - v_e dm}{dt} \tag{H.30}$$

The ideal rocket model assumes that there are no external forces such as gravity or air resistance acting on the rocket, therefore, these forces can be set to zero. The exit velocity of the propellant with respect to the rocket v_e can be assumed to be constant while

the mass m and velocity V of the rocket are always changing, and therefore, considered to be variables. This will result in a differential equation H.31.

$$m\frac{dV}{dt} - v_e\frac{dm}{dt} = 0 \tag{H.31}$$

Multiplying both sides by dt and rearranging will yield equation H.32.

$$dV = \frac{v_e}{m}dm \tag{H.32}$$

The general solution to this differential equation will yield an arbitrary constant. This can be avoided by integrating both sides of the equation between the limits of travel. These limits of travel are defined by initial and final values. The initial values are defined as the initial mass of the rocket or wet mass m_i and initial velocity of the rocket or V_i. The final values are defined as the final mass of the rocket or dry mass m_f and final velocity of the rocket or V_f. Applying these limits will result in equation H.33.

$$\int_{V_i}^{V_f} dV = \int_{m_i}^{m_f} \frac{v_e}{m}dm \tag{H.33}$$

Evaluating the integrals between these limits will yield the famous Tsiolkovsky's Rocket Equation H.34.

$$\boldsymbol{\Delta V = V_e \ln\left(\frac{m_i}{m_f}\right)} \tag{H.34}$$

H.4 Derivation of the Seeded Propellant Initial Volume

From Tsiolkovsky's equation, it is possible to derive the amount of propellant volume required to achieve a specific change in velocity given the propellant seed amount. This will require the utilization of idealized compressible flow theory as well as the previously derived specific heat capacities and density formulas. Dissecting Tsiolkovsky's equation reveals that the exit velocity is nothing more than the exit Mach number multiplied by the speed of sound at the nozzle exit. Both of these can be found relatively easy provided that the stagnation temperature T_0 and throat area to exit area ratio $\frac{A^*}{A_e}$ are known. The exit Mach number M_e is determined numerically from equation 4.5 given that this equation is transcendental. Assuming that the stagnation temperature and pressure inside the chamber are known, an analytical equation for the initial propellant volume, based on the molar percentage of the seed inside the propellant, can be found. The exit velocity, shown in equation H.35, is a required parameter.

$$V_e = M_e\sqrt{\gamma R T_e} \tag{H.35}$$

Equation 4.2 shows the relationship between the stagnation temperature and the temperature at any point in the nozzle based on the ratio of specific heats and Mach number. The ratio of specific heats, equation 2.5, will change as a function of the molar fraction of seed. By analyzing equations 4.39a and 4.39b for the specific heats of a mixture, it becomes evident that these equations depend on the temperature as well as the pressure at any given point inside the nozzle. Furthermore, the temperature and pressure inside the nozzle depends on the ratio of specific heats as well as the Mach number at that point given by a

transcendental equation. The result of all of this is that a single analytical equation for the exit velocity cannot be analytically derived. To show this, equations 4.17a and 4.17b will be placed into equation 2.5 and the gas constant *R* will be replaced with $\frac{\Re}{\sum_{i=1}^{n} f_{X_i} mw_{X_i}}$ resulting in equation H.36. This equation already shows the necessity for evaluating the specific heats at the temperature and pressure of interest.

$$\gamma_x = \frac{c_{p_x}}{c_{v_x}} = \frac{\sum_{i=1}^{n} f_{m_i} c_p(P_x, T_x)_i + P_x \left[\frac{2\left(\sum_{i=1}^{n} f_{m_i} A_{0i}^{1/2}\right)^2}{\frac{\Re}{\sum_{i=1}^{n} f_{X_i} mw_{X_i}} T_x^2} + \frac{12 \sum_{i=1}^{n} f_{m_i} c_i}{T_x^4} \right]}{\sum_{i=1}^{n} f_{m_i} c_v(P_x, T_x)_i + P_x \frac{6 \sum_{i=1}^{n} f_{m_i} c_1}{T_x^4}} \qquad \text{(H.36)}$$

Simplifying this will yield equation H.37.

$$\gamma_x = \frac{T_x^4 \Re \sum_{i=1}^{n} f_{m_i} c_p(P_x, T_x)_i + 2P_x \left[T_x^2 \sum_{i=1}^{n} f_{X_i} mw_{X_i} \left(\sum_{i=1}^{n} f_{m_i} A_{0i}^{1/2}\right)^2 + 6\Re \sum_{i=1}^{n} f_{m_i} c_i \right]}{\Re\left(T_x^4 \sum_{i=1}^{n} f_{m_i} c_v(P_x, T_x)_i + 6P \sum_{i=1}^{n} f_{m_i} c_1\right)} \qquad \text{(H.37)}$$

Further, replacing T_x and P_x with equations 4.2 and 4.3 respectively, will show the interdependence of the ratio of specific heats and the necessity of the Mach number which is a solution to a transcendental equation 4.5. This would result in an equation too lengthy to put here. It should be noted that since the ratio of specific heats changes as the exhaust flows through the nozzle, some value of the ratio of specific heats between the stagnation point inside the chamber and the exit conditions at the nozzle must be found in order to use a single value to find the true exit conditions and exit velocity. In order to do this, an engine model was constructed and matched to experimental data of the PEWEE-1 NERVA derived engine including the physical engine parameters [18]. The process of building this

model was explored in Chapter 5. At this time, the fitted ratio of specific heats to experimental data will be denoted by $\bar{\gamma}$ being a weighted average.

In equation H.35, the gas constant R was replaced by $\frac{\Re}{\sum_{i=1}^{n} f_{X_i} mw_{X_i}}$ and the exit temperature T_e was replaced by $\frac{T_0}{1+\frac{\bar{\gamma}-1}{2}M_e^2}$ which will yield the general expression for the exit velocity of a propellant with n components shown in equation H.38.

$$V_e = M_e \sqrt{\bar{\gamma} \cdot \frac{\Re}{\sum_{i=1}^{n}\left(f_{X_i} mw_{X_i}\right)} \cdot \frac{T_0}{1+\frac{\bar{\gamma}-1}{2}M_e^2}} \tag{H.38}$$

Algebraically cleaning this equation up will eventually lead to equation H.39.

$$V_e = M_e \sqrt{\frac{2\bar{\gamma}\Re T_0}{[2+(\bar{\gamma}-1)M_e^2]\sum_{i=1}^{n}\left(f_{X_i} mw_{X_i}\right)}} \tag{H.39}$$

Going back to Tsiolkovksy's equation H.34, m_i and m_f must be expressed in terms of propellant volume $\forall$ and density ρ. Based on current Mars vehicle estimates, the vehicle must reserve 10% of the propellant mass for startup sequence, residual propellant in ducts, etc. [4] This report also discusses the vehicle dry mass. In order to keep the equations general, the reserve propellant mass fraction will be denoted by $f_{\forall}$. Putting this together will yield the initial mass and the final mass shown in equations H.40 and H.41 respectively in terms of propellant volume $\forall$ and density ρ shown in equation 4.9.

$$m_i = \rho \forall_i + m_{dry} = \frac{\forall_i}{\sum_{i=1}^{n}\left(m_{f_i} v_i\right)} + m_{dry} \tag{H.40}$$

$$m_f = \frac{\forall_f}{\sum_{i=1}^{n}\left(f_{m_i} v_i\right)} + m_{dry} = \frac{f_\forall \forall_i}{\sum_{i=1}^{n}\left(f_{m_i} v_i\right)} + m_{dry} \tag{H.41}$$

Putting equations H.40, H.41, and H.38 into H.34 will yield Tsiolkovksy's equation in terms of volume and density of a propellant with *n* components shown in equation H.42. Equation H.43 shows equation H.42 with the two species propellant.

$$\Delta V = M_e \sqrt{\frac{2\bar{\gamma}\Re T_0}{\left[2 + (\bar{\gamma} - 1)M_e^2\right]\sum_{i=1}^{n}\left(f_{X_i} m w_{X_i}\right)}} \ln\left(\frac{\frac{\forall_i}{\sum_{i=1}^{n}\left(f_{m_i} v_i\right)} + m_{dry}}{\frac{f_\forall \forall_i}{\sum_{i=1}^{n}\left(f_{m_i} v_i\right)} + m_{dry}}\right) \tag{H.42}$$

$$\boldsymbol{\Delta V = M_e \sqrt{\frac{2\bar{\gamma}\Re T_0}{[2 + (\bar{\gamma} - 1)M_e^2][(1 - f_s) m w_H + f_s m w_s]}} \ln\left(\frac{\forall_i \frac{\rho_H \rho_s [(1 - f_s) m w_H + f_s m w_s]}{(1 - f_s) m w_H \rho_s + f_s m w_s \rho_H} + m_{dry}}{f_\forall \forall_i \frac{\rho_H \rho_s [(1 - f_s) m w_H + f_s m w_s]}{(1 - f_s) m w_H \rho_s + f_s m w_s \rho_H} + m_{dry}}\right)} \tag{H.43}$$

Figure 4.3 showed the comparison among argon, krypton, and xenon for the percent of ΔV increase for a specified $\forall_i$ using equation H.43 with vehicle specifications taken from reference [4].

Equation H.43 is solved for the initial volume $\forall_i$ showed in equation H.44.

$$\boldsymbol{\forall_i = m_{dry} \sum_{i=1}^{n}\left(f_{m_i} v_i\right) \frac{\exp\left(\frac{\Delta V}{M_e \sqrt{\frac{2\bar{\gamma}\Re T_0}{\left[2 + (\bar{\gamma} - 1)M_e^2\right]\sum_{i=1}^{n}\left(f_{X_i} m w_{X_i}\right)}}}\right) - 1}{1 - f_\forall \exp\left(\frac{\Delta V}{M_e \sqrt{\frac{2\bar{\gamma}\Re T_0}{\left[2 + (\bar{\gamma} - 1)M_e^2\right]\sum_{i=1}^{n}\left(f_{X_i} m w_{X_i}\right)}}}\right)}} \tag{H.44}$$

Applying the two species propellant to equation H.44 will yield the equation for the required initial propellant volume in terms of the seed molar fraction for a given ΔV as shown in equation H.45.

$$\forall_i = \frac{m_{dry}}{\frac{\rho_H \rho_s [(1-f_s)mw_H + f_s mw_s]}{(1-f_s)mw_H \rho_s + f_s mw_s \rho_H}} \frac{\left[\exp\left(\frac{\Delta V}{M_e \sqrt{\frac{2\bar{\gamma}\Re T_0}{[2+(\bar{\gamma}-1)M_e^2][(1-f_s)mw_H + f_s mw_s]}}}\right) - 1\right]}{\left[1 - f_\forall \exp\left(\frac{\Delta V}{M_e \sqrt{\frac{2\bar{\gamma}\Re T_0}{[2+(\bar{\gamma}-1)M_e^2][(1-f_s)mw_H + f_s mw_s]}}}\right)\right]} \quad \text{(H.45)}$$

APPENDIX I

Supplementary Component Temperature and Pressure Distribution Graphs

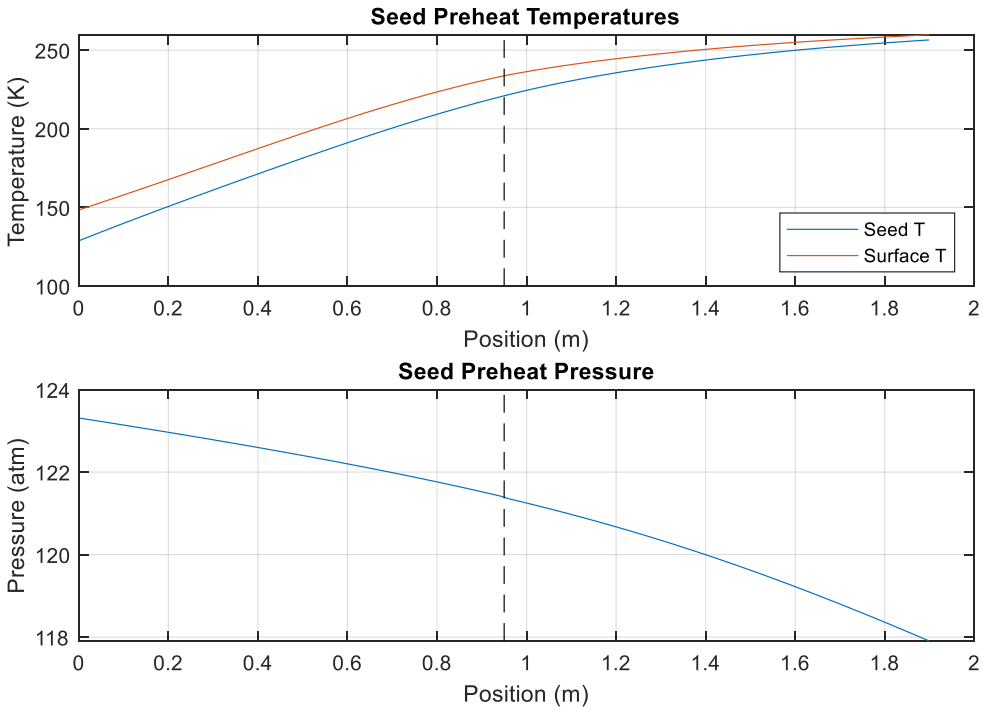

Figure I.1: Krypton Preheating Temperature and Pressure at Maximum Concentration

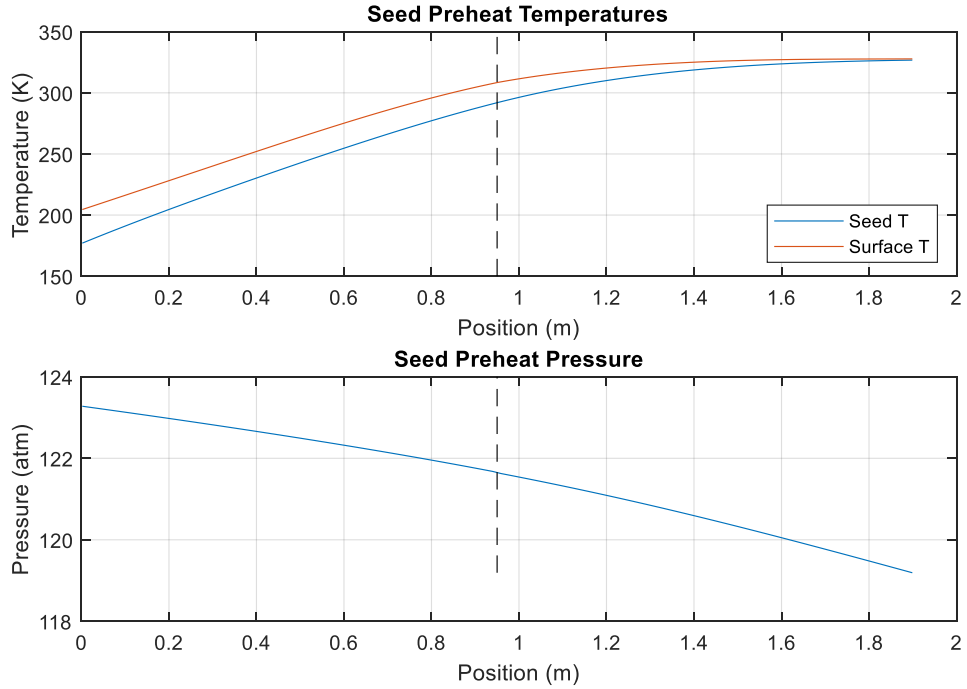

Figure I.2: Xenon Preheating Temperature and Pressure at Maximum Concentration

WORKS CITED

[1] W. H. Robbins and H. B. Finger, "A Historical Perspectyive of the NERVA Nuclear Rocket Engine Technology Program," Analytical Engineering Corporation, North Olmsted, Ohio, 1991.

[2] J. Stanfield, "NASA.gov," NASA, 2 August 2017. [Online]. Available: https://www.nasa.gov/centers/marshall/news/news/releases/2017/nasa-contracts-with-bwxt-nuclear-energy-to-advance-nuclear-thermal-propulsion-technology.html. [Accessed 24 June 2019].

[3] R. C. Joyner, M. Eades, J. Horton, T. Jennings, T. Kokan, D. J. H. Levack, B. J. Muzek and B. Reynolds Christopher, "LEU NTP Engine System Trades and Mission Options," in *Nuclear and Emerging Technologies for Space, American Nuclear Society*, Richland, WA, February 25-28, 2019.

[4] "Architectural Analysis Summary Baseline," Aerojet Rocketdyne, 2018.

[5] T. J. Rudman and K. L. Austad, "The Centaur Upper Stage Vehicle," Lockheed Martin, Denver, CO, 2002.

[6] B. Palaszewski, "High Power Electric and Advanced Space Propulsion: Making the Impossible Possible," in *National Atomic Museum*, Albuquerque, NM, 2005.

[7] J. W. Clark and G. H. McLafferty, "Summary of Research on the Nuclear Light Bulb Reactor," United Aircrajt Research Laboratories, 1971.

[8] H. J. Hoge and R. D. Arnold, "Vapor Pressures of Hydrogen, Deuterium, and Hydrogen Deuteride and Dew-Point Pressures of Their Mixtures," *Journal of Research of the National Bureau of Standards*, vol. 47, no. 2, pp. 63-74, 1951.

[9] A. L. Aureon, Z. E. Thomas and L. D. Thomas, "Mars Transport Optimization," in *Joint Army Navy NASA Air Force Joint Subcommittee Meeting*, Long Beach, CA, 2018.

[10] Энергия [Energia], "Ракетно-космический комплекс Н1-Л3 [Space-Rocket Complex N1-L3]".

[11] R. Zubrin, "Nuclear Rocket Using Indigenous Martian Fuel," Martin Marietta Astronautics, 1991.

[12] H. H. Voge, "Carbon-Hydrogen Bon Strengths in Methane," *The Journal of Chemical Physics*, vol. 16, no. 984, pp. 984-986, 1948.

[13] "Bond Dissociation Energies in Simple Molecules," U.S. Department of Commerce, National Nurea of Standards, 1970.

[14] A. H. White and W. Melville, "The Decomposition of Ammonia at High Temperatures," *American Chemical Society,* vol. 27, no. 4, pp. 373-386, 1905.

[15] G. H. McLafferty, "Gas-Core Nuclear Rocket Engine Technology Status," *Journal of Spacecraft and Rockets,* vol. 7, no. 12, pp. 1391-1396, 1970.

[16] S. K. Borowski, D. R. McCurdy and T. W. Packard, "Nuclear Thermal Propulsion (NTP): A Proven Growth Technology for Human NEO / Mars Exploration Missions," NASA, Cleveland, OH, 2012.

[17] W. J. Emirch, Principles of Nuclear Rocket Propulsion, Kidlington, Oxford, United Kingdom: Butterworth-Heinemann is an imprint of Elsevier, 2016.

[18] "Rover/NERVA-Derived Near-Term Nuclear Propulsion," Rockwell International, 1992.

[19] M. Berman, U. Kaldor, J. Shmulovich and S. Yatsiv, "Rydberg states and the observes spectrum ArH," *Chemical Physics,* vol. 63, pp. 165-173, 1981.

[20] G. J. Schrobilgen, "Krypton," Encyclopeadia Britannica Inc., 2018.

[21] M. Somayazulu, P. Dera, A. F. Goncharov, S. A. Gramsch, P. Liermann, W. Yang, Z. Liu, H.-k. Mao and R. J. Hemley, "Pressure-induced bonding and compound formation in xenon-hydrogen solids," *Nature Chemistry,* vol. 2, pp. 50-53, 2010.

[22] NASA, "Ion Propulsion," NASA, Cleveland, OH, 2016.

[23] J. E. Colvin and L. G. A, "Effect of Inert Propellant Injection on Mars Ascent Vehicle Performance," Sverdrup Technology, Brook Park, OH; Nashville, TN, 1992.

[24] M. V. Zagarola and J. A. McCormick, "High-capacity turbo-Brayton cryocoolers for space applications," *Science Direct*, vol. 46, pp. 169-175, 2006.

[25] G. N. Sapkale, S. M. Patil, U. S. Surwase and P. K. Bhatbhage, "SUPERCRITICAL FLUID EXTRACTION," *International Journal of Chemical Science*, vol. 8, no. 2, pp. 729-743, 2010.

[26] M. Poliakoff, "Supercritical Fluid Miscibility," June 27, 2019.

[27] T. M. Tomsik, "Performance Tests of a Liquid Hydrogen Propellant Densification Ground System for the X33/RLV," NASA, Cleveland, Ohio, 1997.

[28] T. M. Tomsik, "Recent Advances and Applications in Cryogenic Propellant Densification Technology," NASA, Cleveland, OH, 2000.

[29] J. H. Baik and A. T-Raissi, "R&D Processes for Increasing Density of Cryogenic Propellants at FSEC," *Cryogenics*, vol. 44, pp. 451-458, 2004.

[30] S. Mustafi, W. Johnson, A. Kashani, J. Jurns, B. Kutter, D. Kirk and J. Shull, "Subcooling for Longterm Duration In-Space Cryogenic Propellant Storage," in *AIAA Space 2010 Conference and Exposition*, Anaheim, CA, 2010.

[31] S. H. Ho and M. M. Rahman, "Three-dimensional Analysis for Liquid Hydrogen in a Cryogenic Storage Tank with Heat Pipe-Pump System," *Cryogenics,* vol. 48, pp. 31-41, 2008.

[32] M. S. Haberbusch, R. J. Stochl and A. J. Culler, "Thermally Optimized Zero Boil-Off Densified Cryogen Storage System for Space," *Cryogenics,* vol. 44, pp. 485-491, 2004.

[33] A. Aueron and D. Thomas, "Nuclear Thermal Propulsion Vehicle Scaling and the Importance of Densified Propellant," in *AIAA Propulsion & Energy Forum*, Indianapolis, IN, 2019.

[34] A. F. Mills and C. F. M. Coimbra, Heat Transfer 3rd Edition, San Diego, CA: Temporal Publishing LLC, 2016.

[35] S. Kakaç and A. Pramuanjaroenkij, "Review of convective heat transfer enhancement with nanofluids," *International Journal of Heat and Mass Transfer,* vol. 52, pp. 3187-3196, 2009.

[36] T. A. Davidson, "A Simple and Accurate Method for Calculating Viscosity of Gaseous Mixtures," International Bureau of Mines, Pittsburgh, PA, 1993.

[37] H. Cheung, L. A. Bromley and C. R. Wilke, "Thermal Conductivity of Gas Mixtures," *American Institute of Chemical Engineers,* vol. 8, no. 2, pp. 221-228, 1962.

[38] J. A. Beattie, "The Heat Capacities of real Gases and Mixtures of Real Gases," *Physical Review,* vol. 34, pp. 1615-1620, 1929.

[39] B. A. Stradi, J. F. Brennecke, J. P. Kohn and M. A. Stadtherr, "Reliable Computation of Mixture Critical Points," University of Notre Dame, Notre Dame, IN, 2000.

[40] A. Kreglewski, "Critical and Pseudocritical Pressure of Binary Mixtures," *Jounral of Physical Chemistry,* vol. 72, no. 6, pp. 2280-2281, 1968.

[41] I. Pioro and S. Mokry, "Thermophysical Properties at Critical and Supercritical Conditions," in *Heat Transfer - Theoretical Analysis, Experimental Investigations and Industrial Systems*, Rijeka, Croatia, InTech, 2011, pp. 573-592.

[42] T. Jennings, "PBM 3.0 Configuration and Discussion," Aerojet Rocketdyne, 2019.

[43] Aerojet Rocketdyne, "LEU NTP OMS/Cooldown Design Feasibility Status," NASA, 2019.

[44] D. Manski and G. Hagemann, "Influence of Rocket Design Parameters on Engine Nozzle Efficiencies," *Journal of Propulsion and Power,* vol. 12, no. 1, pp. 41-47, 1996.

[45] Y. Cengel and A. Ghajar, Heat and Mass Transfer: Fundamentals and Applications, New York, NY: McGraw-Hill, 2011.

[46] I. H. Bell, J. Wronski, S. Quoilin and V. Lemort, "Pure and Psuedo-pure Fluid Thermophysical Property Evaluation and the Open-Source Thermophysical Property Library CoolProp," *Industrial & Engineering Chemistry Research,* vol. 53, pp. 2498-2508, 2014.

[47] Y. A. Cengel, in *Heat Transfer: A Practical Approach*, Boston, MA, McGraw-Hill, 2003, p. 112.

[48] H. J. Hoge and R. D. Arnold, "Vapor Pressures of Hydrogen, Deuterium, and Hydrogen Deuteride and Dew-Point Pressures of Their Mixtures," *Journal of Research of the National Burea of Standards,* vol. 47, no. 2, pp. 63-74, 1951.

[49] W. Knuth, Interviewee, [Interview]. 6 June 2019.

[50] M. Sippel, R. Yamashiro and F. Cremaschi, "Staged Combustion Cycle Rocket Engine Design Trode-Offs for Future Advanced Passenger Transport," in *Space Propulsion*, Bordeaux, France, 2012.

[51] D. L. Ellis and D. J. Keller, "Thermophysical Proeprties of GRCop-84," NASA, Cleveland, OH, 2000.

[52] D. L. Ellis, "GRCop-84: A High-Temperature Copper Alloy for High-Heat-Flux Applications," NASA, Cleveland, OH, 2005.

[53] R. Kurz and K. Brun, "Gas Turbine Performance - What Makes the Map?," in *29th Turbomachinery Symposium*, Texas A&M University, 2000.

[54] Q. Z. Al-Hamdan and M. S. Y. Ebaid, "Modeling and Simulation of a Gas Turbine Engine for Power Generation," *Journal of Engineering for Gas Turbines and Power,* vol. 128, pp. 302-311, 2006.

[55] J. Gustafson, D. A. Raine, M. Stewart and J. T. Oswald, "Performance/Mechanical Analysis," NASA, 2019.

[56] Engineering ToolBox, "Ventilation Ducts - Roughness & Surface Coefficients," Engineering ToolBox, 2003.

[57] K. B. and A. E. Larsson, "Improvement of Reactor Fuel Element Heat Transfer by Surface Roughness," Aktiebolaget Atomenergi, Stockholm, Sweden, 1967.

[58] R. E. Williams, J. M. Rowe and P. Kopetka, "The Liquid Hydrogen Moderator At The NIST Research Reactor," in *Proceedings of the International Workshop on Cold Moderators for Pulsed Neutron Sources*, Lemont, IL, 1997.

[59] S. B. Ross, M. S. El-Genk and R. B. Matthews, "Thermal conductivity correlation for uranium nitride fuel between 10 and 1923 K," *Journal of Nuclear Materials,* vol. 151, pp. 313-317, 1988.

[60] J. Sreenivas, "Bends, Flow and Pressure Drop In," Thermopedia, 2011.

[61] V. Patel and P. Tsvetkov, "SNR EigenValue Uncertainty Quantification from Nuclear Data Sources," in *Nuclear and Emerging Technologies for Space, American Nuclear Society Topical Meeting*, Richland, WA, February 25-28, 2019.

[62] C. R. Joyner, *Conversation*, Indianapolis, IN, 2019.

[63] K. Benensky, "Summary of Historycal Solid Core Nuclear Thermal Propulsion Fuels," The Pennsylvania State University, 2013.

[64] "Chemicool," 2019. [Online]. Available: https://www.chemicool.com/elements/. [Accessed 2019].

[65] NIST Chemistry WebBook, NIST Standard Reference Databse Number 69, Gaithersburg, MD: National Institute of Standards and Technology, 2018.

[66] J. Finseth, "Overview of Rover Engine Tests," Sverdrup Corporation, Huntsville, AL, 1991.

[67] Materion, "A Guide to Designing and Fabricating with Beryllium," Materion, Elmore, OH, 2019.

[68] J. R. Lamarsh and A. J. Baratta, Introduction to Nuclear Engineering, Hoboken, NJ: Pearson, 2018.

[69] "Special Feature Section," *Neutron News*, vol. 3, no. 3, pp. 29-37, 1992.

[70] J. Cassibry, D. Thomas, R. Wood, R. Frederick and S. Kumar, "Development Plan for a Fission and Fusion Powered Propulsion System to Reach Mars in 45 Days," in *42nd Annual AAS Guidance and Control Conference*, Breckenridge, CO, 2019.

[71] B. Danciu, *Interplanetry Mission Design*, MathWorks, 2018.

[72] J. Tusek and M. Suban, "Experimental research of the effect of hydrogen in argon as a shielding gas in arc welding of higfh-alloy stainless steel," *Internaltional Journal of Hydrogen Energy*, vol. 25, pp. 369-376, 2000.

[73] P. C. T. De Boer and J. F. Hulet, "Performance of a hydrogen-oxygen-noble gas engine," *Internation Journal of Hydrogen Energy*, vol. 5, pp. 439-452, 1980.

[74] M. L. Meyer, S. M. Motil, T. F. Kortes and W. J. Taylor, "Cryogenic Propellant Storage and Transfer Technology Demonstration for Long Duration In-Space Missions," in *Space Propulsion 2012*, Bordeaux, France, 2012.

[75] J. A. Halchak, J. L. Cannon and C. Brown, "Materials for Liquid Propulsion Systems," NASA, 2015.

[76] R. D. V. Rao, C. S. Babu and S. V. Prabhu, "Effect of Turn Region Treatments on the Pressure Loss Distribution in a Smooth Square Channel with Sharp 180 Degree Bend," *International Journal of Rotating Machinery*, vol. 10, no. 6, pp. 459-468, 2004.